The Development of Bipolar Electrochemiluminescence Sensing Systems using Thin-layer Electrochemistry and AC Excitation

by

Songyan Yu

A dissertation submitted to the Graduate Faculty of
Auburn University
in partial fulfillment of the
requirements for the Degree of
Doctor of Philosophy

Auburn, Alabama
December 15, 2018

Keywords: Bipolar electrode chemistry, Electrochemiluminescence,
Thin layer, AC square wave

Approved by

Curtis Shannon, Chair, Andrew T. Hunt Professor of Chemistry & Biochemistry
Christopher J. Easley, C. Harry Knowles Professor of Chemistry & Biochemistry
Vince Cammarata, Professor Emeritus of Chemistry & Biochemistry
Wei Zhan, Associate Professor of Chemistry & Biochemistry

Abstract

Bipolar electrochemistry, which generates an asymmetric reactivity on the surface of conductive objects in a wireless manner, has become a promising field for various applications. It enables the coupling of anodic and cathodic redox reactions at the opposite ends of the bipolar electrode (BPE) and provides a new paradigm for electrochemical sensing. Electrochemiluminescence (ECL), the light-emitting process generated by electrochemical means, could transfer the electrochemical signal into light emission under bipolar electrochemistry. The primary goal of this dissertation is to develop reliable BPE ECL sensing systems of detecting electroactive species and bio-targets using thin-layer electrochemistry and AC square wave excitation with merits of high-throughput, miniaturization, multiplicity, versatility, low cost, and simple instrumentation.

Chapter 1 first presents a detailed literature review on the principle and background of bipolar electrochemistry with its relevant applications such as electrodeposition, electrocatalysts screening, and motion generation. Specifically, the ECL application in bipolar electrochemistry is discussed in detail on its history, mechanism, and application in analyte sensing. The concept and recent development of the closed BPE system are also illustrated.

Chapter 2 describes the process of designing the bipolar electrode thin-layer (BETL) ECL system in detecting electroactive species in a low-concentration range. 3D printing techniques are used to fabricate versatile bipolar cells containing the reporting system and a thin-layer structure. Preliminary tests of the BETL system are performed to investigate the effects of different cell configurations and experimental parameters. With the help of the pre-attempts of cell design, the final established BETL system with an isolated double-cell design is demonstrated. In addition to the ECL performance, simultaneous electrochemical simulation is employed to provide an insight view of the BETL system and correlate the electrical signal with the ECL response. Ferrocyanide/ferricyanide and hydroquinone/benzoquinone redox systems are studied, providing their concentration profiles and other important electrochemical parameters by addressing the real-time ECL response from electrochemical reactions within the thin-layer cell. Also, the electric field distribution in the BPE system is extensively

studied concerning many influential factors and it explains explicitly the ECL intensity variation during the experiment.

Chapter 3 highlights the development of the AC square wave bipolar ECL system with high sensitivity and flexibility. This ECL sensing system, in a closed configuration with the phase separation, is capable of amplifying the signal from the regeneration of analyte by employing the AC square wave excitation. Significant signal/noise gain is achieved by accumulating the ECL response over multiple measure-regenerate cycles. Ferricyanide in the solution, polymerized MB confined on the surface, MB-conjugated DNA monolayer, and DNA loop as a model of ECPA are respectively quantified. Also, the frequency-dependent electric field distribution is the AC BPE cell is characterized by the help of the solution potential measurement.

Chapter 4 focuses on the related studies to improve the performance of the AC square wave bipolar ECL system. Efforts have been taken including the modification of carbon electrodes, the use of a photon counting photomultiplier tube (PMT), and the MB intercalation method with DNA.

Chapter 5 summarizes the findings of the research. The recommended future work for both the BETL and AC square wave bipolar ECL system are stated according to the contributed topics to these projects.

Acknowledgments

First and foremost, I would like to express my deepest gratitude to my advisor, Dr. Curtis Shannon, for his invaluable guidance and general support during the entire course of my Ph.D. research. Without him, I would not have had the great opportunity to pursue my Ph.D. at Auburn University. His patience, motivation, and immense knowledge help me from a freshman who just graduated from the college to grow gradually as a research scientist. His expertise in electrochemistry and surface science has been such an inspiration and provided me with many creative ideas in the journey of research. As the chairman of our department starting from my second year, his great effort in balancing between the administrative work and our academic research has set a perfect role model for me to study. His many thoughtful suggestions, both at the scientific and personal level, will always be remembered in my entire professional career.

Next, I would like to offer my sincere gratitude for the incredible contributions from my committee members, Dr. Christopher Easley, Dr. Vince Cammarata, Dr. Wei Zhan in the direction of helpful insights and important suggestions for my research and the preparation of this dissertation. Dr. Easley has always been amicable and put me at ease every time talking with him. He is a constant source of support in providing useful guidance in many aspects related to my projects and allows me to work at any time in his lab. Dr. Vince Cammarata is one of the best teachers during my graduate study at Auburn. I will always remember his dedication and rigorous in teaching and remarkable ability to impart knowledge to the next generation. I am quite appreciated of him for agreeing to keep serving in my committee after his retirement. I would like to give my sincere appreciation to Dr. Wei Zhan for his concern and kind-hearted support towards me. I still remember his affirmation and encouragement to my assignments when I took the photochemistry class. He gave me generous access to his laboratory and research facilities such as AFM. His forgiveness helped me go through the hard time when a malfunction happened on my hand. A great acknowledge should also be sent to Dr. Minseo Park, who is willing to be my university reader and participate in the process towards the final defense. I have not imaged I could get his cordial reply immediately after I sent the request. It seems like you are trying to cross a raging river, but in a twinkling, you have already been on the other side of it. It is nice of him to serve as my university reader.

A special thanks to Prof. Masoud Mehrgardi from the University of Isfahan as who is penchant in electrochemistry. Not only by his insightful comments and encouragement but also for his numerous key advice that incented me to widen my research from various perspectives. I learned from him many experimental techniques and tips for research by his selfless and diligent instruction. He is a tremendous mentor both in the academic field and life.

I am particularly thankful to all the previous and current group members. I am really lucky to work with my awesome lab mates. Thanks to the senior graduate students: Sanjun Fan, Li Zhang and Apu Mazumder who trained me on many aspects on electrochemistry and DNA assay. My thanks go as well to the current awesome lab mates: Buhua Wang, MD Akteruzzaman, Waliul Khan and Humaira Yeasmin for the consecutive conversations, collaborate work and simply for being great colleagues. I am honored to work with them. Best of luck to them and new coming members would be in our laboratory in the future.

The acknowledge must be made to students from Dr. Easley's group for many valuable collaboration opportunities. I want to show my gratitude to Dr. Jessica Brooks and Dr. Xiangpeng Li for their enthusiastic help in microfluidic chips and data acquisition. I would like to say thanks a lot to Dr. Subramanian Somasundaram for many patient and extensive discussions between us that enlightened me so much. I am willing to pay tribute to Mark Holtan for his continuous assistance to me including 3D printing, photolithography, and electronics. I am also very thankful to Dr. Juan Hu for her support during the five years in the lab.

My thanks also go to Chao Li and Shamin Iqbal and Dr. Michael Miller for helping and training me with skills of atomic force microscopy, scanning electron microscopy, transmission electron microscopy.

Many thanks go to Dr. Christian R. Goldsmith, Dr. Steven Mansoorabadi, Dr. Bradley L. Merner, Dr. Konrad Patkowski. From their courses, I learned not only the knowledge but also the intelligence and rigorous scientific attitude. I have also received so much support from the faculty, administration assistants, and graduates in our department. I own gratitude for all my success and accomplishments to them as well. Many thanks to all the graduate students in our department for creating such a harmonious atmosphere.

Lastly, but my first priority, a special thanks to my family. Words cannot express how grateful I am to my parents: my mother, Guizhen Gao, and my father, Quande Yu, for all of the sacrifices that you have made on my behalf. Your love for me was what sustained me thus far. I would also like to thank all my relatives and my friends, no matter where they are, for all the matters that shape me into a particular being who I am now.

Table of Contents

List of Figures

List of Schemes

List of Tables

Chapter 1 Introduction

1.1 Bipolar Electrochemistry

1.1.1 Basic Concept and Background

Over the past decade, bipolar electrochemistry (BPE) which generates an asymmetric behavior on the surface of conductive materials in the absence of a direct ohmic contact (wireless), has emerged as a useful tool in various aspects of applications, such as electrodeposition[1], concentration enrichment[2-9], sensing[10-13], photosplitting[14], catalysis[15], and motion generation[16,17]. With its novel configuration, it is capable of overcoming many drawbacks of existing electrochemical techniques and apparatuses, including the difficulty of making electrical contact to subscale electrodes, nonuniform potential difference control over the electrode surface, and simultaneous regulation and readout of large electrode arrays.

In bipolar electrochemistry, a conducting object, which is called a bipolar electrode (BPE), is positioned in an electrolyte solution under the influence of an external electric field, which is applied between two driving electrodes by a power source. Without the electric field, the immersed object is at a mixed potential E_m. When the electric field is applied, due to the current flowing through the system, a polarization of two sides of this object occurs and makes it into separate cathodic and anodic regions. Both anodic and cathodic reactions can occur on different sides of the same electrode.

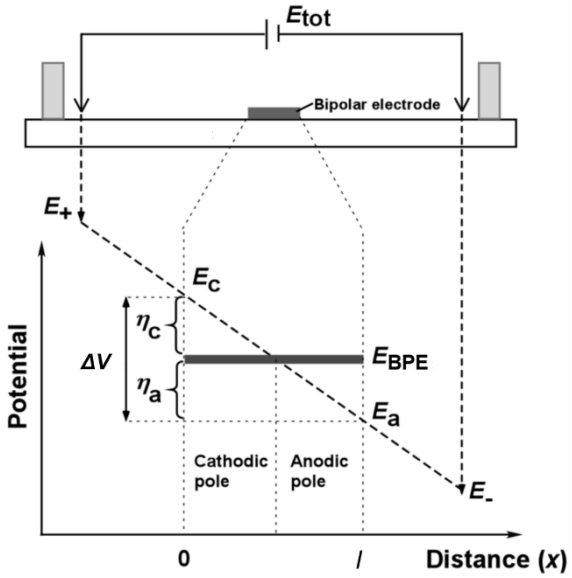

Scheme 1.1.The principle of bipolar electrochemistry and its configuration[18]. Adapted with permission from [18]. Copyright © (2009) American Chemical Society.

The principle of bipolar electrochemistry is illustrated in Scheme 1.1, a conducting object with a length of l is immersed in the electrolyte without wire connection. When an external voltage (E_{tot}) is applied between two driving electrodes by the power supply, a linear potential gradient is established in the electrolyte solution. If we assume the distance between the two driving electrodes is L and ignore the inevitable potential drop on the two driving electrodes, then the electric field (potential gradient) in the solution is given by

$$\delta = \frac{E_{tot}}{L}$$

As a consequence of the electric field, the BPE, as an equipotential body, will float to an equilibrium potential value E_{BPE}, adjusted by the surrounding solution potential. Accordingly, there would be a potential difference at each lateral position of the electrode/solution interface. In other words, a polarization potential, given by the difference of the solution potential with respect to the BPE, arises. It will serve as the driving force that leads to electrochemical reduction and oxidation at the cathodic region and anodic region, respectively[19]. If we assume the solution potential at the cathodic end of the bipolar electrode is E_c, and at the anodic end is E_a. $E_c - E_a$, as a fraction of E_{tot}, denote as ΔV, is the maximum polarization potential difference between the extremities of the BPE. It is proportional to the length (l) of the bipolar electrode and the applied voltage (E_{tot})[18,20].

$$\Delta V = E_c - E_a = \delta \times l = \frac{E_{tot}}{L} \times l$$

Note that in a more accurate calculation, the numerator over L should not be the applied voltage E_{tot} but the potential difference between the two driving electrodes due to the inevitable potential drop at the driving electrode/solution interface. That is the overpotential required for the electrochemical reaction to happen at the driving electrode and to provide the current that polarizes the BPE. One idea of minimizing the interfacial potential drop and maximizing the utilization of potential drop across the solution is to put the bipolar electrode in a microchannel that almost has the same length as the electrolytic bath in which it resides[18]. Because of the high resistance of the channel, the overwhelming majority of E_{tot} is dropped linearly across the length of the microchannel. It facilitates the accurate measurement of the potential difference across the BPE and quantitively theoretical analysis of reactions happen at both BPE ends. In addition, by using this configuration, we can significantly reduce the required applied voltage and also weaken the reaction happening on both driving electrodes by introducing a considerable solution resistance. As a result, unexpected surface chemistry on the driving electrode and the massive concentration change in the solution can be prevented.

The value of ΔV is directly related to the reactivity at the ends of the polarized bipolar electrode interface. With a sufficient ΔV, reduction and oxidation can take place at the cathodic end and anodic end

simultaneously. The object behaves at the same time as a cathode and anode, that is why we refer it as a bipolar electrode (BPE). More accurate speaking, there is a particular location where the potential of the solution equals $E_{BPE.}$ On both the cathodic and anodic poles, the overpotential (polarization potential) η, noted as the potential difference between the solution and the electrode at a location along *l* is the driving force that leads to the reduction and oxidation, respectively (η_c for the overpotential at the cathodic end and η_a for the overpotential at the anodic end). Because of charge neutrality within this conductive bipolar electrode, an electrochemical process at one pole of the BPE must be coupled electrically at the same rate by an opposite process at the other pole.

For example, electroactive species, R and O′, can undergo the following reactions: $R - ne^- \rightarrow O$ and $O' + ne^- \rightarrow R'$. Therefore, the minimum potential value, ΔV_{min}, that is needed to trigger these two reactions at the polarized interfaces at both extremities of the bipolar electrode can be obtained from the Nernst equation regarding the standard potentials of the two redox couples and their concentrations in the solution. An accurate way (for experimental conditions) to determine this value, would be to perform a cyclic voltammetry experiment, using a comparable material to the BPE as working electrode[21]. If the condition $\Delta V > \Delta V_{min}$ is fulfilled, these faradaic reactions occur spontaneously at both extremities.

The BPE could be any conductive material, such as carbon, metals, semiconductors or coated insulators, with any characteristic dimension and geometry. One important point is the substrate must have a higher conductivity than the surrounding medium. The dimension of the BPE, which determines the electric field applied across it, will have a direct influence on the kinetics of the two redox reactions by determining the magnitude of polarization. In the case of the electrodeposition process, this will, therefore, have a considerable influence on the morphology of the deposit, ranging from crystalline to amorphous.

Bipolar electrochemistry, like conventional electrochemistry, requires an electrolyte that can support the separate oxidation and reduction reactions. A very concentrated electrolyte, with a large number of free mobile ions, is too conductive to support the electric fields to induce bipolar electrochemistry. A dilute electrolyte, with a low number of free or mobile ions, is a relatively poor conductor and can support the electric fields needed for bipolar electrochemistry. This difference in conductivity provides a driving force for the movement of current through the bipolar electrode.

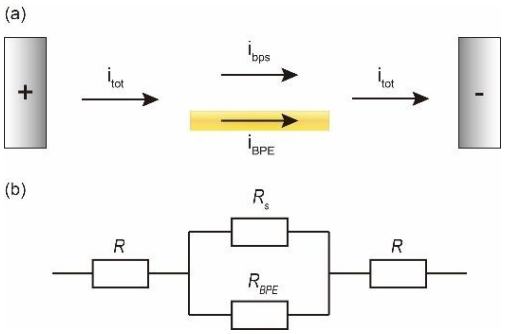

Figure 1.1.Current flow and (b) Resistance distribution in the open BPE cell.The total current i_{tot} flowing through the BPE cell (in an open system) could be divided into two fractions in the vicinity of the bipolar electrode[21]. One fraction of it, i_{BPE}, is the faradaic current which flows through the bipolar electrode via electronic conduction. This current ensures the electrochemical reactions occurring at both ends of the BPE. The other fraction, the bypass current i_{bps}, is the current flow in the solution caused by migration of charged species. There is a direct relation between these three terms (Figure 1.1(a)):

$$i_{tot} = i_{bps} + i_{BPE}$$

$$\frac{i_{BPE}}{i_{tot}} = 1 - \frac{i_{bps}}{i_{tot}} = \frac{R_S}{R_S + R_{BPE}}$$

The relative fraction of the current passing through the solution and the electrode depends on the solution resistance R_s, and global resistance R_{BPE} from both electron and mass transfer effect (Figure 1.1(b)). Due to a much smaller R_s than R_{BPE}, the solution resistance determines the electric field in the solution in this parallel circuit. As a result, the potential difference obtained at the two ends of the BPE/solution interface is mainly governed by the uniform potential gradient across the solution. The determination of i_{BPE} can be achieved directly through the use of split bipolar electrodes[22]. Increasing the ionic strength of the solution leads to an increase in the bypass current. Comparably, the majority of the total current passes through the electrolyte solution rather than through BPE in an open system. Therefore, the deformation of the electric field by faradaic reactions on the BPE will be negligible and resemble a linear electric field if the conductivity of the electrolyte solution is high. Using a very conductive bipolar electrode and a high-resistance solution will minimize i_{bps}. Another approach to completely overcome the bypass current is to use a closed bipolar configuration, so the current could only flow through the bipolar electrode.

When considering the kinetics, we could build up a straightforward model of electron-transfer limited reaction for qualitatively understanding the faradaic current profile along the bipolar electrode by using the Butler–Volmer relation[23]. Several aspects can influence the kinetic behavior of bipolar electrochemistry. First, the applied voltage dominates the interfacial potential difference across the

length of the BPE, and consequently the electrochemical reactions happening on the surface. Second, the electrode nature and geometry (both driving and the bipolar electrodes) also play an essential role in determining the reaction condition. In addition, electrochemical processes, like adsorption, heterogeneous electron transfer, and mass transfer, would have effects on the bipolar electrochemistry, like what is happening in conventional electrochemistry. For example, when dealing with large bipolar electrodes or high electric fields, there would be a competition between electron and mass transfer (including diffusion and migration of electroactive species). In bipolar electrochemistry, the potential gradient across the solution is treated as even and uniform. However, when i_{BPE} becomes comparable with i_{bps}, as in cases when the BPE is a similar size as the driving electrode, then the electric field distribution influenced by the generated concentration gradients should also be taken into account[24-26].

As found by the researchers, instead of a single object, the bipolar electrode could also be assembled by connecting separated electrodes electrically together. Nyholm and co-workers recognized that two individual electrodes could be connected outside the electrochemical cell and thus act as a single bipolar electrode. They found that the induced potential difference between two microband electrodes in capillary electrophoresis under high separation voltage increased as a function of the applied voltage and interelectrode distance. In addition, the induced current was proportional to the potential difference and concentration of the redox couple in the solution. Consequently, this phenomenon is realized useful in characterizing the behavior of bipolar electrochemistry. Based on this method, the current flowing through can thus be measured by creating split BPEs and wiring them to an ammeter exterior to the fluidic space directly[18]. They also measured the solution potential and current density distribution in the BPE system, and the result was examined by surface plasmon resonance (SPR) spectroscopy. Two small modified reference electrode tips were put in different locations in the solution under the externally applied voltage and connected outside to a voltmeter. As a result, the exact solution potential difference between these two specific points was accurately measured, reflecting the electric field across the solution. Besides, the current density distribution at the BPE/solution interface could be acquired by positioning the tips close to the BPE surface. The voltage between these two very closely placed reference electrode tips was proportional to the current density passing in the region of the tips[27].

In the theoretical work done by Crooks' group, they addressed the BPE potential profile by using a split electrode design. The middle portion of the bipolar electrode was removed, leaving two microband electrodes separated at their outer edges. These two microband electrodes were connected outside by a voltmeter to measure the potential difference. By way of connecting the two split electrodes to an ammeter instead of a voltmeter, the current that should pass through a continuous BPE of the same length as the separating distance between the two microbands could also be measured directly. This measured current is in great agreement with the calculated current from the theoretical assumption.

1.1.2 Applications of Bipolar Electrochemistry

As mentioned before, bipolar electrochemistry is a phenomenon that has been known for quite a long time but was less popular for a few decades. At that time, the community of chemists mainly worked in the field of electrolysis, corrosion, and batteries[24,28]. However, recently, it has attracted considerable attention. The fabrication of electric contacts between Cu particles by bipolar electrochemistry opened the door to interests of materials and nanoscience. It has various aspects of applications, such as electrodeposition, ECL, motion generation[29], sensing[30], separation, detection, photosplitting[31], and catalysis. Some applications will be discussed here as an insightful understanding of bipolar electrochemistry.

1.1.2.1 Electrodeposition

One topic related to bipolar electrochemistry is Janus particles, named after the Roman god depicted with two faces. These objects exhibit different physicochemical properties on two opposite sides and are key components of a significant number of applications that have attracted an increasing interest in the past several years[32,33]. Special effects are devoted to the synthesis and surface modification of these anisotropic objects, endowing them with many amazing features as a unique class of materials ranging from solid-state libraries, sensor, motion generation, optics, electronic devices, self-healing materials to photocatalysis. So far, the great majority of methods existing for the generation of Janus particles break their symmetry by using interfaces or surfaces but are limited by a low time-space yield[31]. Because bipolar electrochemistry allows the bulk production in a single-step technique with a highly controlled deposit structure and morphology as well as a significantly improved yield[34], it now becomes an appealing and unique tool for bulk and wireless synthesis of asymmetric materials compared with other techniques such as microfluidic systems[35], protection/deprotection mechanisms[36], lithography[37], Langmuir–Blodgett deposition[38], microcontact printing[39], and metal stripping[40]. The production quantity often limits the latter techniques because the modification occurs in a two-dimensional reaction space. However, breaking the asymmetry by way of bipolar electrochemistry has two significant features. First, the gradient of polarization potential along the surface of the object could be manipulated; second, it allows an intrinsically asymmetric reactivity by the varying potential difference between the solution and the BPE.

For metal deposition, the pioneering works were carried out by Bradley's group. They have extensively studied the use of BPE for electrodeposition of Pd catalysts onto micro-scale particles, graphite powder, carbon nanotubes, and nanofibers[41-43]. For the first publication, a Pd salt was reduced at the cathodic pole with the organic solvent oxidized at the anodic pole on the micrometer-sized amorphous graphite particles[44]. The etched membranes or cellulose papers with one absorbing layer of particles were used to ensure their immobilization.

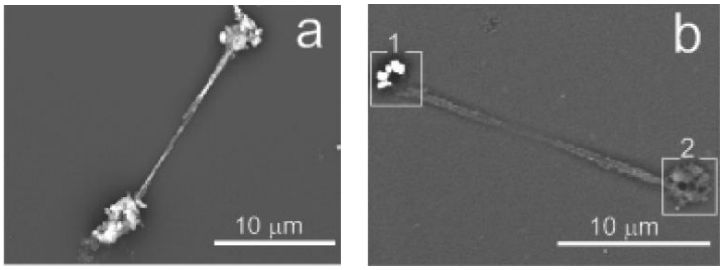

Figure 1.2.Symmetric (a) and antisymmetric (b) dumbbell-like object with copper deposits on both sides by pulsed bipolar electrodeposition[45]. Adapted with permission from [45]. Copyright © (2011) American Chemical Society.

Based on their development of controlled bipolar micro- and nanoelectrodeposition of Pd catalysts, gold[34], copper[46], nickel[47], and many other metals have been successfully deposited on various types of substrates. For example, Bohn et al. experimented to deposit Cu on a very thin Au electrode[48]. Fattah took advantage of BPE to functionalize carbon substrates with asymmetric copper particles electrodeposited from a bulk solution[46]. The spatial orientation of this metal deposit was highly controlled by two successive potential steps and adjusting the viscosity of the surrounding medium as well as manipulating the applied electric field. By SEM study, they found that different electric field orientations dominated the copper cluster topology (centered or noncentered). The BPE was well adapted to modify carbon substrates with metal asymmetrically, and the topology of the deposit was controlled by the alignment of substrates in the electric field (Figure 1.2). By a philosophy of using electric field pulse, the modification of two sides of the electrode with copper was achieved[45].

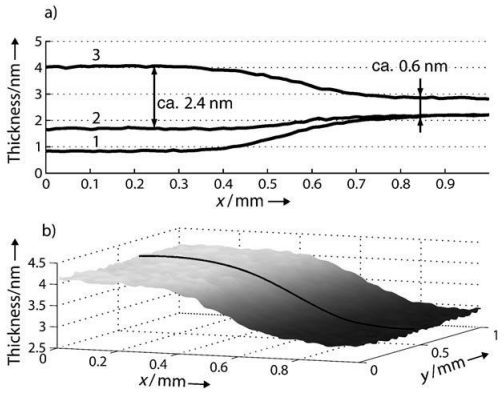

Figure 1.3.(a) Line profile shows the thicknesses of the gradients observed after different preparation steps. (b) Thickness map of the protein gradient[27]. Reprinted with permission from [27]. Copyright © (2008) John Wiley and Sons.

Ulrich et al. proposed the use of a bipolar electrode to create a surface gradient of molecular functionality[27]. The adsorption or desorption of specific molecules could be controlled along the conducting surface by the gradients of polarization potential. A self-assembled monolayer (SAM) of HS-C_2H_4-(O-C_2H_4)$_6$-COOH (mPEG) was first formed on the gold electrode by employing protein-immobilization procedures. By desorbing the thiols both cathodically and anodically, it then generated a functional molecular gradient across the BPE surface (Figure 1.3).

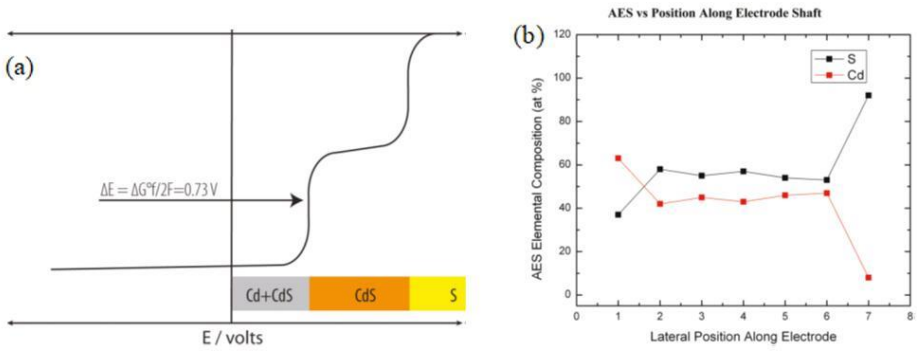

Figure 1.4.(a) The expected current-potential response of a solution containing a mixture of $S_2O_3^{2-}$ and Cd^{2+} showing conditions under which CdS can deposit. The predicted variation of chemical composition with applied potential is shown in the lower right portion of the frame. (b) A plot of the AES atomic percentage of Cd and S as a function of lateral position along the BPE[49]. Adapted with permission from [49]. Copyright © (2010) American Chemical Society.

Ramakrishnan in our group used bipolar electrodeposition to form a one-dimensional chemical composition gradient of CdS on a Au surface (Figure 1.4(a))[49]. Under AES and Raman spectroscopy characterization after electrodeposition, they found that the film formed represented the continuous one-dimensional solid-state material libraries. As predicted from simple thermodynamic consideration, there were three distinct deposition zones: Near the cathodic pole of the BPE, the CdS deposit was Cd-rich; at the middle point, there was an excess of S element; and between these two regions, a nearly stoichiometric CdS was obtained (Figure 1.4(b)).

Our group also reported the bipolar synthesis of Ag–Au alloy gradients on a stainless steel substrate[50]. The interfacial potential gradient in bipolar electrochemistry caused the rates of electrodeposition of Ag and Au to vary along the length of the BPE and so with the chemical composition. The resulting surface morphology of the Ag–Au film showed a uniform coverage of deposited material composed of a broad distribution of spheroidal surface asperities. Simultaneous Energy-dispersive X-ray spectroscopy (EDS) characterization indicates a nearly linear gradient across the lateral position from approximately 55% Ag to 100% Ag. A self-assembled monolayer of a Raman-active benzenethiol molecule was then allowed to form on the alloy surface for Surface-enhanced Raman spectroscopy (SERS) study with the result in agreement with the observation reported, that the optical extinction of Ag–Au alloy would increase proportionally to the Ag fraction due to the electromagnetic enhancement of Raman scattering.

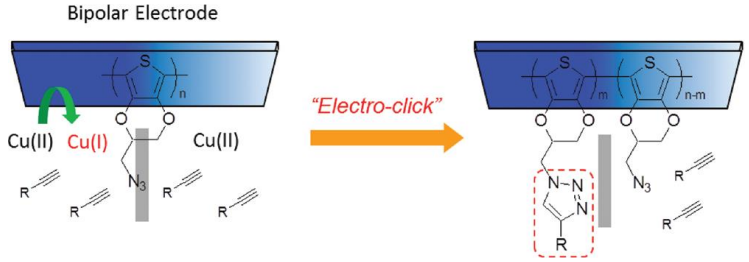

Figure 1.5.The electro-click reaction of PEDOT-N_3 film and terminal alkyne using cathodically generated Cu(I) species on a bipolar electrode[51]. Adapted with permission from [51]. Copyright © (2012) American Chemical Society.

Ishiguro et al. used the bipolar manner to achieve electrochemical doping by the introduction of the dopant. Conducting polymers were formed across the bipolar electrodes with composition gradients[1,52,53]. They also investigated an electrochemical surface modification via an electro-click reaction, namely, the azide-alkyne cycloaddition using electrogenerated Cu(I) species on a bipolar electrode (Figure 1.5)[51]. The Cu(I) ion generated by reduction on the cathodic pole would catalyze the electro-click reaction. After introducing different groups such as the perfluoroalkyl group and rhodamine, they found that this electro-click method made it possible to create versatile functionality-gradient surfaces in a BPE manner.

Loget reported indirect bipolar electrodeposition via the pH-triggered precipitation mechanism[54]. A localized pH gradient was established at the surface of the polarized object by way of water electrolysis, and it could be used to toposelectively deposit organic layers such as electrophoretic deposition paints (EDPs) or inorganic layers, which are nonelectroactive precursors. By this method, localized and asymmetric generation of EDP, silica, silicone, titanate, and titanium dioxide was achieved.

Laurent reported the first BPE experiment carried out in an ionic liquid with different characteristic sizes ranging from the millimeter to the micrometer scale[55]. They used a room-temperature ionic liquid to produce Janus particles modified with a conducting polymer, polypyrrole (PPy). The films electropolymerized on the glassy carbon beads were thinner and smoother with improved properties like low surface roughness, thickness, and better mechanical stability.

1.1.2.2 Electrocatalysts Screening

One approach for discovering effective electrocatalysts is to rapidly evaluate candidate materials by array-based screening[56-58]. People can extract kinetic and thermodynamic information from it and then subject promising materials to more extensive and quantitative testing. Several methods have been utilized for screening electrocatalysts. The first approach which involved methanol oxidation was reported by Smotkin using a pH-sensitive fluorescent indicator[59]. An alternative method is to monitor the current passing through individually addressable working electrodes yet at the cost of sophisticated microfabrication and smaller libraries[60-64]. A third technique employs scanning electrochemical microscopy (SECM)[65], rastered laser beam[57] or optical fiber[66]. However, this method is slow because each array is scanned serially. Recently, Tao took advantage of SPR microscopy[67] to measure changes in the local refractive index from electrocatalytic reactions.

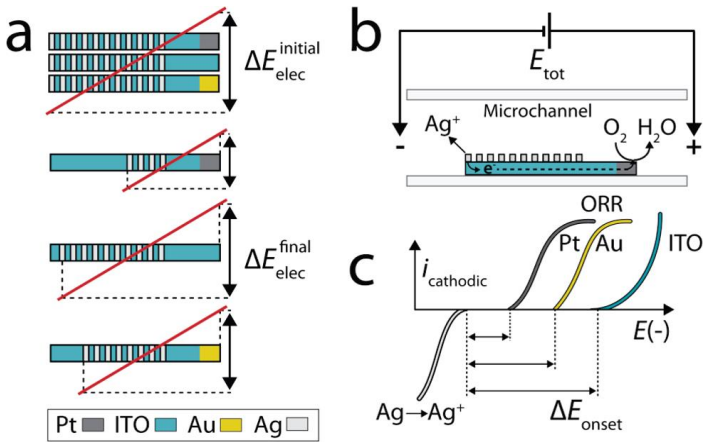

Figure 1.6.(a) The number of Ag microbands remaining after the experiment (b) the experiment device (c) Thermodynamic link between the overpotential required for the oxygen reduction reaction (ORR)[69]. Reprinted with permission from [69]. Copyright © (2012) American Chemical Society.

To develop a parallel and straightforward means for screening electrocatalyst candidates, the method of electrodissolution at bipolar electrodes has been introduced. At first, Crooks' group reported a new type of sensing platform based on Ag electrodissolution of a metallic bipolar electrode[68]. This dissolution provided a permanent record of a sensing/recognition event. Fosdick et al. reported a method that was suitable for rapid screening of a large-scale array of electrocatalysts[69]. The approach relied on simultaneous Ag electrodissolution and activation of oxygen reduction reaction (ORR) at the anode and cathode of the BPE, respectively. The anodic poles were composed of parallel Ag microband electrodes, and ORR electrocatalyst candidates were deposited onto the cathodic poles of the indium-doped tin oxide (ITO) bipolar electrode (Figure 1.6). When different overpotentials were required to drive ORR for different catalysts at the cathode, the numbers of Ag microbands that dissolved were different. That means there was a thermodynamic relationship between the dissolved number and the activity of the electrocatalysts present on the cathodic pole.

Then, according to this idea, Crooks et al. extended the catalysts screening method of ORR to bimetallic electrocatalyst candidates[70]. He changed the identity of the reporter from Ag to Cr, in case that ORR and Ag oxidation took place spontaneously due to a comparable negative potential of Ag. He deposited Cr microbands at the anodic poles of ITO bipolar electrode. Pd−M candidates with different composition were dispensed at the cathodic poles of the array of BPEs by using a piezo-jet controller. They calculated the E_{onset}^{ORR} by counting the number of Cr microbands eliminated and proved that the Pd–Co electrocatalyst was the most effective which was consistent with SECM results. This method was also suggested to provide quantitative kinetic information about electrocatalytic reactions.

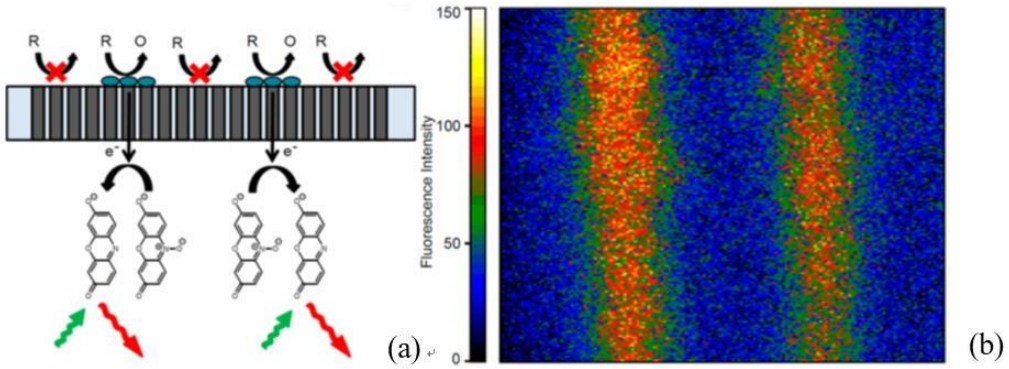

Figure 1.7.(a) Scheme of the experimental design. (b) Fluorescence-enabled electrochemical microscopy image showing the oxidation of 10 mM H_2O_2 in 0.1 M NaOH at catalytically active "hot-spots" where Pt was deposited on a CF array[15]. Adapted with permission from [15]. Copyright © (2013) American Chemical Society.

Apart from the dissolution approach, Zhang reported the use of a closed bipolar electrode combined with an electrogenerated fluorescent probe to reveal electrochemical and electrocatalytic activity[15]. Heterogeneous electrochemical processes were imaged spatially and temporally by coupling a conventional oxidation reaction to a specific fluorogenic reduction with a large array containing thousands or more parallel bipolar microelectrodes (Figure 1.7). The time derivative of fluorescence intensity can be used to obtain information comparable to traditional electrochemical current and their mutual correlation, makes it a useful platform for high-throughput, multicomponent and parallel screening in submicrometer or even diffraction-limited resolution.

1.1.2.3 Electrochemiluminescence (ECL)

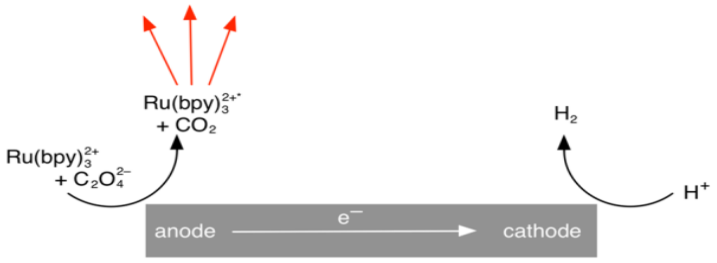

$$Ru(bpy)_3^{2+} \longrightarrow Ru(bpy)_3^{3+} + e^- \quad (1)$$

$$Ru(bpy)_3^{3+} + C_2O_4^{2-} \longrightarrow C_2O_4^{\bullet-} + e^- \quad (2)$$

$$C_2O_4^{\bullet-} \longrightarrow CO_2^{\bullet-} + CO_2 \quad (3)$$

$$Ru(bpy)_3^{3+} + CO_2^{\bullet-} \longrightarrow Ru(bpy)_3^{2+*} + CO_2 \quad (4)$$

$$Ru(bpy)_3^{2+} + CO_2^{\bullet-} \longrightarrow Ru(bpy)_3^{+} + CO_2 \quad (5)$$

$$Ru(bpy)_3^{3+} + Ru(bpy)_3^{+} \longrightarrow Ru(bpy)_3^{2+*} + Ru(bpy)_3^{2+} \quad (6)$$

$$Ru(bpy)_3^{2+*} \longrightarrow Ru(bpy)_3^{2+} + h\nu \quad (7)$$

Figure 1.8.The generation of ECL at a BPE and the ECL mechanism in the presence of coreagent[11]. Adapted with permission from [11]. Copyright © (2013) American Chemical Society.

The advantage of bipolar electrochemistry lies in the absence of direct electrical connection, and it facilitates portable device fabrication, endowing it with a promising sensing platform for spatially resolved analytical measurement with the merits of miniaturization, multiplicity and even integration on lab-on-chip systems with low cost. With the extension of this methodology to a large-scale bipolar array format, it is possible to achieve high throughput electrochemical detection on multiple electrodes simultaneously attributing to its wireless manner. However, due to the lack of physical contact, the implementation of bipolar electrochemistry has been hampered by an inability to monitor the current fling through the BPE. Electrochemiluminescence (ECL), the light-emitting process generated by electrochemical means, is an alternative to transduce the chemical (electrical) signal to an optical signal. It has been widely used in various analytical applications as a convenient and high-throughput reporting method. The ECL platform does not require an excitation light source and is free from the effects of scattered light compared with fluorescence. A very commonly used ECL system consists of $Ru(bpy)_3^{2+}$ as the light-emitting species and TPrA or oxalate anions as a co-reactant[71,72]. In this case, $Ru(bpy)_3^{2+}$ and TPrA get oxidized to form $Ru(bpy)_3^{3+}$ and $TPrA^{\bullet+}$. After a subsequent electron transfer, the excited state $Ru(bpy)_3^{2+}$* forms and then it relaxes with concomitant emission of a photon. The mechanism of $Ru(bpy)_3^{2+}$ ECL in the presence of $C_2O_4^{2-}$ is shown in Figure 1.8. In the BPE system, due to the charge neutrality, the ECL reporting reaction will be coupled with the analyte sensing reaction. Thus the ECL intensity here can directly show the analyte information. The intensity of light could be directly read out by charge-coupled device (CCD) cameras or optical microscopes. ECL is a very useful tool for analytical detection because it can provide us with the current information in the bipolar electrode. Bipolar electrochemistry, which allows sensor readout without a direct electrical connection to the working electrode, when combined with ECL, could serve as a powerful way of collecting information on processes occurring at bipolar electrodes. The reduction of the analyte of interest at the cathode will be related to the $Ru(bpy)_3^{2+}$ oxidation at the anode with the following ECL emission proportional to the BPE current.

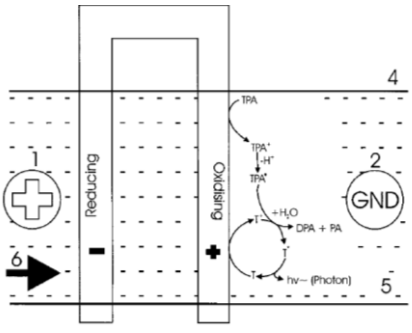

Figure 1.9.The pictorial representation of detection TPA using U-shaped Pt film electrode[73]. Adapted with permission from [73]. Copyright © (2001) American Chemical Society.

Manz and co-workers were the first to use ECL to detect analytes in a separation system using a "wireless" detector, which was a bipolar electrode[73]. They described a microfluidic system housing a

floating, U-shaped platinum electrode to detect the presence of $Ru(bpy)_3^{2+}$ related light-emitting compounds by the electrokinetic chromatography (Figure 1.9). This bipolar system was also employed in separating and detecting various amino acids (co-reactants for $Ru(bpy)_3^{2+}$ ECL at the anodic pole). However, Manz's approach was limited to the detection of co-reactants for $Ru(bpy)_3^{2+}$-based ECL (typically molecules bearing amine functionalities)[72,74,75].

Crooks' group then proposed an indirect detection using ECL emission at bipolar electrodes[71], which decoupled the ECL reporting reaction from the electrochemical sensing reaction. The analyte in the sensing reaction does not interact chemically with the light-emitting species in the ECL process. The system was configured so that the faradaic process occurring at the cathodic end of the BPE was correlated to the ECL emission at the anodic end. Due to the intrinsic charge balance of electrochemical cells, the sensing and ECL reactions were electrically coupled. This method broadens the spectrum of analyte candidate that can be detected by ECL to any electroactive species by the presence of co-reactant in the system, beyond the former limit that only analytes participating in the ECL reaction at the anode could be measured. They also found that changing the relative size and geometry between anode and cathode could enhance the detection sensitivity.

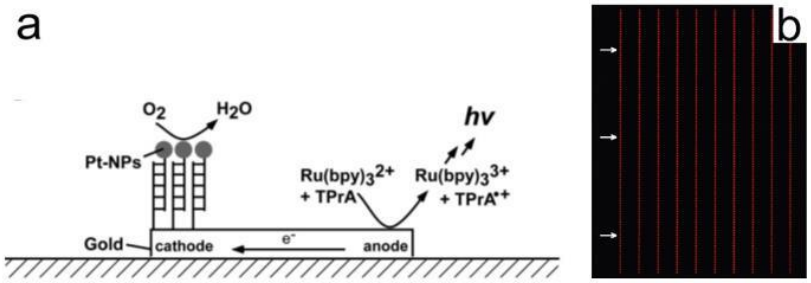

Figure 1.10.(a) The experimental configuration of Pt-labeled DNA detection using BPE ECL[10]. (b) ECL emission on bipolar electrode array at E_{tot} = 85.0 V[76]. Adapted with permission from [10] [76]. Copyright © (2008) (2009) American Chemical Society.

Since this interesting work by Crooks, ECL, especially for the $Ru(bpy)_3^{2+}$ system, has been frequently used in indirect reporting of bipolar current, thus creating an idea of analytical detection with advantages like high sensitivity, low cost and fabricating portable devices[77]. An ECL analytical platform for detection of DNA was exemplified, based on the concept of DNA hybridization. A bipolar electrode array consisting of a variety of 1 mm long gold microbands was decorated with a specific oligonucleotide as probes. In this case, cDNA labeled with platinum nanoparticles was recruited to the cathode of these bipolar electrodes. These Pt particles catalyzed O_2 reduction at the cathode and triggered ECL emission at the anode (Figure 1.10(a)). The platform can be used to detect the presence of biological molecules without electrical contact[10]. Many similar experiments have been done to verify the feasibility of DNA detection, such as bipolar arrays[76,78-80] (Figure 1.10(b)).

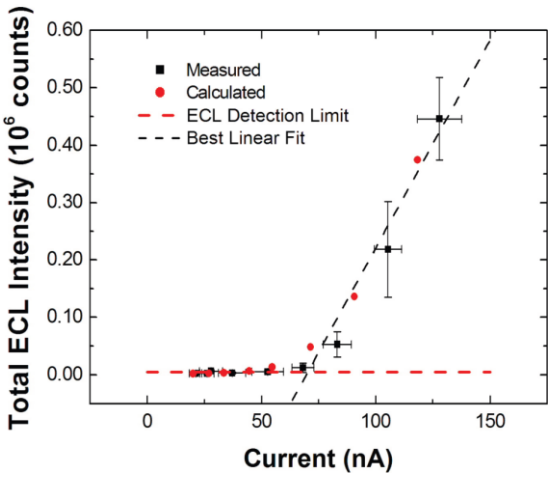

Figure 1.11.The relationship between the total ECL intensity and the faradaic current[18]. Reprinted with permission from [18]. Copyright © (2009) American Chemical Society.

Based on the method proposed by Nyholm that two individual electrodes could behave as a bipolar electrode and facilitate direct current measurement by connecting to an ammeter[81], Crooks' group extended this approach to provide a theoretical work to correlate ECL emission and current profile at the BPE, confirming the viability and accuracy of BPE ECL to chemical analysis[18]. Their strong correlation confirms the viability and accuracy of ECL to chemical analysis (Figure 1.11). Besides, a method of snapshot voltammetry relying on the potential difference between the electrolyte solution was created with a triangular-shaped bipolar electrode for extracting useful electrochemical parameters in the spatial domain, which was in good agreement with traditional voltammetry[82].

Another helpful application is ECL quenching. Landers and co-workers developed an intramolecular ECL quenching assay for the detection of DNA hybridization, according to the phenomenon that ECL intensity decreased proportionally to the concentration of ferrocenemethanol quencher[83]. Sanjun employed this idea for sensitive detection of ferrocenemethanol and molecular oxygen[11].

Laurent et al. broadened the emerging field of analytical applications of ECL, using a new approach to detect redox-active molecules indirectly relying on the generation of local pH gradients[84]. They combined a pH-sensitive fluorescent dye such as fluorescein with redox-active biomolecules. These biomolecules are either oxidized or reduced at one extremity of a BPE, and the analytical event is visualized by localized modulation of fluorescence intensity detected by fluorescence spectroscopy.

The ECL BPE platform thus provides a new paradigm for electrochemical sensing with excellent sensitivity, versatility without the requirement of an excitation light source and free from the effects of scattered light compared with fluorescence. According to its indirect measurement, a variety of analytes, such as biomarkers[78,85], DNA[10], RNA[80], drug[79], and quencher molecules[11] were detected and quantified using the BPE platform with high throughput, low cost, multiple-array and portable device fabrication[76,78].

1.1.3 Closed Bipolar Electrochemistry

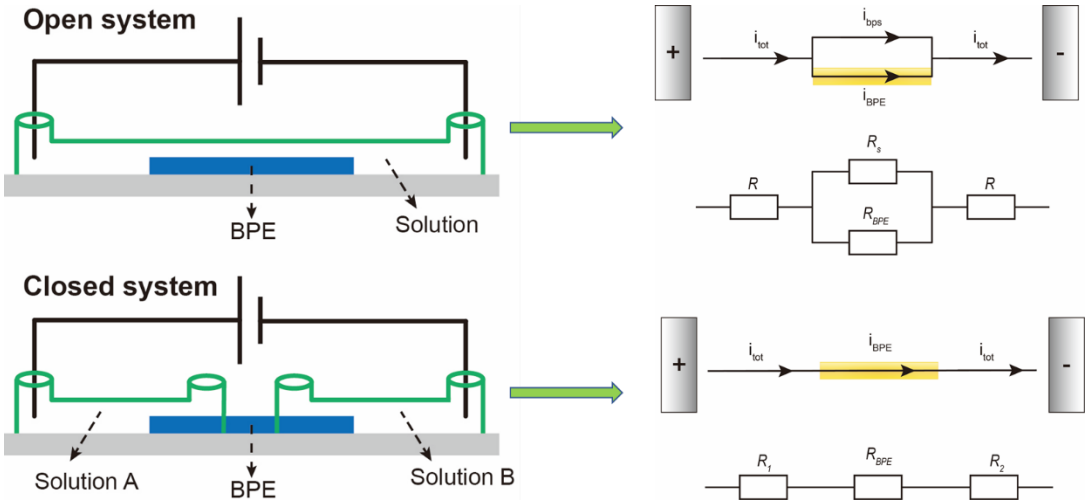

Figure 1.12.Comparison of (a) open BPE system and (b) closed BPE system.

Bipolar electrochemistry can be divided into open bipolar electrochemistry and closed bipolar electrochemistry. Figure 1.12 illustrates the difference between the two configurations. Open bipolar electrochemistry (Figure 1.12(a)) occurs when BPE is wholly immersed in a suitable electrolyte, with two driving electrodes present in the same solution. In closed bipolar electrochemistry (Figure 1.12(b)), a physical barrier is created between two driving electrodes and separates the electrolyte into distinct compartments. A single BPE, of which the anodic and cathodic poles are physically isolated by this barrier, becomes the only current pathway itself. Regardless of the potential drop of the driving electrodes/electrolyte interface, in the closed bipolar electrochemistry, the fraction of voltage dropped at the BPE/electrolyte interface is substantially equal to the potential applied on the driving electrodes, due to its serial circuit. In other words, the BPE will behave as an infinite resistance before reactions can happen on two poles. The potential drop in the solution is thus minimized, and the electrolyte in practice acts as a metal wire between the driving electrodes and BPE. On this account, electrochemistry will occur at a relatively low applied voltage. At each pole of the BPE, the surrounding solution is isolated from the other pole by the barrier, leading to a phase separation entirely.

Several advantages have been shown from the closed BPE system compared with the open one. First, there is no bypass for the current to flow. Consequently, i_s, the current flowing in the solution caused by migration of charged species is eliminated, and theoretically, 100% current efficiency (the current flow through the BPE/the current flow through the driving electrodes) is achieved. Electrochemistry could thus be initialized with a much lower applied voltage with only faradaic current flowing through this closed system, allowing the analyte detection with the merits of energy saving. Second, because of the phase separation of two compartments in the presence of a barrier, it eliminates possible interferences from one to another, satisfying the requirement of spatial resolution in microscale application. Owing to the phase separation, reactions happening at two compartments can have different

chemical compositions and solvent environments, such as aqueous/organic isolation. Therefore, the analyte would not be consumed at the driving electrode. More importantly, in the case of ECL sensing, the overwhelming background ECL from the driving electrode will be removed. Third, this separated configuration permits remote control of detection. Accordingly, disposable sensing half cells can be coupled to the same half reporting cell, applicable for rapid and consecutive on-chip diagnostics. Fourth, the closed BPE setup allows simultaneous sensing using an electrode array with changing analyte and different electrode modification, overcoming the limitation in an open system in which one universal solution environment is used. Last, the BPE is not size dependent. In an open system, the polarization potential difference across the BPE body depends on the electric field in solution and the length of the BPE, while in the closed system, the external potential is mainly applied at the BPE/electrolyte interface to facilitate electron transfer at the BPE with the minimized potential drop across the electrolyte.

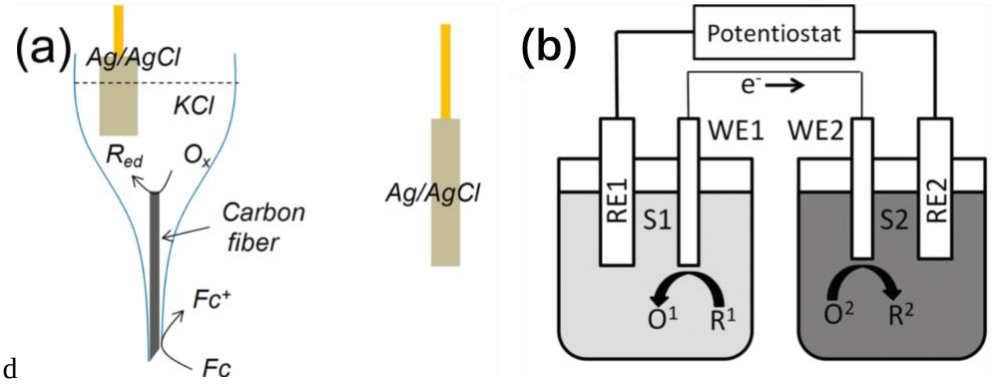

d

Figure 1.13.(a) Schematic diagram of a carbon fiber electrode (CFE) being used to study the oxidation of Fc. (b) Simplified cell configuration of a closed bipolar microelectrode[86]. Adapted with permission from [86]. Copyright © (2012) American Chemical Society.

The concept of a closed BPE system was formed initially from a Ph.D. thesis from Drexel University in 2004[42]. Even though there were examples of closed BPE before that, such as carbon fiber electrode (CFE), they were not described in that way. This first paper involved the closed BPE system as the established concept was published in 2012[86]. The configuration depicted using a carbon-fiber microelectrode, which was different from the closed BPE system people studied later on (Figure 1.13(a)). A small carbon fiber was sealed in a pulled glass capillary pipet as a bipolar electrode. The carbon disk pointing outside was the anode for Fc oxidation, while the internal carbon fiber served as the cathodic pole of the BPE with backfilled electrolyte. Two nonpolarizable Ag/AgCl reference electrodes were used with a relatively small driving voltage, and this voltage was dropped almost entirely at the solution interface adjacent to the two ends of the BPE. Because of its series connection, they could directly measure the electrochemical response of the BPE from the driving electrode. When replacing the internal solution with ferricyanide, the $E_{1/2}$ shifted about 250 mV negatively. Because of the difficulty to control the size of the interior fiber and completely replace the internal solution confined in the capillary, they then created an experimental setup with two separate two-electrode cells. Two

microworking electrodes 1 and 2, are connected as the two ends of the BPE (Figure 1.13(b)). Therefore, the current flowing through the BPE could be just read from the working terminal of the potentiostat. In a later work, a theoretical and experimental study of the steady-state voltammetric behavior on the closed bipolar microelectrodes were discussed[87]. The result showed the additional requirement of voltage to drive the faradaic reaction slowed down the voltammetric response, with its shape depending on the ratio of limiting current on both poles.

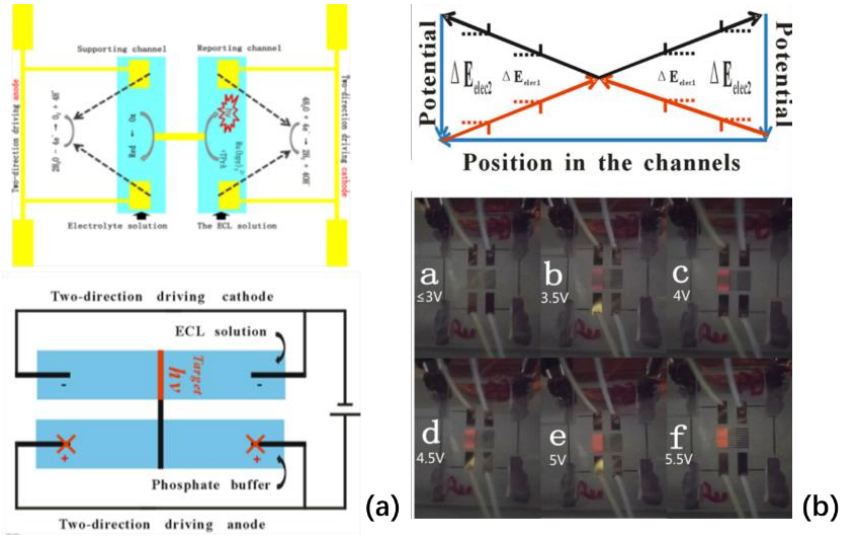

Figure 1.14.(a) The fundamental configuration of the dual-channel bipolar ECL sensor. (b) The potential distribution. (c) The visual ECL behavior under different driving voltages[79]. Adapted with permission from [79]. Copyright © (2013) American Chemical Society.

With its development, the closed BPE system has been widely used in detection, especially in the ECL approach. For example, a microfluidic-based closed bipolar system used as an ECL sensing platform was presented by Zhang[79]. The driving anode and cathode were inserted into respectively a reporting channel and supporting channel created by photolithographic microfluidics (Figure 1.14). Because the BPE in the middle served as the single path for this dual channel mode, the current efficiency was improved to 100% as we mentioned earlier. The large background ECL signal from the driving anode was eliminated because the supporting channel contains no ECL solution. By using this cell design, TPrA as the co-reagent, dopamine as the quenching agent, were detected with either an increasing or a decreasing CL versus concentration when injecting them into the reporting channel. H_2O_2 and ferricyanide in the supporting channel were also detected with ECL intensity proportional to their concentration, exhibiting a detection limit of several μM.

This ECL sensing platform, with one closed BPE in the middle between two separated channels, was further extended to a multichannel closed bipolar system[88]. Pt-deposited ITOs were used as two bipolar electrodes with improved signal stability. In this full-featured double-bipolar electrode ECL sensing platform, all the oxidants and reductants were directly related to a single ECL process in the central

reporting reservoir. H_2O_2, ascorbic acid, TPA, glucose and blood sugar were detected with good performance under high-throughput parallel sensing in a molecular keypad lock approach.

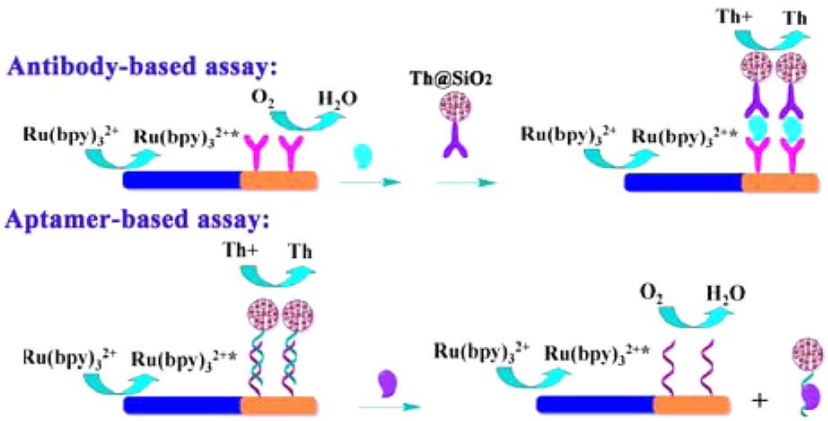

Figure 1.15.The principle of (a) antibody and (b) aptamer-based assay[89]. Reprinted with permission from [89]. Copyright © (2015) American Chemical Society.

In addition to those common analytes, cancer biomarkers based on a closed BPE array were also detected in multichannel microfluidics with excellent reproducibility under ECL imaging[89]. A group of parallel ITO BPEs connected detection channels and sensing channels on a glass substrate. Nano-bioprobes were immobilized on the cathodes electrochemically deposited with Au film. Those probes were coupled with silica nanoparticles doped with thionine, which is a good electron-transfer mediator with a much more negative reduction potential than O_2. In the antibody-based assay demonstrated, the first-antibody was immobilized on the surface, and the secondary antibody was conjugated with thionine silica nanoparticles (Figure 1.15(a)). When introducing the cancer biomarker, a sandwich assay was formed, so the reaction happening on the bipolar cathode shifted from O_2 reduction to thionine reduction, resulting in an enhanced ECL signal at the anode. While in the aptamer-based assay, the thionine silica nanoparticles labeled aptamer was hybridized with capture DNA on the surface at the beginning (Figure 1.15(b)). After incubation with the target protein, the nanoparticles were released, and hence decreasing the ECL signal. By these methods, AFP, PSA, ATP, and thrombin were detected by either of the two assays with ECL increase versus concentration or vice versa. The cancer biomarker adenosine in K562 cells extract was quantified to about 3.23 pmol/cell.

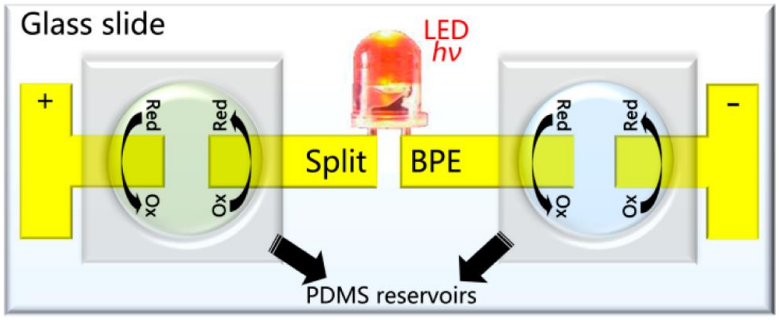

Figure 1.16.The structure and mechanism of the dual-channel bipolar LED electrode sensor[12]. Adapted with permission from [12]. Copyright © (2015) American Chemical Society.

A novel sensing strategy was reported on the closed bipolar system by connecting a split BPE with a light-emitting diode (LED) (Figure 1.16)[12]. Here the current flowing through the BPE could be read out by the luminescence of the LED, and the LED luminous intensity was quantitively related to the reaction at the end of the BPE. The reactions happening at both ends of the BPE could be sensitively read and recognized by even naked eyes owing to the ultrahigh current efficiency in the closed bipolar system. By using this sensing strategy, there is no need for expensive ECL reagent and instruments, yet with improved signal stability. Various model analytes were measured with good performance using this LED BPE array.

Chapter 2 Electrochemiluminescence (ECL) Sensing Using the Bipolar Electrode Thin-layer (BETL) System

2.1 Introduction

2.1.1 Thin-Layer Electrochemistry

Electrochemical processes often need to be studied not only on the macroscopic but also the microscopic scale of analyte[90]. The concept of thin-layer electrochemistry was first introduced in the 1960s, which built up the foundation of studies both theoretically and practically in the electrolysis of solutions in a narrow gap between two electrodes. They later applied this technique to the study of the kinetics of hydrolysis of *p*-benzoquinoneimine[91]. The electrochemical behaviors of adsorbed molecules, such as iodide and iodine ions at platinum electrodes were demonstrated by thin-layer chronopotentiometry with considerable elucidative power due to that the total amount of reactant within such small volume is no greater than the amount adsorbed on the electrode surface at equilibrium[92,93]. Instead of chronopotentiometry, slow linear sweep voltammetry in the thin layer was derived theoretically and verified experimentally. It could distinguish the second reaction from the background current. Great simplicity was inherent in it owing to the presence of diffusion-limited mass transfer. Briefly, depending on the method used to display information, thin-layer electrochemistry can be classified into thin-layer chronopotentiometry[94], linear sweep voltammetry[95], steady-state current method, etc. A variety of designs and modified electrodes are applied for minimizing the IR drop, eliminating edge effect, suppressing residual current, precise position manipulation, fast solution fill, and wash-out for the sake of good accuracy and reproducibility[96,97]. Thin-layer electrochemistry has significant benefits over the corresponding methods involving the bulk solution, such as small sample volume (~10^{-3} ml), negligible convection, simplified mathematical description, and enhanced signal response. Hence, important kinetic parameters such as rate constant *k*, diffusion coefficient *D*, and the number of electrons *n* can be evaluated without difficulty[91,98]. Before thin-layer electrochemistry, the study of the kinetics of chemical reactions following electron transfer was limited to systems in which the rate of the chemical reaction is relatively rapid (with small half-life). While in thin-layer chronopotentiometry, the species are confined at the electrode so that accurate measurements of considerably smaller rate constants can be carried out.

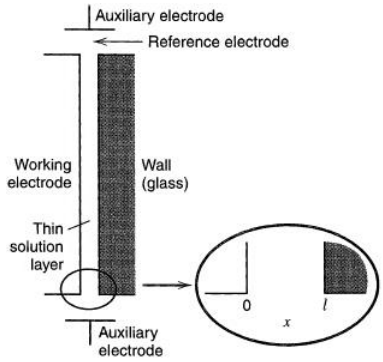

Figure 2.1.Schematic diagram of a single-electrode thin layer cell[99]. Reprinted with permission from [99]. Copyright © 2000, John Wiley and Sons.

A thin-layer cell can have many different electrode materials such as gold, graphite, platinum, mercury, or other metals. In addition, it can have various configurations, for example, a plan-parallel electrode configuration. A thin layer of solution of thickness *l* is held between two plane-parallel electrodes with an area A. To keep the solution concentration in the thin layer constant, the experimental solution can be held in contact with a large volume of the same solution through the face of the thin layer. A four-electrode setup or three-electrode setup could either be employed. The former one consists of a pair of plane-parallel electrodes, a counter electrode, and a standard reference electrode, as shown in Figure 2.1. Two working electrodes can be controlled independently at a different potential. A three-electrode setup will use an inert wall instead of one of the planar electrodes. Last, if omitting the reference and counter electrodes, we will have a simple two-electrode thin-layer cell.

The application of the steady-state method is a unique feature of thin-layer electrochemistry, that is impossible to achieve under ordinary electroanalytical conditions. Anderson and Reilly have proposed the principles and potential applications by measuring the D values of a redox couple based on the measurement of the limiting steady-state current, i_{ss}, followed by a coulometric analysis of the thin layer[100,101]. The i_{ss} between closely spaced twin working electrodes is given by the equation:

$$(i_d)_{ss}=\left[\frac{nFADC}{l}\right]\left[\frac{2D_R D_O}{D_R+D_O}\right]$$

where *n* is the number of electrons transferred in the redox reaction, *F* is the value of the Faraday, *A* is the projected electrode area, *C* is the total concentration of electroactive species in the thin layer, *l* is the thickness of the solution between the two working electrodes, D_O and D_R is the diffusion coefficient of the oxidized and reduced species, respectively. *D* values are calculated according to the following equations:

$$D_O = (i_d)_{ss(c)} l^2/2Q_C;\quad D_R = (i_d)_{ss(a)} l^2/2Q_a$$

where $i_{ss(c)}$ and $i_{ss(a)}$ are the limiting steady-state currents at the cathode and anode, respectively. Q_c is the charge required to reduce all the oxidized species between the electrodes once the condition of i_{ss}, has been reached. Q_a is the charge required to oxidize all of the reduced species in the thin layer at the i_{ss} condition. The IR effect is not very important once the steady-state condition has been achieved because the current flows between the two working electrodes and not through the bulk solution.

In the steady-state method, a limiting steady-state current is generated through the cell if two facing electrodes are made sufficiently cathodic and anodic, thus maintaining the concentration of the reduced form and oxidized form of reactant at zero at the respective electrode surfaces. Species obtained by reduction at one electrode can diffuse to and be oxidized at the other working electrode. This existence of a limiting diffusion current depends on the establishment of steady-state concentration polarization. The paired, thin-layer cell enables a constant concentration gradient to be built up; the value of the gradient can be controlled by varying the interelectrode spacing.

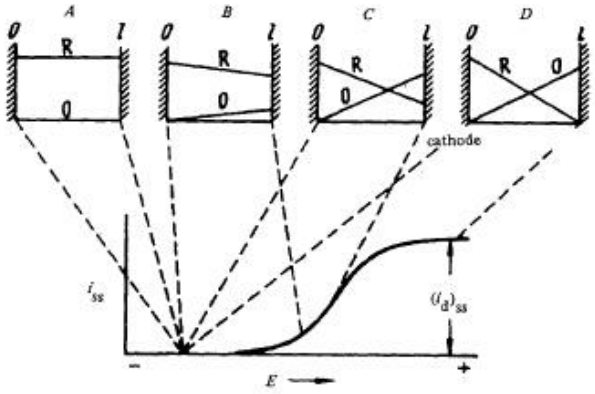

Figure 2.2.Schematic illustration of the formation of a steady-state current by reference to the concentration profile of O and R in a thin layer for gradually increasing values of E at one of the electrodes (anode)[101]. Reprinted with permission from [101]. Copyright © (1965) Elsevier B.V.

Figure 2.2. illustrates the formation of the steady-state current i_{ss}. Initially, the potential applied to both the working electrodes is made sufficiently negative to ensure that the species in the solution are all reduced form. If the potential of one of the electrodes (the anode) is shifted towards positive values, oxidation of R will begin at some value of the anode potential; the concentration of the oxidized form will increase, and the concentration of the reduced form will decrease. The flow of each form across the thin layer can be expressed regarding its surface concentration:

$$\frac{i_{ss}}{nFA} = D_R \frac{(c_R)_{x=0} - (C_R)_{x=l}}{l} = D_O \frac{(C_O)_{x=l}}{l} \quad (1)$$

The total number of molecules of O and R in the thin layer is constant: $N_O + N_R = N$

$$\frac{lA(C_O)_{x=l}}{2} + \frac{(c_R)_{x=0} + (C_R)_{x=l}}{2} = N \quad (2)$$

By solving (1) and (2)

$$(C_O)_{x=l} = \frac{i_{ss} l}{nFD_O} \quad (3)$$

$$(C_R)_{x=l} = -\frac{i_{ss} l}{2nFA}\left(\frac{1}{D_R} + \frac{1}{D_O}\right) + \frac{N}{lA} \quad (4)$$

$$(C_R)_{x=0} = \frac{i_{ss} l}{2nFA}\left(\frac{1}{D_R} - \frac{1}{D_O}\right) + \frac{N}{lA} \quad (5)$$

When the anode potential becomes sufficiently positive $(C_R)_{x=l}$ vanishes and the current becomes a maximum value $(i_d)_{ss}$. Hence it follows from Eqn. (5) (6) that

$$(i_d)_{ss} = \frac{nFADc_0}{l},$$

where $c_0 = c_R + c_O$, and $D = \frac{2D_R D_O}{D_R + D_O}$

Thus, the limiting steady-state current is directly proportional to a function of the diffusion coefficients of the oxidized and reduced forms, total analyte concentration the electrode area, and inversely proportional to the distance between the electrodes.

This steady-state method can be used in several ways, for example, the determination of the diffusion coefficient. If the concentrations of the oxidized form at $x = 0$ and of the reduced form at $x = l$ are both zero, Eqn. (1) can be rewritten

$$(i_d)_{ss} = nFAD_R(c_R)_{x=0} = nFAD_O(c_O)_{x=l} \quad (6)$$

If one of the electrodes in the thin layer cell is disconnected (for example, the anode) the current will flow only to the cathode as long as the oxidized material remains in the thin layer. By measuring the electric quantity Q used in the reduction of O (because $Q_C = nFAlc_O$, and $c_O = \frac{1}{2}(c_O)_{x=l}$, inserting then into (1)), we obtain $D_O = (i_d)_{ss} l^2 / 2Q_C$ and $D_R = (i_d)_{ss} l^2 / 2Q_a$

In addition, if the reactant concentration in the thin layer can be disturbed by a chemical reaction, the rate of appearance or decay may just be followed by recording the current. It is generally applicable in investigating the rates of first or higher-order chemical reactions following (or preceding) electron transfer by continuously monitoring the reactant concentration with time. For example, this principle has been applied to the study of the rate of the benzidine rearrangement under varying conditions of acidity and ethanol concentration[102]. After establishing a limiting steady-state current by maintaining the concentration of both species at zero at the respective electrode surfaces, then the current would decay exponentially with time as the reduced species R is removed by the irreversible pseudo-first-

order rearrangement to produce an electro-inactive species P under the potential range. The determination of *k* by steady-state current decay is independent of thin-layer parameters *l* and *A*, as well as the initial concentration of reactant, provided the signal i_{ss} is of a measurable magnitude.

The edge effect causes the deviation of experimental results from the theoretically expected value and an important portion of the background current in thin-layer electrochemistry. It is defined as the diffusion of the electroactive species into the thin layer from the perimeter of the volume element[103]. In a typical scenario in which the solution inside is in contact with the bulk solution surrounding the thin layer, the semi-infinite diffusion from the bulk causes a residual current proportional to the concentration of all species electrolyzed at the potential of the working electrode. This diffusional transfer of material will thus result in nonlinearity in the voltammogram when trying to deduce useful electrochemical information. Complete elimination of this edge effect poses a difficult design problem because a solution contact must be made with the reference and auxiliary electrode. Contributions to the current from the reduction of surface metal oxides or catalytic reduction of the solvent will also be more important in thin layer than in semi-infinite techniques because a typical thin layer of solution contains only 6×10^{-10} mole of electroactive species, equivalent to approximately three monolayers on the electrode surface. In practice, much small residual currents can be attained by excluding oxygen, using small solution thickness, and minimizing the current contribution from electrolysis of hydrogen ion or formation/reduction of the surface metal oxides by posing the electrode in moderate potential range.

The edge effect can be minimized by confining the solution peripheral to the thin layer to a small volume, such as in a thin layer also. A well-minimized edge effect then would be achieved by creating a minimized electrode edge to area ratio[104]. Edge effect diffusion can also be avoided if a quantity of solution is just sufficient to fill the thin layer between the two working electrodes[101]. In the case of a thin-layer cell with two working electrodes, independent potential control could be applied to them with a reference electrode and auxiliary electrode externally. However, when the potential is applied, a sudden rise and fall of anodic current were observed, probably associated with switching transients, capacity currents, and IR drop between the working electrode and the auxiliary electrode. In addition, the steady-state current obtained with the four-electrode technique does not reflect the proportion of oxidized to reduced forms initially present in the solution. Alternatively, two-electrode steady-state voltammetry is suggested to be more convenient with the elimination of the external reference and auxiliary electrodes. It will produce a steady-state current limited by that species initially present in a smaller concentration and may be arranged to produce steady-state currents even proportional to a species following/proceeding with the chemical process or forming an insoluble product[101]. The two-electrode steady-state voltammetry can be classified into three conditions: if the two working electrodes of a thin-layer cell are connected in series with a variable voltage supply and no oxidizable or reducible

substances are present in the solution, no current will flow (excepting background and capacitive currents) until the applied potential reaches the decomposition potential of the solvent. If an oxidizable or reducible species is present (but not both), the applied potential at which the current flows will be the difference between the decomposition potential of the solvent on one side and the potential of oxidation/reduction of the electroactive species on the other side. If both oxidizable and reducible forms are soluble in the solution, for example, Fe(II)-Fe(III), then the current flowing at the steady state will be determined by the smaller of the two quantities, $D_R[(C_R^{ss})_{x=0} - (C_R^{ss})_{x=l}]$ or $Do[(C_O^{ss})_{x=0} - (C_O^{ss})_{x=l}]$[101].

A feature of the two-electrode system is that the background current at the working electrode must be negligible compared to the initial steady-state current, thus, to exclude oxygen and other impurities and surface oxide formation is of great necessity. In the paper published by Mcduffie, a chloride medium with mercury-coated working electrodes was used. The anode of the pair then served as an "internal" calomel reference electrode[100]**,** minimizing IR drop and facilitating potential control. A Teflon cup and collar isolated the solution in the thin layer from the bulk solution by effectively trapping the solution between mercury-coated electrodes.

In 1987, Bard's group described an electrochemical cell with near atomically smooth electrode surface and an apparatus to produce adjustable and variable interelectrode spacing with piezoelectric drive elements of 0 to >500 nm, to probe homogeneous and heterogeneous electron transfer reactions[105]. After applying a step potential, the current response would undergo a transition from Cottrell state to the steady state. Under a higher step potential with sufficient separation, the chronoamperometric curve would follow Cottrell behavior, proportional to $t^{-1/2}$, over a reasonably wide time window. The results of electrochemical measurements with dissolved species and polymer layers were reported, showing good agreement of steady-state current for $Fe(CN)_6^{3-/4-}$ concerning the physical diffusion of species between electrodes.

2.1.2 Nanogap Towards Single Molecule Detection

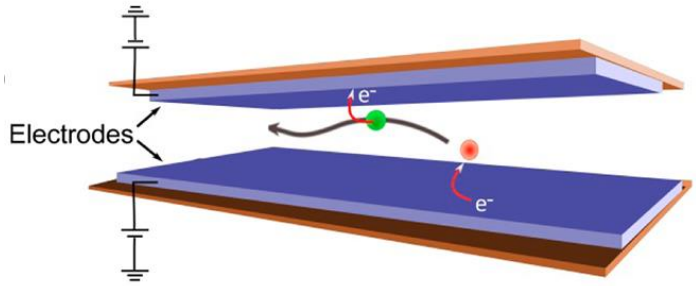

Figure 2.3.Nanogap electrode device with charge amplification by repeated electron transfer[106]. Reprinted with permission from [106]. Copyright © (2013) American Chemical Society.

When this thin layer comes down to smaller nanometer gap (even smaller), single molecule electrochemistry can be achieved[106]. The development of methods for detecting and manipulating

matter at the level of individual macromolecules represents one of the critical scientific advancements of recent decades. The approach on single molecule detection based on the electrochemical method with ultimate sensitivity becomes more and more appealing because it can be easily combined with microelectronics or a microfluidics chip to create large parallel assays at relatively low cost. There are three primary motivations in performing electrochemistry near or at single molecule limit. First, it allows the verification of fundamental theories of electron-transfer reactions, including double-layer structure, mass transfer, heterogeneous kinetics, and even statistical nature, in regimes that are unable to be tested before, thus exploring the limits of long-established assumption[107]. Second, a new window on population heterogeneities and the microscopic dynamics of systems ranging from catalytic nanoparticles to single enzymes is provided by enabling the new technique on nanoscale fundamental experiments. Third, new types of electrochemical assays on mesoscale systems such as individual living cells with single molecule fingerprinting can be envisioned, so that the sensitivity and selectivity would be improved, even though the absolute number of target molecules is inherently limited. Because only one or a few electrons are transferred per molecule in the electrochemical faradaic process, it is impossible to detect this tiny amount of charge using the conventional electrochemical instrument. Thus, charge amplification by redox cycling, a means of increasing the number of electrons involved, is necessary for single molecule electrochemical detection. A thin-layer cell geometry consisting of two parallel electrodes is employed: one of the electrodes is biased at sufficient anodic potential, and one of the electrodes is biased at sufficient cathodic potential both in the diffusion limiting region, so that target molecules undergo repeated alternating reduction and oxidation, as illustrated in Figure 2.3. Each redox molecule thus shuttles thousands or even millions of electrons per second between the electrodes in a short time with a gap distance comparable or smaller than the thickness of the diffusion layer time, generating a detectable current. This approach is in principle applicable to all redox species that are chemically reversible over the time scale of the measurement.

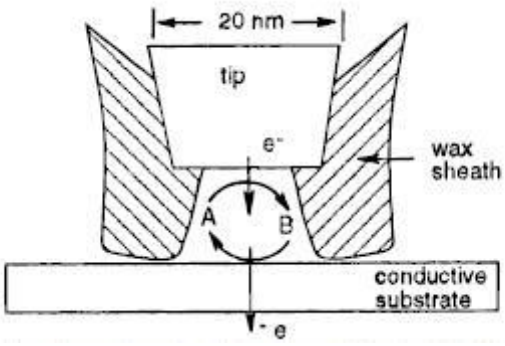

Figure 2.4.Single-molecule detection with SECM. Molecule A trapped between the tip and surface[108]. Reprinted with permission from [108]. Copyright © (1995) American Association for the Advancement of Science.

The first report of single-molecule detection by electrochemical approach was published in 1995 using a scanning electrochemical microscope by a tip-based structure[108]. The electrochemical behavior of a

single molecule could be monitored by trapping a small volume of a dilute solution of the electroactive species between a Pt-Ir ultramicroelectrode tip within ~10 nm and a conductive substrate (Figure 2.4). As the molecule moved into and out of the electrode-substrate gap, the anodic current peaks were observed stochastically.

Recently, the challenge of achieving spatial localization of a single molecule that could diffuse freely in solution has been overcome[109,110]. A simple "quad-probe" pipet cell was reported for single molecule electrochemical detection with current anticorrelation and low background noise realized in droplet format[111]. Two of the four channels were filled with the electrolyte solution and Ag/AgCl quasi-reference counter electrodes. The potential between the two reference electrodes in the barrels was controlled with a small offset, and the resulting ion current was used as a feedback signal to detect the meniscus contact with the working electrode surface[112,113]. Pyrolyzed carbon was filled into the other two channels to create two working microelectrodes. The two working electrodes were then connected in series and measured as a whole to increase the overall electrode area. In addition to the low surface area of the carbon microelectrodes, which significantly enhanced the electrochemical signal-to-noise ratio, an extremely low background noise level of ca 1 fA was then accomplished by further confining the analyte in the droplet format at the end of the pipet. The order of magnitude improvement compared with state-of-the-art microfabricated devices about (~10 fA) is capable of detecting individual molecule by redox cycling in a dilute concentration condition[114]. In the case of using $Ru(NH_3)_6^{3+}$, individual redox cycling about ca. 30 fA was also shown after bringing the tip into contact with the substrate and then continuously retracting it until a molecule was trapped within the droplet. In the case of ionic liquid, due to the exceptional low diffusion coefficient in such relatively viscous media[115,116], the single molecule redox cycling event is resolved with a peak current of ~ 4 fA at both the tip and the substrate working electrodes, different from the background current of about 1 fA. The enhanced electric field by this diffusion layer effect increases the limiting current across the nanogap by emphasizing the role of migration[117], It resembles the scenario that a 2000-fold limiting current enhancement is made as a result of migration by a larger electric field between the generator and collector electrodes[118].

Other than the tip-based nanoelectrode, the geometry of a dual-plate system using lithographic microfabrication seems to be more promising in single molecule detection. First, microfabrication yields excellent flexibility in a variety of shapes[119], arrays design[120], and point-of-care integration of channels, valves, and pumps[121,122], e.g., multiple and identical devices can be fabricated in parallel in the same chip, allowing for systematic readout and studies[123]. Second, independent characterization can be greatly facilitated. In the dual-plate system, for example, by sacrificing one of the parallel devices, the resulting knowledge about the device structure dramatically reduces the number of unknowns when modeling the devices theoretically. Third, the well-proven fabrication processes, which harness the vast expertise existing in the field of lithography-based fabrication, will improve its reliability and

reproducibility by a systematic and iterative design, rather than the labor-intensive tip-based nanoelectrode fabrication. Fourth, the anodic and cathodic current are anticorrelated by nanofluidic redox cycling, useful for the discrimination of interfering signals. These distinct advantages endow this technique an exciting candidate for biosensing applications[124-126].

Nanofluidic channels with integrated electrodes have demonstrated an increase in molecular sensitivity by several orders of magnitude compared with conventional voltammetry[127,128]. A novel chip-based device was fabricated for the detection of redox-active compounds such as hexacyanoferrate and neurotransmitter dopamine fluctuations in real time[120]. The dependence of the current on the concentration of hexacyanoferrate was determined in an amperometric measurement, showing a characteristic anticorrelated behavior for anodic and cathodic currents with almost 100% cycling efficiency. In the spatiotemporal detection of chemical fluctuations, the chip was incorporated into the flow cell. It is capable of resolving chemical gradients and minimal local concentration fluctuations at various positions in real time, featuring the crucial requirement for future applications such as mapping the neurotransmitter release from chemical synapses in a cellular network.

Studying the heterogeneous electron-transfer kinetics of fast outer-sphere reactions ($k^0 > 1$ cm/s) by conventional voltammetric methods represents a major experimental challenge because these measurements are only sensitive to heterogeneous kinetics with electron-transfer rates comparable to the mass transport rates. While by knowing the exact geometry of the electrode by dual-parallel design and lithographic method, fast kinetic information is accessible. Zevenbergen and co-workers used a nanogap fluidic channel about 50 nm in height to determine electron-transfer kinetics for fast chemically reversible reactions. By using this device, they found that the standard heterogeneous rate constant k^0 for ferrocenedimethanol, $Fc(MeOH)_2$ depends sensitively on the composition of the supporting electrolyte.

A bionanofluidic sensing device integrating all the elements of molecular recognition, signal transduction, and detection into a confined, femtoliter-scale reaction volume, was fabricated. The recognition element, copper-containing protein enzyme tyrosinase is locally immobilized in a microfabricated nanochannel which serves as an electrochemical transducer. The presence of phenol results in a real-time steady-state current because each enzyme molecule produces a stream of product molecules at a given rate until they routinely diffuse into the external reservoir. The volume is sufficiently small to study the content of an individual biological cell and electrochemically explore enzyme kinetics at the single-molecule level. The adding of biological recognition enzyme element will reduce the common electrochemical specificity problem to a selection of a few molecular species from a complex mixture.

2.2 Preliminary Design of the BETL System

2.2.1 Motivation for Research

We design and investigate a novel ECL sensing platform to detect electrochemically active species at low concentration, using bipolar electrochemistry in a thin-layer configuration. The platform, which is called the bipolar electrode thin-layer (BETL) system, is assembled from 3D printed components. A key advantage of bipolar electrochemistry is that electrochemical reactions can proceed without a direct electrical connection to the bipolar electrode. In a conventional three-electrode system, the total information is provided by measuring the current at the working electrode. The ECL intensity, representing the coupled reaction rates happening at both ends of the BPE, could be recorded by a CCD camera or photomultiplier tube in the absence of direct electrical connection. As discussed in the introduction, thin-layer electrochemistry can address the electrochemical behavior of low concentration of analyte at microvolumes with great mathematical simplicity. More importantly, an enhanced response could be achieved by charge amplification from repeated redox cycling in the thin layer between two paired electrodes. A standard power supply could be employed as the excitation source for the necessary sensing and reporting processes, making the bipolar ECL device a promising candidate for point-of-care device fabrication. In the BETL system, the thin layer and the bipolar cell could be isolated entirely. As a result, the analyte in the thin layer and other species related to ECL reporting will not interfere with each other. Apart from other sophisticated cell fabrication methods such as photolithography, the emerging 3D printing technique can supplant the previous methods due to its rapid prototyping, easy testing of new concepts and configurations, versatility, and lower cost.

2.2.2 Reagents and Device Fabrication

Tris(2,2′-bipyridyl) dichlororuthenium (II) hexahydrate ($Ru(bpy)_3Cl_2 \cdot 6H_2O$, 99.95%, Sigma-Aldrich), Potassium ferricyanide (III) ($K_3Fe(CN)_6$, 99%), Potassium hexacyanoferrate(II) trihydrate (III) ($K_4Fe(CN)_6 \cdot 3H_2O$, ≥99.5%, Sigma-Aldrich), Hexaaminеruthenium (III) Chloride ($Ru(NH_3)_6Cl_3$, 98%, Sigma-Aldrich), Hexaaminеruthenium (II) Chloride ($Ru(NH_3)_6Cl_2$, 99.9%, Sigma-Aldrich), Sodium perchlorate monohydrate ($NaClO_4$) (≥99.0%, Fluka), Sodium oxalate (≥ 99.5%, Alfa Aesar), Sodium phosphate monobasic (≥99.0%, Fisher Scientific), Sodium phosphate, Dibasic, anhydrous (≥99.0%, EMD), p-Benzoquinone (≥99.5% HPLC, Fluka), Hydroquinone (99%, Alfa Aesar).

All solutions were prepared using deionized, ultrafiltered water (18.3 MΩ cm) generated from the Milli-Q water purification system (MilliporeSigma, Burlington, MA). All reagents were used as received without further purification.

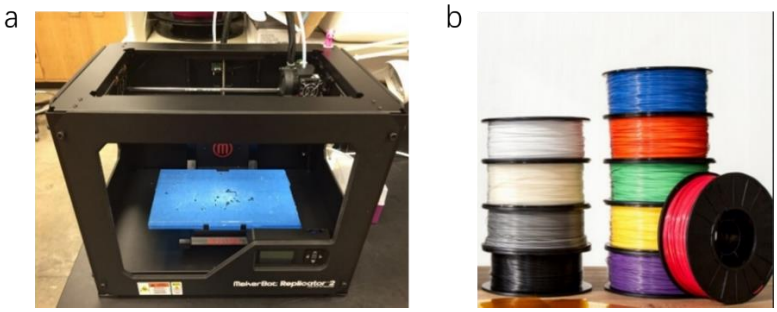

Figure 2.5.(a) 3D printer (Maker Bot Replicator). (b) PLA filament.

3D printing was used to fabricate the whole electrochemical cell design. The 3D printer used here was a Maker Bot Replicator 2 (Figure 2.5(a)). The material used for the device fabrication in the experiment was the inexpensive PLA filament (polylactic acid) which was durable and consistent for high-impact strength prototypes and fixtures (Figure 2.5(b)). In the printing process, the filament was fed into the printing head through a rotating gear, then heated above the glass transition temperature and ejected from the nozzle to the printing stage in a pre-defined rate. Through layer-by-layer construction, the desired structure was built up.

All the 3D building components were designed using Sketch Up© (Trimble Navigation Limited) with STL extension.

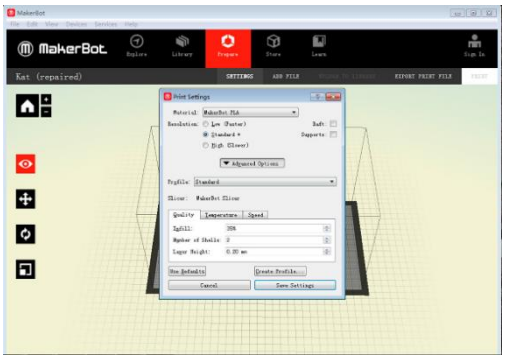

Figure 2.6.MakerBot: Printing software.

The STL file was loaded into MakerBot Print (Brooklyn, NY), attached to the printer (Figure 2.6). The desired resolution, infill percentage, and speed were all adjusted to create a specific object property. For a typical print the setting was as follows: infill density: 35%; infill pattern: hexagonal; layer height: 0.1 mm, number of shells: 2; filament diameter: 1.77 mm; travel speed: 150 mm/s; extruder temperature: 184°C; building plate temperature: 64 °C. The extruder will be heated up to about 180 °C by the heating element built in the printing head.

Surface smoothing of the printed objects was accomplished via exposure to THF vapor. 30 mL THF was poured into a glass dish and heated to 80 °C while covered with a lid. Once the THF condensation level reached the top 1/4 of the dish, the printed objects attached to a secondary lid via metal wire were suspended under the THF vapor for 60 s just above liquid THF. After treatment, pieces were rinsed

with deionized (DI) water and allowed to degas for approximately 60 min at room temperature to remove the excess THF before use[129].

Driving electrodes are two 10 mm x 10 mm x 1 mm gold foils , located at the sides of the bipolar cell (like in Scheme 2.1). A DC power supply (9122A, BK Precision) was used to provide an applied voltage between two driving electrodes. Images from ECL emission were collected by a CCD camera (D510, Nikon) operated in manual mode with parameters set as follows: ISO sensitivity: 6400; shutter speed 1s; white balance: auto. Then the images stored in RAW. format were transferred to the computer and analyzed using ImageJ software[62]. The ECL intensity was obtained by measuring the integrated density from the RGB signal.

2.3 Preliminary Test of the BETL System and Influencing Factors on the ECL Performance

2.3.1 Cell Design

2.3.1.1 Open Cell Design

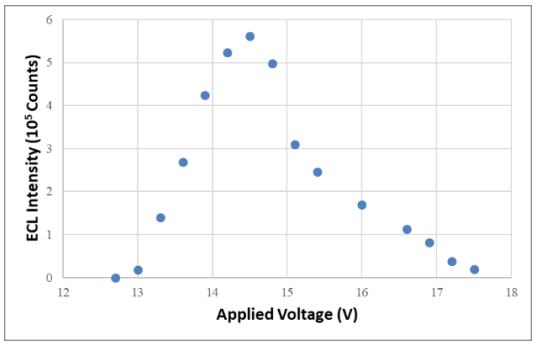

Figure 2.7.ECL intensity of gold rod bipolar electrode in a glass petri-dish.

The first device tested here was a glass petri-dish (10 cm in diameter) with a gold rod sitting in the middle between two driving electrodes on both sides, as an open bipolar cell. The distance between two driving electrodes was 10 cm, and the bipolar gold rod was about 20 mm in length, 2 mm in diameter. According to the literature, ECL could be quenched by anion radicals, especially in the presence of oxygen from the environment[11]. The ECL solution (5 mM $Ru(bpy)_3Cl_2$, 25 mM $Na_2C_2O_4$ in pH=7 PBS buffer) was therefore degassed with N_2 for 20 min before transferring it to the petri-dish. The first ECL experiment was operated by focusing the camera onto the bipolar anode while gradually increasing the applied voltage in darkness. As shown in Figure 2.7, there is no observable ECL emission until applied voltage passes 12 V, then ECL intensity starts to increase; but after an inflection point, the ECL intensity then decreases to approximately zero. This effect can be explained by two reasons: (i) If the externally applied voltage is too high, the potential difference between two ends of the BPE is far beyond the thermodynamic threshold of the ECL reaction, causing competing reactions to occur at the BPE anode such as water oxidation, which can be confirmed by the bubbles on the gold anode after the ECL experiment. (ii) Film formation (black deposit) on the BPE anode with the oxidation of gold/$Ru(bpy)_3^{2+}$,

which impedes the ECL emission. As a result, it is necessary to select the appropriate applied voltage, avoiding too high to preclude competing reactions or significant film formations, or too low to trigger bipolar electrochemistry.

2.3.1.2 Closed Cell Design

Instead of an open cell, a closed bipolar electrode system was tested, in which the bipolar electrode was isolated into two compartments. It has two significant advantages, first, in a closed setup, the ECL solution and the analyte are separated, that is critically necessary for analytical work considering the presence of interference. Second, the potential across the substrate is essentially equal to the potential applied across the driving electrodes. As a result, the applied voltage needed to trigger ECL emission would be remarkably lowered. Third, since there is no bypass current, the total reaction rate is limited by the bipolar reaction, ensuring a more stable performance with less surface chemistry on the driving electrodes. More importantly, in the case of ECL bipolar sensing, the background emission from the driving electrode will be eliminated.

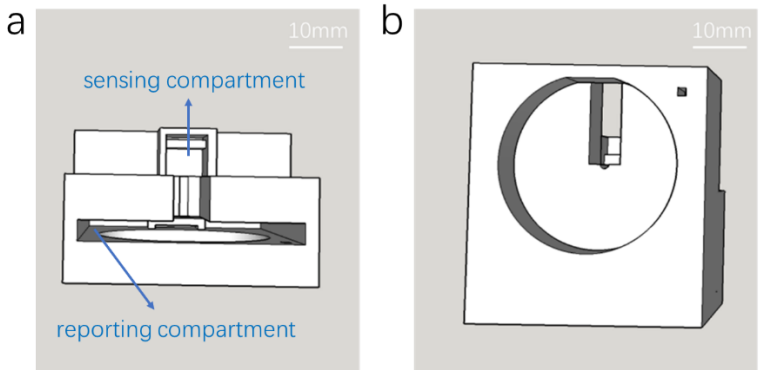

Figure 2.8.Top view (a) and side view (b) of the mounting cell.

A new mounting cell design is shown in Figure 2.8 with its top view (a) and side view (b). The cell was composed of two compartments, the ECL solution reporting compartment and sensing compartment. In the middle of the cell, a half round notch with a diameter of 2.1 mm accommodates the BPEs gold rod, and a small printed rectangular block with another half round notch at the bottom was used to hold the BPE and create two compartments. High vacuum grease was used to fill in any gaps. Due to the closed configuration, the reporting compartment (10 mm × 10 mm × 10 mm) for the analyte could be much smaller than ECL one, thus allowing detection at low volumes. In the sensing compartment (5 mm × 50 mm × 56 mm), a cylinder (42 mm in diameter) was printed out to accommodate a C camera mount (CMR, 1.00”-32, Thorlabs). An external high-resolution secondary lens (Computar TV lens 12.5 mm, 1:1.3) was screwed into this camera mount. The lens was set to a focal length of “infinity” and the lowest f-number was used to have the largest aperture for capturing the maximum amount of light. The focal length of it was served as the pre-designed length between the lens and the bipolar electrode anode. As a result, the ECL light emitted from the bipolar anode would enter the lens and then exit as parallel

light. With a CCD camera aligned in the optical path, the parallel light can be captured entirely, thus ensuring an efficient way to record the ECL emission intensity. In addition to the optical optimization, the side view design allowed the camera to focus the ECL emission at the cross-sectional surface of the bipolar anode which had a uniform polarized electric field. Two slots were printed for holding the driving electrodes, with a small hole on top of each side wall for wire connection pass-through.

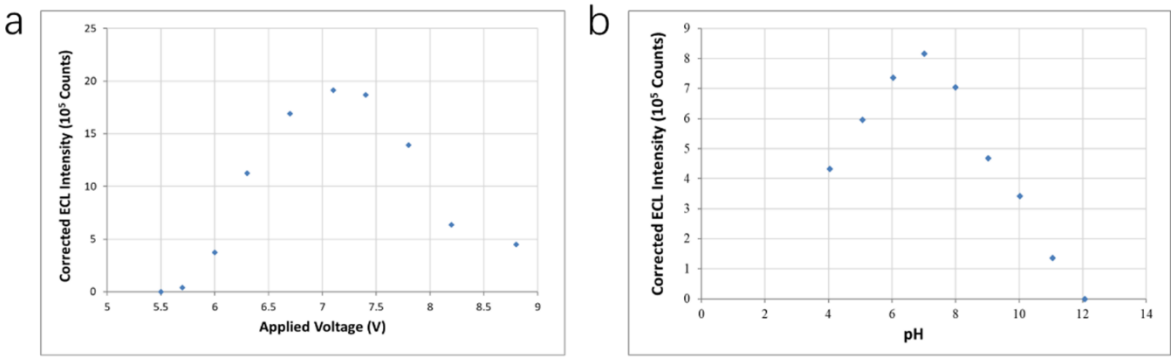

Figure 2.9.ECL intensity as a function of (a) applied voltage (pH=7) (b) pH (at 7 V).

By using this 3D printed mounting cell, the ECL intensity dependence on applied voltage and pH was examined. The analyte in the sensing compartment was 0.1 M PBS buffer (pH = 7) for initial tests. In Figure 2.9(a), it shows a similar trend as shown in Figure 2.7. At 5.5 V, the ECL becomes observable, since it passes the thermodynamics threshold of both reactions occurring on the bipolar electrode. With a higher applied voltage, an increasing trend of ECL emission appears first, then followed by a decreasing trend. The onset voltage (5.7 V) is reduced compared to the open cell, implying the extremely reduced voltage loss in a closed BPE system. Figure 2.9(b) shows the ECL intensity change as a function of pH adjusted by $HClO_4$ or NaOH when maintaining the cell at 7 V. Based on the peak emission, the optimal pH for ECL emission is between 6-8, which agrees with the previous literature[74,75,130,131]. The oxalate/$Ru(bpy)_3^{2+}$ system goes through an oxidative-reduction reaction, in which $C_2O_4^{2-}$ as the reactive species (Pk_a=5.18 at 25 °C) needs to be oxidized at an appropriate pH condition.

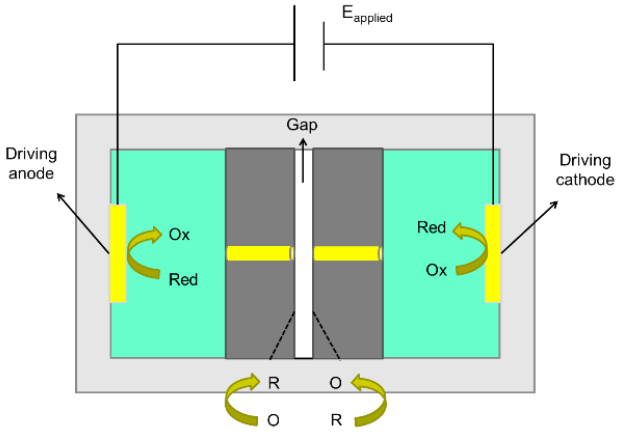

Scheme 2.1.The schematic illustration of the gap cell.

After establishing the working framework of ECL sensing in the bipolar electrode system, a novel gap cell configuration was proposed to have much-enhanced sensitivity under the twin-electrode redox cycling on the basis of a multichannel closed bipolar system[88]. The basic principle is shown in Scheme 2.1: two driving electrodes provided the electric field across the cell, and two bipolar electrodes embedded in two blocks are separated by a small gap, thus dividing the cell into three parts: the anode compartment, the gap, and cathode compartment. The solution in the cathode compartment is the ECL solution, while the solution in the anode compartment is a supporting electrolyte solution. The solution in the gap contains a redox couple, in this case, ferricyanide/ferrocyanide. If the applied voltage is high enough to trigger electrochemical reactions in the gap, simultaneously there would be six reactions happening in the cell together with ECL emission. The reaction on the driving electrode in the cathode compartment is hydrogen evolution, and that in the anode compartment is water oxidation. The reaction on the BPE surface in the cathode compartment is the ECL reaction, which is coupled with the $Fe(CN)_6^{3-}$ reduction on the opposite end in the gap. The reaction on the BPE surface in the anode compartment is the hydrogen evolution, which is coupled with the $Fe(CN)_6^{4-}$ oxidation in the gap. In a small gap, the redox couple will undergo repeatable redox cycling with an amplified current. Because the redox analyte in the gap is usually at a low-concentration scale, the ECL emission in the cell is determined by the redox couple in the gap.

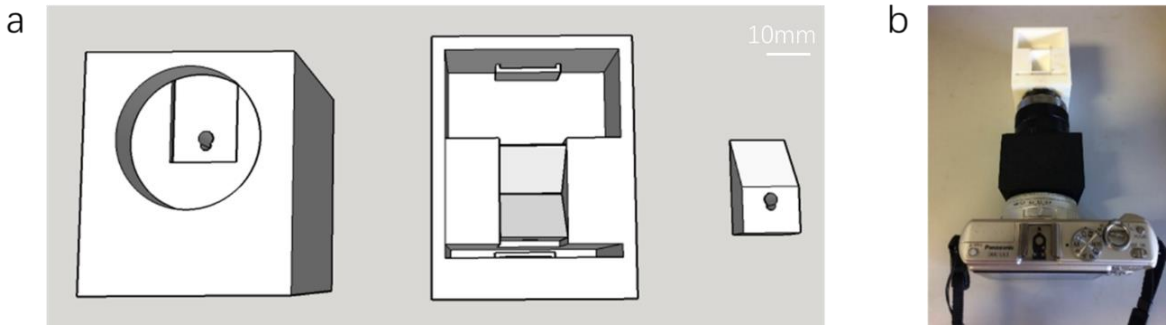

Figure 2.10.(a) The 3D model of mounting gap cell. (b) the measuring setup with a secondary lens and camera.

The gap cell design was combined with the camera mounting system previously described, and the final detection system is shown in (a)and (b). Except for the anode (5 mm × 40 mm × 48 mm) and cathode compartment (20 mm × 27 mm × 25 mm), the gap in the middle was built up by two small 3D printed blocks (10 mm × 15 mm × 25 mm). In the middle of each block, there is a hole. A gold rod (the BPE) was inserted into the hole and sealed by epoxy. After 24 hours curing, the gold rod ends were polished by abrasive sand paper (MicroCut Discs, P800, P1500, P2500, P4000, Buehler) and finely polished by alumina (1.0 μm, 0.3 μm, 0.05 μm, Buehler) in sequence, until the electrode surface was flush with the block face and the electrode had a mirror-like finish. By fixing one block and changing the horizontal position of the other one, the gap distance could be adjusted for each experiment. A syringe was used to fill the gap chamber with the sample solution. A clamp was used to tightly hold these two building

blocks together. The anode compartment, filled with ECL solution was only 5 mm in length to match the focal length of the secondary lens. The cathode compartment was filled with 10 mM $HClO_4$.

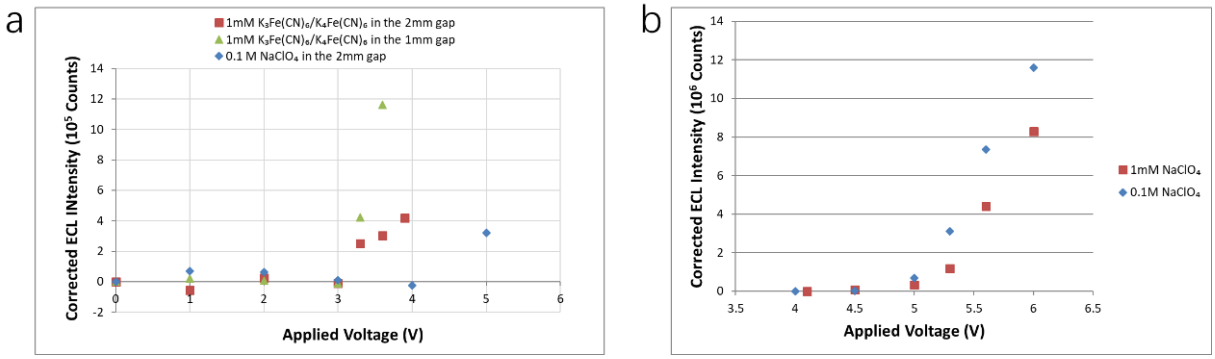

Figure 2.11.(a) ECL comparison of the gap in 1 mm and 2 mm in the mounting gap cell. (b) ECL comparison of 0.1 M $NaClO_4$ and 1 mM $NaClO_4$ with a gap size of 100 μm.

A rough comparison was made by arranging the gap into two different sizes of about 1 mm and 2 mm. As shown in Figure 2.11, when introducing ferri-ferrocyanide into the 2 mm gap, the onset voltage of ECL changes from approximately 5 V to 3.2 V. After narrowing the gap to 1 mm, the onset voltage shifts to the left and shows a larger ECL response at the same applied voltage. The intensity of the ECL is strongly inversely proportional to the gap size though considering the minimized potential difference due to the shrinking of the gap from 2 mm to 1 mm. The role of the supporting electrolyte concentration was also examined. As illustrated in Figure 2.11(b), 0.1 M $NaClO_4$ with a higher supporting electrolyte concentration shows an enhanced ECL response compared to 1 mM $NaClO_4$ in the same 100 μm gap. Accordingly, both the supporting electrolyte and redox couple will influence the onset voltage of ECL emission and its intensity. High concentration of redox couple contributes to the redox cycling in the gap; while a high concentration of the supporting electrolyte lowers down the IR drop in the thin layer by reducing the resistance, providing more overpotential for faradaic reactions happening on the bipolar electrode inner surfaces.

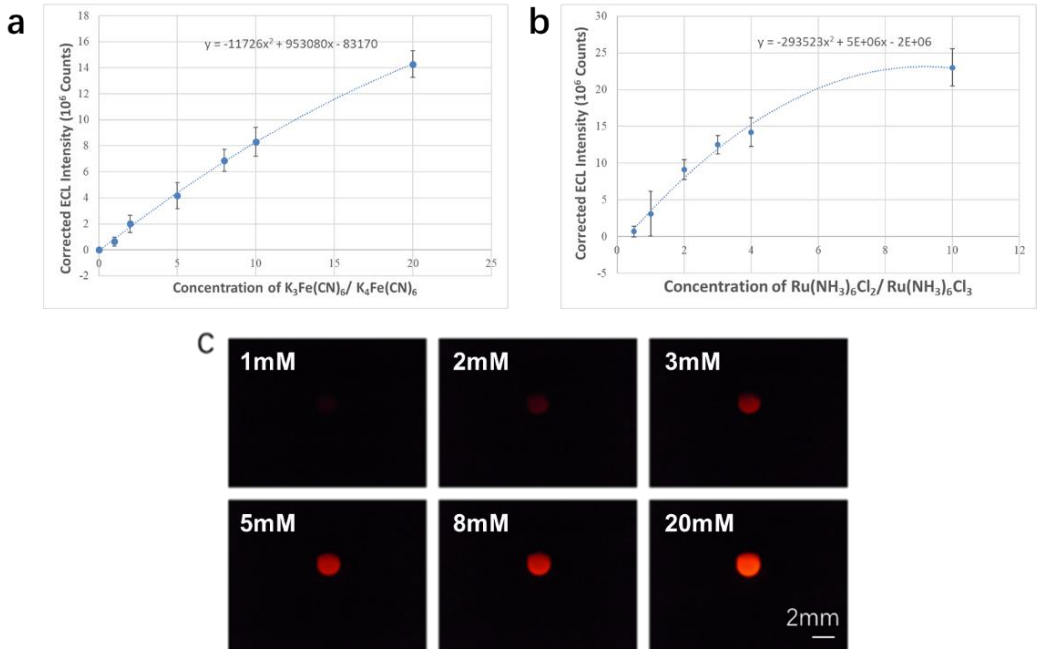

Figure 2.12.(a) ECL calibration plot versus $K_3Fe(CN)_6/K_4Fe(CN)_6$ concentration, each error bar represents the standard deviation of five independent measurements. (b) ECL calibration plot versus $Ru(NH_3)_6Cl_2$/ $Ru(NH_3)_6Cl_3$ concentration, each error bar represents the standard deviation of 5 independent measurements. (c) Images of ECL from BPE of $K_3Fe(CN)_6/K_4Fe(CN)_6$ concentration of 1,2,3,5,8 and 20 mM.

The optimal ECL measurement is obtained by setting the applied voltage such that significant water oxidation reactions and considerable film formations do not occur, while still maintaining a stable bipolar ECL emission. A calibration curve was plotted by applying a constant voltage at 5.0 V and measuring its ECL response of $K_3Fe(CN)_6/K_4Fe(CN)_6$ couple from 0 mM to 20 mM in 0.1 M $NaClO_4$ (Figure 2.12(a) (c)). It shows a proportional relationship between the ECL intensity and analyte concentration, yet is not perfectly linear. ECL calibration of another redox couple $Ru(NH_3)_6Cl_2/Ru(NH_3)_6Cl_3$ was then tried from concentrations of 0.5 mM to 10 mM, showing a linear region before 3 mM and then become plateauing (Figure 2.12(b)).

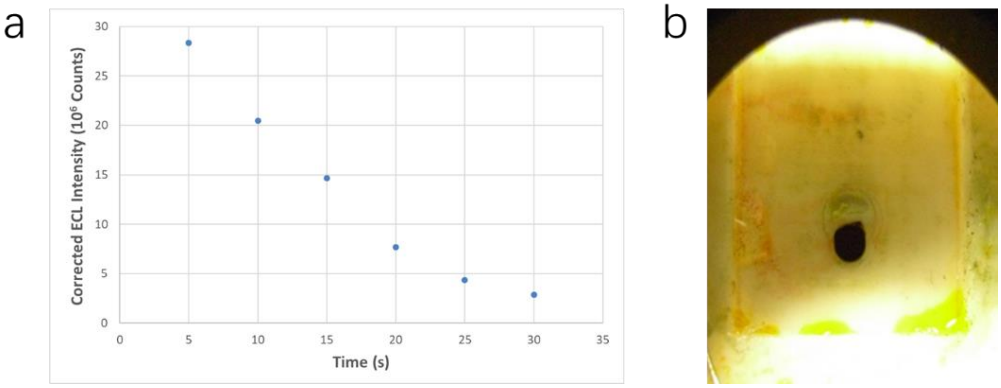

Figure 2.13.(a) Corrected ECL intensity as a function of time after potential switching from 0 to 5.5 V of 1 mM $K_3Fe(CN)_6$/ $K_4Fe(CN)_6$. (b)The blackening of the gold bipolar electrode surface due to film formation.

One phenomenon observed was the gradual loss of signal over time, after potential was applied to the ECL cell. The ECL signal was always the strongest at the beginning when turning on the DC supply and then it decreased as time went on in a step-down speed. For example, if the ECL voltage was stepped to 5.0 V, and while collecting optical images, ECL signal decays over time (Figure 2.13(a)). Another phenomenon was the gradual blackening of the gold bipolar anode surface. At 4.5 V which only produces very weak ECL emission, the BPE surface becomes dark black after 30 min, demonstrating the gradual gold film formation from gold oxidation/ruthenium oxidation (Figure 2.13(b)).

2.3.2 Electric Field Characterization and its Influence on the ECL Performance in the BPE System

2.3.2.1 Potential Profile in the Open BPE System

Literature[26,81,132] suggests an electric field distribution measurement can aid in understanding the instability of ECL emission and obtain a well-defined calibration curve, enlightened by the literature about the electric field distribution measurement[26,81,132]. A series of experiments were conducted to address the potential profile in the BPE system.

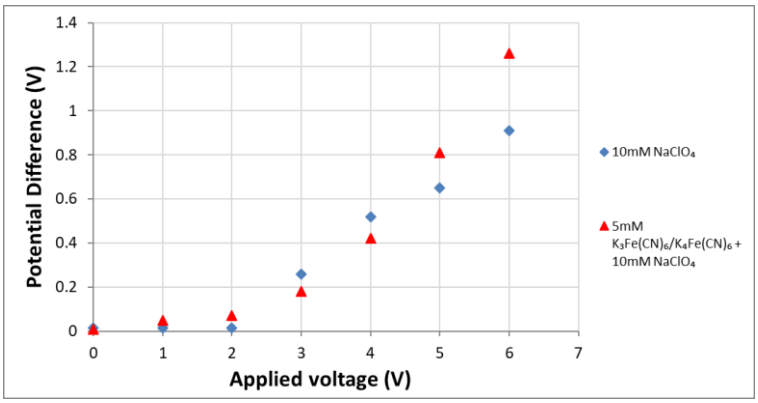

Figure 2.14.The potential difference between two gold wire in an open glass petri-dish cell versus applied voltage with 10 mM $NaClO_4$ and 5 mM $K_3Fe(CN)_6/K_4Fe(CN)_6$.

Two small gold wires (0.05 mm in diameter) were immersed in an open BPE cell consisting of a petri-dish (5 mm in diameter) and separated by a distance of 2 cm. They were connected to an external voltmeter. The DC power supply was then used to provide the electric field in the BPE system. Therefore, the reading on the voltmeter, which equaled to the solution potential difference at these two points, could be directly measured as a function of applied voltage (the polarization of gold wires by the electric field could be ignored due to the subtle current flowing across it). Two solutions of 10 mM $NaClO_4$ and 5 mM $K_3Fe(CN)_6/K_4Fe(CN)_6$ were tested as shown in Figure 2.14. The potential difference

between two gold wires is proportional to the applied voltage after a rising point that corresponds to the thermodynamic threshold of reactions happening at two driving electrodes. Before that value, a tiny amount of nonfaradaic charging current could be immediately generated after applying the voltage by the temporary charging of driving electrodes. However, the resulting electric field would quickly fall close to zero by the development of the double layer. Only after the threshold, could a relatively stable potential gradient generated in the solution. Figure 2.14 shows that 5 mM $K_3Fe(CN)_6/K_4Fe(CN)_6$ has a greater potential difference than 10 mM $NaClO_4$ past 4 V. According to the literature[133], a lower ionic strength should lead to a higher potential gradient in the BPE system. The opposite observation in our result indicates that the larger current from the reaction of redox-active species on the driving electrodes will enhance the electric field in the solution.

We found the electric field in the solution should be determined by two main factors, and sometimes they work together contradictorily: (1) The ionic strength of the solution. For the same magnitude of current flow, lower ionic strength with higher solution resistance would create a larger potential drop in the solution. However, if the solution resistance becomes the main reason for impeding the current flow, after a certain applied voltage, the amount of current increase of solution with higher ionic strength would compensate for the weakening of solution resistance, thus creating a larger electric field in the solution. (2) The redox-active species and its concentration in the solution. In similar ionic strength, the electroactive species with a lower thermodynamic potential barrier would offer more faradaic current flow under the same applied voltage, and thus enhancing the electric field across the system: the higher concentration, the higher faradaic current generated. The alternation of reaction mechanism from solvent decomposition would strongly shift the onset potential of establishing a sustainable potential gradient in the solution.

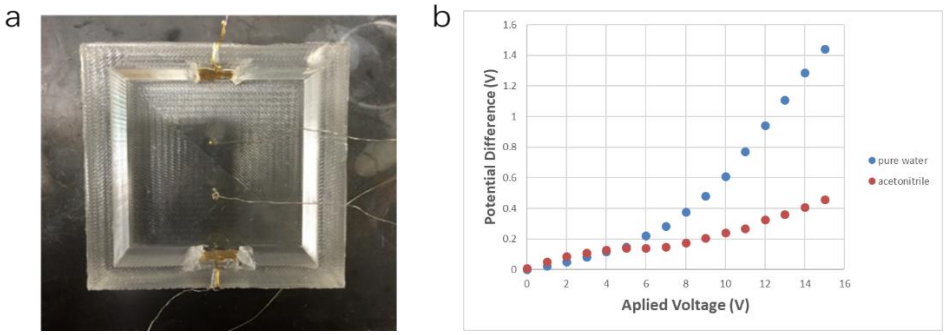

Figure 2.15.(a) Potential measurement setup in an open PDMS cell. (b) Potential difference versus applied voltage in water, 1 mM $NaClO_4$, and acetonitrile.

These conclusions were confirmed by using an open PDMS cell (40 mm × 40 mm) using pure water and non-aqueous solvent acetonitrile as the electrolyte (Figure 2.15(a)). As expected, in Figure 2.15(b), at the applied voltage below 5 V, acetonitrile has a larger potential difference than pure water because acetonitrile has a higher solution resistance resulting from its lower dielectric constant. While after 5 V,

acetonitrile demonstrates a lower potential difference, in that its solvent decomposition potential is much larger than the aqueous solution.

One phenomenon observed here was a large initial potential difference across two gold wires, that decays exponentially after power is applied to the cell. It resembles the observation from the ECL experiment (). Other than the undesirable surface change on the bipolar electrode, the potential gradient change across the BPE plays a more important role in determining the ECL deterioration.

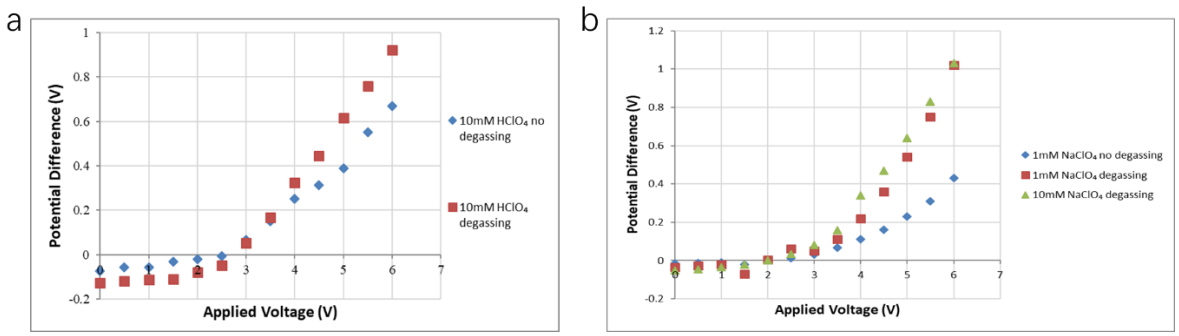

Figure 2.16.(a) Potential difference measurement in 10 mM $HClO_4$ with/without degassing. (b) Potential difference measurement in 1 mM $NaClO_4$ with/without degassing.

The effect of degassing during the experiment on the electric field was also examined by this open cell, as shown in Figure 2.16(a). In the same solution of 10 mM $HClO_4$, before the applied voltage of 3 V, the one without degassing shows a higher potential difference than the one without degassing. While after 3 V, the potential difference of the degassed solvent now exceeds the non-degassed solvent. In another measurement of 1 mM $NaClO_4$, a similar behavior is demonstrated (in Figure 2.16(b)). When comparing the potential difference variation in 1 mM $NaClO_4$ and 10 mM $NaClO_4$, below 3 V, the solution with a lower supporting electrolyte concentration has a larger potential difference, while above 3 V, the contrary is the case. At the low voltage range, the one with higher solution resistance from lower ionic concentration will result in a larger electric field in the case of charging current only (the establishment of the double layer is more difficult with lower ionic concentration), or only small faradaic current is present. Above this range, lower solution resistance from higher ionic strength will facilitate the current flow by an adequate faradaic reaction, for instance, solvent decomposition. Now the current enhancing effect dominates in the electric field distribution and shows a larger potential gradient in the solution.

Degassing during the experiment leads to convection in the solution. However, this convection will have a double-sided effect in determining the electric field distribution. At low applied voltage, in which charging current from ion migration prevails, the solvent without degassing exhibits a higher electric field. Through charging, double-layers form on both driving electrodes. On the driving anode which is positively charged, the total excess charge density on the solution side of the double layer (both the

Helmholtz plane and diffusion-layer) should be in an opposite sign to the charge on the metal electrode. Excess anions are thus attracted to the double layer of the driving anode; in the same way, excess cations are attracted to the double layer of driving cathode by the electrostatic force. The ion migration caused by the formation of the double layer generates the nonfaradaic charging current and gives rise to the electric field across the solution. In the presence of a convection force, the process of double layer formation will be interrupted, thus reducing the charging current and the magnitude of the electric field. However, as the applied voltage increases, the contribution from faradaic reaction starts to dominate the current flow. An accelerated mass transfer, at this voltage range, would lead to a higher current flow, thus creating a larger electric field than in a stationary condition. However, the drawback of degassing is the instability of the electric field caused by disturbed mass transfer. For a stable ECL to be measured, degassing is not optimal.

2.3.2.2 Potential Profile in the Closed BPE System

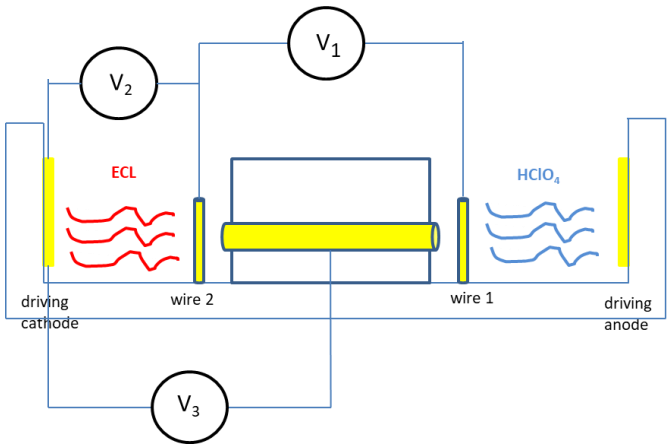

Scheme 2.2.Illustration of the setup of potential difference measurement in the closed BPE cell.

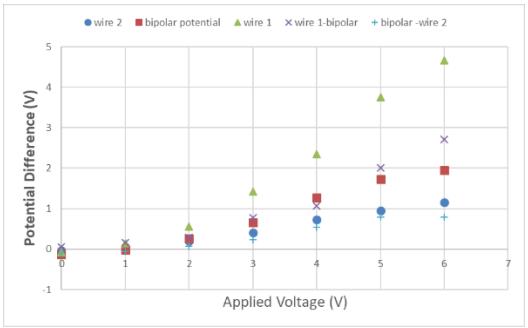

Figure 2.17.The solution potential at the positions of wire 1 and 2, BPE potential and their difference as a function of applied voltage

Next, we examine the potential profile measurement in a closed BPE cell. As shown in Scheme 2.2, two small gold wires were on either side close to the gold bipolar rod surface. The ECL solution was added to the anode compartment, and 10 mM $HClO_4$ was added to the cathode compartment. Three voltmeters were used to measure the potential difference between gold wire 1 and wire 2, driving cathode and wire 2, and driving cathode and the BPE. By calculation, the polarized potential of wire 1,

2, and the bipolar electrode and all also obtained as shown in Figure 2.17. Initially, there was no faradaic current, the potential of the wire came from the charging polarization of the solution temporarily. As the applied voltage increased, it shows a clear potential separation between the solution potential at the BPE cathodic and anodic ends. The interfacial potential drop on the BPE surfaces from heterogeneous electron transfers accounted for this separation. Surprisingly, the potential difference between the BPE and wire 2 was much smaller than that between wire 1 and the BPE. This imbalance should be attributed to the different capability of the two solutions to polarize the BPE. To be more exact, the overpotential requirement for H_2 evolution in $HClO_4$ solution was larger than that for $Ru(bpy)_3^{2+}$ oxidation in the ECL solution in order to keep an equivalent heterogenous faradaic electron transfer. Furthermore, the generated H_2 bubbles from H_2 evolution would be absorbed on the BPE surface and cause a significant potential drop.

2.3.2.3 Potential Profile in the Gap BPE System

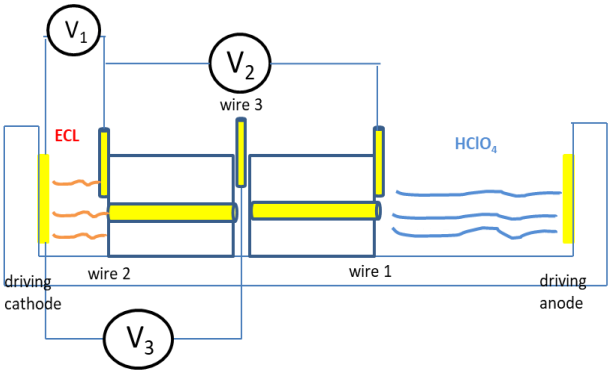

Scheme 2.3.The illustration of the setup of potential difference measurement in the mounting gap cell.

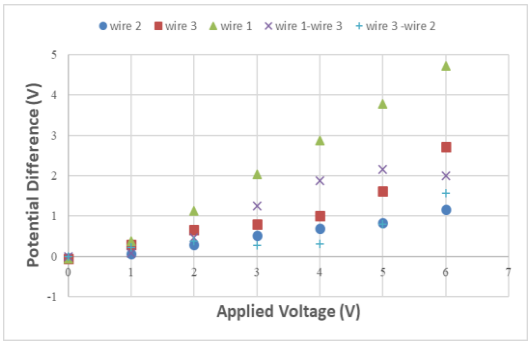

Figure 2.18.The solution potential at the positions of wire 1 and 2, wire 3 in the gap, and their difference as a function of applied voltage when the gap solution is 1 mM $K_3Fe(CN)_6/K_4Fe(CN)_6$.

Following the ECL experiment, the characterization of the potential profile was undertaken in the gap cell. Similarly, ECL solution was added to the anode compartment and 10 mM $HClO_4$ was added to the cathode compartment. A wire 3 was embedded into the gap to measure the solution potential in the gap. Voltmeter 3 measured the potential difference between the gold wire and the driving cathode (Scheme 2.3). When the gap was filled with 1 mM $K_3Fe(CN)_6/K_4Fe(CN)_6$, the potential of wire 1 was linear to the applied voltage, while the potential of wire 3, which represented the solution potential in the gap,

behaved like an “S” curve (Figure 2.18). The potential of wire 3 increased slowly at the beginning and then grew in a steep slope after 4 V, demonstrating a self-adjustment of the gap solution. After the inflection point at 4 V, the increment of potential required to maintain the equilibrium of the reactions at the left BPE (wire 3 - wire 2) became significantly higher than the reactions at the right BPE (wire 1 - wire 3). The value of wire 1 - wire 3 was relative stable, indicating that it had reached the diffusion-limited region for $Fe(CN)_6^{4-}$ oxidation on the right BPE inner surface; while the reactions on the left BPE ($Ru(bpy)_3^{2+}$ oxidation at 1.2 V and $Fe(CN)_6^{3-}$ reduction at 0.30 V, with a potential separation of 0.90 V), still required a larger overpotential to facilitate the electron transfer rate.

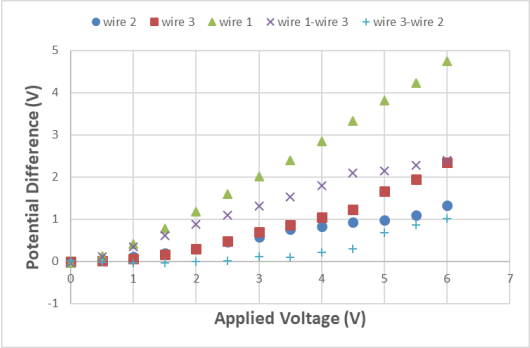

Figure 2.19.The solution potential at the positions of wire 1 and 2, wire 3 in the gap, and their difference as a function of applied voltage when the gap solution is 10 mM $HClO_4$.

By changing the gap solution from $K_3Fe(CN)_6/K_4Fe(CN)_6$ couple redox couple to $HClO_4$, the data exhibited an exponential growth (Figure 2.19). The redox reaction of $K_3Fe(CN)_6/K_4Fe(CN)_6$ couple in the gap, would to some extent act as an effective depolarizer, modifying the potential in the gap. A similar phenomenon was previously discussed as a mixed potential in the mixed potential theory according to the literature of corrosion experiments[134]. It would depolarize the potential in the gap at the initial stage, in which a small potential increase could promote a larger current generation in the gap. While in $HClO_4$, the solution potential would increase until initiation of redox reactions from the solvent decomposition.

In summary, the whole potential profile study provides us the insights on bipolar electrochemistry on the basis of the electric field distribution and reveals to us that:

(1) The time decay of the potential gradient in the BPE system after applying the external voltage has an important influence on the stability of the ECL signal.

(2) Low ionic strength with high solution resistance shows a larger potential drop only before a certain voltage, then high ionic strength with lower resistance facilitates solvent decomposition and increase the current in the system with a larger potential drop. Higher concentrations of active redox couple would always enhance the current flow in the system as well as the electric field.

(3) A small amount of nonfaradaic charging current is not capable of generating a sustainable electric

field across the solution for BPE reactions after the establishment of the double layer.

(4) For the closed BPE cell configuration, different solutions in the anode and cathode compartment will have different polarizabilities towards the bipolar electrode. Both the ionic strengths and the redox reactions in the separate compartments determine the current flowing through the BPE. As shown in Figure 1.12, with changing R_1 and R_2 (solution resistance) and active species in the solution, the total resistance ($R_{tot} = R_1 + R_2 + R_{BPE}$) in this series circuit would vary accordingly, resulting in the simultaneous change in i_{BPE}.

(5) For a gap cell with two BPEs, the potential drop between each BPE is determined by the overpotential requirement for reactions happening at both ends; and the solution potential in the gap will adjust itself proportionally. Electroactive species in the gap acts as a depolarizer to modify the potential.

(6) The effect of degassing as convection force shows a dual-effect in electric field distribution. When charging current from ion migration prevails, degassing will interrupt the process of double layer formation and cause a reduction of electric field strength; when the faradaic reaction starts to dominate, the faster mass transfer will lead to a higher electric field by a greater current flow. However, in both cases, degassing will result in an instability in the magnitude of the electric field.

2.3.2.4 Effect of Channel on Potential Profile

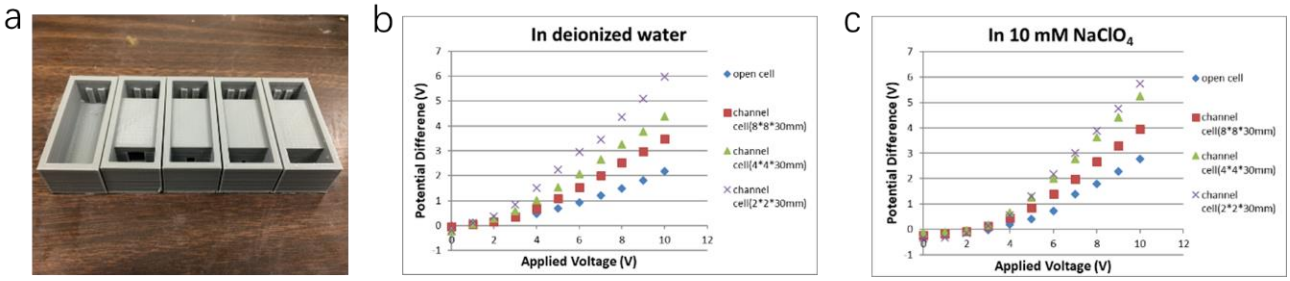

Figure 2.20.(a) 3D-printed channel cells for potential profile measurement. (b) Potential difference versus applied voltage in deionized water (c) Potential difference versus applied voltage in 10 mM $NaClO_4$.

As discussed earlier, in the open cell, lowering the electrolyte concentration to decrease the applied voltage is noneffective. Instead, a channel design may be more useful to increase the potential drop as the driving force for bipolar electrochemistry. Multiple cells (50 mm × 20 mm × 15 mm) with different channel sizes were fabricated by 3D printing. In addition to a fully open cell which was 30 mm wide, cells with channel size of 2 mm, 4 mm, and 8 mm in square shape were fabricated as shown in Figure 2.20(a). Two gold wires were placed at the exits of the channel or separated by the same distance as the channel length in the fully open cell to measure the solution potential difference. As shown in Figure 2.20(b)(c), the potential difference in either deionized water or 10 mM $NaClO_4$, is inverse proportional

to the channel size, with 2 mm channel having a value more than twice as large as the open channel. Therefore, a channel design is more effective to enhance the electric field.

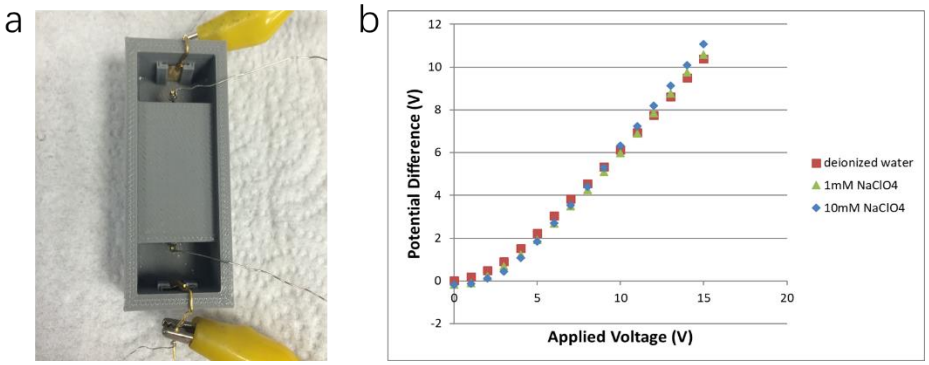

Figure 2.21.(a) 3D printed channel cells with 2 mm in a square shape for potential profile measurement. (b) Potential difference versus applied in the cell of pure water, 1 mM $NaClO_4$, and 10 mM $NaClO_4$.

	conductance(μs/cm)	resistance(MΩ)
Deionized water	0.62	1.612903226
1mM $NaClO_4$	112	0.008928571
10mM $NaClO_4$	1084	0.000922509

Table 2.1.the resistance of different solution measured by a conductivity meter

In the 2 mm channel cell, as the applied voltage increases to 15 V, the potential difference is about 11 V, showing an enhanced electric field in the cell (Figure 2.21(a) (b)). Note that the potential profile for different solutions with changing ionic strength shows almost no difference, even with a hundred-fold resistance change (Table 2.1). Still, deionized water has a slightly larger potential difference at the low voltage range due to its higher resistance; while 10 mM $NaClO_4$ has a higher potential difference at the high voltage range due to greater faradaic current contribution.

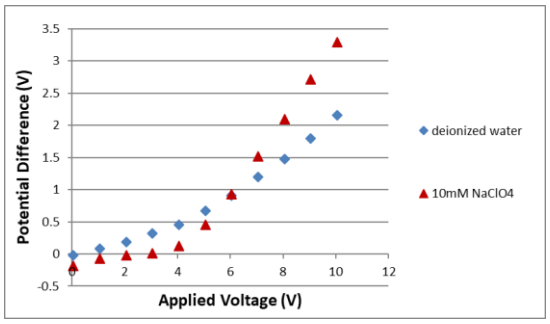

Figure 2.22.Potential Difference in the open cell versus applied voltage in deionized water, 10 mM $NaClO_4$ in the open cell.

When replacing the channel cell with the fully open one, the effect of ionic strength is evident. The potential gradient in deionized water is higher at first, then exceeded by 10 mM $NaClO_4$ (Figure 2.22). At a low applied voltage, during the formation of the double layer by ion migration, the counterions will come close to the driving electrode (anions to the anode and cations to the cathode), thus creating a reversed electric field which could offset part of the external electric field. As a result, an electrolyte

solution with more ions would have a lower potential gradient than the one with fewer ions. However, at a high voltage, in the solution with less resistance, the reactions at both driving electrodes can proceed faster, hence generating more positive ions at the anode and negative ions at the cathode, following by subsequent faradaic current from ion migration. This created electric field in the forward direction can be added to the original one to provide a higher potential gradient in solution.

2.3.2.5 ECL Performance under the Electric Field Change

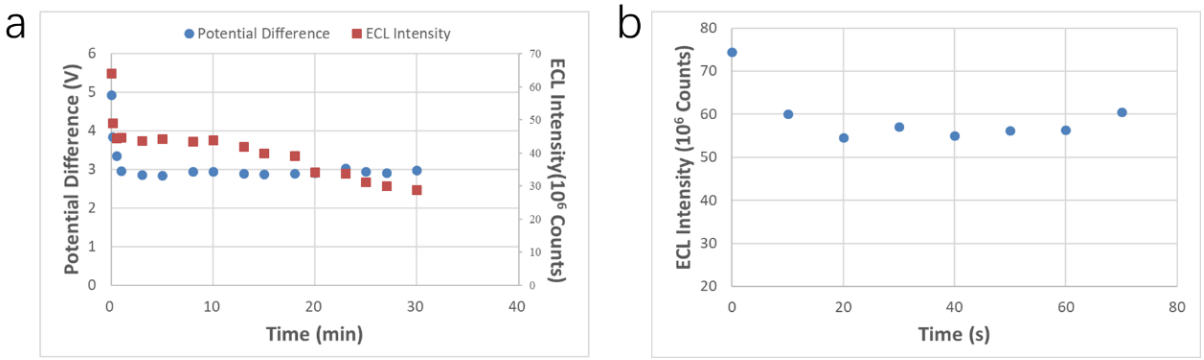

Figure 2.23.(a) Simultaneous measurements of the potential difference and ECL intensity as a function of time in 30 min at an applied voltage at 7.5 V. (b) ECL intensity measurement as a function of time in 70 s at 7.5 V.

At last, the ECL intensity change was correlated with the time decay of the electric field. As shown in Figure 2.23(a) (blue circle), after switching the voltage to 7.5 V, the potential difference between two gold wires decreases exponentially at the first 1 min, then stabilizes at around 3 V even after 30 min. The ECL intensity measured simultaneously also shows a rapid deterioration initially; then it holds relatively constant for a few minutes. After that, the ECL intensity decays again gradually for an extended period. The anode surface was observed blackened after the experiment. Another ECL experiment was also taken by recording its emission for a short time about 80 s. A fast decay is observed before 20 s, and then the ECL intensity reaches a comparably stable value (Figure 2.23(b)).

Based on the results, the fast decay of the ECL signal in the BPE system should be ascribed to the potential gradient decrease when a voltage is applied. On the one hand, transient charging current will pass across the system with the formation of the double layer; on the other hand, the surface concentration of reactive species will be the largest at the beginning, then the concentration gradient drops as the thickening of the diffusion layer. The exponential decay of the potential gradient is described as the same as the Cottrell behavior of current in a chronoamperometry experiment. While, the slow ECL decay is not related to the potential gradient, but from the chemistry occurring on the BPE anode surface. Bubbles (oxygen) formed on the BPE anode surface that suppressed the ECL. More importantly, the accumulated film formation on the anode was responsible for the gradually ECL signal deterioration.

In a word, from all the studies above, besides the analyte concentration, we have figured out the applied voltage, measuring time point, degassing, the composition and resistance of the solution (both in the compartments and the gap) and surface chemistry on the BPE, all could affect the ECL performance. An appropriate time point for measurement should be carefully selected to balance the potential instability at the beginning stage, time consumption, and undesired surface chemistry.

2.3.3 Remaining Issues in the Printed Thin Layer

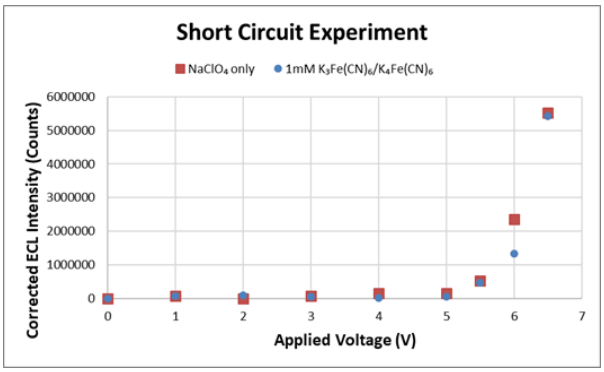

Figure 2.24.ECL intensity of $NaClO_4$ only and 1 mM $K_3Fe(CN)_6/K_4Fe(CN)_6$ under short circuit.

Th Up to this point, the thin layer regions width has been created by manually assembling parts, to set the BPE inner surface distance. Therefore, the two BPEs had the possibility of short-circuiting. Like shown in Figure 2.24, the ECL intensity of 1 mM $K_3Fe(CN)_6/K_4Fe(CN)_6$ overlaps with that of $NaClO_4$ only. Thus, a spacer is expected to be incorporated in the next fabrication to further improve the performance of the thin layer. In addition, a flow cell design is required to facilitate the solution replacement.

2.4 Experimental Section: Cell Design and Electrochemical Analysis

2.4.1 Reagents

Tris(2,2'-bipyridyl) dichlororuthenium (II) hexahydrate ($Ru(bpy)_3Cl_2 \cdot 6H_2O$, 99.95%, Sigma-Aldrich), Potassium ferricyanide (III) ($K_3Fe(CN)_6$, 99%), Potassium hexacyanoferrate(II) trihydrate (III) ($K_4Fe(CN)_6 \cdot 3H_2O$, ≥99.5%, Sigma-Aldrich), Sodium perchlorate monohydrate ($NaClO_4$) (≥99.0%, Fluka), Sodium oxalate (≥99.5%, Alfa Aesar), Sodium phosphate monobasic (≥99.0%, Fisher Scientific), Sodium phosphate, Dibasic, anhydrous (≥99.0%, EMD), p-Benzoquinone (≥99.5% HPLC, Fluka), Hydroquinone (99%, Alfa Aesar).

All solutions were prepared using deionized, ultrafiltered water (18.3 MΩ cm) generated from the Milli-Q water purification system (MilliporeSigma, Burlington, MA). All reagents were used as received without further purification.

2.4.2 Device Fabrication

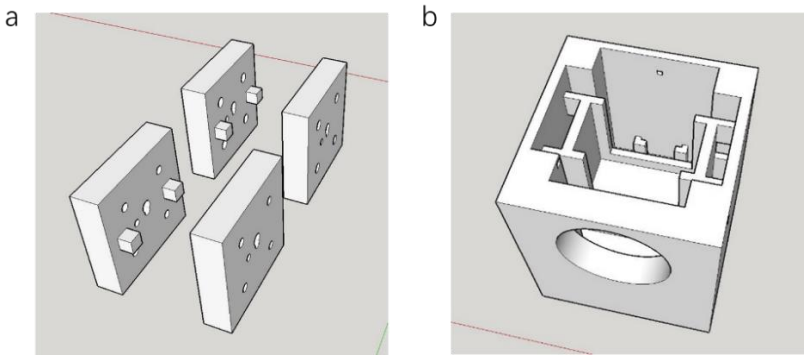

Figure 2.25.(a) Printed central building block with a large hole in the middle for holding BPE rod and four holes around for screws. (b) The peripheral cell for central thin-layer cell insertion and collecting window for the lens.

From the success of the previous gap cell, a new double-cell configuration adapted for the ECL measurement was fabricated with the use of a commercially-available spacer and flow cell design as follows:

The bipolar electrode thin-layer (BETL) system with double-cell configuration was fabricated by MakerBot Replicator 2 3D printer. All the 3D parts constructing this system were fabricated as described in Section 2.2.2.

The double-cell configuration was composed of two parts: the peripheral ECL cell and the central bipolar electrode thin-layer cell. For the central bipolar cell, a gold rod (GF85112232, diameter 2.0 mm, Sigma-Aldrich) was cut into two identical pieces (15 mm long) as bipolar electrodes. Each of the BPE was respectively inserted and sealed by an epoxy adhesive (Loctite, 1C) in a cylindrical hole in the middle of a printed central building block (Figure 2.25(a)) as half of the thin-layer cell, for 24 hours until its full solidification. Then the inner face of each half thin-layer cell was coarsely polished following the same procedure in Section 2.2.2. After each step of polishing, the block was sonicated in 1:1 water/ethanol mixture for 10 min to remove the particle residues. This design minimizes the edge effect by also creating a thin layer of solution instead of the bulk solution around the electrode. Simultaneously, the other end of the bipolar electrode was polished in a similar sequence while allowing it to extrude out of the block surface to provide enough electrode surface area for ECL emission and wire connection for electrochemical characterization afterward. Electrochemical cleaning was then applied to both the inner and outer surfaces of the bipolar electrodes by cycling them in 0.5M sulfuric acid from -0.5 to +1.5 V at a scan rate of 0.1 V/s for 40 cycles. The cleaned gold electrodes were throughly washed with D.I. water and ethanol, and dried under flowing nitrogen. In addition, each block had a small round cavity of 1.55 mm in diameter as inlet/outlet, 5 mm side away from the cylindrical hole, and centrosymmetric to each other. Tygon microbore tubing (0.508 ID × 1.524 mm OD; Cole-Parmer, Vernon Hills, Illinois) was implanted into the inlet/outlets, and o sealed by epoxy. A crossflow

cell gasket (MF-1044, 12.7 μm, BaSi) was placed inside the inner faces of two blocks serving as the spacer to create a micron-size cavity between bipolar electrodes, with BPEs aligned in the middle of the elliptical cavity of it. By this design, the edge effect was minimized by confining the solution in a thin layer in the elliptical cavity surrounding the BPE. In each of the building block, there were four printed holes, and they were threaded by a hand tap (M4, High-Speed Steel, Grainger). Nylon screws, rubber o-rings, non-metal washes, and nylon hex nuts (Grainger) were used to mechanically clamp the two half-thin-layer cells together to achieve a solution-tight seal. Metal parts were not used here to avoid their corrosion and polarization caused by the electric field present under bipolar electrochemistry. The whole assembly resembled a two-electrode flow cell configuration. The inlet tubing was connected directly to a syringe pump, and the outlet tubing was placed in a collection reservoir. Solution sample was injected from the syringe through the inlet, passing across the confined thin-layer region between the inner faces of two bipolar electrodes and flowed to the to the waste reservoir via the outlet. This fluidic arrangement allowed facile solution exchange.

In addition to the thin-layer cell, a peripheral ECL cell was also 3D printed for holding the thin-layer cell and bipolar ECL experiment (Figure 2.25(b)). One side wall of the peripheral cell perpendicular to the bipolar electrode alignment was printed with a circular hollow for installing a C-mount for a secondary lens (Computar TV lens 12.5 mm, 1:1.3) followed by the epoxy seal. The setting of the secondary lens was described in Section 2.3.1.2. In the middle of the peripheral ECL cell, a rectangular groove was reserved to embed the central thin-layer cell. Parallel channels are on both sides allowing the ECL solution to flow through the whole ECL cell as an open BPE system. Two 10 mm×10 mm slots with 1 mm thickness were printed next to the side wall for driving electrodes placement. Considering the chemical compatibility of PLA material and possible permeation through layers, Polydimethylsiloxane (PDMS, Sylgard® 184; 10:1, base : curing agent) coating was introduced to all the inner faces of the ECL cell to isolate it from the electrolyte solution. The PDMS mixture was carefully coated on the surface and cured in an oven at 50 °C (below the PLA glass transition temperature of 65 °C) for 3 hours.

2.4.3 ECL experiment

Two gold foils (1 mm in thickness) with the size of 10 mm×10 mm were used as driving electrodes and located in printed slots in the peripheral ECL cell. A DC power supply (9122A, BK Precision) was used to provide the electric field in the BPE system. Images from ECL emission were collected by a custom CCD camera (D7000, Nikon) with an exposure time of 5 s. The camera was operated in manual mode with parameters set as follows: ISO sensitivity: 6400; shutter speed 5 s; white balance: auto. Images were stored in RAW. format and analyzed by ImageJ software from RGB value. In the ECL intensity-voltage measurement, the applied voltage is gradually increased with a time interval of 10 s. In the

intensity-time dependent measurement at constant applied voltage, the voltage is applied first for 60 s until the stabilization of electric field in the system. Then the ECL is recorded immediately after changing the solution by a syringe pump.

2.4.4 Thin Layer Characterization

The preliminary characterization of the thin layer was tested using a conventional three-electrode system. Silver wire was used as a quasi-reference electrode, and platinum wire counter electrode was inserted into the thin-layer cell through the microfluidic tube attached to the inlet and outlet. Basic cyclic voltammetry test was employed to indicate the successful fabrication of thin layer based on 3D printed building blocks. Linear sweep voltammetry (LSV) and chronoamperometry (CA) in a two-electrode system and dual electrode voltammetry (DECV) in the generator-collector system were employed to characterize the thin layer. The parameters are respectively described in the main text.

A two-electrode setup was used instead of a three-electrode system to resemble the behavior of a thin layer under the BETL system. Linear sweep voltammetry (LSV) and chronoamperometry (CA) experiments were performed at room temperature while the reference and countering terminals were shorted together as a simulation of the two-electrode configuration in the BETL ECL experiments. All potentials are reported as the difference between the two bipolar electrodes. In the LSV study, the potential of one bipolar electrode was held constant, and potential of the other bipolar electrode was swept linearly from zero to the desired value with different scan rates (1 mV/s to 50 mV/s) until observing plateau current. It represents the ECL variation when gradually increasing applied voltage in the BETL system. In the CA study, a series of step potentials (100 mV to 1100 mV) was applied first; then the current is recorded immediately after changing the solution. As a result, the current response can be correlated with ECL intensity change under constant applied voltage in the BETL system, implying the gap solution composition change as a function of time. All the electrochemical characterizations were performed under a bipotentiostat/galvanostat (Model WaveDriver 20, Pine) for system control and data acquisition.

The microscopic electrochemical active surface area of each BPE inner surface was characterized by the integration of the gold oxide reduction peak in a cathodic scan. The current minimum that follows the gold oxidation peak in the voltammogram is usually taken as an indication that a monolayer coverage of gold : oxygen ratio of 1:1 is reached[135]. It was done by using 0.1 M phosphate buffer (pH 7.4) and consisted with two CV scans between -0.1 and +1.2 V at a scan rate of 50 mV/s following the literature[136]. Oxide formation started at +0.65 V, and the area under the gold oxide stripping peak in the second scan was taken as a measurement of active surface area. According to the average calculated value integrated from different measurements, the BPE 1 had an active surface area of 0.039 cm^2 with

a roughness factor of 1.25, and the BPE 2 had an active surface area of 0.041 with a roughness factor of 1.31.

After characterizing the BPE surface, the thin layer cells dimensions need to be determined next. However, there is no well-defined method in a three-electrode system. Instead, linear sweep voltammetry (LSV) used in a two-electrode system and chronoamperometry (CA) in the generator-collector system are adapted to characterize the thin layer.

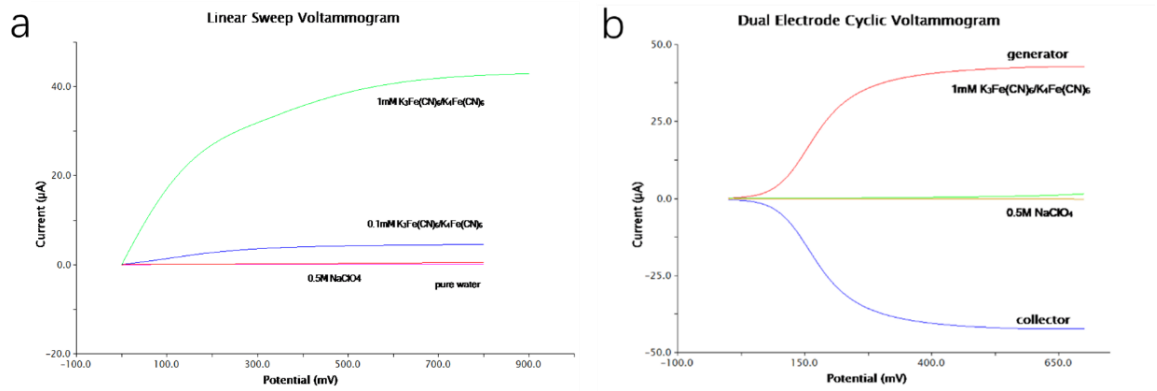

Figure 2.26.(a) LSV of pure water, 0.5 M $NaClO_4$, 0.1 mM $K_3Fe(CN)_6/K_4Fe(CN)_6$, and 1 mM $K_3Fe(CN)_6/K_4Fe(CN)_6$ in 0.5 M $NaClO_4$ in the 3D printed thin-layer cell using a two-electrode system. (b) Dual-electrode cyclic voltammogram (DECV) of 0.5 M $NaClO_4$, and 1 mM $K_3Fe(CN)_6/K_4Fe(CN)_6$ in 0.5M $NaClO_4$ in the 3D printed thin-layer cell with the collector potential set as -200 mV, and the generator potential scanning from 0 to 700 mV, scan rate: 30 mV/s.

First, LSV was taken using the thin-layer cell with the working terminal connected to one of the BPE, while the reference and counter terminals were shorted together and connected to the other BPE. As shown in Figure 2.26(a) (blue), the one with 0.5 M $NaClO_4$ has only a negligible capacitive current linear to the applied voltage around several hundred nA until the appearance of water decomposition. When the solution is changed to 0.1 mM $K_3Fe(CN)_6/K_4Fe(CN)_6$ (green), it shows a significant current from the faradaic redox reaction in the thin layer. A higher concentration of 1 mM has a much larger current response. Both the currents display a plateau after 500 mV, indicating the diffusion-limited steady-state in an ideal twin-electrode thin layer.

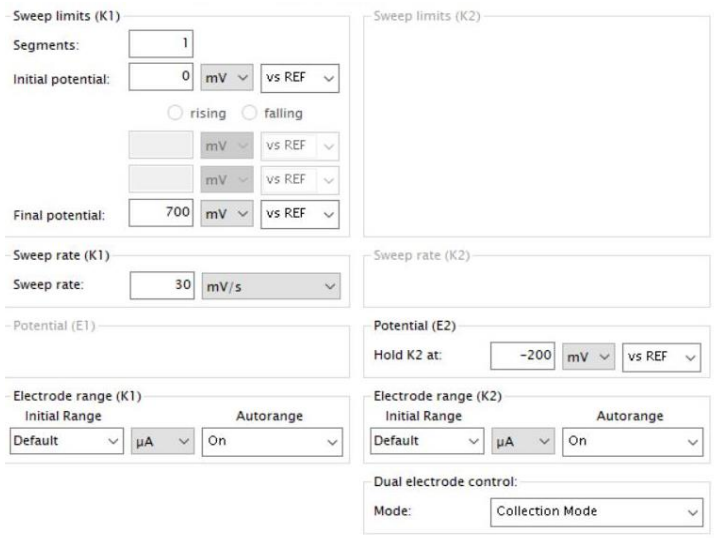

Figure 2.27.The parameter setting of a DECV experiment as a generator-collector system.

While treating it as a generator-collector system, several potentiostat parameters on the setting require clarification. A conventional three-electrode system was employed here, with two working electrodes for collecting both current responses. The reference and counter electrode were quasi-silver wire and platinum wire respectively inserted in the microfluidic tubings as mentioned previously. Dual electrode cyclic voltammetry (DECV) was performed. As depicted in Figure 2.27, the potential of one BPE is scanned from 0 mV to 700 mV, which is significantly positive to oxidize $K_4Fe(CN)_6$; while the potential at the other electrode is fixed at -200 mV for a fast reduction of $K_3Fe(CN)_6$ back to $K_4Fe(CN)_6$.

DECV was first operated to compare the voltammogram of 0.5 M $NaClO_4$ and 1 mM $K_3Fe(CN)_6/K_4Fe(CN)_6$ in this electrolyte in only a half forward scan (Figure 2.26(b)). In 0.5 M $NaClO_4$, both current responses are flat, with the generator current increasing slightly after 700 mV. It should be attributed to the trace amount of gold oxidation on the generator BPE that can not be collected on the collector. 1 mM $K_3Fe(CN)_6/K_4Fe(CN)_6$ with equivalent reduced and oxidized form shows much larger responses in which the generator and collector currents are in exact symmetry. It is worth mentioning that the plateau currents of the two-electrode system LSV and three-electrode DECV are at approximately the same value of 42.3 µA. The thin-layer distance can be obtained based on the equation:

$$I_{lim} = \frac{nFADC_0}{\delta}$$

with parameters: n=1, F=96485 C, geometric surface area=0.031416 cm^2, since the thickness of the spacer is around 10 µm, the time scale it takes to build up such a diffusion layer thickness is around 0.1s. Therefore, the electrode geometric area is treated as the same as the cross-sectional area of the diffusion field. $D = \frac{2D_R D_O}{D_R + D_O}$=7.01*$10^{-6}$$cm^2$/s, $C_0 = \frac{2\ mM}{L} = 0.000002\ mol/cm^3$ The thickness of the thin layer is then calculated to be 10.4 µm, which is close to the thickness of the spacer of 12.7 µm. If

we consider the roughness factor of 1.25, it would be calculated to be 13 µm (as obtained from previous surface characterization).

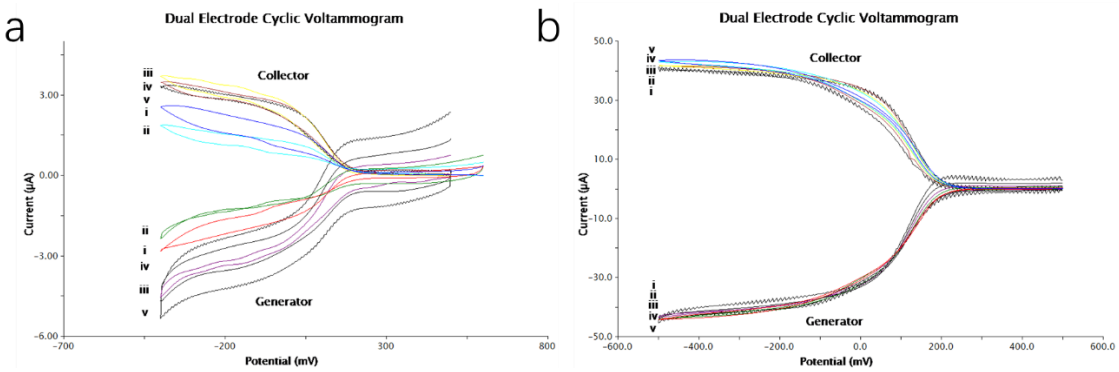

Figure 2.28.(a) DECV of (a) 0.2 mM $K_3Fe(CN)_6$, (b) 2 mM $K_3Fe(CN)_6$ in 0.5 M $NaClO_4$ in the 3D printed thin-layer cell with the collector potential set as 500 mV, and the generator potential scanning from 500 to -500 mV (scan rate (i) 10 mV/s, (ii) 30 mV/s, (iii) 50 mV/s, (iv) 100 mV/s, (v) 200 mV/s)

DECV with ferricyanide only in the thin layer was then carried out with concentrations of 0.2 mM and 2 mM. The generator BPE potential was swept from 500 to -500 mV using different scan rates from 10 mV/s to 200 mV/s; and the collector was set at 500 mV. As shown in Figure 2.28(a), contrary to the accepted literature[137], on the generator the response does not display a CV-like curve with a cathodic and anodic peak corresponding to the reduction of $K_3Fe(CN)_6$ and back oxidation. The reason could be explained by the geometry of the thin layer which has a sufficiently small thickness and restricted region of diffusion. Once $Fe(CN)_6^{3-}$ is reduced in the generator, it will quickly diffuse to the collector and be oxidized, thus no more generated $Fe(CN)_6^{4-}$ is present. When the generator scans backward later, barely any $Fe(CN)_6^{4-}$ will be oxidized on the generator in such a confined thin layer. Besides, the current values from the generator and collector are not proportional to the scan rate, especially at the concentration of 2 mM, they almost overlap with each other, also indicating its restricted diffusion region (Figure 2.28(b)).

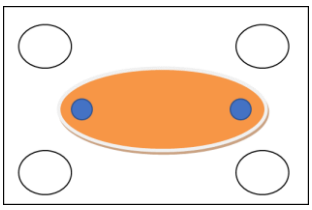

Figure 2.29.The thin layer created by the spacer, blue circles indicate the contact regions as inlet and outlet.

In this 3D printed thin-layer cell, the confined geometry allows a collection efficiency of 1(Figure 2.29). Because of a sufficiently small thickness, redox active species reduced at one electrode will diffuse to the other electrode for oxidation rapidly. Also, the solution is trapped in the thin layer with almost no diffusion from the bulk solution by the thin layer created by the cavity. Even though with a possible diffusional pathway through the microfluidic inlet and outlet, the edge effect could be ignored due to

the minimized contact ratio, it is different from other generator-collector systems in which the bulk solution surrounds the thin layer.

As discussed earlier, the oxide film formation simultaneously occurs with the oxidation of $Ru(bpy)_3^{2+}$ to $Ru(bpy)_3^{3+}$, particularly with a redox couple in a high concentration and under a high applied voltage. Fortunately, this film can be easily removed by a paper towel, and the ECL can recover back to a high magnitude.

In addition to the surface chemistry on the BPE anode outside, the change in the thin layer may also cause the ECL deterioration in repeated measurements, such as the passivation of BPE surface in the thin layer. Such a surface structure variation can change electron-transfer kinetics and the active surface area. A convenient method was employed to reactivate the BPE surface without dismantling the thin-layer cell for polishing. Instead, the BPE surface was electrochemically cleaned by filling the thin layer with a 0.5 M H_2SO_4 and independently scanning each BPE from -0.2 to +1.5 V at a scan rate of 0.1 V/s for 40 cycles using the three-electrode system. Experimental data shows that with the help of electrochemical cleaning inside the thin layer, the surface was regenerated to almost its original condition.

Another inextricable problem of using the thin-layer cell under BPE electrochemistry is the method of voltage application. If the solution is introduced first followed by switching the power supply to a certain voltage, because of the electric field time decay, the driving force for the thin-layer reactions and ECL reaction are not constant before the stabilization of the electric field. If the DC power is turned on first for a period, it can provide a stable electric field afterward. However, the infill of the sample will induce an enhanced mass transfer by convection. The second case is selected since it takes a short time for the solution to equilibrate.

In order to mitigate all the problems discussed, an optimized experimental design with a double-cell configuration was used as the final approach to precisely correlate the ECL emission intensity with the electrochemical behavior in the thin layer. The BPE anode outside the thin layer was cleaned after each set of ECL experiments to remove gold film formation. For constant-voltage measurement, the DC power supply was set to a specific applied voltage for 60 s until a stable electric field in the solution was attained. Next, employing a syringe pump, about 50 μL of the solution was introduced into the thin layer through the inlet to ensure complete evacuation of the old solution. The ECL intensity was subsequently recorded as a function of time by continuous images capture.

2.5 Results and Discussion

2.5.1 Principle and Theoretical Illustration

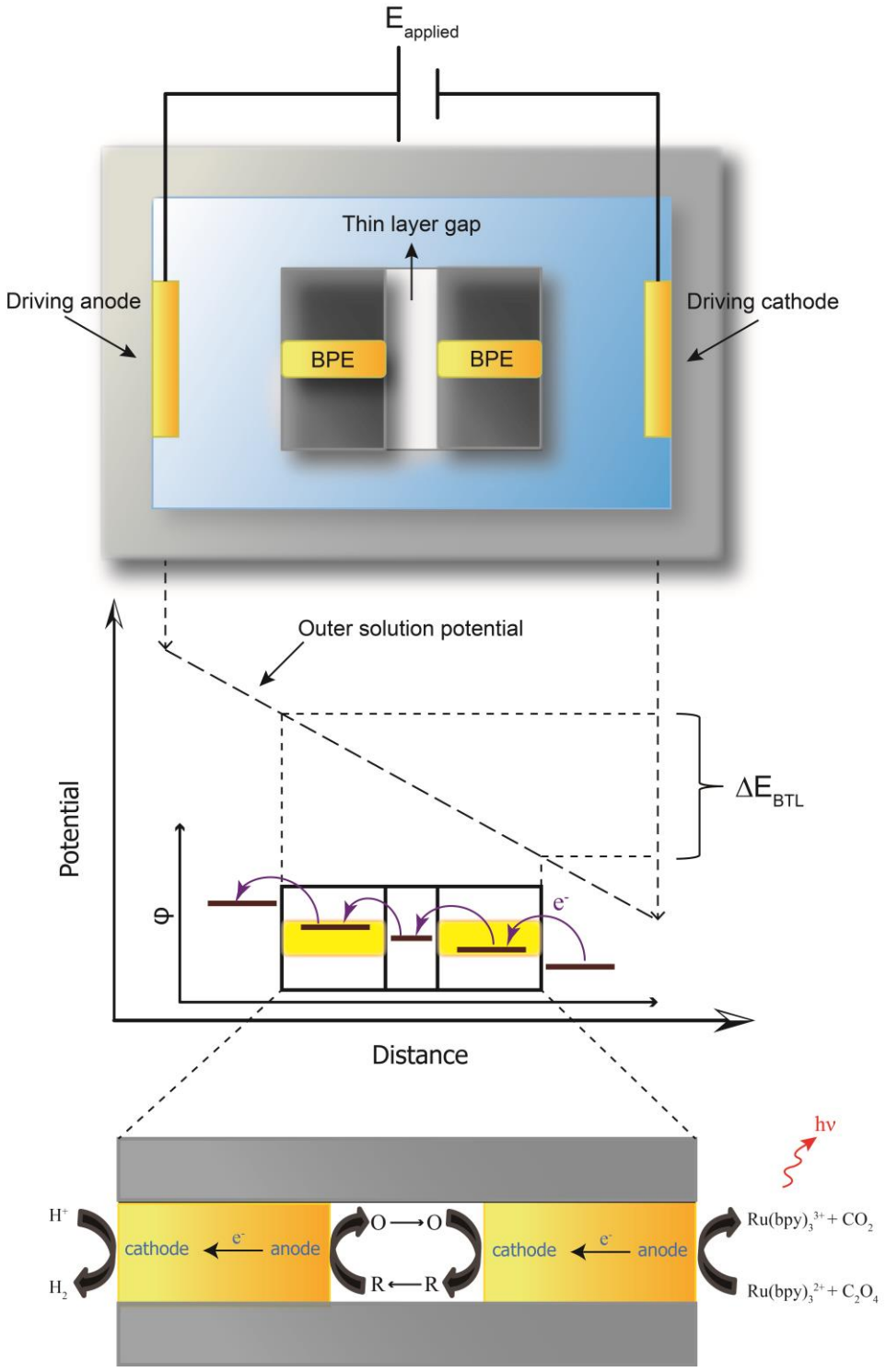

Scheme 2.4.Schematic illustrations of the bipolar electrode thin-layer (BETL) system and its potential profile.

The basic working principle of this bipolar electrode thin-layer (BETL) system is illustrated in Scheme 2.4. An external voltage provided by a DC power supply is applied to two driving electrodes placed at

both ends of the open peripheral cell, to sustain the electric field necessary for bipolar electrochemistry. In the middle of the cell, two bipolar electrodes sealed in two separate barriers are placed parallel to each other with a thin layer between them, serving as an embedded central thin-layer cell. Two solution channels are positioned alongside the thin-layer cell, allowing the reporting ECL solution to flow across the entire reservoir as an open BPE system. The electric field distribution is thus simplified without the consideration of the depolarizability of active species in the thin layer, creating a uniform and continuous potential gradient imposed on the central thin-layer cell section. The sizes of the solution channels are minimized (4 mm × 8 mm) to ensure a substantial solution potential decline along the channel length which is in the same horizontal position as the thin layer. Another benefit of this system is that the isolated double-cell design physically and chemically separates the sensing reaction within the central thin-layer cell and reporting reaction outside. Moreover, the analyte will not be consumed at the driving electrode, while the design also avoids the possible interference or contamination from the reporting solution in the peripheral cell.

Under the influence of the externally applied voltage, a potential gradient will be established in the solution in the peripheral cell. When redox-active analyte O/R is introduced in the thin layer, different potential energy levels all imposed on the solution and the BPE by polarization. By satisfying the overpotential requirement, a sequential and cascade electron transfer occurs across the thin-layer cell. Six redox reactions take place simultaneously in the whole system. In this particular experiment, the peripheral cell is filled with the ECL reporting solution consisting of 5 mM $Ru(bpy)_3^{2+}$ as the light-emitting species, and 25 mM $Na_2C_2O_4$ as co-reagent dissolved in pH=7 PBS buffer to maintain a constant pH. The reaction taking place on the right BPE anode is the oxidation of $Ru(bpy)_3^{2+}$ to $Ru(bpy)_3^{3+}$ followed by ECL emission, which is coupled with the reduction of oxidized form O on the cathode in the thin layer. The reaction taking place on the right BPE cathode surface is H_2 evolution coupled with the oxidation of reduced form R on the other end. The ECL provides a convenient way of indirect analyte detection as an alternative to current readout. Due to the low analyte concentration in the thin layer compared to excess active species in the ECL solution, under the proposed BETL system, the behavior of ECL is determined by the electrochemical performance inside the thin layer. The analyte in the thin layer, in other words, actually acts as an "electrochemical gating" to couple the ECL emission and H^+ reduction at the two terminals of the thin-layer cell.

For better understanding this system, electrochemical characterizations under potentiostat control using this thin-layer cell were also taken to simulate the ECL experiments. The driving force for the BETL system deriving from the electric field across the solution can be directly represented by applying a potential to the two BPEs. In the simulation, electrical contact was made by connecting one BPE to the working terminal and connecting the other BPE to the counter and reference terminal of the potentiostat. Linear Sweep Voltammetry (LSV) and Chronoamperometry (CA) were employed to mimic this BETL

system. In the LSV study, one of the electrodes was grounded, while the potential of the other electrode was swept linearly in time. The current response thus represented ECL signal intensity as a function of the applied voltage in the ECL experiment. In contrast, in the CA study, the potential of one electrode was stepped to a certain value, and the current response was recorded as a function of time. The obtained voltammogram could thus be used to elucidate the ECL intensity variation versus time when maintaining a constant applied voltage. In this dual-electrode thin-layer configuration, redox species could undergo electron transfer on both electrodes and diffuse back and forth rapidly. As a result, unlike in common bulk LSV and CA, with the except of the initial process, no substantial depletion effect in the diffusion layer would be observed.

Moreover, to mitigate the edge effect, the solution in the thin layer was almost isolated from the bulk solution by only the narrow inlet and outlet connections to the microfluidics tubes. The solution samples were degassed with N_2 at least 15 min to eliminate oxygen from ambient as a means of reducing reduce the background current. Due to the tightly screwed thin-layer cell, the deaerated solution in the thin layer was effectively trapped between dual electrodes within the cross-flow cell gasket. Given that the small gravitation flow in the cell caused by its vertical alignment is infinitesimally small and thus has a negligible effect on the behavior of the solution in the thin layer, it could be treated as stationary. As previously explained, in each replacement run, the first small portion of the solution was discarded to avoid remaining analyte from the previous experiment set. A partial correction for charging of the double layer can be therefore made by subtracting the current response when only the supporting electrolyte is present at the same potential.

Figure 2.30.(Left) Simple ECL instrumentation of the BETL system with a double-cell configuration, CCD camera and mounted secondary lens. (Right) The images of 1 mM $Fe(CN)_6^{4-}/Fe(CN)_6^{3-}$ from 6 to 12 V with an exposure time of 5 s.

The final double-cell configuration consisted of a peripheral cell and a central thin layer, as shown in Figure 2.30 (left). A CCD camera is used to record the ECL intensity through a secondary lens. Figure 2.30 (right) shows typical images when gradually increasing the voltage. The reason for these nonideal focused images is from the edge of the extruded BPE surface that emits the ECL light in a dispersive way.

2.5.2 ECL and Electroanalysis of the BETL System Using Ferrocyanide/Ferricyanide Redox Couple

$Fe(CN)_6^{4-} - e^- \rightarrow Fe(CN)_6^{3-}$ ①

$Fe(CN)_6^{3-} + e^- \rightarrow Fe(CN)_6^{4-}$ ②

$H_2O + e^- \rightarrow 1/2H_2 + OH^-$ ③

$1/2H_2O - e^- \rightarrow 1/4O_2 + H^+$ ④

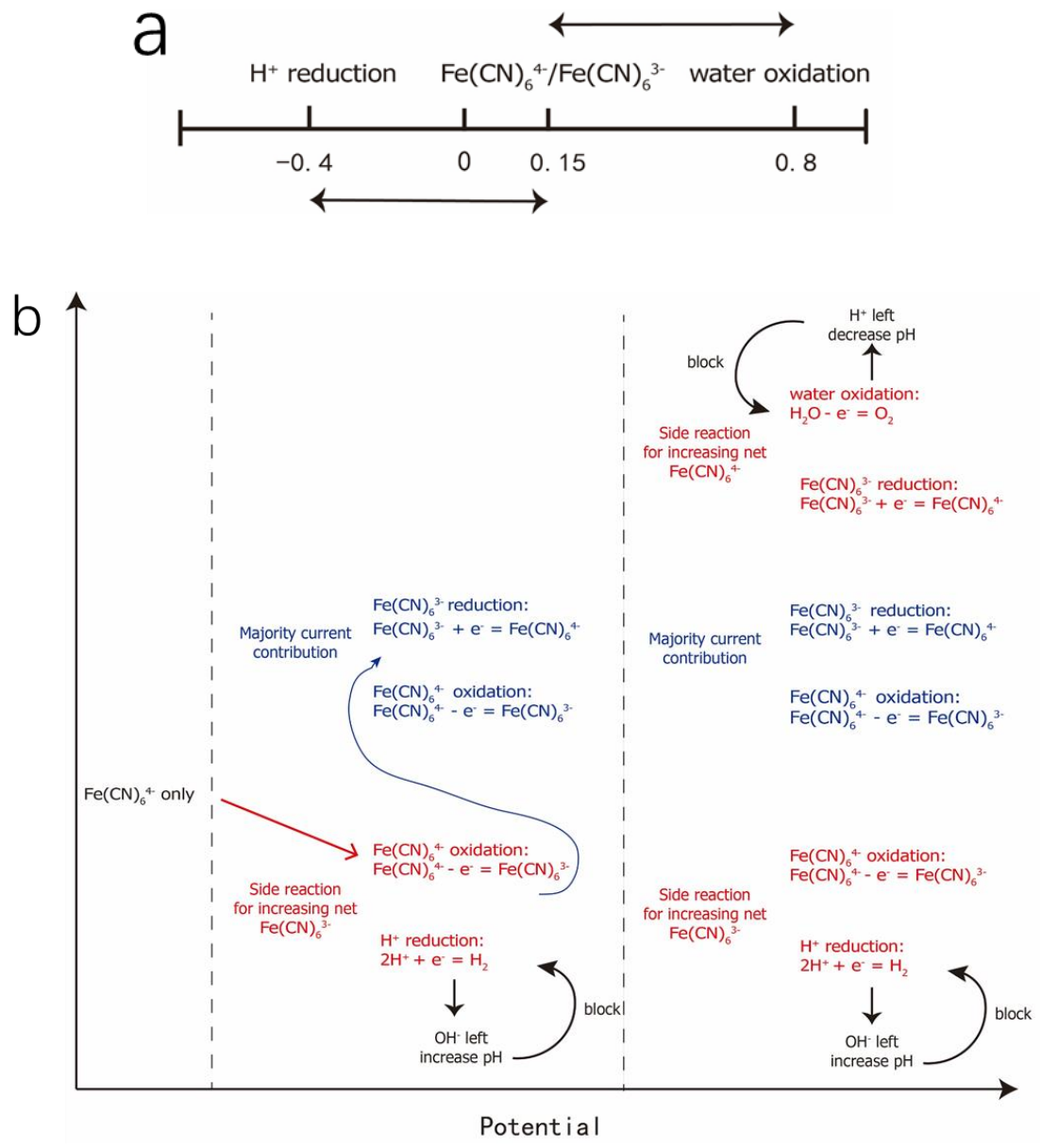

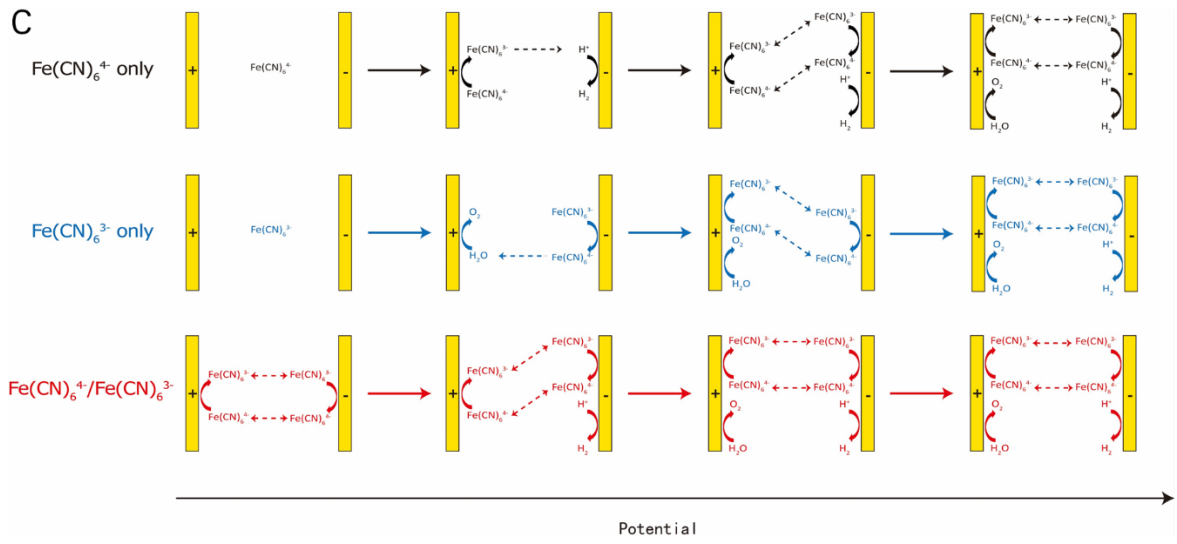

Scheme 2.5.(a) Potential diagram showing E_0 value of H+ reduction, $Fe(CN)_6^{4-}/Fe(CN)_6^{3-}$ redox reaction and H_2O oxidation and their potential separation. (b) Thin-layer reaction processes of $Fe(CN)_6^{4-}$ only versus potential between two bipolar electrodes in the unbuffered solution. (c) The cartoon demonstrating three cases of $Fe(CN)_6^{4-}$ only, $Fe(CN)_6^{3-}$ only, and equal $Fe(CN)_6^{4-}/Fe(CN)_6^{3-}$.

Ferrocyanide/ferricyanide couple, the most commonly used electrochemical redox molecules, were employed in the thin layer, as the first "gating valve" for the two separate bipolar electrodes to investigate the BETL system. Taking only $K_4Fe(CN)_6$ present in the unbuffered solution in the thin layer as an example (Scheme 2.5(b)). When gradually increasing the potential between two bipolar electrodes, there will be no redox reaction at the beginning. The current response is only from the nonfaradaic charging effect and possible background current (impurities), in which the charging current will not produce faradaic-relevant ECL emission. After passing the thermodynamic threshold, solvent (water) starts to decompose via H^+ reduction, $Fe(CN)_6^{4-}$ gets oxidized by coupling with it and generates $Fe(CN)_6^{3-}$. Once $Fe(CN)_6^{3-}$ is generated, it can diffuse to the inner bipolar cathode and be reduced, then the redox cycling of $Fe(CN)_6^{4-}/Fe(CN)_6^{3-}$ in the thin layer initiates and contributes to the current response. Because the formal potential E_0 of $Fe(CN)_6^{3-}$ reduction is far more positive than H^+ reduction, the redox cycling of $Fe(CN)_6^{4-}/Fe(CN)_6^{3-}$ can proceed at a fast speed with lower overpotential requirement. At the same time, H^+ reduction is still proceeding, that is the driving force of the net $Fe(CN)_6^{3-}$ increase in the thin layer. Besides, the pH in the thin layer would increase due to continuous H^+ reduction, and its change corresponds to the net $Fe(CN)_6^{3-}$ amount increase. Later on, current contribution from H^+ reduction is not sufficient as a "one-off" reaction, and it would be stopped by the shifted equilibrium from the pH change. The current from $Fe(CN)_6^{3-}/Fe(CN)_6^{4-}$ redox reaction contributes the most because of their equal E_0. If further increasing the potential, water oxidation with a higher potential barrier can also take place. Finally, all four reactions ①②③④ co-occur (oxidation ①+④ = reduction ②+③ due to the electroneutrality) and reach their steady state.

In summary, for only $K_4Fe(CN)_6$ present in the thin layer as the example, the direct reason for the current increase is the net amount increase of $K_3Fe(CN)_6$ and consequent enhancement of redox cycling. While H^+ reduction, served as a side reaction, is the indirect but essential reason. Without H^+ reduction, $Fe(CN)_6^{3-}$ cannot be generated, let alone the ferro-/ferricyanide redox cycling. Even so, the substantial current response comes from $Fe(CN)_6^{4-}/Fe(CN)_6^{3-}$ redox cycling with only little contribution from H^+ reduction due to their difference in potential separation (Scheme 2.5(a)). A cartoon demonstrating three cases of $Fe(CN)_6^{4-}$ only, $Fe(CN)_6^{3-}$ only and equal $Fe(CN)_6^{4-}/Fe(CN)_6^{3-}$ in the thin layer is shown in Scheme 2.5(c).

2.5.2.1 ECL and Electroanalysis of Ferrocyanide/Ferricyanide in the Unbuffered Solution

Bipolar ECL experiments and electrochemical simulations for the BETL system were carried out initially in an unbuffered solution of 0.5 M $NaClO_4$ using three different ratios of ferrocyanide/ferricyanide species with a same total concentration of 2 mM: ferrocyanide only, ferricyanide only and equal ferrocyanide/ferricyanide.

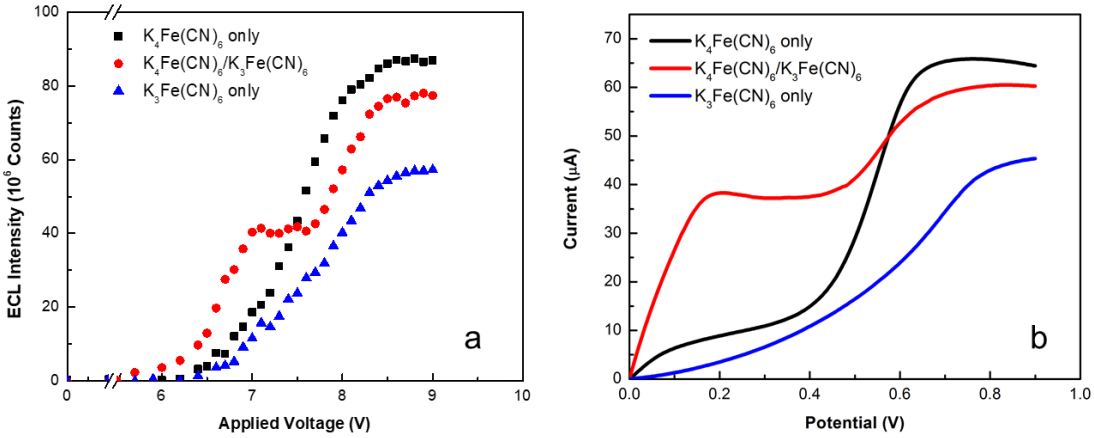

Figure 2.31.(a) ECL emission intensity of 2 mM ferrocyanide only, ferricyanide only and equal ferrocyanide/ferricyanide in 0.5 M $NaClO_4$ as a function of applied voltage. (b) LSV curve for the electrochemical simulation as a function of potential between bipolar electrodes, scan rate: 5 mV/s.

The black curve in Figure 2.31(a) shows the ECL performance of 2 mM $K_4Fe(CN)_6$ in 0.5 M $NaClO_4$ when gradually increasing the applied voltage between two driving electrodes. Around 6 V, the background-corrected ECL signal starts to increase and then reaches a relatively stable region at 8.3 V. The LSV simulation was taken under a two-electrode system (Figure 2.31(b), black curve). In the beginning, there is a small increase in the current response due to the nonfaradaic charging and the possible trace amount of background current, which is not capable of generating observable ECL emission in the BETL system. The apparent onset appears at around 0.4 V, indicating the participation of proton reduction. With its presence, $Fe(CN)_6^{4-}$ can be oxidized to $Fe(CN)_6^{3-}$. In this case, $Fe(CN)_6^{3-}$ is always the rate-limiting reagent for $Fe(CN)_6^{3-}/Fe(CN)_6^{4-}$ redox cycling. As the net amount of $Fe(CN)_6^{3-}$ increases, current keeps growing until it reaches the diffusion-limited steady state

(approximately at 8.5 V in Figure 2.31(a) and 0.75 V in Figure 2.31(b)). In the steady state, the ratio of $Fe(CN)_6^{4-}$/$Fe(CN)_6^{3-}$ stays constant, showing a well-defined plateau current as well as the stable ECL emission.

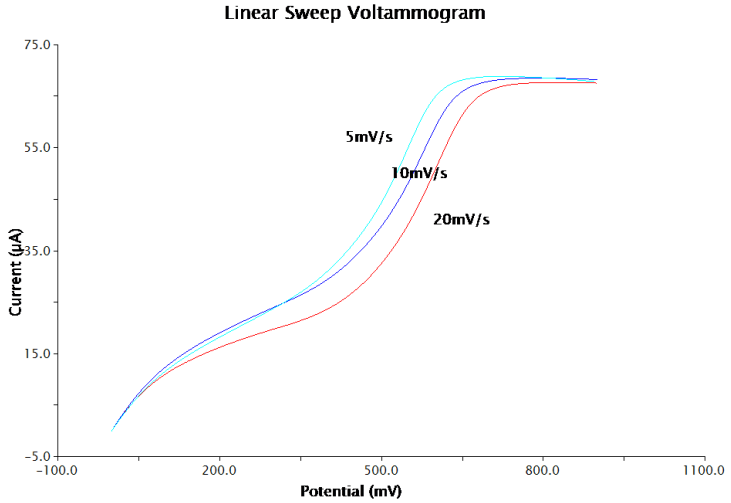

Figure 2.32.LSV of 2 mM $K_4Fe(CN)_6$ in 0.5 M $NaClO_4$ in the thin layer at different scan rates from 5 mV/s to 20 mV/s.

In the LSV data, what is also interesting is the influence of scan rate, the one with slow scan rate shows an early onset and higher current response in the growth region, though they have the same plateau current eventually (Figure 2.32). This phenomenon can be explained as follows: During the scan, the one with a slower rate will generate more $Fe(CN)_6^{3-}$ by H^+ reduction at the same potential point, making an upshift of the curve. Usually, in the common bulk LSV, because of the presence of diffusion and depletion effect, fast scan rate should display a higher current response than low scan rate. However, in the two-electrode thin-layer cell, both oxidation and reduction of ferro-/ferricyanide on the opposite electrode cooperate to decide the current response. More $Fe(CN)_6^{3-}$ would enhance the $Fe(CN)_6^{4-}$/$Fe(CN)_6^{3-}$ couple redox cycling, generating higher current in that $Fe(CN)_6^{3-}$ is the limiting reagent in the case of $K_4Fe(CN)_6$ only. As a consequence, slower scan rate with more $Fe(CN)_6^{3-}$ formation would show higher current response before they reach the same steady state asynchronously. In this system, instead of diffusion control, the steady-state nature is more dominant in the case of $K_4Fe(CN)_6$ only, at these scan rates. However, because $Fe(CN)_6^{3-}$ to $Fe(CN)_6^{4-}$ conversion will cease at the same extent by a “pH blocking effect”, there will be no difference in the final $Fe(CN)_6^{4-}$/$Fe(CN)_6^{3-}$ ratio and pH as well as the current response in the steady state even at different scan rates.

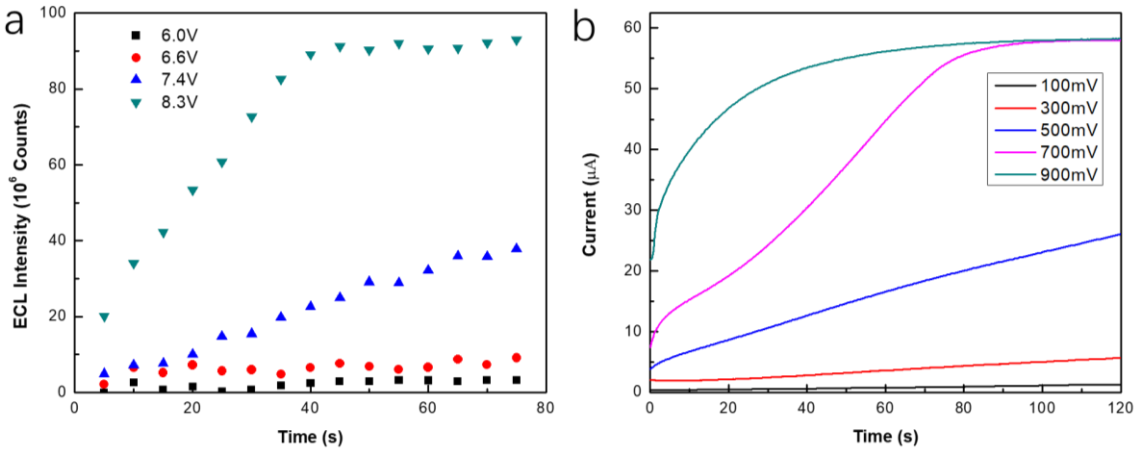

Figure 2.33.(a) ECL emission intensity of 2 mM potassium ferrocyanide in 0.5 M $NaClO_4$ as a function of time. (b) CA curve for the electrochemical simulation at different step potentials. The step potential was held at 100, 300, 500, 700, and 900 mV.

Instead of gradually increasing the applied voltage, by keeping the system at a constant applied voltage, the ECL behavior can give out the composition profile of active species in the thin layer. Figure 2.33(a) demonstrates the ECL intensity change as a function of time when controlling the voltage. In this case, the applied voltage is preset for 60 s, and then the analyte solution is introduced to the thin layer. It minimizes the inevitable electric field drop immediately after the voltage switching. At 7.4 V, there is an obvious upward trend, while at a higher voltage of 8.3 V, ECL intensity increases much faster and finally reaches a plateau region. CA simulation with different step potentials reflects the ECL intensity change while maintaining the applied voltage constant (Figure 2.33(b)). At 100 mV, there is only the charging current. The very slow increase at 300 mV is probably due to the reduction of a trace amount of trapped O_2. At a potential of 500 mV, the current response grows up clearly via $Fe(CN)_6^{3-}$ accumulation by the help of H^+ reduction, however, this accumulation is not fast enough on account of the small overpotential, so there is still a gradually increasing trend in the time range of 120 s. It resembles the ECL intensity change at 7.4 V. While at 900 mV, the necessary conversion from $Fe(CN)_6^{4-}$ to $Fe(CN)_6^{3-}$ is accelerated. Finally, the $K_3Fe(CN)_6/K_4Fe(CN)_6$ couple ratio reaches a stable value with a well-defined steady-state current. The ECL plot shows the appearance of a steady state with stable ECL emission at 8.3 V as well.

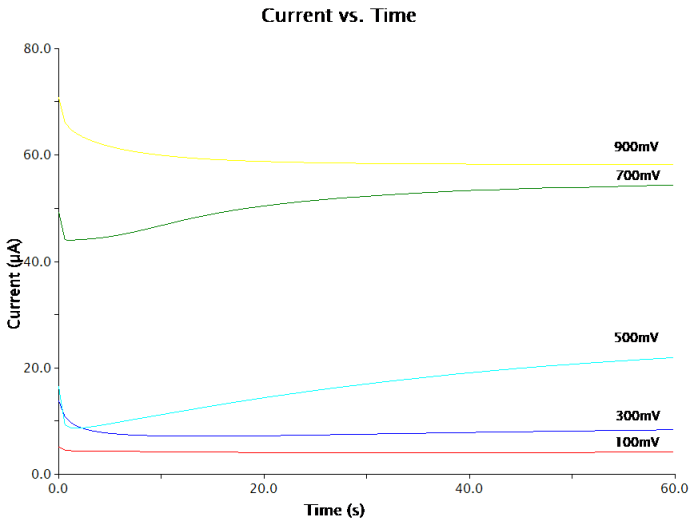

Figure 2.34.CA of 2 mM $K_4Fe(CN)_6$ at different step potentials in the thin layer cell with solution change first. The step potential was held at 100, 300, 500, 700, and 900 mV.

Figure 2.34 shows the results of chronoamperometry operated after the solution change with the nonfaradaic charging current decay exhibiting at the beginning. The faradaic current then increases by the conversion of $Fe(CN)_6^{4-}$ to $Fe(CN)_6^{3-}$, similar to in Figure 2.33. The only difference lies at the potential of 900 mV. Here the necessary conversion is accomplished during the period of charging current decay, obscuring the growth of the faradaic current. The slow conversion in Figure 2.33(b) is also due to the presence of flow that expels some product after immediately replacing the solution.

Then the solution in the thin layer was changed to ferricyanide only. Its result shows a larger onset voltage of observable ECL signal than ferrocyanide only, also with a smaller slope of increment versus applied voltage (see blue curve in Figure 2.31(a)). It intrinsically suggests a larger potential separation of $Fe(CN)_6^{3-}$ reduction coupled with water oxidation rather than that of $Fe(CN)_6^{4-}$ oxidation coupled with H^+ reduction. Also, the steady-state ECL intensity is much smaller than the case of $K_4Fe(CN)_6$ only. In the LSV simulation (Figure 2.31(b)), the large onset potential and a gentle slope of current growth, verifying this higher potential requirement and the slow $Fe(CN)_6^{3-}$ to $Fe(CN)_6^{4-}$ conversion from its slow kinetics. In addition, in the unbuffered solution, water oxidation would lower the pH in the thin layer, further impeding this conversion. As a result, $Fe(CN)_6^{4-}$ accumulation would be slowed down and even stopped.

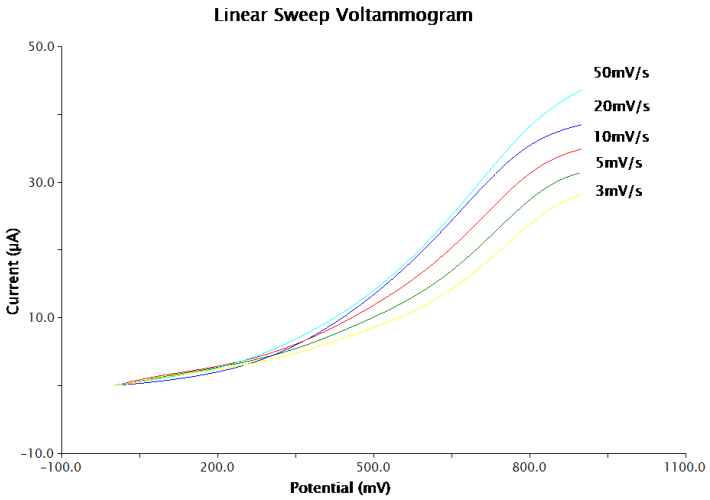

Figure 2.35.LSV of 2 mM $K_3Fe(CN)_6$ in 0.5 M $NaClO_4$ in the thin layer at different scan rates from 5 mV/s to 50 mV/s.

Another significant phenomenon lies in the LSV behaviors of various scan rates (Figure 2.35). Different from ferrocyanide only, here the current response of the fast scan is higher than the slow scan in similar potential range, which complies with the LSV of the common three-electrode system. Even though $Fe(CN)_6^{4-}$ is the limiting reagent at the beginning, once it is generated, its oxidation backward is fast enough. As a result, the current response is mainly controlled by $Fe(CN)_6^{3-}$ reduction coupled with water oxidation. The slow kinetics of $Fe(CN)_6^{3-}$ reduction makes the linear diffusion–limited nature now more dominant (decided by $v^{1/2}$).

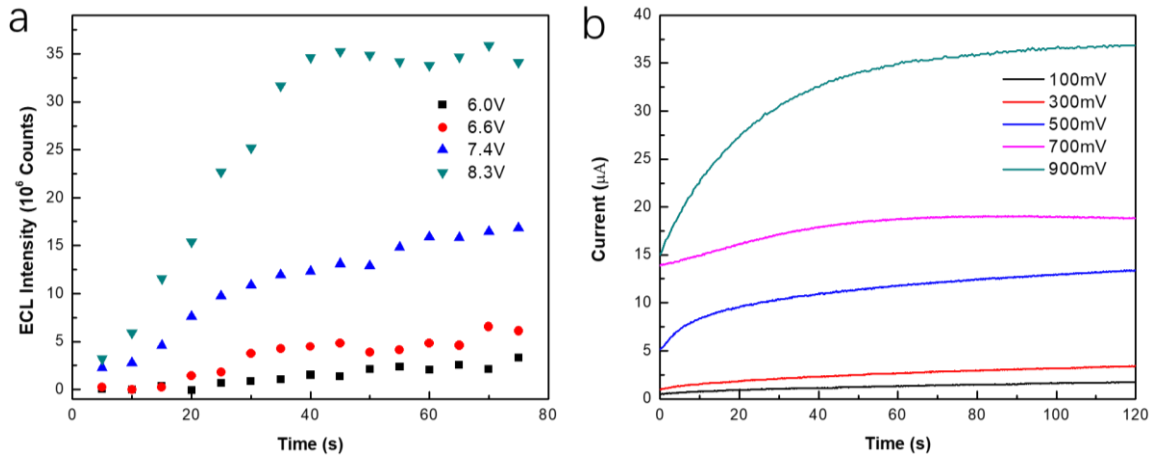

Figure 2.36.(a) ECL emission intensity of 2 mM potassium ferricyanide in 0.5 M $NaClO_4$ as a function of time. (b) CA curve for the electrochemical simulation at different step potentials. The step potential was held at 100, 300, 500, 700, and 900 mV.

In the intensity-time-dependent study of ferricyanide only at a constant applied voltage, a noticeable ECL signal increase shows up at 7.4 V due to the gradual accumulation of $Fe(CN)_6^{4-}$ by water oxidation (Figure 2.36(a)). For applied voltage at 8.3 V, it finally reaches the steady emission state, yet with its magnitude much less than for ferrocyanide only. It should be attributed to the bigger potential barrier together with the declining of pH in the thin layer which works as stronger negative feedback to stop

net $Fe(CN)_6^{4-}$ accumulation. In the CA simulation curves of Figure 2.36(b), they have much flatter slopes compared to those for ferrocyanide only, and have lower current responses as well, implying the larger potential requirement of $Fe(CN)_6^{3-}$ reduction coupled with water oxidation. Because of the slow rate of $Fe(CN)_6^{3-}$ to $Fe(CN)_6^{4-}$ conversion, for potential at 900 mV, in the end, the plot still does not reach its steady state.

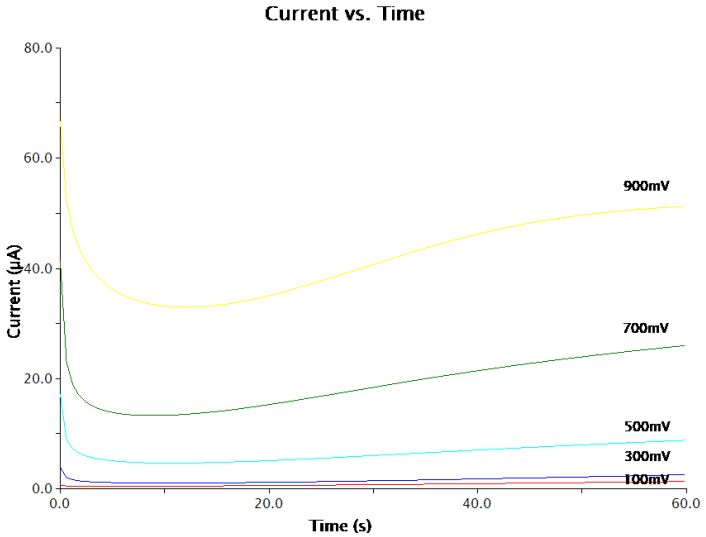

Figure 2.37.CA of 2 mM $K_3Fe(CN)_6$ at different step potentials on the thin-layer cell with solution change first. The step potential was held at 100, 300, 500, 700, and 900 mV.

Figure 2.37 shows the CA of 2 mM $K_3Fe(CN)_6$ after the infill of the solution. Now different from 2 mM $K_4Fe(CN)_6$, the necessary conversion at 900 mV can not be done in the time range of 60 s, confirming the slow kinetics of $Fe(CN)_6^{3-}$ reduction.

Experiments based on the BETL system were also carried out with an equal ferrocyanide/ferricyanide couple as a function of applied voltage. What is distinct is, a two-step ECL increment and a relatively stable intermediate stage are shown in Figure 2.31(a). The onset voltage of observable ECL signal becomes much smaller followed with a rapid increase in the first step. The LSV voltammogram also shows the corresponding two-step current increment, which is more evident at a slow scan rate (Figure 2.31(b) and Figure 2.38). As mentioned before, the majority of current contribution stems from $Fe(CN)_6^{3-}$/ $Fe(CN)_6^{4-}$ redox cycling. Because of the same E_0 in reduction and oxidation, a small increase in the overpotential would result in an apparent current increase until it reaches its first plateau current. At this stage, almost no side reaction can occur, so the ratio of $Fe(CN)_6^{3-}$/ $Fe(CN)_6^{4-}$ remains at 1:1, and the plateau current is diffusion limited. However, when further increasing the potential (above 500 mV), a second step growth appears with the help of side reaction and provides a pathway of changing redox couple ratio. Based on their diffusion coefficients: $D_{Fe(CN)_6^{4-}} = 0.65\times10^{-7}$ cm^2s^{-1}, $D_{Fe(CN)_6^{3-}} = 0.76\times10^{-7}$ cm^2s^{-1}, the optimized $Fe(CN)_6^{4-}/Fe(CN)_6^{3-}$ ratio for maximum current should be around 1.1: 1. Therefore, the second current increase is mainly due to the result of $Fe(CN)_6^{3-}$ to $Fe(CN)_6^{4-}$ net conversion, also with some contribution from water decomposition.

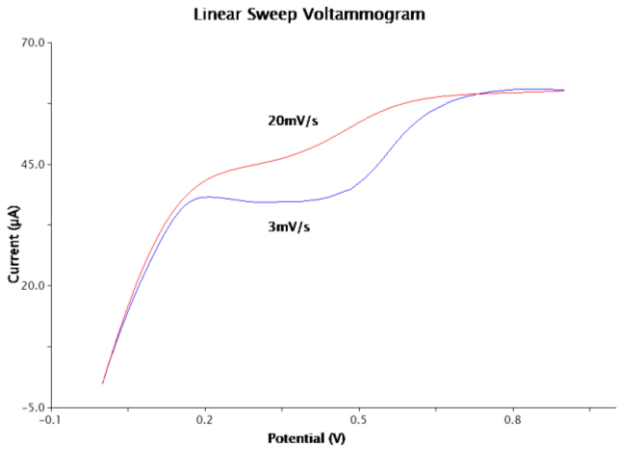

Figure 2.38.LSV of 1 mM $K_4Fe(CN)_6/K_3Fe(CN)_6$ in 0.5 M $NaClO_4$ in thin-layer cell at scan rates of 3 mV/s and 20 mV/s.

When comparing the LSV curves with different scan rates, for example, the one at 20 mV/s demonstrates a vague two-step current increase compared with that of 3 mV/s. The fast scan shows higher current value than the low scan in the second step before reaching the steady state, resembling the performance of ferricyanide only. It further proves the reason for the second current increase, that is, $Fe(CN)_6^{4-}$ to $Fe(CN)_6^{3-}$ conversion by water oxidation (Figure 2.38). The steady current in the intermediate stage at 3 mV/s is owing to the build-up of a constant concentration gradient by the thickening of the depletion layer under a slow scan rate. The two current curves overlap together in the first step, indicating that the reactions in the thin layer are only kinetic controlled in this process.

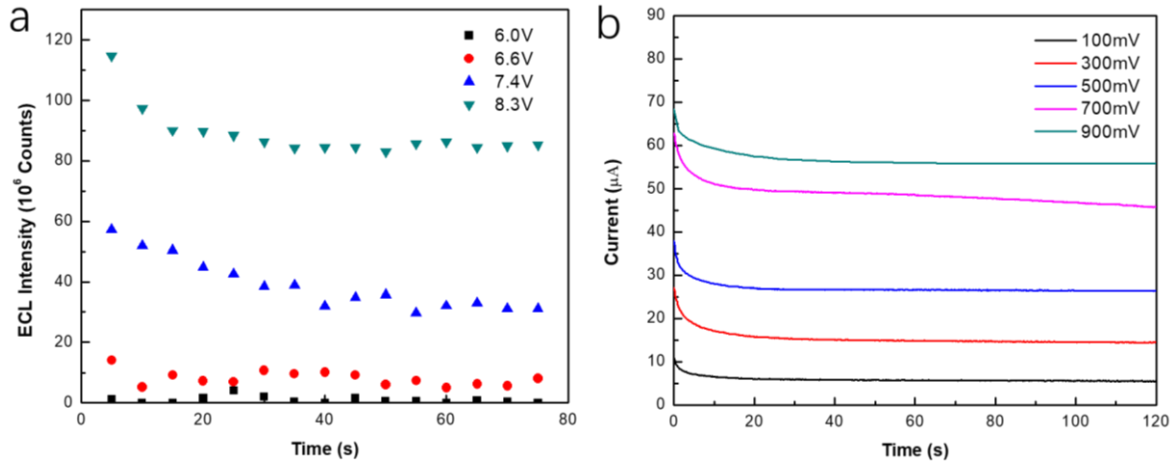

Figure 2.39.(a) ECL emission intensity of 2 mM equal ferrocyanide/ferricyanide in 0.5 M $NaClO_4$ as a function of time. (b) CA curve for the electrochemical simulation at different step potentials. The step potential was held at 100, 300, 500, 700, and 900 mV.

Figure 2.39(a) shows the time-dependent ECL performance of equivalent ferrocyanide/ferricyanide. Instead of nearly no ECL emission, it now initiates from a considerable magnitude and experiences a period of decay, finally reaching the stable emission region. The intensity decay should be ascribed to the reduced mass transfer, from both the stagnancy of flow in the thin layer after solution introduction and the depletion effect from thickening of the diffusion layer. The responses of CA in the

electrochemical simulation is similar to the ECL study, but with a small contribution of nonfaradaic charging effect. It arrives a quasi-steady state with a relatively fixed $Fe(CN)_6^{4-}/Fe(CN)_6^{3-}$ ratio much faster than ferro- or ferricyanide only (Figure 2.39(b)).

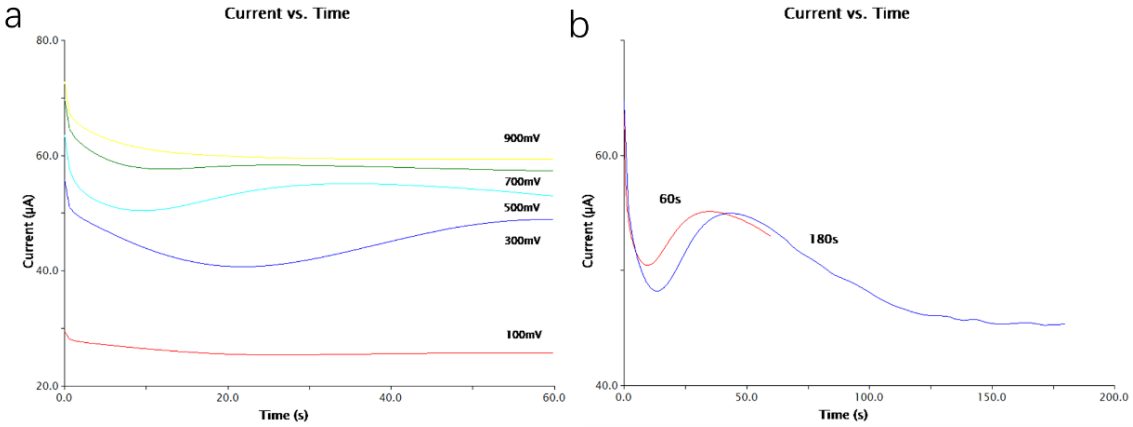

Figure 2.40.(a) CA curve of 1 mM $K_4Fe(CN)_6/K_3Fe(CN)_6$ in 0.5 M $NaClO_4$ at different step potentials with solution change first. The step potential was held at 100, 300, 500, 700, and 900 mV. (b) At 500 mV for 60 s and 180 s.

Figure 2.40(a) demonstrates the CA of 1 mM $K_4Fe(CN)_6/K_3Fe(CN)_6$ after the solution change. All the curves still show a quick decay, but this time the nonfaradaic charging current decay is mainly the reason rather than the reduced mass transfer due to the gradual resting of the solution flow. At some step potential, a "wave" like behavior is observed, which is more evident at the longer time range (see Figure 2.40(b)). The initial current drop is assigned to the charging effect and depletion of reactive species on the electrode surface. Then, the back diffusion of reduced/oxidized species from opposite electrodes re-builds the concentration gradient and recovers the current. Notice that there is a second current drop afterward. As mentioned before, the potential separation of $Fe(CN)_6^{4-}$ oxidation coupled with H^+ reduction is smaller than that of $Fe(CN)_6^{3-}$ reduction coupled with water oxidation. At 500 mV, only H^+ reduction could keep going to convert $Fe(CN)_6^{4-}$ to $Fe(CN)_6^{3-}$ in the net amount. However, only the net conversion of $Fe(CN)_6^{3-}$ to $Fe(CN)_6^{4-}$ can lead to a current increase due to their diffusion coefficient difference. Hence, it makes the redox couple ratio further deviate from the optimized value, leading to a current decrease.

When comparing the ECL intensity of the ferrocyanide only, ferricyanide only, and equivalent ferrocyanide/ferricyanide having the same total concentration together in 0.5 M $NaClO_4$ solution as a function of applied voltage, equal $K_4Fe(CN)_6/K_3Fe(CN)_6$ has the smallest onset voltage, because the $K_3Fe(CN)_6/K_4Fe(CN)_6$ couple can undergo redox cycling itself with small overpotential in advance to the side reaction. Onset voltage for 2 mM $K_4Fe(CN)_6$ appears second, followed by 2 mM $K_3Fe(CN)_6$ (Figure 2.31(a)), due to the difference in potential separation. The stable ECL intensity abides by this order: $K_4Fe(CN)_6$>$K_4Fe(CN)_6/K_3Fe(CN)_6$>$K_3Fe(CN)_6$, as a result of the pH change in the thin layer. The LSV simulation of them has three distinct plateau currents, analogous to the ECL performance

(Figure 2.31(b)). Based on the previous discussion, the current of the final steady state depends on the $Fe(CN)_6^{4-}/Fe(CN)_6^{3-}$ ratio. For $K_3Fe(CN)_6$ only, in addition to the slow conversion of $Fe(CN)_6^{3-}$ to $Fe(CN)_6^{4-}$, the pH decrease from water oxidation would actively slow down and even stop $Fe(CN)_6^{4-}$ accumulation, preventing it from reaching the optimized Fe ratio. Besides, a solution of 2 mM $K_4Fe(CN)_6$ has a slightly higher plateau current than that of 1 mM $K_4Fe(CN)_6/K_3Fe(CN)_6$. In the confined thin layer, pH change is directly relevant to the $Fe(CN)_6^{4-}/Fe(CN)_6^{3-}$ mutual conversion. Equal $K_4Fe(CN)_6/K_3Fe(CN)_6$ should have a lower pH in the steady state than $K_4Fe(CN)_6$ only, of which the oxidation is required by H^+ reduction. This more acidic condition that facilitates H^+ reduction but hinders water oxidation results in more $Fe(CN)_6^{3-}$ but less $Fe(CN)_6^{4-}$, which is adverse to their optimized ratio based on the diffusion coefficient.

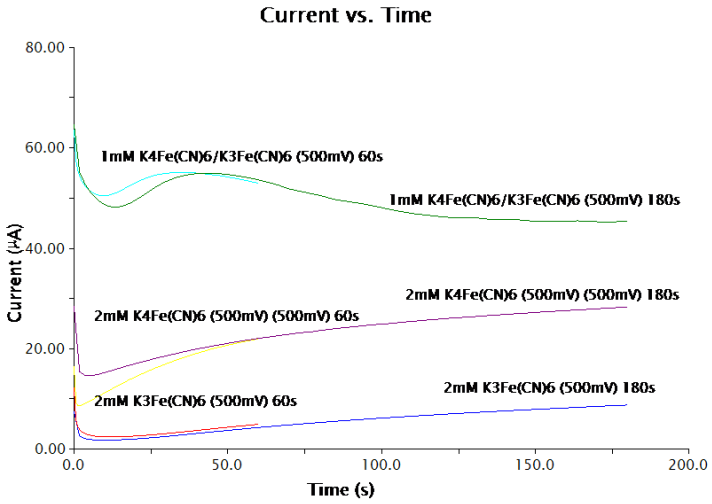

Figure 2.41.CA of 2 mM ferrocyanide, ferricyanide and equal ferrocyanide/ferricyanide with solution change first for step potential held at 500 mV in 60 s and 180 s.

When comparing the CA results of 2 mM $K_4Fe(CN)_6$, 1 mM $K_3Fe(CN)_6/K_4Fe(CN)_6$, and 2 mM $K_3Fe(CN)_6$ by applying a step potential of 500 mV after the solution change, three current magnitudes are demonstrated with an initial charging current decay (Figure 2.41). Equal $K_3Fe(CN)_6/K_4Fe(CN)_6$ has the highest current due to the coexistence of the reduced and oxidized forms. The difference between the other two can be explained by the smaller potential barrier between $K_4Fe(CN)_6$ oxidation and coupled H^+ reduction rather than that between $K_3Fe(CN)_6$ reduction and coupled water oxidation. 2 mM $K_4Fe(CN)_6$ displays a higher current response than 2 mM $K_3Fe(CN)_6$ since 500 mV is only capable of triggering the oxidation of $K_4Fe(CN)_6$ to $K_3Fe(CN)_6$.

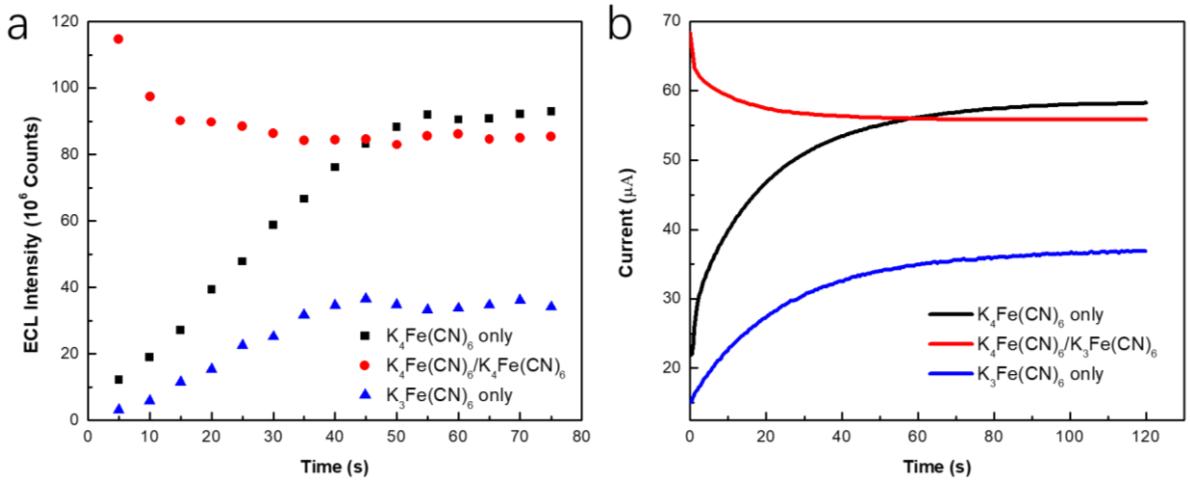

Figure 2.42.ECL emission intensity of 2 mM ferrocyanide, ferricyanide and equal ferrocyanide/ferricyanide in 0.5 M $NaClO_4$ as a function of time for applied voltage setting at 8.3 V (b) CA curve for the electrochemical simulation of step potential held at 900 mV.

For analyte detection, a relatively high applied voltage should be employed to generate enough potential gradient in the BETL system to have a stable ECL emission. At this voltage, both H^+ reduction and water oxidation can proceed with fast kinetics, providing two directions for adjusting the $Fe(CN)_6^{4-}$ /$Fe(CN)_6^{3-}$ ratio and reaching the steady state in a short time. A direct comparison is made from the ECL intensity-time change at 8.3 V (Figure 2.42(a)). In the beginning, equal ferrocyanide/ferricyanide has the highest ECL intensity by the coexistence of reduced and oxidized form. The decreasing trend is due to the stagnancy of flow in the thin layer and the depletion effect. For the other two solutions, the $Fe(CN)^{4-}$/ $Fe(CN)_6^{3-}$ ratio can be changed with the help of water decomposition, followed by the ECL increase. When arriving at the steady state, ferricyanide only has the lowest intensity due to the strongly shifted equilibrium by the pH blocking effect and its slow reduction kinetics; the ECL intensity of ferrocyanide only overpasses that of equal ferrocyanide/ferricyanide, owing to that the former one would have a more optimized $K_4Fe(CN)_6/K_3Fe(CN)_6$ composition in a higher pH condition at the steady state. The corresponding CA study is operated at 900 mV (Figure 2.42(b)), showing different steady-state currents. The pH change from this unbuffered environment a is an apparent obstructive factor for the current response of $Fe(CN)_6^{3-}$ only. Basically, it lies in the fact that the potential barrier between reaction ①③ is larger than that between reaction ②④.

2.5.2.2 ECL and Electroanalysis of Ferrocyanide/Ferricyanide in the Buffered Solution

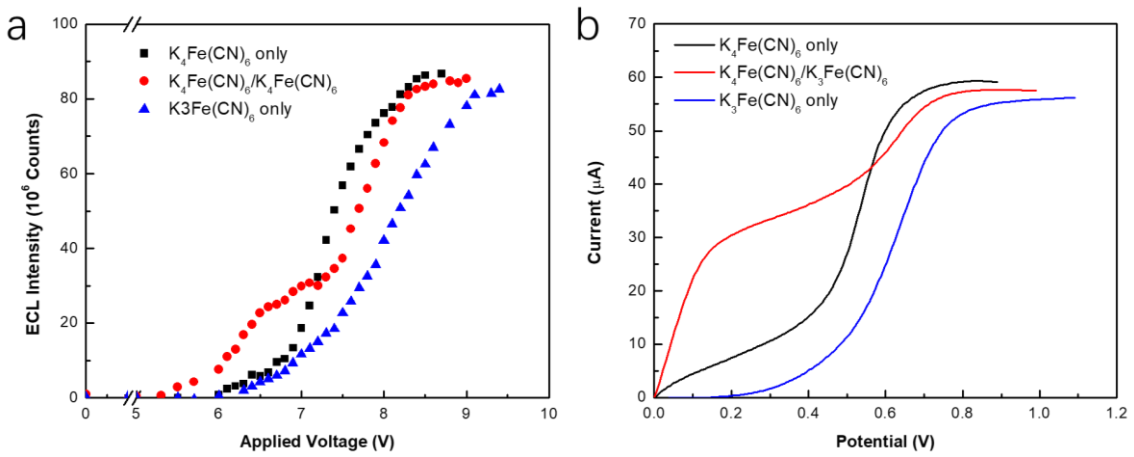

Figure 2.43.(a) ECL emission intensity of 2 mM ferrocyanide only, ferricyanide only and equal ferrocyanide/ferricyanide in 0.1 M pH=7 PBS buffer as a function of the applied voltage between driving electrodes. (b) LSV curve for the electrochemical simulation as a function of potential between bipolar electrodes, scan rate: 5 mV/s.

To understand further the role that pH plays in determining the ECL behavior of ferrocyanide/ferricyanide species in the BETL system and address the best approach of redox-active analyte detection, 0.1 M phosphate buffer solution (PBS) of pH=7 was utilized as an alternative to the solution environment. The buffer capacity is in excess of the likely pH change induced by ferro-ferricyanide couple conversion. The black curve in Figure 2.43(a) and (b) shows the ECL behavior versus applied voltage and its LSV simulation of 2 mM $K_4Fe(CN)_6$ in the buffer. Same as in the unbuffered condition, $Fe(CN)_6^{4-}$ converts to $Fe(CN)_6^{3-}$ by H^+ reduction and that facilitates the redox cycling between them until reaching a well-defined steady state. Moreover, the slope of the current increase is larger than in the unbuffered solution because of this adequate H^+.

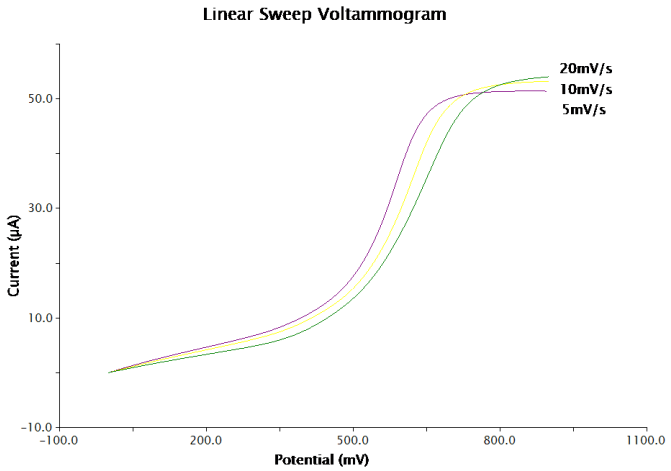

Figure 2.44.LSV of 2 mM $K_4Fe(CN)_6$ in 0.1 M PBS buffer in the thin-layer cell at different scan rates from 5 mV/s to 20 mV/s.

A slight difference here is that in the LSV simulation, the current response at a fast scan rate of 20 mV/s does not reach its steady state while scanning to 900 mV compared with the unbuffered solution (Figure 2.44). In this case, adequate buffer keeps providing H^+ for the $Fe(CN)_6^{4-}$ to $Fe(CN)_6^{3-}$ conversion, eliminating the pH blocking effect. While in the unbuffered solution, the pH increase generates negative feedback that stops the net conversion, in other words, to reach steady state earlier. The eliminating of the blocking effect also accounts for the smaller current response in the slower scan (for example, at 5 mV/s), owing to the overrun of the optimized redox couple ratio under continuous conversion.

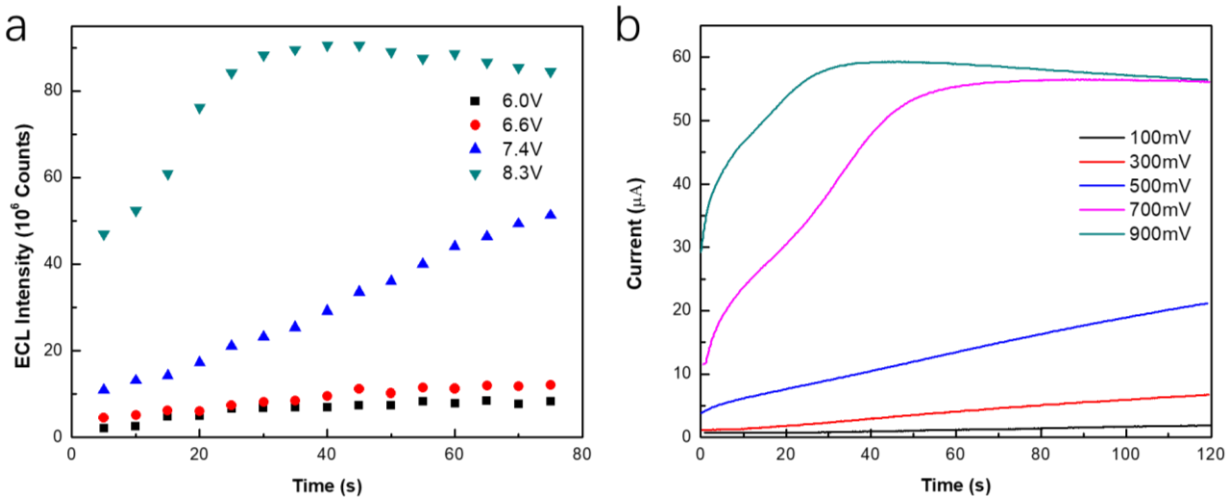

Figure 2.45.(a) ECL emission intensity of 2 mM potassium ferrocyanide in 0.1 M PBS buffer as a function of time. (b) CA curve for the electrochemical simulation at different step potentials. The step potential was held at 100, 300, 500, 700, and 900 mV.

Figure 2.45(a) demonstrates the ECL intensity variation for ferrocyanide only with constant applied voltage. At 8.3 V, the ECL intensity increases quickly and reaches its plateau region. The corresponding CA accurately simulates the ECL performance (Figure 2.45(a)). Notice that at 900 mV, the current response drops a little like the ECL at 8.3 V. That confirms the assumption that the steady state in the thin layer herein is not the one with the optimized $Fe(CN)_6^{4-}/Fe(CN)_6^{3-}$ ratio for maximum current response, but a coordinated one relying on the controlled pH. After reaching the optimized ratio, the sustaining H^+ donor enables a further conversion $Fe(CN)_6^{4-}$ to $Fe(CN)_6^{3-}$, thus lowering the current response.

A smaller slope and larger onset voltage are still observed on ECL of ferricyanide only in the buffered solution when gradually increasing the applied voltage, demonstrating its large potential requirement and slow kinetics (Figure 2.43(a), blue). Whereas, here the ECL intensity in the relatively stable emission region at the end is close to ferrocyanide only. LSV simulation in Figure 2.43(b) resembles the ECL result, in which the blue curve and black curve show the same magnitude of plateau current. In the buffered solution, sufficient buffer capacity is capable of maintaining the pH constant no matter the extent of the side reaction, and it excludes the hindrance from the subsequent pH decrease.

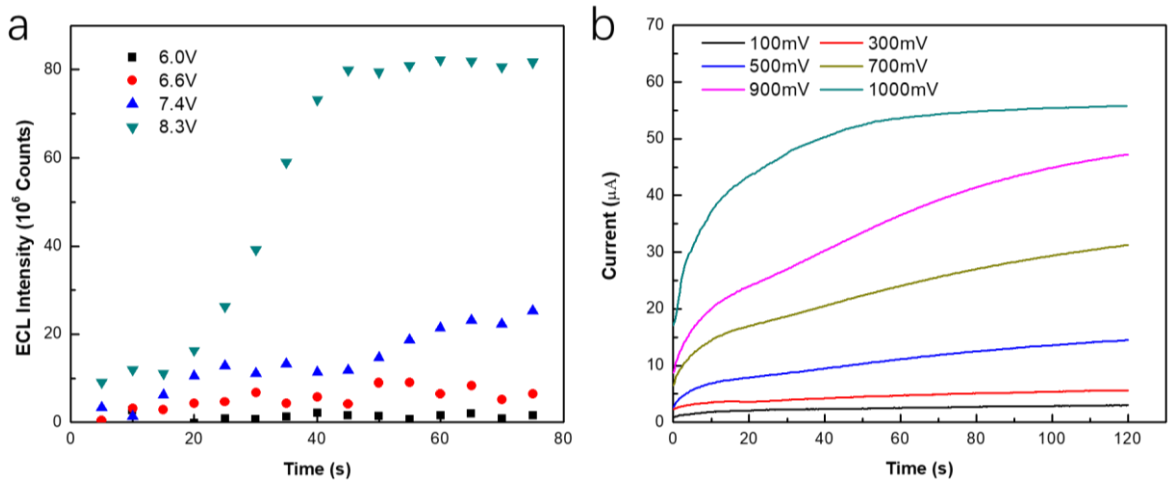

Figure 2.46.(a) ECL emission intensity of 2 mM potassium ferricyanide in 0.1 M PBS buffer as a function of time. (b) CA curve for the electrochemical simulation at different step potentials. The step potential was held at 100, 300, 500, 700, 900, and 1100 mV.

Figure 2.46(a) demonstrates the ECL-time performance of ferricyanide only in 0.1 M PBS buffer. At 8.3 V, it reaches the stable region with intensity much larger than in 0.1 M $NaClO_4$. In this case, the stable pH will not retard the generation of $Fe(CN)_6^{4-}$ by water oxidation. When looking at the CA curve in Figure 2.46(b), at 900 mV, the plateau current is not achieved within 120 s, unlike the result in the unbuffered solution. The buffered solution used here extends the time required to reaching the steady state by eliminating the pH blocking effect. A higher step potential (1100 mV) would facilitate the process to the steady state in 60 s.

For the equal ferrocyanide/ferricyanide couple in 0.1 M PBS buffer, its ECL and electrochemical behavior as a function of voltage are equivalent to those in the unbuffered solution with a two-step increase and an intermediate stage (Figure 2.43(a) and (b), red). The ECL or current change should be divided into two parts: (1) increase from the overpotential applied to the origin $Fe(CN)_6^{4-}/Fe(CN)_6^{3-}$ couple; (2) signal increase from its following ratio change by water decomposition.

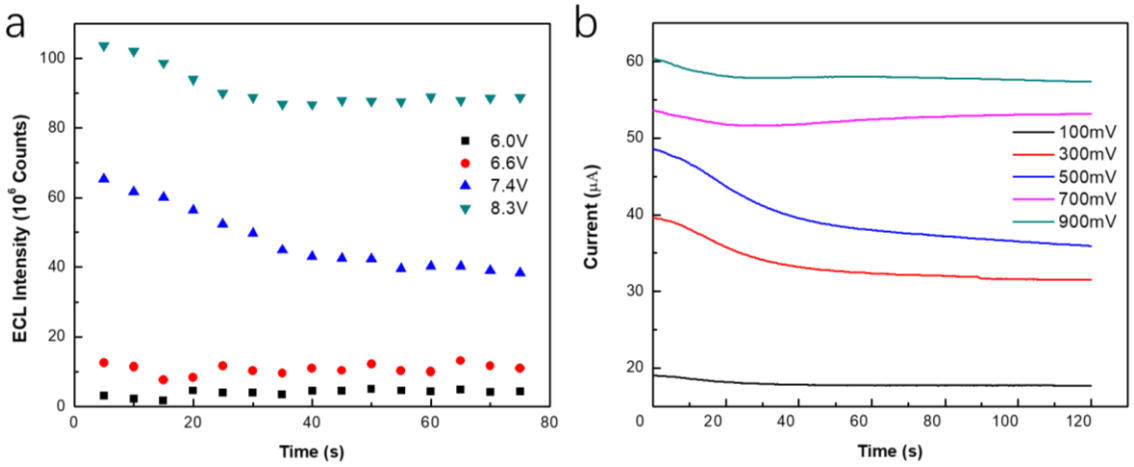

Figure 2.47.(a) ECL emission intensity of 2 mM equal ferrocyanide/ferricyanide in 0.1 M PBS buffer as a function of time. (b) CA curve for the electrochemical simulation at different step potentials. The step potential was held at 100, 300, 500, 700, and 900 mV.

For equal $Fe(CN)_6^{4-}$/$Fe(CN)_6^{3-}$ at a constant applied voltage, the ECL intensity undergoes a time decay and then becomes relative stable, behaving the same as in the unbuffered solution (Figure 2.47(a)). CA data gives out the exact simulation of ECL plot, with CA curve of 500 mV resembling ECL with applied voltage at 7.4 V and curve of 900 mV resembling ECL with applied voltage at 8.3 V (Figure 2.47(b)). The intensity or current decay are ascribed to the stop of convection after solution replacement and the depletion effect.

The significant conclusion is drawn from Figure 2.43(a) when comparing ECL intensity versus applied voltage of the three compositions in 0.1 M PBS buffer. Their onset voltages follow the same sequence as in the unbuffered solution. However, the ECL intensity of ferricyanide only, at the end grows to a similar level as the other two. No matter ferrocyanide only, ferricyanide only or both present, under a controlled pH, they should have the same steady-state response finally. The sufficient buffer capacity eliminates the negative feedback which stops $Fe(CN)_6^{4-}$ accumulation caused by a shifted equilibrium. In their linear sweep voltammograms (Figure 2.43(b)), even though with different shapes of current response, they would have the same steady-state current value.

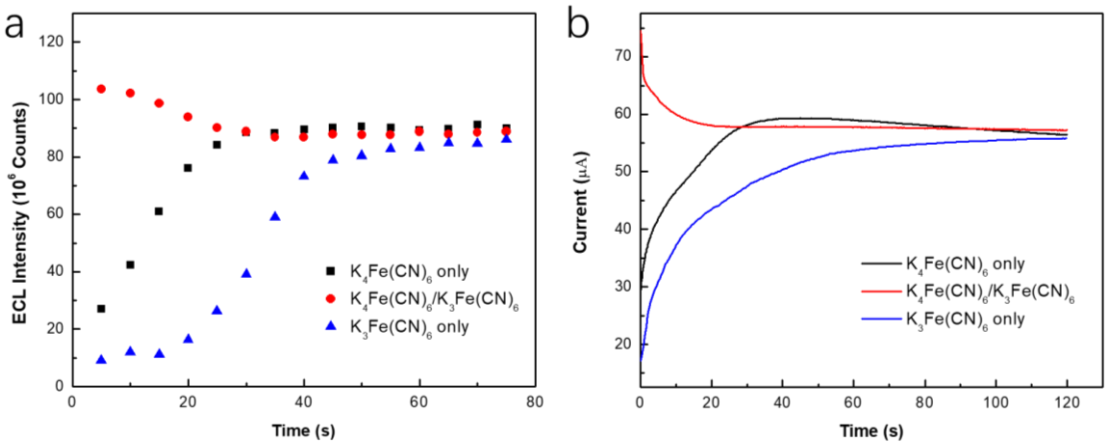

Figure 2.48.(a) ECL emission intensity of 2 mM ferrocyanide, ferricyanide and equal ferrocyanide/ferricyanide in 0.1 M PBS buffer as a function of time for applied voltage at 8.3 V (b) CA curve for the electrochemical simulation of step potential held at 900 mV (black and red curve) or 1100 mV (blue curve).

While looking at their ECL intensity change at a high applied voltage of 8.3 V, different from in the unbuffered solution, they have the same magnitude of ECL intensity when reaching the steady state (Figure 2.48(a)). At this voltage, both H^+ reduction and water oxidation inside the thin layer can proceed with fast kinetics. In the buffered solution, without pH blocking effect, regardless of their origin ratios, their ECL emission at the steady state would be the same under a fixed pH. In the corresponding CA study, step potential at 900 mV is not significant enough to reach the steady state in the time range. While a step potential at 1100 mV could facilitate the slow kinetics of $Fe(CN)_6^{3-}$ to $Fe(CN)_6^{4-}$ conversion and reach the steady state timely (Figure 2.48(b)).

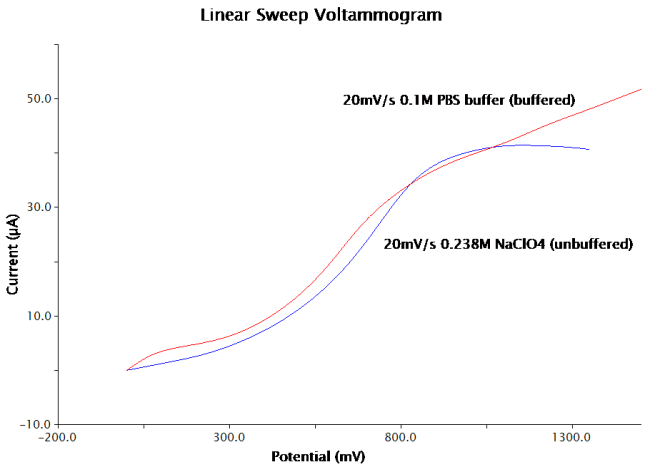

Figure 2.49.LSV of 2 mM $K_4Fe(CN)_6$ in 0.1 M PBS buffer and 0.238 M $NaClO_4$ in the thin-layer cell at a scan rate of 20 mV/s.

The difference between the unbuffered and buffered solution is evident in the LSV of $Fe(CN)_6^{4-}$ only in a broader scan range while keeping the same ionic strength (Figure 2.49). In the thin layer, IR drop plays a vital role in determining the current response compared to the bulk electrolysis. In a pre-experiment not discussed in the dissertation, the solution with a higher ionic strength always produces a larger current response. To make a rational comparison, the concentration of $NaClO_4$ in the unbuffered solution was carefully controlled to 0.238 M that has a same ionic strength as 0.1 M PBS buffer (pH=7). The current can be reached the steady state at around 900 mV at a scan rate of 20 mV/s in the unbuffered solution; while in the buffered solution, it keeps going up even after 1400 mV, showing a continuous conversion of $Fe(CN)_6^{4-}$ to $Fe(CN)_6^{3-}$ at the controlled pH together with water electrolysis.

In Figure 2.45, the CA of ferrocyanide only at a high stepped potential in the buffered solution declines slightly after achieving the maximum current. We call it the “biased reaction condition”. As discussed, the current response should be determined by the $Fe(CN)_6^{4-}$/$Fe(CN)_6^{3-}$ redox cycling. Based on their diffusion coefficients, the optimized ratio for maximum current should be about 1.1: 1. However, the steady state is necessarily not the one with the optimized Fe ratio in the presence of side reactions. Regarding the CA of ferrocyanide only, after reaching the optimized ratio, $Fe(CN)_6^{4-}$ would keep being oxidized by H^+ reduction, leading to an attenuated current response (Figure 2.45(b), green curve). Also, in the CA of equal ferrocyanide/ferricyanide, there is a potential range during which only H^+ reduction can be triggered. This “biased reaction condition” would keep forcing the conversion of $Fe(CN)_6^{4-}$to $Fe(CN)_6^{3-}$, thus reducing the current slightly (Figure 2.47(b), blue curve).

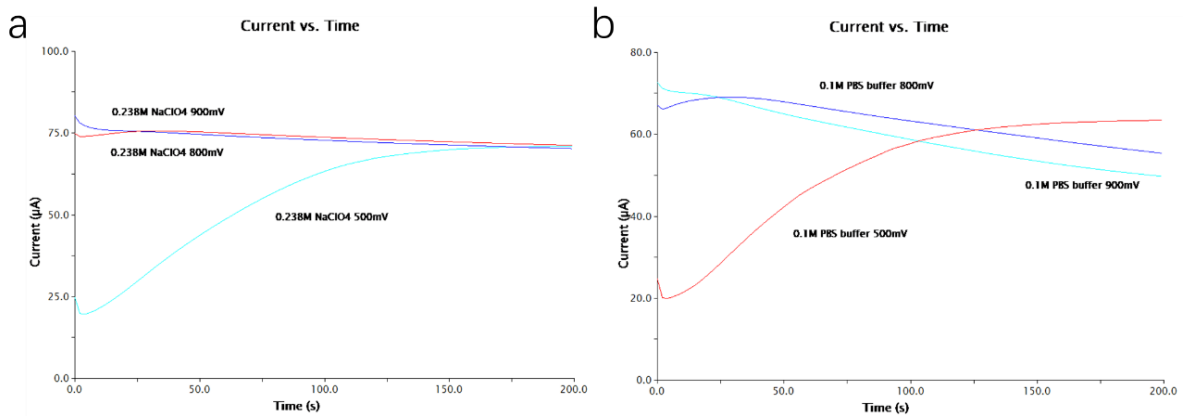

Figure 2.50.CA curves of 2 mM $K_4Fe(CN)_6$ in the thin-layer cell at step potential at 500, 800, and 900 mV in (a) 0.1 M PBS buffer (b) 0.238 M $NaClO_4$.

The "biased reaction condition" in the thin-layer system is further testified by the CA of 2 mM $K_4Fe(CN)_6$ in both 0.1 M PBS buffer and 0.238 M $NaClO_4$ under a longer time range at 500 mV, 800 mV, and 900 mV. As in 0.238 M $NaClO_4$ (Figure 2.50(a)), at 500 mV, 160 s is required for $Fe(CN)_6^{3-}$ accumulation to reach the steady state; while at 900 mV, the vast majority of accumulation can proceed in a few seconds. Finally, all three current curves reach the same value with an identical redox cycling of $Fe(CN)_6^{4-}/Fe(CN)_6^{3-}$. On the contrary, in 0.1 M PBS buffer, they are different at the end, and the one at 500 mV exceeds that at 900 mV after about 100 s (Figure 2.50(b)). The "biased reaction condition" can easily describe it: In the unbuffered $NaClO_4$ solution, the subsequent pH increase from H^+ reduction will retard and even stop the coupled conversion of $Fe(CN)_6^{4-}$ to $Fe(CN)_6^{3-}$; while in the conversion of $Fe(CN)_6^{4-}$ to $Fe(CN)_6^{3-}$, the controlled pH would facilitate the continuous conversion, resulting in a $Fe(CN)_6^{4-}/Fe(CN)_6^{3-}$ ratio that passes the optimized one. At 900 mV, the optimized ratio is reached in a short time, followed by a further conversion which leads to a current deterioration. Instead, the relative slow conversion under a potential of 500 mV makes the $Fe(CN)_6^{4-}/Fe(CN)_6^{3-}$ composition still before the optimized one. Essentially, the final goal of the processes in the thin layer is to balance reactions ①②③④ with different potential separations. In the unbuffered solution, the gradual pH change will balance H^+ reduction and water oxidation rapidly. As a consequence, CAs at different step potentials would have the same current response, in that they have the same initial "reactant", same pH variation, and subsequently the same final steady state with a fixed $Fe(CN)_6^{3-}/Fe(CN)_6^{4-}$ ratio. It can be confirmed by the same plateau current level in Figure 2.32. In Figure 2.50, the current in 0.238 M $NaClO_4$ at 500 mV coincides with that in 0.1 M PBS buffer, indicating that an ignorable negative feedback of pH change; while at a higher potential, the current response in 0.1 M PBS buffer is higher than in 0.238 M $NaClO_4$, implying that at these potentials, the final steady state in an aqueous solution of pH>7 will give rise to a higher current response with a better $Fe(CN)_6^{3-}/ Fe(CN)_6^{4-}$ ratio than that in the solution of pH=7.

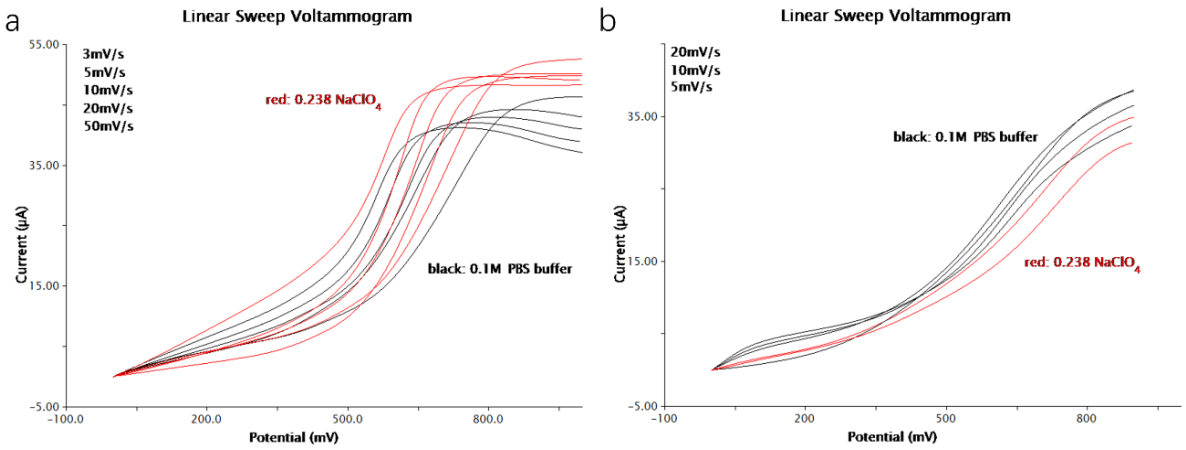

Figure 2.51.Comparison of LSV of (a) 2 mM $K_4Fe(CN)_6$ in 0.1 M PBS buffer and 0.238 M $NaClO_4$ in the thin-layer cell at scan rates from 3 mV/s to 50 mV/s. (b) 1 mM $Fe(CN)_6^{3-}/Fe(CN)_6^{4-}$ in 0.1 M PBS buffer, 0.238 M $NaClO_4$ and 0.5 M $NaClO_4$ in the thin-layer cell at scan rates from 5 mV/s to 20 mV/s.

The LSV shows a similar result that 2 mM $K_4Fe(CN)_6$ in 0.238 M $NaClO_4$ always displays a higher current response than in 0.1 M PBS buffer, at each scan rate (Figure 2.51(a)). A higher pH condition than the neutral condition can thus contribute to a fast redox cycling in the thin layer. Figure 2.51(b) implies the same conclusion in another way, in which a lower current value is obtained by an acidic pH condition resulting from the water oxidation used for $K_3Fe(CN)_6$, compared to constant pH = 7.

In conclusion, in this ferro-ferricyanide system with equal total concentration, regardless of the initial compositions, if the pH is controlled, the final steady state should be identical and share the same $Fe(CN)_6^{4-}/Fe(CN)_6^{3-}$ ratio. Because of the electrical equality on both bipolar electrodes in the BETL system, once an imbalance between water oxidation and H^+ reduction occurs, it would result in the corresponding change of the $Fe(CN)_6^{4-}/Fe(CN)_6^{3-}$ ratio, thus varying the current response. This process will not be ceased until the rebalance of them; then the current remains constant. In a word, it is the final pH in a thin layer that determines the final $Fe(CN)_6^{4-}/Fe(CN)_6^{3-}$ ratio as well as the current response under a certain potential. In the unbuffered solution, the pH change is corresponding to the $Fe(CN)_6^{4-}/Fe(CN)_6^{3-}$ composition change synchronously. As a result, different initial compositions would have various steady states with inconsistent pHs and final $Fe(CN)_6^{4-}/Fe(CN)_6^{3-}$ ratios. Also, the time it takes to reach the steady state in the unbuffered solution is shorter than in the buffered solution owing to the pH blocking effect.

2.5.2.3 Sample Detection and Analysis

From the aforementioned systematic study on the BETL system, the concentration profile of the redox active species should be analyzed in solution with sufficient buffer capacity. It allows the efficient interconversion of redox couple by “side reaction” and proceeds towards the same final steady state in the thin layer regardless of its initial composition. Because the ECL intensity varies over time under the

applied voltage, as a reflection of the real-time solution composition, the ECL intensity in the stable emission region under enough overpotential should be measured. In that case, both the oxidation and reduction of electroactive species coupled with the solvent decomposition inside the thin layer can proceed with fast kinetics, providing both directions for adjusting the redox couple ratio and reaching its steady state with a diffusion-limited current in a short time under a constant pH.

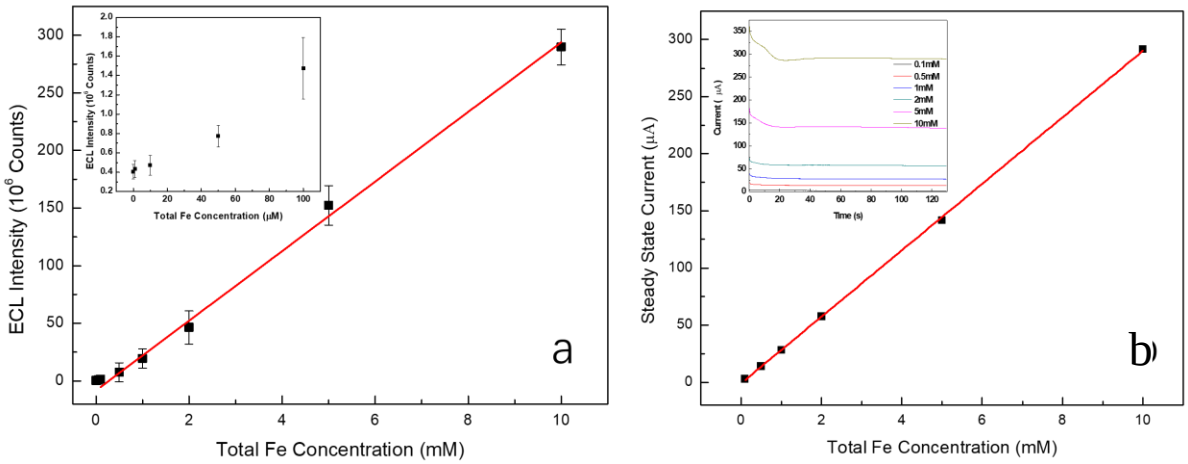

Figure 2.52.(a) Steady-state current as a function of total ferro-ferricyanide concentration, the values are sampling at 60 s from the inset plot. Inset: Chronoamperometry (CA) curves of different total ferro-ferricyanide concentrations in 0.1 M PBS buffer for potential held at 900 mV. (b) Stable ECL emission intensity as a function of total ferro-ferricyanide concentration with applied voltage held at 8.3 V. The values represent at least three independent measurements, and each measurement is at 60 s after the replacement of the analyte solution. Concentration range: 1 μM to 10 mM.

CA simulation and ECL experiments in the BETL system for the ferro-ferricyanide redox couple with different total concentrations from 1 μM to 10 mM in 0.1 M PBS buffer were carried out (Figure 2.52). In the CA, the step potential between two bipolar electrodes was held at 900 mV, which was high enough for it to reach the diffusion-limited steady state quickly. Then the steady-state current was sampled at 60 s and plotted versus total concentration (Figure 2.52(b)). It demonstrates excellent linearity, indicating the reliability of analyte detection by the diffusion-limited steady-state current. According to the CA simulation, ECL experiments were carried out under similar concentration range in the same buffer with the applied voltage held at 8.3 V, which was proved before to provide enough overpotential for the thin-layer cell. The ECL intensity was measured with an exposure time of 5 s at a sampling time of 60 s as in the CA simulation, explicitly in the region of stable ECL emission. Each experiment was at least taken three times to testify its reproducibility. A precise linear correlation between the stable ECL emission intensity and total redox couple concentration is demonstrated with an R^2 value of 0.98, in great agreement with our expectation (Figure 2.52(a)). The inset plot shows the ECL signal for concentration below 100 μM, still in a proportional relationship. Based on the standard deviation from background measurement, the detection limit of this system towards ferro-ferricyanide is about 7 μM according to a signal (S) to noise (N) ratio of 3. The detection limit should be further minimized easily by increasing the exposure time and better detecting device.

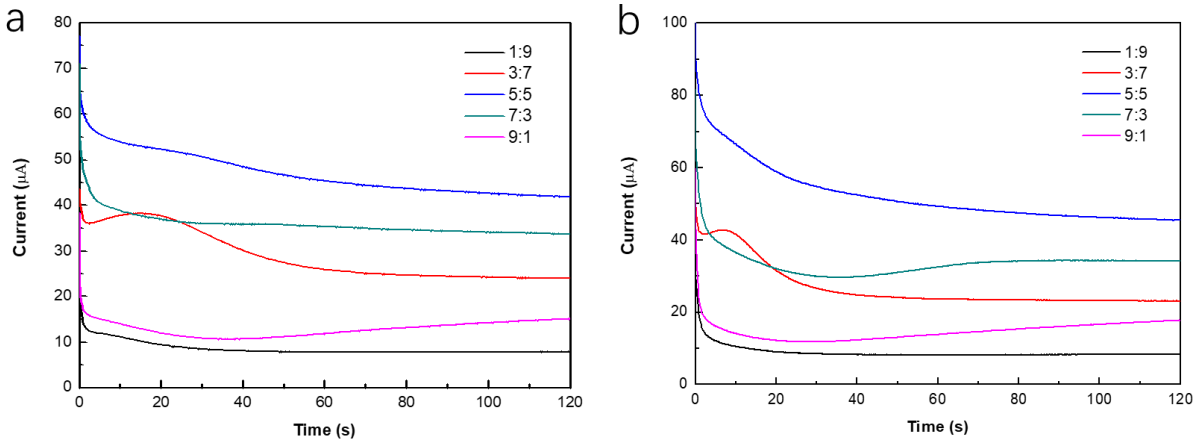

Figure 2.53.CA curves of $Fe(CN)_6^{4-}/Fe(CN)_6^{3-}$ in total concentration of 2 mM with ratios of 1:9, 3:7, 5:5, 7:3, 9:1 in 0.1 M PBS buffer at (a) 200 mV (b) 300 mV.

In addition to the concentration calibration, by taking advantage of the potential separation, it can differentiate the composition of the reduced and oxidized forms of a certain redox-active species in the BETL system from its steady state, by employing a moderate applied voltage. As mentioned earlier, there is a two-step ECL increase and a relatively flat emission in the intermediate stage versus applied voltage when using equal ferrocyanide/ferricyanide. During this stage, the $Fe(CN)_6^{4-}/Fe(CN)_6^{3-}$ couple can undergo rapid redox cycling in the absence of solvent decomposition, so the ratio of $Fe(CN)_6^{4-}/Fe(CN)_6^{3-}$ remains constant and generate a diffusion-limited current. This current value is co-determined by the concentration of each form and its diffusion coefficient. It can then be used to provide the composition information of the analyte. Chronoamperometry of different ratios of $Fe(CN)_6^{4-}/Fe(CN)_6^{3-}$ at 1:9, 3:7, 5:5, 7:3, 9:1 in total concentration of 2 mM in 0.1 M PBS buffer were operated at 200 mV and 300 mV, those are proven to be moderate potentials among the intermediate stage. Figure 2.53 shows the results, with 5:5 ratio exhibiting the highest current response and 1:9 ratio exhibiting the lowest current response after the initial decay.

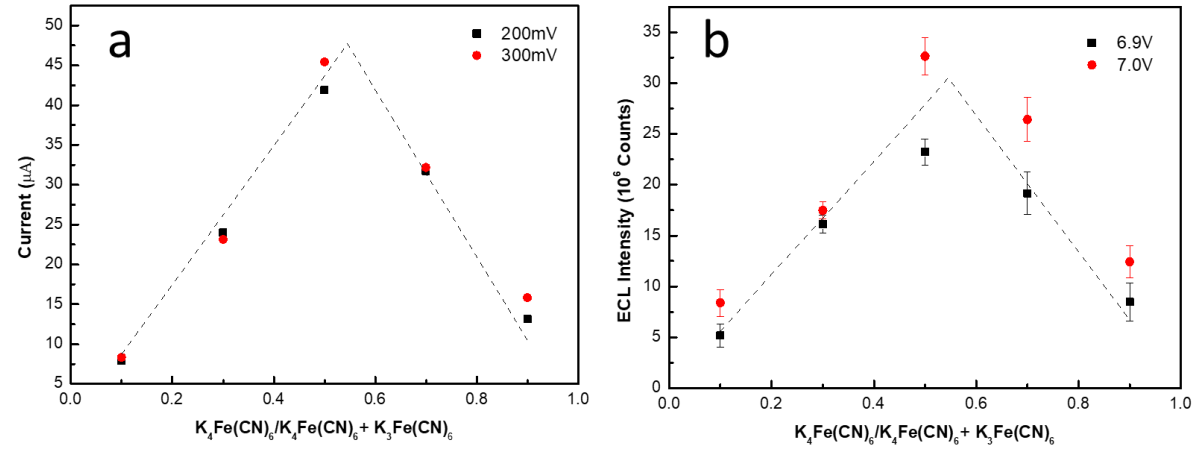

Figure 2.54.(a) Stable CA current response as a function of ferrocyanide/ferricyanide ratio with the same total concentration of 2 mM in 0.1 M PBS buffer. Black: 200 mV, Red: 300 mV. Inset: Chronoamperometry (CA) curves of different ferrocyanide/ferricyanide ratio in 0.1 M PBS buffer for potential held at 200 mV. (b) Stable ECL emission intensity as a function of ferrocyanide/ferricyanide ratio of 2 mM in total concentration at the constant applied voltage. Black: 6.9 V, Red: 7.0 V.

Figure 2.54(a) compares their relatively stable current by sampling each of the CA curves in Figure 2.53 at 60 s. A triangular plot is shown with an ascending trend described by an increasing $Fe(CN)_6^{4-}$ concentration, leading to a larger anodic current on one BPE inner surface with excess $Fe(CN)_6^{3-}$. However, after the highest point in the middle, a descending current response is then observed. The reduced $Fe(CN)_6^{3-}$ concentration causes it now to be the limiting reagent in the thin layer and further diminishes the current response with less of it. The modeled current response according to their diffusion coefficient is drawn as the dashed line, exactly matching with the experimental data. The applied voltages of corresponding ECL experiments were carefully chosen at 6.9 and 7.0 V to ensure a moderate electric field in the BETL system as an adequate overpotential for redox cycling yet without the presence of the side reaction. Stable ECL emission intensity at 60 s is measured to obtain the intensity-ratio plot. A similar triangular-like plot is in excellent agreement with its electrochemical simulation and matches well with the modeled ECL emission, demonstrating the possibility of using the BETL system to readout composition information of redox-active species as the analyte.

2.5.3 ECL and Electrochemical Study of the BETL System Using Hydroquinone/Benzoquinone Redox Couple

To illustrate its application, the BETL system was subsequently employed in the electrochemical analysis of the biologically active, aromatic molecule 1,4-benzoquinone (Q) and its reduced form: hydroquinone (QH_2), which has a much more complicated electron-transfer mechanism and often serves as a model for the neurotransmitter diagnosis.

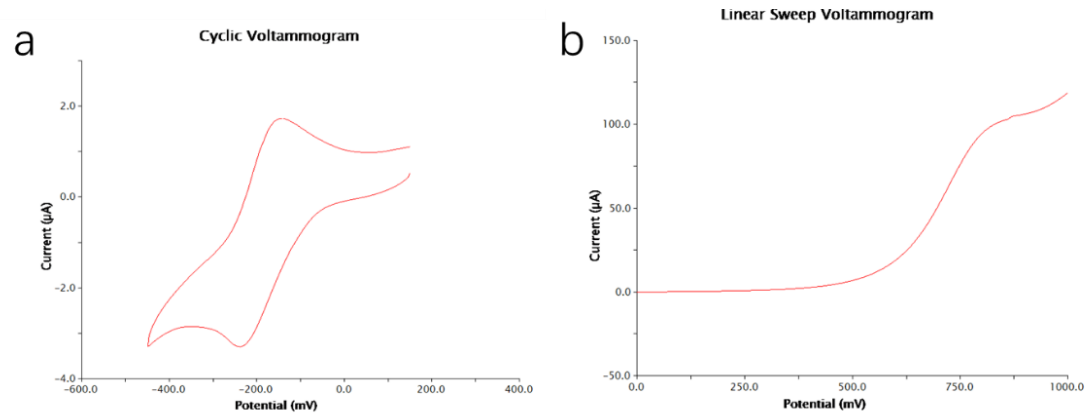

Figure 2.55.(a) CV of 1 mM Q/QH_2 in the thin-layer cell in 0.1 M $NaClO_4$ from 150 to -450 mV, scan rate at 30 mV/s. (b) LSV of 1 mM Q/QH_2 in 0.1 M $NaClO_4$ in the thin-layer cell from 0 to 1000 mV, scan rate at 30 mV/s.

The hydroquinone/benzoquinone system was first characterized by cyclic voltammetry (CV) using a three-electrode system with an equal amount of hydroquinone/benzoquinone（1 mM Q/QH_2）in the 3D printed thin-layer cell. After sweeping the potential from 150 to -450 mV at a scan rate of 30 mV/s, it showed a reduction peak at -230 mV, indicating the reduction of Q (Figure 2.55(a)). An anodic peak corresponding to the back oxidation appeared at -140 mV in the reverse scan. In the following linear

sweep voltammogram (LSV) carried out using the same solution, surprisingly, even with an equal amount of Q and QH, the onset voltage of a significant current growth showed up until 500 mV. This behavior was completely different from the previous ferri-ferrocyanide system in which only a small overpotential is necessary for an apparent current response. This irreversibility of Q and QH_2 must be related to the complexity of their electron-transfer mechanisms. Notice that the current response of the hydroquinone/benzoquinone system involved with a two-electron transfer was two times larger than the ferricyanide/ferrocyanide system involved with a one-electron transfer.

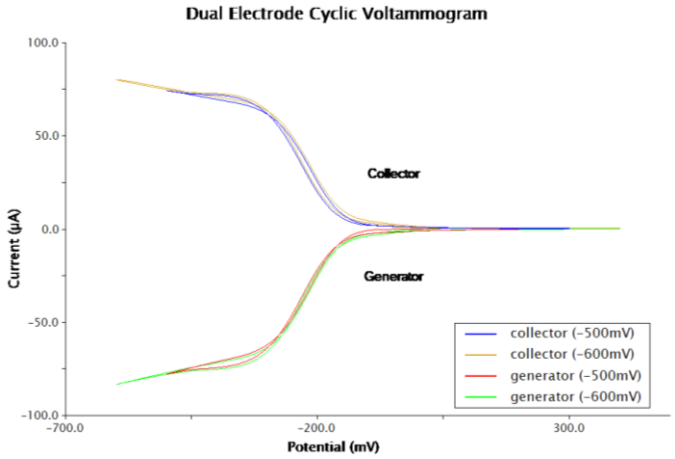

Figure 2.56.DECV of 1 mM Q/QH_2 in 0.1 M $NaClO_4$ in the 3D printed thin-layer cell with generator potential scanning from 300 to -500 mV or -600 mV/s, scan rate at 30 mV/s, collector potential at 300 mV.

The DECV was conducted by scanning the generator from 300 to -500 mV or -600 mV at 30 mV/s while keeping the collector potential at 300 mV (Figure 2.56). The reduction current response on the generator and oxidation current response on the collector both increased after -150 mV, matching well with the reduction peak in the CV curve. When changing the final potential from -500 to -600 mV, a second current increase was observed due to the participation of H^+ reduction on the generator. Also, the response from the collector was in exact symmetric with the generator, indicating the well-defined geometry of the thin-layer cell.

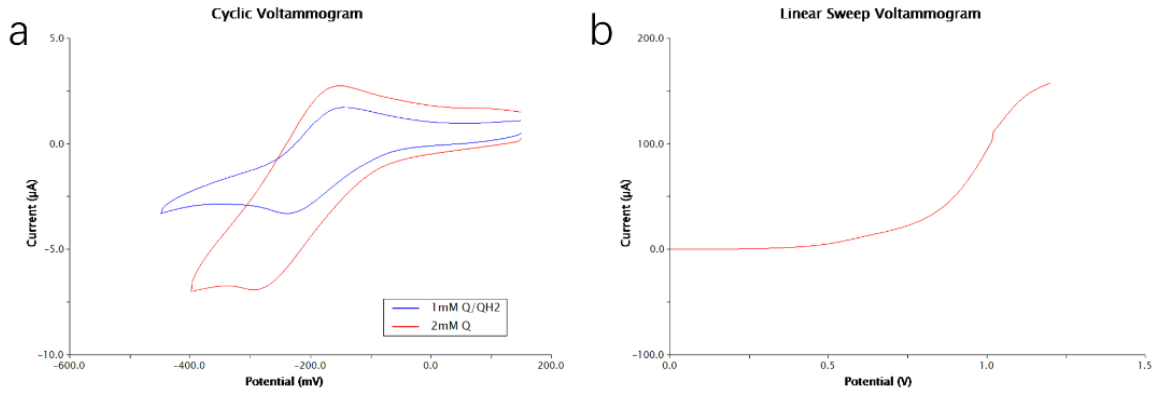

Figure 2.57.(a) CV of 2 mM Q in the thin-layer cell in 0.1 M $NaClO_4$ from 200 to -400 mV, scan rate is 30 mV/s. (b) LSV of 2 mM Q in 0.1 M $NaClO_4$ in the thin-layer cell from 0 to 1000 mV, scan rate at 30 mV/s. Both compared to 1 mM Q/QH_2.

The CV curve of benzoquinone only (2 mM Q) exhibited a significantly larger cathodic peak at the same position as 1 mM Q/QH_2 (Figure 2.57(a)), elucidating the reduction of Q. However, it also showed a larger anodic peak compared to 1 mM Q/QH_2. We ascribed the anodic peak to the back-oxidation of the reduction product of Q, but not the oxidation of original QH_2. Figure 2.57(b) displayed a large onset voltage of current at 800 mV with slow current growth. As obtained from the CV result, the reduction peak of Q appeared at about -200 mV. In order to reduce Q in a two-electrode system, water oxidation needs to proceed at the BPE anode as a coupled reaction. After that, the redox cycling in the thin layer could then be initiated between Q and its reduced form. In other words, it is the potential separation between Q reduction and water oxidation that lead to the large onset potential and slow current growth.

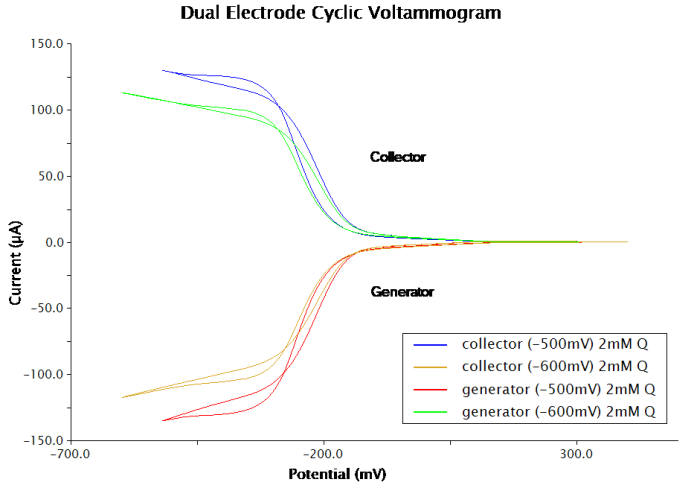

Figure 2.58.DECV of 2 mM Q in 0.1 M $NaClO_4$ in the 3D printed thin-layer cell with generator potential scanning from 300 to -500 mV or -600 mV, collector potential set as 300 mV, compared with previous DECV of 1 mM Q/QH_2.

In the DECV, Figure 2.58 showed a similar symmetric behavior for 2 mM Q as 1 mM Q/QH_2, but with the current response 2 times larger. It proved that both the current responses were only from the reduction of Q and the oxidation of its conjugated reduced form, while not from QH_2. If QH_2 was oxidized during this process, the collector current should be higher than generator current. Besides, the collector potential at 300 mV was not enough to oxidize QH_2 effectively. Otherwise, the collector current should resemble the magnitude of DECV of 2 mM Q.

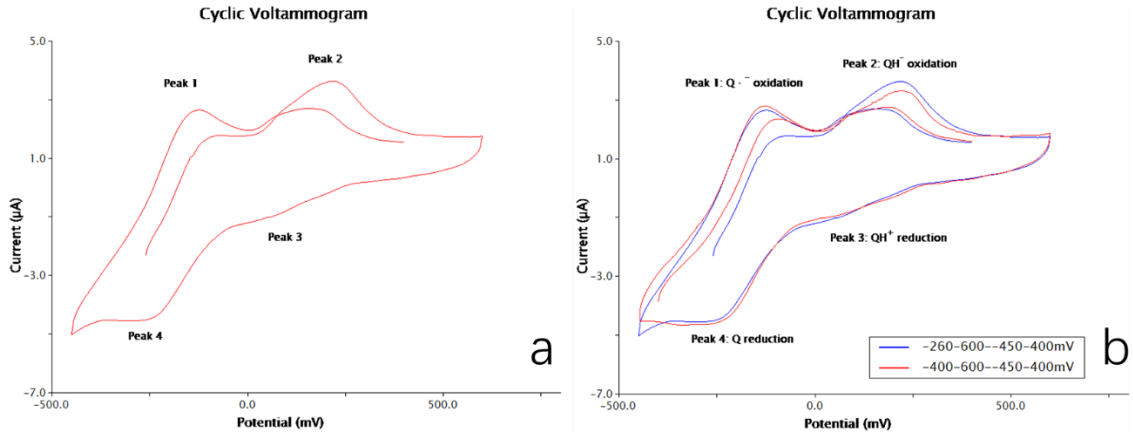

Figure 2.59.CV of 2 mM QH_2 in the thin-layer cell in 0.1 M $NaClO_4$ (a) -260 – 600 – - 450 – 400 mV. (b) -400 – 600 – - 450 – 400 mV. Both scan rates are 30 mV/s.

When performing the CV of hydroquinone only (2 mM QH_2), the electro-active species and their corresponding redox reactions in the benzoquinone-hydroquinone system was elucidated. The appearance of two anodic peaks and two cathodic peaks indicated the complexity in electron-transfer mechanisms (Figure 2.59(a)). According to the literature, the active species and reduction/oxidation potential in the Q/QH_2 system strongly depend on the protonation/deprotonation form influenced by the pH condition. The anodic peak 1 at -126 mV was assigned as the oxidation of $Q\cdot^-$, which was the radical anion from the deprotonation of QH_2 followed by H radical dissociation. The anodic peak 2 at 217 mV was assigned as the oxidation of QH^-, which is the deprotonated form of QH_2. An ambiguous cathodic peak 3 at 87 mV was assigned as the reduction of QH^+, which was the protonated form of Q. The other reduction peak 4 at -250 mV was assigned as the reduction of the original Q (Another saying was the reduction of semi-ketals $(QH)_2$ by the dimerization of $QH\cdot$ from one-electron transfer). Note that the peak 1 increased while the peak 2 decreased in the second scan after the first one. However, the integration of the two peaks in the first and second scan was equivalent, indicating the change in the relative ratio of $Q\cdot^-$ and QH^- after the first scan.

A similar CV was shown by only changing the initial potential from -260 mV to -400 mV (Figure 2.59(b)). However, the $Q\cdot^-$ oxidation peak in the first scan in the latter situation became larger than the former situation followed by a smaller QH^- oxidation peak. This change in peak sizes, which corresponded to the difference in the composition of $Q\cdot^-$ and QH^-, should be attributed to the local pH variation near the electrode surface from the induction period of the CV. The initial potential at -400 mV was negative enough to trigger H^+ reduction, inducing a subsequent pH increase which converted more QH^- to $Q\cdot^-$. Surprisingly, the two peaks in the second scan in both the two CV curves matched well with each other, owing to the same lower limit potential before the second scan for pH adjustment.

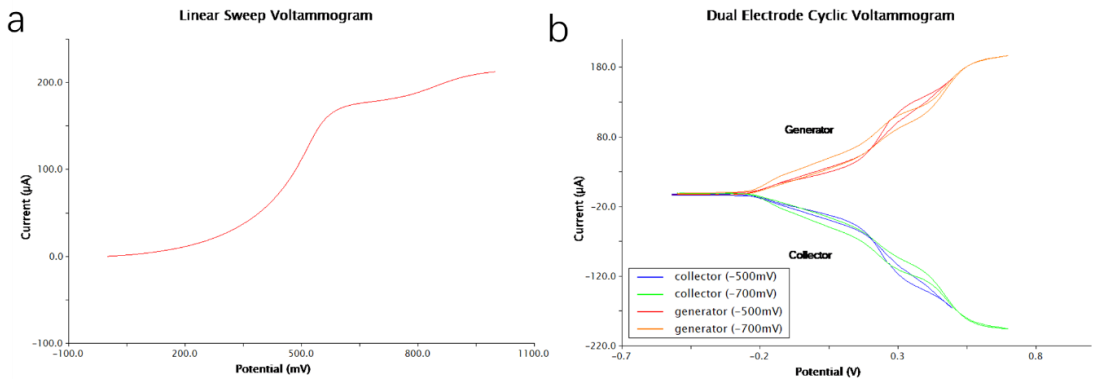

Figure 2.60.(a) LSV of 2 mM QH_2 in 0.1 M $NaClO_4$ in the 3D printed thin-layer cell from 0 to 1000 mV. (b) DECV of 2 mM QH with generator potential scanning from -500 to 500 mV or 700 mV, collector potential set as -500 mV. Scan rates: 30 mV/s.

Figure 2.60(a) showed the LSV curve of hydroquinone only (2 mM QH_2) in the 3D printed thin-layer cell. It started to grow up at about 300 mV, then reached a first semi-plateau region at around 620 to 900 mV. The rising of the current response must be related to the accumulation of the oxidized form with the help of H^+ reduction. According to the previous CV characterization, $Q^{\cdot -}$ should be oxidized to Q first. The potential difference between $Q^{\cdot -}$ at -126 mV and H_2 evolution at around -400 mV was very close to 300 mV. By increasing the overpotential, a great many oxidized form was generated with the participation of QH^- oxidation, facilitating an enhanced redox cycling and showing a relatively stable current response in the semi-plateau region. A further increase after 900 mV might be related to the participation of water oxidation or the oxidation of undissociated QH_2 itself.

DECV was carried out when the sweeping the generator potential from -500 to 500 mV or 700 mV while keeping the collector at -500 mV for hydroquinone only (Figure 2.60(b)), showing a two-peak feature. We assigned the first peak starting at -0.2 V to $Q^{\cdot -}$ oxidation and the second peak starting at 0.2 V to QH^- oxidation. A relative stable peak current appeared after 0.6 V, analogous to the LSV behavior.

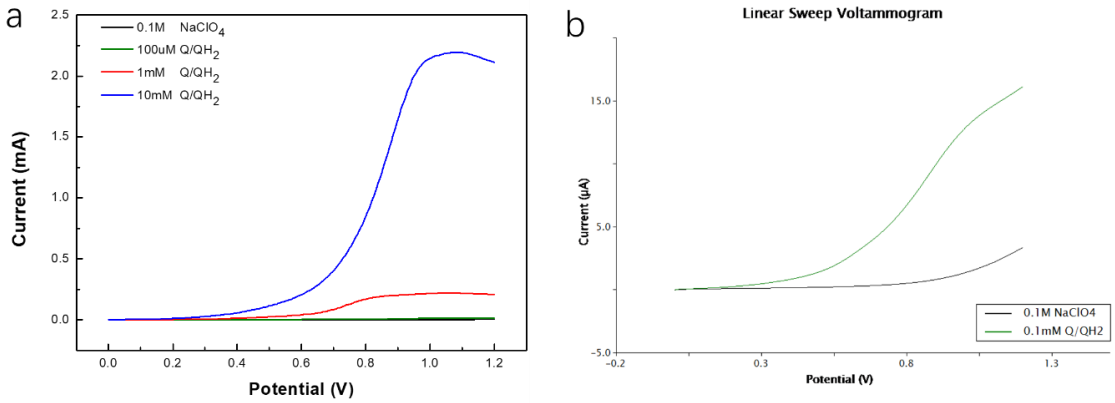

Figure 2.61.(a)LSV of 0.1 M $NaClO_4$, 100 μM Q/QH_2, 1 mM Q/QH_2, and 10 mM Q/QH_2 in the thin-layer cell from at a scan rate at 30 mV/s. (b) LSV comparison of 0.1 M $NaClO_4$ and 100 μM Q/QH_2.

Figure 2.61(a) compared the linear sweep voltammograms of 0.1 M $NaClO_4$, 100 μM Q/QH_2, 1 mM Q/QH_2, and 10 mM Q/QH_2 together, with 10 mM Q/QH_2 having the largest current response close to 2.2 mA. The onset voltage at around 0.5 V could be explained explicitly by the overpotential

requirement to couple Q reduction with QH^- oxidation. As illustrated in the CV study, most of the QH_2 would be present in the form of QH^- with a small amount of $Q\cdot^-$; and the overwhelming majority of Q would be present in the form of Q with a trace amount of QH^+. Even though a low overpotential of 0.5 V was capable of driving the redox cycling between Q and $Q\cdot^-$, the current was limited by the amount of $Q\cdot^-$. Only after the coupling of the main species, could the current response show a noticeable increase by the redox cycling between $Q\cdot^-$, QH^-, Q and QH^+ entirely. In addition, with the participation of H^+ reduction, the relative ratio of the reduced/oxidized species could also be adjusted, showing a further current increase (by increasing the oxidized form). Aware that for 1 mM or 10 mM Q/QH_2, a steady-state plateau current was observed at 1.0 V; while for 100 µM Q/QH_2, the current continued increasing even after 1.2 V (Figure 2.61(b)). In the thin layer, the oxidation of QH^- and $Q\cdot^-$ were also coupled with H^+ reduction in addition to the reduction of Q and QH^+. As a consequence, pH would keep increasing with more oxidized form generated. For a higher concentration of Q/QH_2, the substantial pH change towards a higher value would hamper the conversion to the oxidized form which producing a higher current response. Also, gold oxide film would on the BPE surface and weaken the current response by retarding the adsorptive electron transfer in the hydroquinone-quinone system, particularly in the case of a higher redox couple concentration. It explained the decrease in current after 1.1 V for 10 mM Q/QH_2.

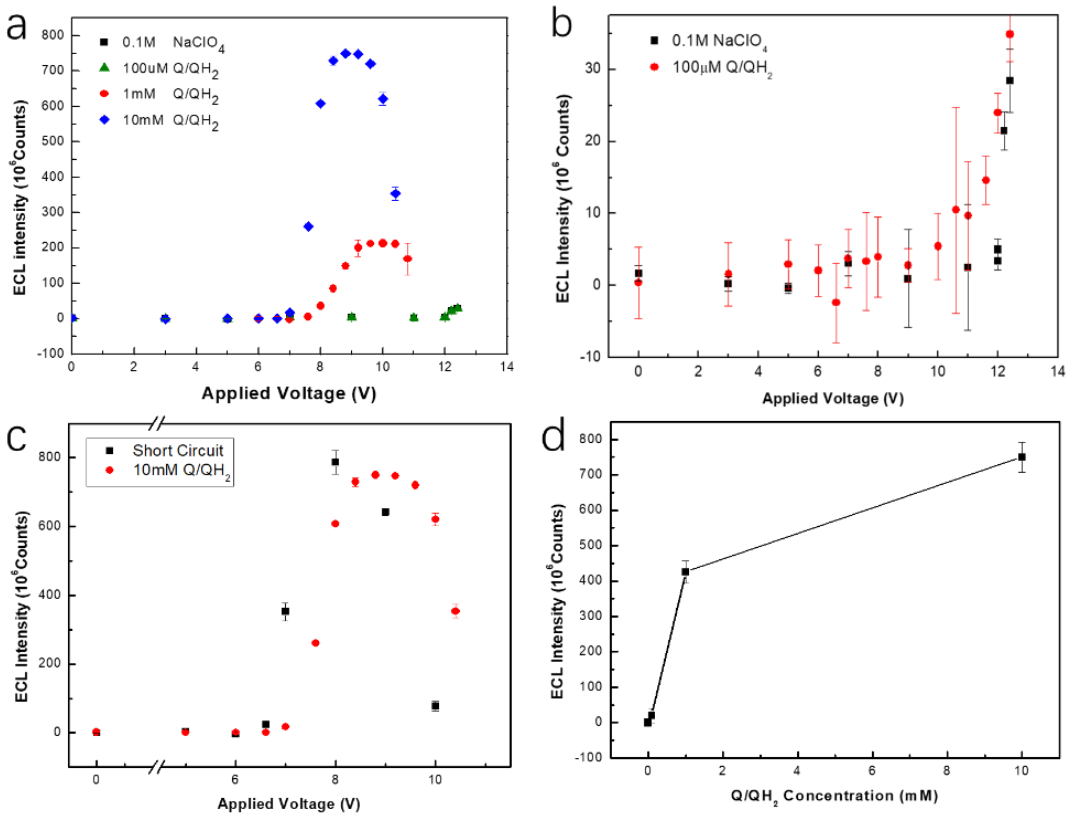

Figure 2.62.(a) ECL emission intensity in the BETL system of 0.1 M $NaClO_4$ and Q/QH_2 (100µM, 1 mM, and 10 mM in each reduced and oxidized form) as a function of applied voltage. (b) Comparison of 0.1 M $NaClO_4$, 100 µM Q/QH_2. (c) Comparison of 10 mM Q/QH_2 and the short circuit condition. (d) Calibration curve of ECL intensity versus Q/QH_2 concentration.

After the electrochemical simulation, the ECL performance of the hydroquinone-benzoquinone system was investigated using the BETL system. Figure 2.62(a) plotted the ECL emission intensity of 0.1 M $NaClO_4$, 100 µM Q/QH_2, 1 mM Q/QH_2, and 10 mM Q/QH_2 as a function of applied voltage. Similar to the LSV result, both the ECL intensities for 1 mM and 10 mM Q/QH_2 increased rapidly after the onset voltage and then reached the plateau region with steady-state emissions. By further increasing the applied voltage, the ECL intensity decline much fast than what was observed in the LSV simulation. For the hydroquinone-benzoquinone system, it had a much higher potential requirement than the ferricyanide-ferrocyanide system. As shown in Figure 2.62(b), the plateau current corresponding to the steady-state appeared after 0.9 V, whereas for the ferricyanide-ferrocyanide system it was around 0.7 V. In the BETL system, this difference was manifested by the appearance of the stable ECL emission at 9.6 V for 1 mM Q/QH_2 compared to 8.3 V for 1 mM $K_3Fe(CN)_6/K_4Fe(CN)_6$. This higher applied voltage, along with the doubled electron-transfer number *n* in the hydroquinone-benzoquinone system, could both result in a fierce competing O_2 evolution on the BPE anode outside, overriding the ECL emission by bubble formation and adsorption on the surface. This hypothesis was supported by an intensity recovery by shifting the applied voltage to a lower value after the ECL decline.

The ECL intensity was calibrated versus Q/QH_2 concentration from 0.1 to 10 mM; each point represented the average of three independent measurements. It showed a linear relationship except for 10 mM (Figure 2.62(d)). 10 mM Q/QH_2, which had a total concentration of 20 mM, was two times the highest total concentration used in the ferricyanide-ferrocyanide system. Beyond that, the number of electrons transferred per redox event was also doubled in the hydroquinone-benzoquinone system (n=2). The $Ru(bpy)_3^{2+}$ in the ECL solution in the peripheral cell, was only of 5 mM. This much-enhanced redox cycling in the thin layer made the $Ru(bpy)_3^{2+}$ oxidation on the BPE anode outside the rate-limited step, which was restricted by the diffusion of 5 mM $Ru(bpy)_3^{2+}$. A validating ECL test was taken by removing the spacer and short-circuiting the two BPE inner surfaces as one BPE. Its intensity started to increase from 6.6 V and reached the maximum before 8 V (Figure 2.62(c)). Competing O_2 evolution just discussed should account for the quick ECL decline after that. It was worth noting that the maximum intensity in the short-circuit situation was at the same magnitude as 10 mM Q/QH_2, proving both the reaction rates dependent on the $Ru(bpy)_3^{2+}$ diffusion. In other words, the reaction in the thin-layer was saturated. The difference in applied voltage rested on the additional overpotential requirement on the two BPE inner surfaces to drive the Q/QH_2 redox cycling; while in the short-circuit situation, the two BPE worked as a single BPE.

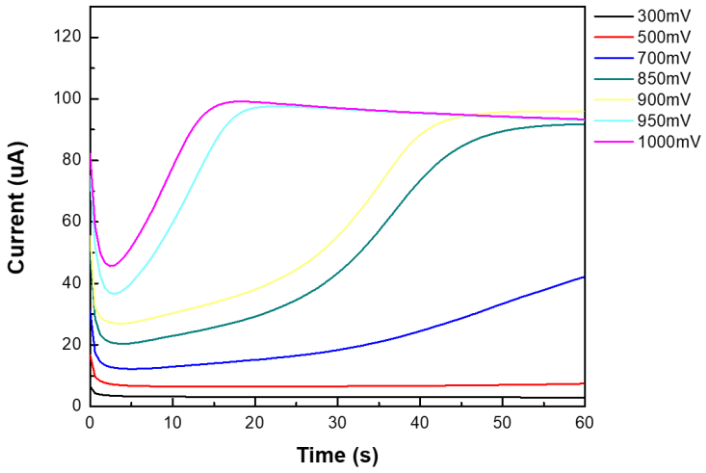

Figure 2.63.CA of 2 mM QH_2 in the thin-layer cell in 0.1 M $NaClO_4$ at potential from 300 to 1000 mV.

Figure 2.63 showed the chronoamperometry (CA) of 2 mM QH_2 by applying step potentials from 300 mV to 1000 mV. Below 500 mV, only a small current was observed. Under such a low potential, only $Q^{\cdot -}$ in small amount was oxidized by the reduction of H^+ to Q, of which the accumulation was considerable slow under a potential just above the requirement. QH^- oxidation did not take place because of its higher oxidation potential requirement. After 600 mV, like 700 mV, for example, the current started to increase apparently. In this condition, QH^- was oxidized to QH^+ or Q, but in very slow reaction kinetics which could not reach the steady state in time. While at 850 mV and 900 mV, it would proceed fast enough under such a larger overpotential, exhibiting the steady-state current before 60 s. At 950 mV or 1000 mV, the current grew up to the maximum rapidly followed by even a small decay. It should be the result of the undesired conversion to the oxidized form together with the small gold oxide formation which induced a larger electron-transfer resistance.

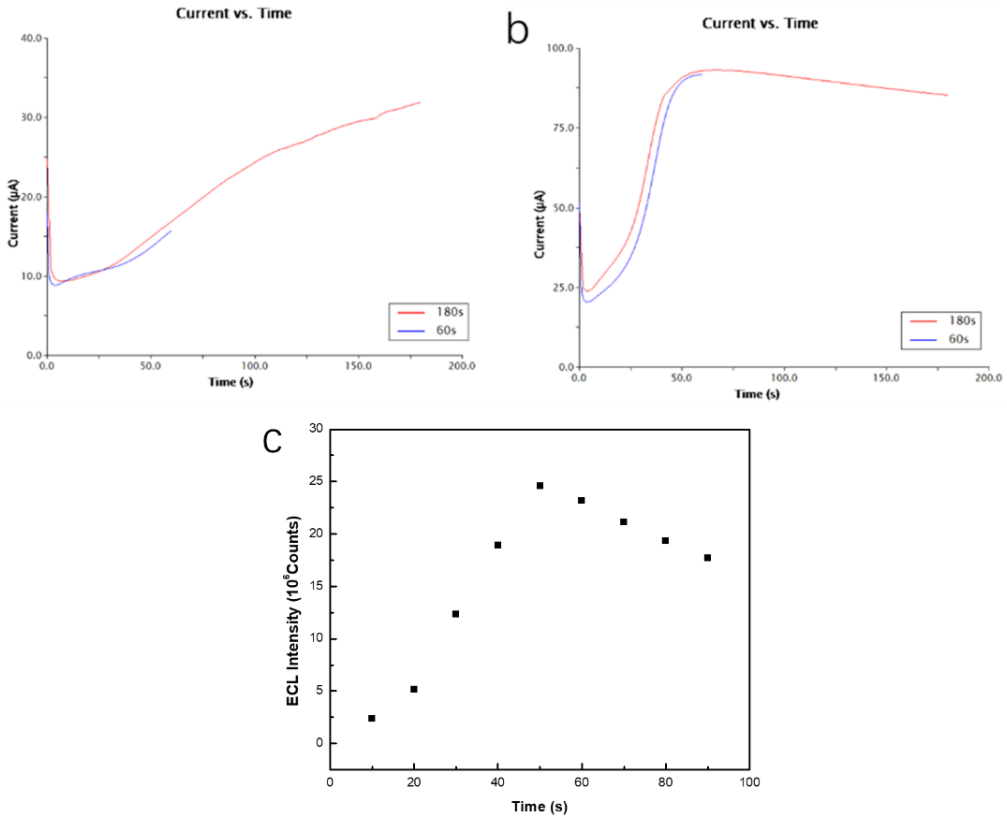

Figure 2.64.(a) CA comparison of 2 mM QH_2 in the 3D printed thin-layer cell for 60 s and 180 s (a) at 650 mV (b) at 850 mV. (c) Corresponding ECL experiment in the BETL system of ECL intensity as a function of time at an applied voltage at 7.0 V.

When comparing the CA curves at 650 mV with a time range of 60 s or 180 s, as shown in Figure 2.64(a), the current kept increasing even after 180s. This slower increase should be attributed to the small conversion of $Q^{\cdot -}$ to Q, and the oxidation of QH^- at a very slow speed. Figure 2.64(b) showed that the CA current at 850 mV reached the maximum at just 60s, indicating the rapid conversion of QH^- to its oxidized form and the obtaining of an optimized oxidized form/reduced form (O/R) ratio. After 60 s, the current dropped in a gentle slope, resembling the similar behavior in the CA at 950 mV or 1000 mV in 60 s (Figure 2.64). It again confirmed the pass of the optimized O/R ratio by the undesired conversion of QH_2. The corresponding ECL experiment was taken simultaneously under an applied voltage of 7.0 V (Figure 2.64(c)), showing a time-dependent performance matched well with the CA result.

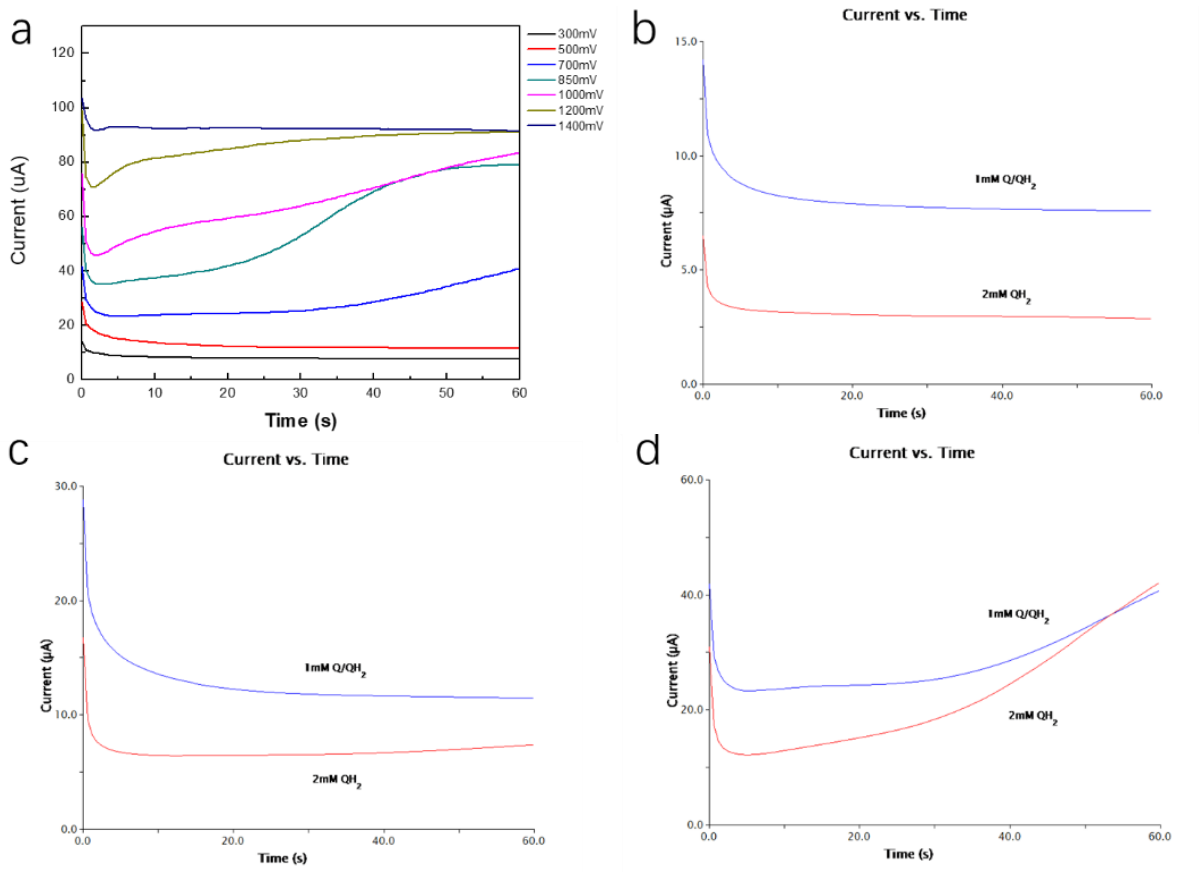

Figure 2.65.(a) CA of 1 mM Q/QH_2 in 0.1 M $NaClO_4$ in the thin-layer cell at potential from 300 to 1400 mV. (b) Comparison of CA of 1 Q/QH_2 and 2 mM QH_2 at 300 mV (c) at 500 mV (d) at 700 mV for 60 s.

Figure 2.65(a) showed the CA of 1 mM Q/QH_2 by applying step potentials from 300 to 1400 mV, with a significant current increase at the potential above 700 mV. In the case of 1 mM Q/QH_2, even though the oxidized and reduced form were both presented in the thin layer originally, the fast redox cycling could only happen until the fulfillment of the potential requirement between QH^- and Q. The re-increase at the potential more than 1000 mV was attributed to the participation of water oxidation that created a new steady state.

When comparing the CA of 1 mM Q/QH_2 and 2 mM QH_2 together, at 300 mV or 500 mV, the current response of 1 mM Q/QH_2 was greater than 2 mM QH_2 (Figure 2.65(b)(c)). This behavior verified the presence of the redox cycling between a small amount of $Q^{\cdot -}$ and Q under the case of equal Q/QH_2. From 300 mV to 500 mV, the larger overpotential would facilitate the $Q/Q^{\cdot -}$ redox cycling and also initiate the Q/QH^- redox cycling, showing a higher current value. However, when stepping the potential to 700 mV, the current response of 2 mM QH_2 exceeded that of 1 mM Q/QH_2 at 53 s (Figure 2.65(d)). In this condition, 2 mM QH_2 with more H^+ as a "buffer" would mitigate the potential barrier between the oxidation of between QH^- and the reduction of oxidized form by the protonation of Q.

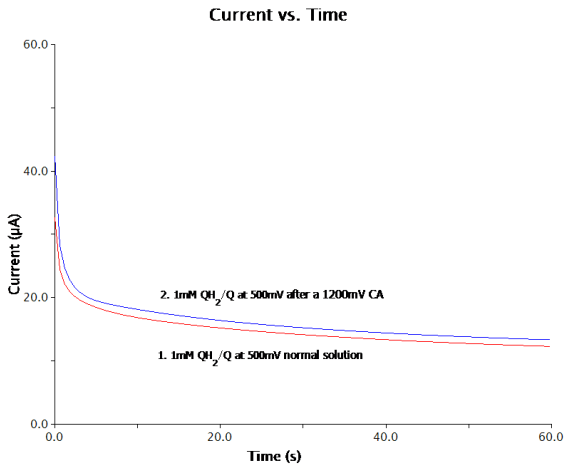

Figure 2.66.CA of 1 mM Q/QH_2 in the thin-layer cell at (1) 500 mV initially (2) 500 mV immediately after a CA at 1200 mV for 60 s.

The CA of 1 mM Q/QH_2 at 500 mV was carried out twice with the second run performed immediately after a pre-CA at 1200 mV. As shown in Figure 2.66, both the current responses had the same magnitude about 20 μA, indicating the moderate redox cycling between $Q^{\cdot -}$ and Q. Moreover, the pre-CA at 1200 mV did not change the O/R ratio and the protonation form (like from QH^- to $Q^{\cdot -}$) in the Q/QH_2 system. According to this behavior, it is apparent to conclude the majority of the current at the potential above 700 mV in Figure 2.65(a) should come from the redox cycling of Q/QH^-, which can not be triggered at 500 mV.

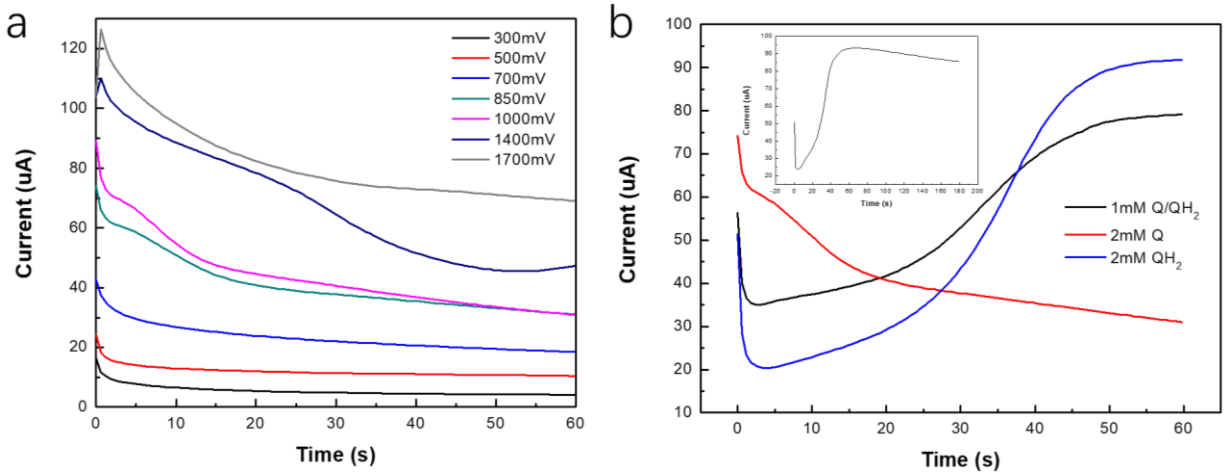

Figure 2.67.(a) CA of 2 mM Q in 0.1 M $NaClO_4$ in the thin-layer cell at potential from 300 mV to 1700 mV. (b) The comparison of CA of 1 mM Q/QH_2, 2 mM QH_2, and 2 mM Q at 850 mV. Inset: CA of 2 mM QH_2 at 850 mV for 200s.

Figure 2.67(a) demonstrated the CA of 2 mM Q at step potentials from 300 to 1700 mV. The significant current decay dominates in all the current responses, which was utterly different from the case in hydroquinone only or equivalent hydroquinone/benzoquinone. The potential separation between Q reduction and the coupled water oxidation in this system was more than 800 mV. As a result, below

850 mV, the current was only from the charging decay and the reduction of trace amount QH^+; while above 850 mV, Q, as a major component, could undergo the reduction to $Q^{\cdot -}$ by the help of water oxidation (or gold oxidation). At an extremely high potential of 1400 mV or 1700 mV, the faradaic current increase would even surpass the charging current decay.

Figure 2.67(b) compared the CA of 2 mM QH_2, 1 mM Q/QH_2, and 2 mM Q together, displaying three completely different behaviors. Initially, 1 mM Q/QH_2 showed a higher current response than 2 mM QH_2 due to the presence of both the reduced form (mainly QH^-) and oxidized form (mainly Q), under an overpotential enough to fulfill the requirement of redox reactions. However, for hydroquinone only (2 mM QH_2), more QH^+ other than Q, as the corresponding oxidized form would be generated by the help of H^+ reduction. The potential separation between QH_2 (mainly QH^-) and its QH^+ pair is much smaller than that between Q and QH_2. Moreover, Q reduction has a very complicated process with slow kinetics and adsorption effect[74]. As a consequence, the redox cycling of 2 mM QH_2 became faster than 1 mM Q/QH_2 when sufficient QH^+ was accumulated, and thus its current response exceeded the latter one. For benzoquinone only (2 mM Q) at 850 mV, only a small amount of Q could be reduced by the help of water oxidation under such a large potential separation, showing a low current response in the CA result. The complexity in Q reduction on one BPE surface and possible gold oxide formation on the other BPE surface as a coupled reaction to convert Q to its reduced form would further attenuate the current response as well.

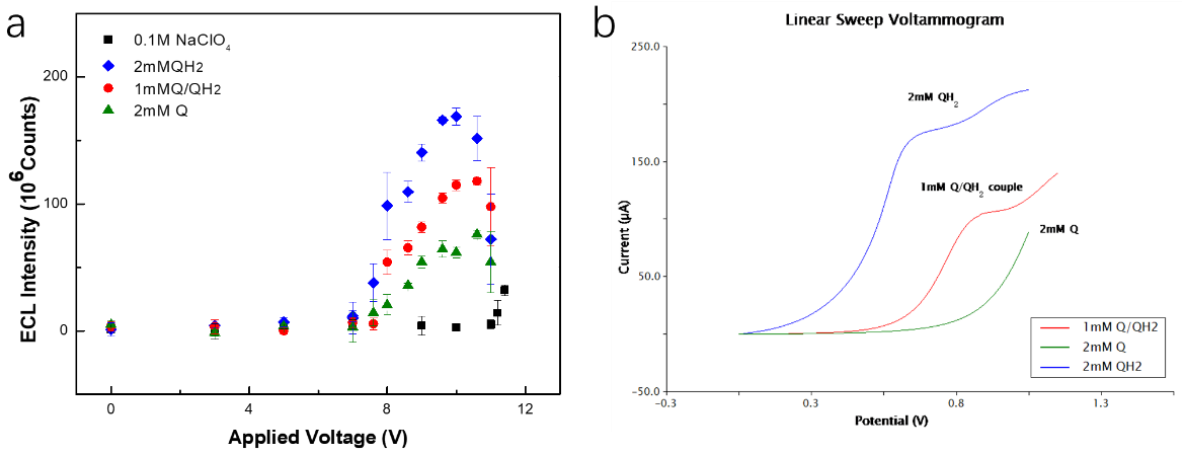

Figure 2.68.(a) ECL emission intensity of 2 mM QH_2, 1 mM Q/QH_2, and 2 mM Q in 0.1 M $NaClO_4$ as a function of applied voltage. (b) LSV simulation as a function of potential between bipolar electrodes, scan rate: 5 mV/s.

The ECL experiments of 2 mM QH_2, 1 mM Q/QH_2, and 2 mM Q in the BETL system were conducted by gradually increasing the applied voltage (Figure 2.68(a)). The sequence in the onset voltage of ECL (2 mM QH_2,1 mM Q/QH_2, and 2 mM Q) and the magnitude of ECL intensity (2 mM QH_2 > 1 mM Q/QH_2 > 2 mM Q) was in agreement with the LSV simulation (Figure 2.68(b)), confirming the effect of potential separation from both the analyte and solvent. The ECL decline after the maximum was ascribed to the competing O_2 reaction under a high applied voltage discussed previously.

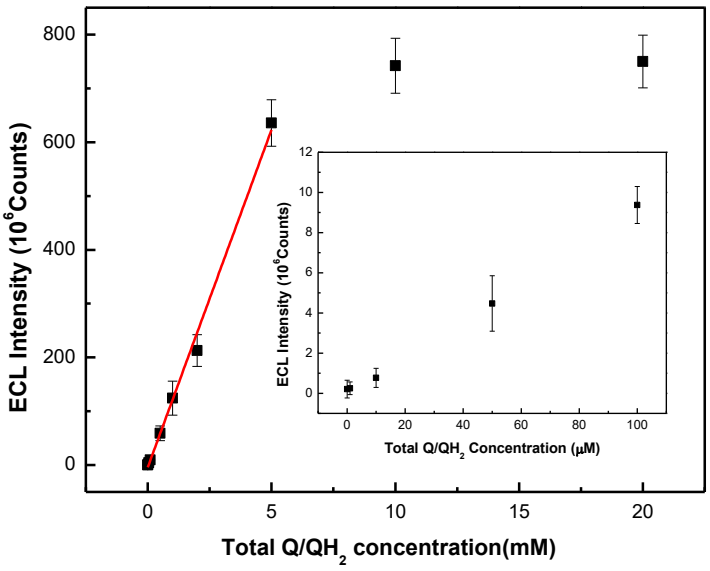

Figure 2.69.Stable ECL emission intensity as a function of total hydroquinone-benzoquinone concentration (1uM to 20 mM) at 9.6 V. Each data point represents at least three independent measurements, and each measurement is sampled at 60 s after the replacement of solution.

Finally, the calibration plot of the hydroquinone-benzoquinone system was obtained by measuring the ECL intensity as a function of its total concentration ranging from 1 μM to 20 mM. The applied voltage was set at 9.6 V, which provided a sufficient overpotential for the thin-layer cell to reach the diffusion-limited steady state with stable ECL emission within a sampling time of 60 s. Figure 2.69 showed that the ECL intensity-concentration plot followed an excellent linear relationship with R^2 = 0.99, except for 10 mM and 20 mM. As mentioned, $Ru(bpy)_3^{2+}$ concentration in the ECL solution in the BETL was 5 mM, with only one electron transferred by its oxidation; while the number of electron transferred per molecule in the Q/QH_2 system is twice of it. With Q/QH_2 concentration higher than 10 mM, due to the overwhelmingly enhanced redox cycling in the thin layer, the rate-limiting step of the BETL system is instead the $Ru(bpy)_3^{2+}$ diffusion in the reporting cell. Calculated from the calibration plot, the detection limit of the BETL system towards the hydroquinone-benzoquinone system was around 3μM with a linear dynamic range about 4 orders of magnitude. This reduced detection limit compared to the ferro-ferricyanide redox system should be attributed to doubled electron transfer number per redox molecule.

2.6 Conclusions

By far, we have designed a novel ECL sensing platform for the detection of electroactive species in the low-concentration range, using a thin-layer configuration on the basis of bipolar electrochemistry. The platform, which is termed as the bipolar electrode thin-layer (BETL) system, is simply fabricated by 3D printed technique. Significantly enhanced charge amplification is achieved by repeatable redox cycling within the thin layer which only requires a small volume of sample. The amplified current response is transduced to a corresponding ECL emission at the BPE outside the thin layer and read out by a commercially-available CCD camera. The sensing case and reporting case are separated in a

double-cell configuration, while under the open bipolar electrochemistry. Analyte such as ferricyanide-ferrocyanide and hydroquinone/benzoquinone redox couples are studied extensively by the ECL performance. The obtained detection limit to date is as low as 7 μM for the ferricyanide-ferrocyanide system and 3 μM for hydroquinone/benzoquinone system with a linear dynamic range about 4 orders of magnitude. Further detailed information such as composition, thermodynamics, kinetics, and pH effect is also studied by addressing electrochemical reactions within the thin layer instantaneously. This system eliminates the need for a direct electrical connection to the BPE by way of ECL readout and avoids a heavy-duty potentiostat setup. Simultaneous electrochemical simulation is employed to provide an insight view of the BETL system and to correlate the ECL intensity with the current response. Moreover, the electric field profile in the BPE system was investigated systematically concerning many influential factors, and it explains explicitly the ECL variation during the experiment.

Chapter 3 AC Square Wave Bipolar ECL System

3.1 Introduction

3.1.1 AC Bipolar Electrochemistry

Bipolar electrochemistry is always carried out by an external DC power supply, which generates a stable, one-direction electric field across the electrolyte solution. The polarity of the driving electrodes defines the BPE cathode and anode. However, instead of a DC voltage, the AC voltage excitation, as a well-established technique in conventional electrochemistry, is also suitable in bipolar electrochemistry. When a time-dependent voltage program (in different shapes or frequencies, i.e., square wave) is employed in the bipolar system, an iterative switch of the electric field across the solution will occur from a continuous alternation of the polarity on the driving electrodes. As a result, a repeating mutual exchange of the reduction and oxidation would happen on the same BPE end from its alternate shift between the cathode and anode. The first topic involving in AC bipolar electrochemistry was the synthesis of bifunctional particles[138]. At first, a DC voltage was tried to synthesize bifunctional particles by switching its direction after a period. However, it turned out to be difficult to control the deposition area by only varying the applied voltage and treating time, since the electric field gradually decreased due to small generated oxygen bubbles on the electrode surface. Then an AC square wave voltage at 50 Hz was employed in the open bipolar cell, showing a relatively constant electric field. A variety of glass carbon (GC) particles that stayed in the agarose gel network sandwiched between driving electrodes were successfully modified with gold or platinum in a site-selective manner in one-step bifunctionalization. The high-speed pulse electrolysis seemed to reduce the formation of oxygen bubbles and to avoid the generation of Joule heat that could dissolve the agarose gel around driving electrodes. Then, this AC bipolar system was employed to address the iterative electropolymerization of aromatic monomers on both ends of a BPE.

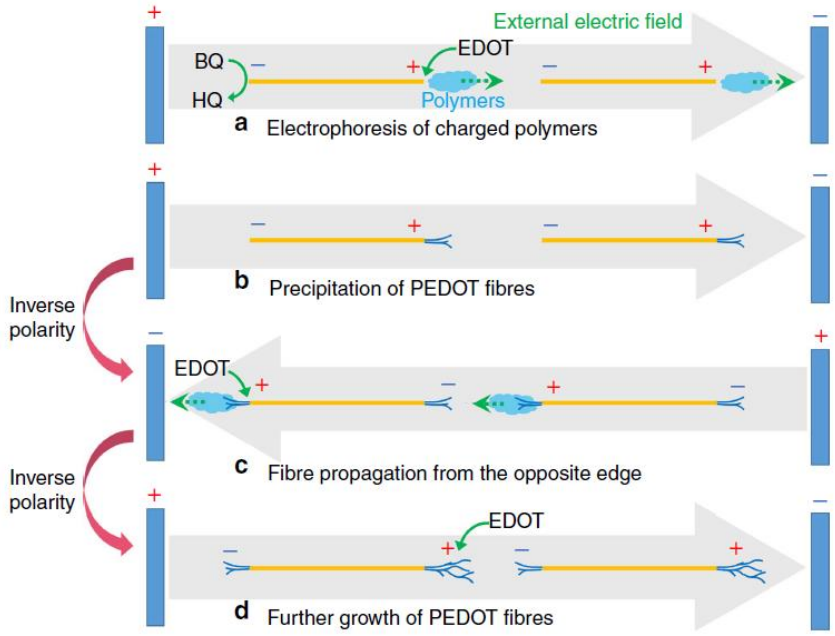

Figure 3.1.Proposed PEDOT fibre-propagation mechanisms. (a) Electrophoresis of charged polymers, (b) precipitation of PEDOT fibres, (c) propagation of fibres from the opposite end and (d) further growth of PEDOT fibres[139]. Reprinted with permission from [139]. Copyright © (2018) Springer Nature.

In contrast to the film formation of aromatic monomers, Koizumi reported the propagation of conducting polymer microfibres and subsequent network formation through the electropolymerization of 3,4-ethylenedioxythiophene and its derivatives by the AC bipolar electrolysis[139]. Two gold wires were placed 1 mm apart as the BPEs in the electrolysis cell having EDOT monomer and BQ in the solution. Initially, when applying an external electric field, the electropolymerization of EDOT took place at the anodic pole, and the sacrificial reduction of BQ to QH_2 proceeded at the anodic pole. Once the polarity was inverted under an AC frequency at 5 Hz, the polymer fibres started to grow from the other end of the Au wire (Figure 3.1). The resulting polymer was typically doped and had cationic charges with good conductivity, and thus it could be electrophoresed under the influence of the external electric field. As a result, it was not deposited as a film but in an anisotropic morphology. During the electrolysis, the PEDOT fibre terminals were activated for a gradual propagation; and finally, the tip of one propagating fibres met the tip of a fibre growing from the other Au wire. After the bridge, the propagation stopped abruptly, and the two Au wires now acted as a single BPE. The change in frequency influenced on the diameter, the degree of branching, and the propagation rate by altering the diffusion length of charged polymers during electrophoresis. A higher frequency with smaller diffusion length increased the number of generated PEDOT fibres and their network connection by a higher local concentration, while at a lower rate. An extremely high frequency would end up in forming barely any polymer fibres since it needed enough time for building up double layers in a lower concentration of the electrolyte.

3.1.2 Transient Potential Step ECL Experiment

$$A + e^- \rightarrow A^{-\bullet} \quad \text{(reduction at electrode)} \quad (1)$$

$$D - e^- \rightarrow D^{+\bullet} \quad \text{(oxidation at electrode)} \quad (2)$$

$$A^{-\bullet} + D^{+\bullet} \rightarrow {}^1A^* + D \quad \text{(excited state formation)} \quad (3)$$

$${}^1A^* \rightarrow A + h\nu \quad \text{(light emission)} \quad (4)$$

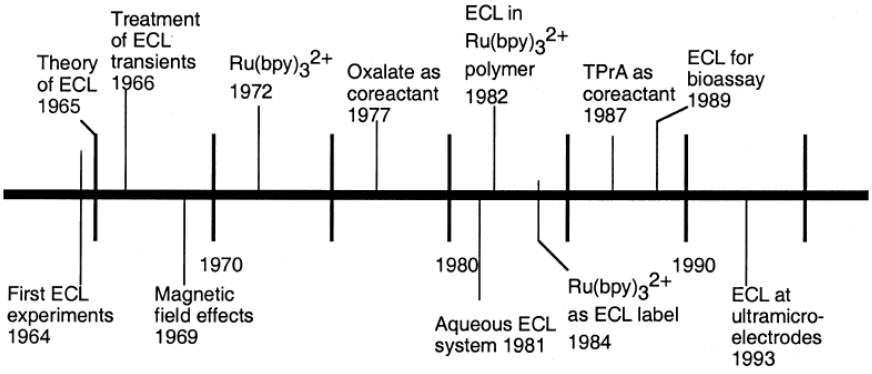

Figure 3.2.Timeline of ECL experiment[140]. Reprinted with permission from [140]. Copyright © (2004) CRC PRESS LLC.

When tracing the history of electrochemiluminescence (ECL), there was no co-reagent involved at the beginning time (Figure 3.2). In a conventional three-electrode system, the ECL is observed on the working electrode by the annihilation between cation radicals and anion radicals. The annihilation generates an excited state of the emission species, and then the emission is produced from the radiative decay of it. At the earliest stage, the cation radicals and anion radicals were generated by cyclic electrochemical steps such as a CV. Hercules was the first to report the production of chemiluminescence by the electrogeneration of the anion and cation radicals of various organic aromatics using AC techniques. Feldberg had derived, using digital computer techniques, theoretical equations which related the ECL intensity to the current, time, and kinetic parameter quantitively in a double potential step mode[141]. In his assumption, the light was produced upon an anion-radical-cation-radical annihilation followed by a very fast radiative decay ($10^8\ s^{-1}$).

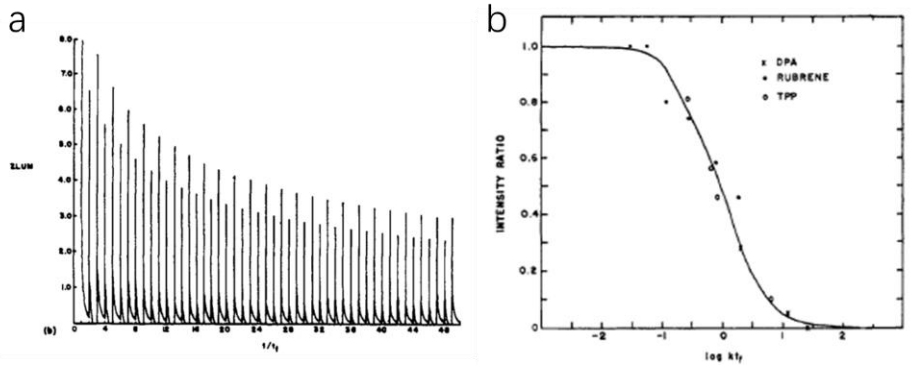

Figure 3.3.(a) Theoretical computer plot of ZLUM versus t/t_f when $kt_f = 0.0$. (b) Theoretical plot of the integrated intensity ratio vs. $\log kt_f$ with experimental fit DPA, rubrene and TPP presented[142]. Adapted with permission from [142]. Copyright © (1969) American Chemical Society.

After that, this method was extended by Bard's group to study the intensity-time profile by passing an AC current through a standard three-electrode cell[142]. Both the cation and anion radicals were generated at the working electrode sequentially, and it then produced the ECL by their annihilation. Theoretical work using computational simulation was carried out by the incorporation of nonradiative decay and self-quenching considering the stability of the radicals, since for most aromatic hydrocarbons either the anion or cation was unstable in the solvents (Figure 3.3(a)). The theoretical intensity matched with the experimental results of diphenylanthracene (DPA), rubrene (R) and other aromatic hydrocarbons in N, N-dimethylformamide solution (Figure 3.3(b)). A linear concentration-intensity relationship was obtained by measuring the peak intensity when adjusting the applied voltage to the limiting region. However, if the applied voltage was too sufficient, the average intensity would decay with time. Under such a voltage, generation of dianion or products from the solvent or the supporting electrolyte could quench the cation radical.

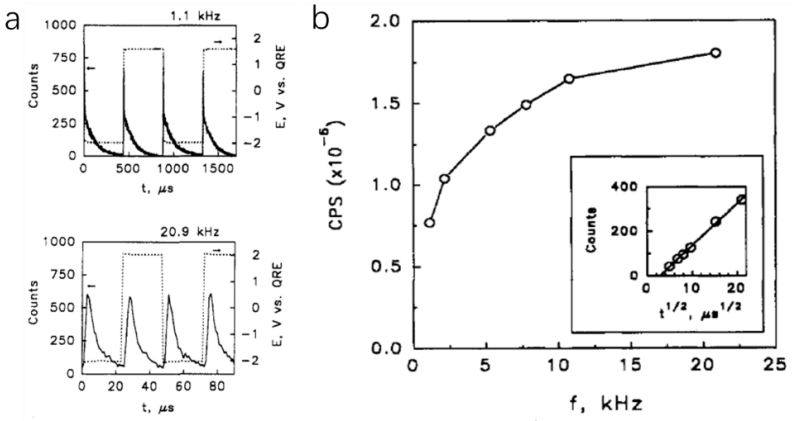

Figure 3.4.(a) The potential waveform with the corresponding ECL curves from 0.6 mM DPA in acetonitrile containing two different frequencies. The luminescence curves were summed 100 times. (b) Frequency dependence of light Intensity during ECL. Inset: integrated light intensity versus square root of step time for 0.6 mM DPA[143]. Adapted with permission from [143]. Copyright © (1993) American Chemical Society.

Since the convenience of generating both anion and cation radials for annihilation, AC technique has been widely applied in fundamental and practical aspects of ECL characteristics. Compared to low frequency, high AC frequency was utilized for the acquisition of thermodynamic and kinetic information from rapid electrochemical reactions, typically involving microelectrodes with reduced effects of double layer capacitance and ohmic drop. Van Duyne measured the rate constant of the annihilation reaction between the radical ions of 9,10-DPA and put a rough upper limit to 10^{10} $M^{-1}s^{-1}$ by employing a triple-potential step at the high frequency without counting the IR drop[144]. Wightman used a multicycle ECL generation under the high frequency at microelectrodes to produce well-defined, stable, and reproducible luminescence curves from non-stable ECL compounds such as DPA, DMA, and PA even with the presence of added water[143]. The electrode was sequentially pulsed between the oxidation and reduction potential to generate cation and anion radicals alternatively. The radicals

reacted in the diffusional layer at a point when the inward and outward fluxes met, followed by subsequent light emission. Even though the light produced per cycle was smaller at a higher frequency, the amount of light produced per unit time was considerably large (Figure 3.4(a)). When the applied frequency increased to 30 kHz, the light intensity declined because of the electrochemical cell time constant. Sufficient time was required to charge the interface to generate the radical ions. The upper-frequency limit before the distortion in the voltammetry or the deterioration of the ECL intensity was greatly increased by about 200 folds compared to the work reported by Bard and co-workers[145] (Figure 3.4(b)). The microelectrode, which could be pulsed 200 to 400 times faster than a conventional-size electrode, possessed greater stability of radicals in the ECL generation.

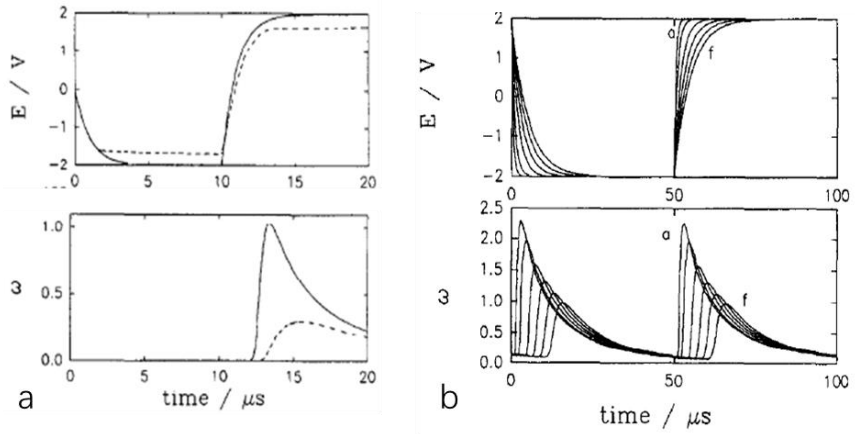

Figure 3.5.(a) Digital simulation of the first cycle of a high-frequency square wave experiment at ultramicroelectrodes on computed electrode potential (E) and dimensionless light intensity (ω). Solid line, S= 7.85×10^{-7} cm^2; dash line, S= 7.85×10^{-5} cm^2. (b) The dependence of E and ω on R_uC_{dl} values. (R_uC_{dl} = 0.5 to 5 μs from a to f)[146]. Adapted with permission from [146]. Copyright © (1995) Elsevier B.V.

The previous simulation works and corresponding experiments discussed by Feldberg and Bard did not account for the double layer charging effect and IR drop in the pulse technique, especially at the high frequency. As pointed out by several authors, the complexities in charging current, time-varying faradaic current, and true potential waveform raise problems in interpreting the experimental results[147]. Wightman addressed the digital simulation of ECL produced by a high-frequency square wave considering the effect of ohmic drop and cell time constant[146]. In the potential waveform, the one with a large surface area showed a smaller final potential than the one with a small surface area (Figure 3.5(a)). The large surface area resulted in a greater faradaic contribution to the IR drop. The greatest distortion of the potential happened when the faradaic current reached their maxima, and this higher IR product near the maximum slowed down the approach to the final potential. The distortion of the potential waveform, as a result, affected the emission responses by shifting the position of the maxima and decreasing its intensity. The cell time constant, R_uC_{dl}, slowed the time of reaching the discharge potential and delayed the faradaic reactions. With R_uC_{dl} changing from 0.5 to 5μs (Figure 3.5(b), a-f), there was a decrease in the light emission with a peak position shift due to the electrochemical

elimination of one of the radicals during the delay caused by the cell time constant. When changing the frequency, R_uC_{dl} became increasingly important. Not only was the delay of the emission peak, but curves with larger λ (dimensionless annihilation constant, $\lambda = kt_sC^*$, k is the rate constant of the second-order annihilation) values were distinguishable from each other.

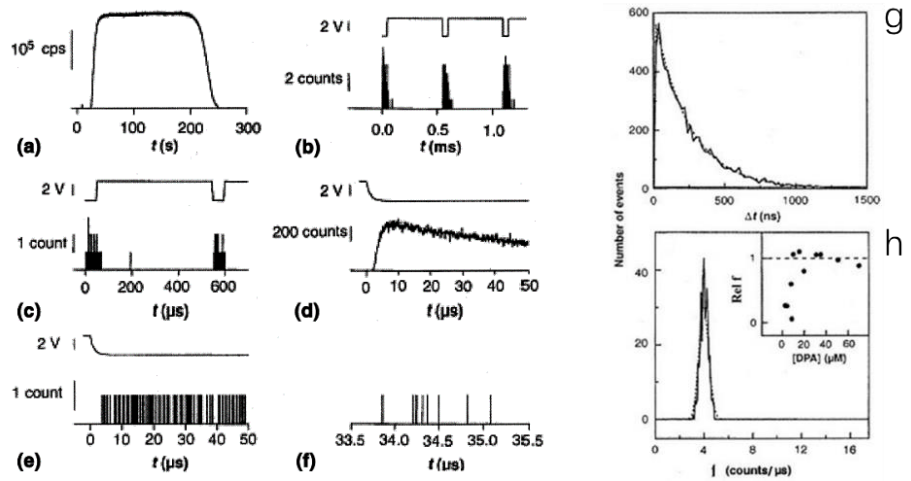

Figure 3.6.(a)-(f): Chemiluminescence from 15 μM DPA in ACN containing 0.1 M $TBAPF_6$. The electrode was pulsed from 1.7 to 2.1 V at 550 μs intervals. Temporal resolution with bin size from 1 s (a) to 1 μs (b), 100 ns [(c) and (d)], and 5 ns [(e) and (f)]. (d) is an ensemble average of events measured during 1000 cathodic pulses. (h) Histogram of interarrival times; (i) Poisson description of the histogram obtained from the photon counts in the last 25μs of 375 cathodic pulses[148]. Reprinted with permission from [148]. Copyright © (1995) American Association for the Advancement of Science.

With the development of ultramicroelectrodes which have significantly reduced double layer capacitance and ohmic drop, the high-frequency pulse techniques enable the study of the kinetics of the electron-transfer reactions and even the observation of individual electron-transfer events. For example, by using these electrodes in low permittivity solvents, the diffusion-controlled kinetics of the ECL processes was investigated[149]. In 1995, the individual electron-transfer event was observed by photon counting with an enough temporal resolution[148]. An unsymmetrical waveform (a 500 μs anodic pulse followed by a 50 μs cathodic pulse) was used. The ECL emission predominantly occurred during the shorter cathodic pulse when the generated radical anions diffused into the sea of the generated DPA radical cations. At the large time interval, there was no evidence for individual reaction events; while with a much better temporal resolution (5ns), the individual photon count from a single chemical reaction between individual DPA radical ions in solution was viewed (Figure 3.6(a)-(f)). A histogram of the time between individual photons was constructed, and it showed an exponential decay of which the frequency f was in excellent agreement with the mean rate of photon arrival obtained by the averaging data ensemble (Figure 3.6(g)). Also, a Poisson distribution was obtained from the photon counts in the last 25 μs of 375 cathodic pulses, giving a similar f value which was a function of the generation rate, radical ions diffusion, the rate of annihilation, the efficiency of light emission, and photon collection efficiency (Figure 3.6(h)).

In another ECL experiment in a similar scenario to the SECM, a high-frequency AC square wave was tried to ECL-image the microelectrodes with dimensions in the micrometer range by employing the DPA in a high concentration (>25 mM) with BN radical anions as co-reactant[150]. The lateral resolution was controlled by rapid potential pulses (1 kHz) that maintained the reaction zone in close proximity to the electrode. The obtained image revealed an electrode area with quite a different topography compared to that inferred from steady-state cyclic voltammograms.

3.2 Experimental Section

3.2.1 Regents

Tris(2,2′-bipyridyl) dichlororuthenium (II) hexahydrate ($Ru(bpy)_3Cl_2 \cdot 6H_2O$) (99.95%, Sigma-Aldrich), Potassium ferricyanide (III) (99%), Sodium perchlorate monohydrate (≥99.0%, Fluka), Sodium oxalate,(≥ 99.5%,Alfa Aesar), Sodium phosphate monobasic (≥99.0%, Fisher Scientific), Sodium phosphate, Dibasic, anhydrous (≥99.0%, EMD), Methylene Blue (>98.5%, TCI), HEPEs (>99.5%, Sigma-Aldrich).

All solutions were prepared using deionized, ultrafiltered water generated from the milli-Q Gradient water purification system (Millipore). All reagents were used as received without further purification.

Oligonucleotides were obtained from Integrated DNA Technologies (IDT; Coralville, Iowa), with purity and yield confirmed by standard desalting and ESI-MS, respectively. Methylene blue-conjugated DNA (MB-DNA) was purchased from Biosearch Technologies (Novato, CA), purified by RP-HPLC. These sequences were designed and optimized by the nucleic acid package web server (NUPACK), computationally.

Sequences of DNA strands used in the experiments are given in Table 3.1.

Name	Abbreviation	DNA sequence, list from 5' to 3'
Thiolated-DNA (40 bases)	T-DNA (40)	/5ThioMC6-D/GCA TGG TGA CAT TTT TCG TTC GTT AGG GTT CAA ATC CGC G
No-Methylene-DNA (10 base pair match)	No MB-DNA (10)	CCA CCC TCC TCC TTT TCC TAT CTC TCC CTC GTC ACC ATG C

No-Methylene-DNA (40 base pair match)	No MB-DNA (40)	CGC GGA TTT GAA CCC TAA CGA ACG AAA AAT GTC ACC ATG C
Methylene-DNA (10 base pair match)	MB-DNA (10)	CCA CCC TCC TCC TTT TCC TAT CTC TCC CTC GTC ACC ATG C /MB-C7/
Methylene-DNA (40 base pair match)	MB-DNA (40)	CGC GGA TTT GAA CCC TAA CGA ACG AAA AAT GTC ACC ATG C /MB-C7/
ECPA-Loop	Loop	TAG GAA AAG GAG GAG GGT GGC CCA CTT AAA CCT CAA TCC ACC CAC TTA AAC CTC AAT CCA CGC GGA TTT GAA CCC TAA CG

Abbreviations: /MB-C7/ = methylene blue modification (Biosearch), /5ThioMC6-D/ = disulfide bond flanked by two six-carbon spacers (IDT).

Table 3.1.Single-stranded DNA sequences used in the AC square wave bipolar ECL system.

3.2.2 Preparation of the AC Bipolar ECL Cell

The electrode design for the AC bipolar ECL cell was fabricated by the printed circuit board (PCB) lithographic method. In the early procedure, a piece of CD (Memorex 52X Pro Gold Archival CDR) was cut off, and the protective layer was removed by putting it in concentrated nitric acid followed by rinsing with distilled water thoroughly[151-155]. Electrode design for two driving electrodes (dimension: 13 mm × 10 mm) and a bipolar electrode (dimension: 18 mm × 5 mm) were drawn using Adobe Illustrator© and then printed on a PCB circuit board thermal transfer paper by a standard printer. This pattern was transferred to the CD piece by using a thermal laminator until all the electrodes region were covered with the black ink. In the late procedure, the gold-coated slide (Dimensions: 1" x 3" x 1.1 mm, Cr/Au Thickness: ~5 nm/100 nm, Deposition Research Lab, Inc) was used instead. A more controllable photolithography method was employed by using the photosensitive dry film (INSMA). One side of the protective layers of the film was peeled of firstly. The exposed film side was carefully pressed on the clean gold substrate surface in a rolling motion to expel all the bubbles. Then it was sent into the thermal laminator repetitively for strong adhesion. New electrode design for the bipolar cell with modification was still conducted on Adobe Illustrator© but in an inversed pattern. The electrode design was left blank while the all the areas needed to be etched out, were painted in black color. In addition to the old driving

and bipolar electrodes pattern, a central strip vertical to the old BPE in the middle with 32 mm × 6 mm in size was incorporated. As a result, the resulting central part would be cross-shaped with one strip laterally as the BPE and the other strip vertically as the electric contact region for electrochemical characterization. This pattern was ink-printed on a transparency film paper (Hewlett Packard) and cut off as the photomask for photolithography. This photosensitive film coated gold substrate was then exposed to an in-house built UV source made by 365 nm LEDs for 60 s with this tightly aligned photomask above. After the exposure, the photosensitive film of the exposed region changed to dark purple. By developing it in 0.1 M Na_2CO_4, the photosensitive of the unexposed region would be washed out followed by removing the protective layer on the other side. In both the early and late procedures, according to the wet chemical method, the exposed gold on the substrate was etched out by potassium iodide-iodine (KI: I_2: H_2O = 4:1:20) solution for 2 min. Chromium etching solution was subsequently used for 30 s to remove the chromium adhesion layer to prevent short circuit. After the etching, the ink was removed by ethanol and the remaining photosensitive film protecting the electrode was removed by 0.1 M NaOH. In each step, the slide was thoroughly washed with distilled water. In the late procedure, the vertical strip extruded out of the framework of the cell and could be wrapped with copper tape as the connection to perform the electrochemistry instead of making a connection to the half BPE in the reporting compartment. Both the working and driving electrodes were cleaned by cycling them in 0.5 M H_2SO_4 from -150 mV to 1400 mV for 30 cycles at a scan rate of 100 mV/s.

A closed cell framework with two compartments configuration for the AC square wave ECL bipolar cell was fabricated using the 3D printer (MakerBot Replicator 2). It was modeled by Sketch Up © (Trimble Navigation Limited) and then printed from the non-conductive polylactic acid filament (PLA, 1.75 mm diameter). The cell was separated into two parts, sensing compartment and reporting compartment, with 19×14 mm in lateral size, 8 mm in height and 3 mm in thickness. After printing, the bottom side of the 3D printed framework was polished with a sand paper until the surface was flat and smooth, Small amount of epoxy (30 min slow-cure, bsi) was applied on it, which was then gently placed onto the patterned gold substrate. Once the epoxy had set, electric connection to the driving electrodes was accomplished by wrapping the gold surface outside the framework with copper tape (3M™, Ted Pella).

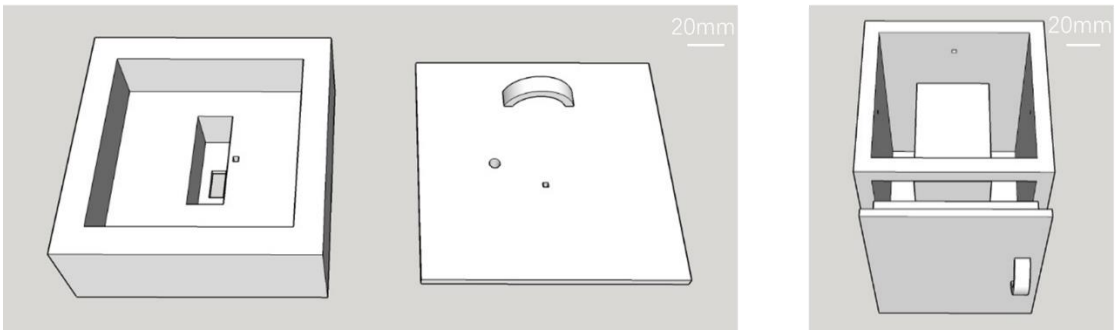

Figure 3.7.3D model of the ECL measuring chamber. Left: Upper room for PMT installation. Right: Lower cell room for the bipolar cell.

A dark room environment was created by designing an ECL measuring chamber with two rooms carefully modeled and printed by the 3D printing technique (Figure 3.7). The upper measuring room (130 mm × 130 mm × 60 mm) had a groove for the photomultiplier tube (PMT, HC-120-05, HAMAMATSU, PhotoSensor Modules) PMT installation. This groove was precisely designed in order to align the PMT detection window (4.0 mm × 13.0 mm) collinearly just on top of an entrance slit (8.0 mm × 17.0 mm), which was larger than the detection window at the bottom of the upper room. A cover lid with a handle was also printed. The lower cell room (100 mm ×100 mm ×180 mm) consisted of a hollow cuboid body and a side door. It was open at the top to fit with the upper room. The bipolar cell was carefully fixed on top of the printed support so that the half bipolar electrode in the reporting compartment was just in front of the PMT detection window to maximize the light collecting efficiency. All the parts of the ECL measurement chamber were fit snugly together and isolated from the ambient light. Several 1.0 mm × 1.0 mm grids were left at the walls of the measuring chamber for wire connections to the bipolar cell. A round hole (6 mm in diameter) was kept at the top of the cover lid reserved for the coaxial cable of the PMT input and output. Every crevice from the conjunctions and holes for electric wire access as wrapped with black tape. The entire measurement chamber was then covered with black cloth. It was placed into a hand-made glove box after ventilating with nitrogen gas for at least 30 min to avoid the interference from air.

Square wave excitation to the bipolar ECL system was applied by a waveform generator (Direct Digital Synthesis (DDS) Function, ATF20B, ATTEN). The applied voltage waveform on the driving electrode was monitored by either a two-channel handheld oscilloscope (DSO8060, Hantek) or a multifunction data acquisition system (DAQ, USB-6002, National Instruments) for data collection for a large number of cycles. The ECL optical response which would be emitted from the half bipolar electrode in the reporting compartment as collected by the PMT (supply voltage: 15 V, amplification voltage: 0.8 V). By connecting the signal out terminal to the other channel of the same oscilloscope or the DAQ device, the amplified analog voltage output corresponding to the ECL emission spectra was recorded simultaneously in a reference single-ended (RSE) mode. For the oscilloscope, the collected data was stored onto the computer in .EXL document. In the DAQ device, simultaneous multichannel data

acquisition was regulated and synchronized through an in-house written LabVIEW (National Instruments™) program on a computer. Different sampling rates (1000/s or 10000/s) were adjusted for ECL response of DNA monolayer at different AC frequency to achieve reasonable temporal resolution. Data arrays were written out in .EXL document. For data generated a huge number of AC cycles, one-one point addition strategy was utilized to avoid tedious data processing: Each data point of the ECL intensity with the same time-mapping in all the AC cycles was algebraically added together. Finally, collected data from many cycles could be simplified and converged to only one integral AC cycle. To prepare calibration curves and calculate standard deviations, ECL intensities were analyzed by Origin 8 with baseline correction, in a specific time domain integration.

3.2.3 Electric Field Measurement

Two small gold probes (4 mm in length and 1 mm in width), which were fabricated by a new photolithography mask design, are etched out together with the previous design. They were extruded inside the cell, perpendicular to the length of the BPE. They both had an outer area with 4.5 mm × 4 mm in size outside the cell, used as the connection region to a recording device. Each probe tip was aligned in the same horizontal position with either end of the BPE. As a result, the solution potential difference measured between the two probes was the same as the driving potential on the BPEs. A secondary DAQ deck was used solitarily to measure the solution potential difference. Synchronized multichannel data acquisition was compiled by the Labview (National Instruments™) visual programming language.

3.2.4 Methylene Blue (MB) Electropolymerization

Methylene blue (MB) was electropolymerized using a bipotentiostat/galvanostat (WaveDriver 20, Pine) with standard three-electrode configuration. It consisted of a Ag|AgCl(s)|KCl(1M) reference electrode (CH Instrument, Inc.), a platinum wire counter electrode (CH Instrument, Inc.), and a gold working electrode, which was in practice the standard gold electrode or the half gold bipolar electrode in the sensing compartment. The solution for electropolymerization contained different concentrations of MB monomer and 0.1 M KCl dissolved in 0.1 M phosphate buffer (PBS buffer, pH=7). After it was added to the sensing compartment, MB was electrochemically polymerized by cycling the bipolar electrode between -0.35 to 1.45 V at a scan rate of 50 mV/s. The polymer growth was controlled by the MB monomer concentration and numbers of deposition cycles. After electropolymerization, the electrode was through rinsed by 0.1 M PBS buffer to remove any monomeric MB.

3.2.5 Preparation of DNA Monolayer Assembly

Before the immobilization of DNA monolayer on the bipolar electrode, 2 µL of 100 µM thiolated DNA (T-DNA) was mixed with 2 µL 10 mM TCEP in a 1000 µL microcentrifuge tube. This tube was incubated for 90 min in the dark condition at room temperature for the reduction of disulfide bonds on the T-DNA. Then the solution was diluted to a total volume of 100 µL in HEPEs/$NaClO_4$ buffer (10 mM HEPES and 0.5 M $NaClO_4$, pH 7.0), to a final concentration of 2 µM reduced T-DNA. For the immobilization, the diluted T-DNA solution was dropped on top of the half gold bipolar electrode in the sensing compartment and covered all the surface area. It was incubated for at least 4 hours at room temperature in the dark. Self-assembled monolayer for the capture DNA was formed during this process by creating Au-S bonds between the DNA and electrode surface, and excess T-DNA and TCEP were washed away using HEPEs buffer at least 5 times. For blocking the nonspecific adsorption and reducing capacitance contribution from ions accessing to electrode surface through pin holes between individual T-DNA strands, 3 mM 6-mercaptohexanol solution was employed to immerse the modified half bipolar electrode for 60 min at room temperature in the dark followed by the same rinsing step. In a typical DNA assembly hybridization, 1 µL 100 µM secondary DNA (MB-DNA or No MB-DNA) was diluted in HEPEs buffer to a total volume of 100 µL, with a final concentration of 1 µM. This dilute MB-DNA solution was dropped onto the previous T-DNA modified half bipolar electrode. It was incubated in the dark at room temperature for a certain amount of time for the double-stranded DNA hybridization or no-match control groups. In the MB-DNA replacement test, after the ECL experiment of BPE hybridized with No-MB-DNA (10), 100 µL 1 µM MB-DNA (40) was added directly onto the same bipolar electrode for 2 hours and ready for the next ECL experiment as a comparison. To produce MB-DNA monolayer calibration curve, different molar ratios (1:9, 3:7, 5:5, 7:3, 9:1, etc.) of MB-DNA (40) and No MB-DNA (40) were mixed together in a total concentration of 1 µM to create the DNA monolayer with varying amount of MB-DNA. In the study of DNA loop as the ECPA model, after the incubation of MB-DNA (10), the BPE was then added with DNA loop which is 10 base pair match to the T-DNA (40) in varying concentrations with different incubation times. At all the hybridizations, the sensing compartment was rinsed and filled with 1mL HEPEs buffer for the ECL sensing experiment.

3.2.6 Electrochemical Measurements

Electrochemical measurements were performed using the same bipotentiostat with three-electrode configuration. All potentials are reported relative to the Ag|AgCl(s)|KCl(1M) reference electrode. Square Wave Voltammetry (SWV) for polymerized MB thin film and hybridized No-MB-DNA and MB-DNA was performed in 0.1 M PBS buffer or HEPEs buffer with a 50 mV amplitude signal at a frequency of 60 Hz, over the range from 0.20 to −0.45 V versus Ag|AgCl reference. The characteristic voltammetric peak of MB was detected by SWV at −210 mV (vs. Ag/AgCl). Cyclic voltammetry was

also performed by scanning the bipolar electrode between 0.20 to -0.45 V vs Ag|AgCl reference electrode at a rate of 50 mV/s, as a reference to quantify the surface density of MB-DNA hybridized by the integrated charge Q.

3.3 Results and Discussion

3.3.1 Preliminary Open AC Bipolar ECL Cell

The AC square wave excitation of ECL emission under bipolar electrochemistry was initiated by placing a rectangular gold foil strip in an open petri-dish with two bigger gold foils serving as the driving electrodes on both sides. 5 mM $Ru(bpy)_3Cl_2$ ECL solution with 25 mM $Na_2C_2O_4$ as the co-reagent in pH=7 PBS buffer was filled into the cell. CCD camera (Nikon, D510) was operated under a dark room condition to collect the ECL signal under an exposure time of 30 s.

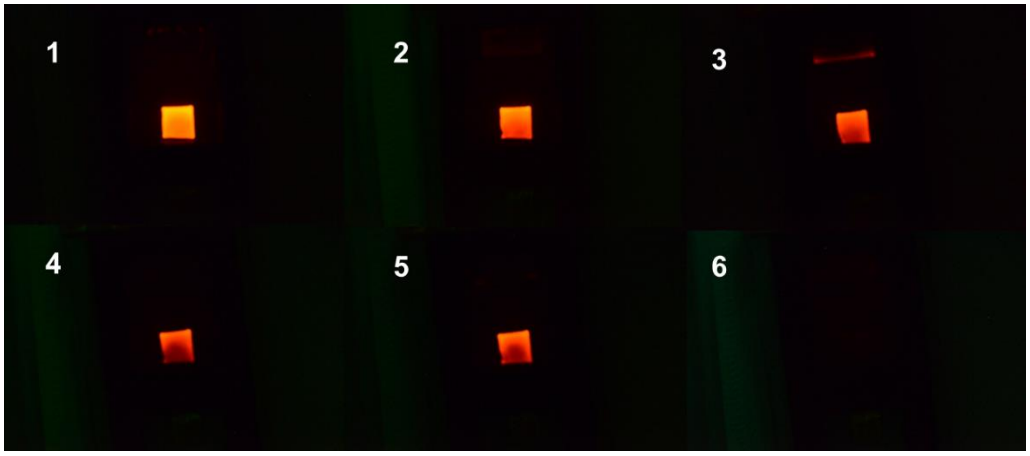

Figure 3.8.Images of ECL emission on rectangular gold foil strip in an open cell under AC square wave at 10.7 V at a frequency of 10 mHz, 500 mHz, 1 Hz, 2 Hz, 3 Hz, and 4 Hz (from 1-6) at an exposure time of 30 s.The DDS function waveform generator (ATF20B, ATTEN) was used to generate a square wave excitation as the AC power supply. 10.7 V in a symmetric square waveform was applied to the bipolar cell at different AC frequency. As shown in Figure 3.8, the lowest frequency exhibits the largest ECL intensity. While as the frequency increases, the ECL signal declines. No ECL emission could be captured by the CCD camera after 4 Hz.

3.3.2 Closed AC Bipolar ECL Cell

Driven by the goal of detecting the monolayer level of analyte, the commercially-available CCD camera with low sensitivity and high noise background needs be replaced. Instead, a photomultiplier tube (PMT), which had a much lower detection limit and the real-time analog or digital output should be employed as the ECL monitoring devices in the following experiment. HC-120-05 PhotoSensor Modules (HAMAMATSU) which integrated a side-on photomultiplier tube (PMT), high voltage supply and buffer amplifier in a compact unit with spectral range from 185 to 900nm was used. The higher

external voltage usually needed to power the PMT is avoided by 10 stage voltage multiplier and feedback regulator. The anode signal is amplified by a transimpdance amplifier having a conversion factor of 1 vol per microamp. 15 V as the supply voltage and 0.8 V as the amplification voltage were both provided by a multi-power supply. By incorporating such a PMT as the detecting device, a closed BPE ECL system was then fabricated as described in the early procedure in the cell preparation.

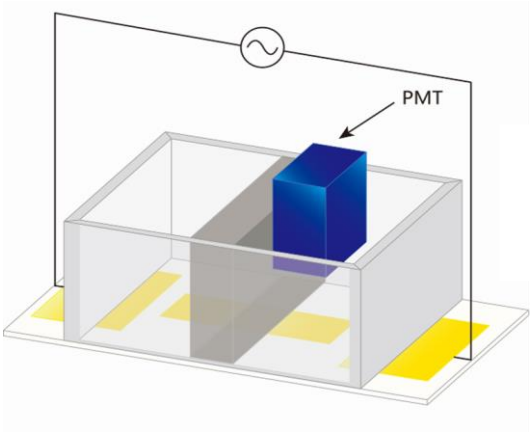

Scheme 3.1.The illustration of AC square wave bipolar ECL cell.

In the presence of a sufficiently large electric field gradient provided by an external power supply across the bipolar system, cathodic and anodic faradaic processes can be induced on the opposite sides of the BPE in the absence a direct ohmic contact. ECL, which can quantify the current flowing through the BPE, enables its amperometric detection. The limitations of this approach are the depletion of the analyte in the case of a diffusion-controlled process or the single-use nature of a very small amount of analyte in a surface-limited reaction. One innovative way to overcome these limitations is to use a time-dependent potential program in which the reaction of interest is quantified in the first half cycle, and the analyte is regenerated in the second half cycle. The simplest implementation of this concept involves the use of a square wave potential program. Scheme 3.1 is the illustration of an AC square wave bipolar ECL cell fabricated by the procedures of photolithography and 3D printing. Two driving electrodes are at each side, and a bipolar electrode is in the middle. The 3D printed cell framework is placed on top of the substrate and divides the bipolar electrode into two physically separated compartments. The sensing compartment (on the left) and the reporting compartment (on the right) are only electrically connected through the BPE. The planar electrodes shown on the outside of the framework are used for external electrical contacts to the AC generator. The photomultiplier tube (PMT) is aligned above the bipolar electrode in the reporting compartment to enable efficient collection of ECL. In a closed bipolar system, the single current pathway of the BPE ensures the electron transfer from the driving electrodes to be electrically coupled to the reaction occurring at the BPE without a massive generation of interfering species, which could alter the performance of this system by changing the active species and pH[87]. This configuration also minimizes the voltage required to drive the system with fewer voltage losses on the driving electrode interface and in the solution. Different from an open system with an interfacial

potential gradient across the BPE, here on each half BPE surface, the interfacial potential is necessarily the same with simplified reaction kinetics. The reporting compartment is filled with the degassed ECL solution, consisting of 0.5 mM $Ru(bpy)_3^{2+}$ and 2.5 mM $Na_2C_2O_4$ as the co-reagent in 0.1 M phosphate buffer (PBS buffer, pH=7), while the sensing compartment contains the analyte in a different environment under the phase separation. The two compartments are designed with enough reservoir sizes to reduce the ohmic drop and facilitate the co-reagent supplement for ECL.

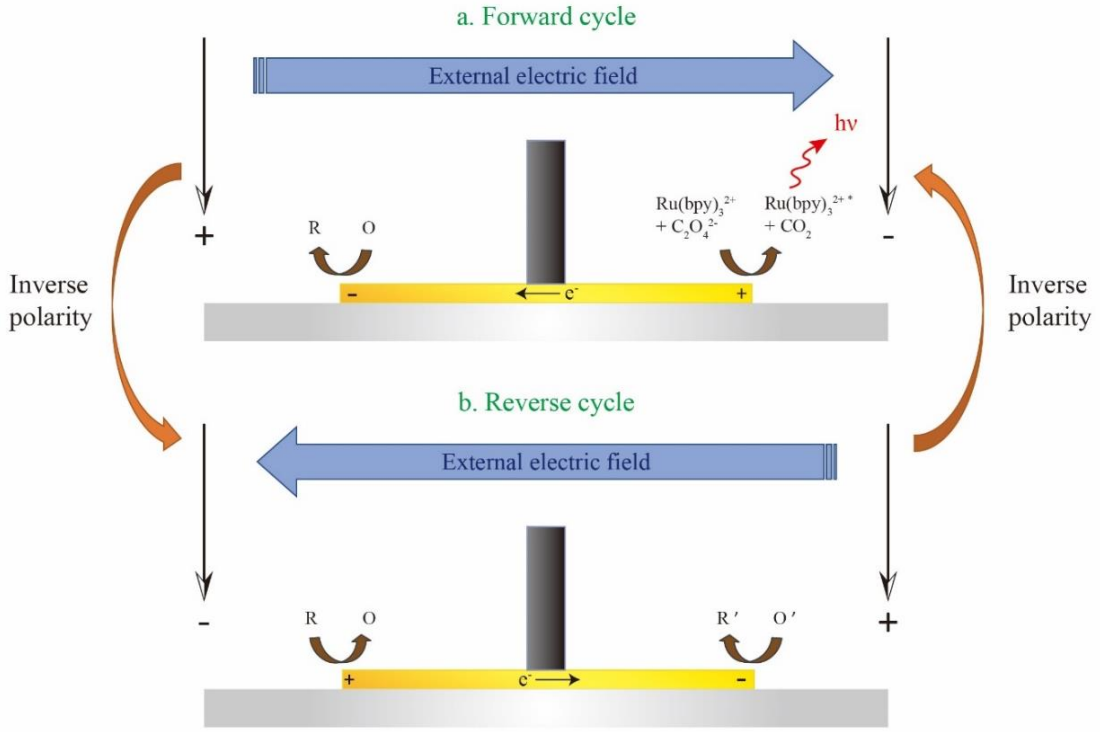

Scheme 3.2.The basic working principle of the AC square wave bipolar ECL system.

As we said, the critical disadvantage of DC BPE system is the single-use nature of the analyte, especially for a surface-limited reaction with a quite small current that flows through the BPE. The AC square wave technique allows us to signal-average over multiple cycles to improve the S/N and lower down the detection limit via a regeneration methodology. Scheme 3.2 illustrates the operating principle of this bipolar ECL system. The sensing compartment (left) and reporting compartment (right) are physically separated by the barrier with only an electrical pathway through the planar bipolar electrode underneath. On the application of the AC voltage, a square wave alternating in polarity of designated frequency is generated between driving electrodes, creating an inverted external electric field back and forth across the bipolar cell. Taking one complete AC cycle as an example, a positive potential is applied in the first half cycle (forward half cycle) as shown in Scheme 3.2(a). Once the potential reaches a critical value, four faradaic reactions are occurring at both the bipolar electrode and driving electrodes simultaneously. The reduction of analyte molecule occurring at the bipolar cathode in the sensing compartment is accompanied by the oxidation of $Ru(bpy)_3^{2+}$ to $Ru(bpy)_3^{3+}$, generating the ECL emission at the bipolar anode in the reporting compartment. Meanwhile, the reaction occurring at the driving electrodes should

be hydrogen evolution and water oxidation with same faradic current flow[49]. In the next half cycle (reverse half cycle), upon the inverse of polarity, a negative voltage is applied as shown in Scheme 3.2(b). Because of the reversed electric field, an interconversion of anode and cathode occurs on the bipolar electrode, the oxidation takes place at the BPE end in the sensing compartment, and the reduction takes place at the BPE end in the reporting compartment, on the contrary to the previous half cycle. If the analyte molecule is reversible, it would be oxidized backward to the starting analyte in the reverse half cycle. It is more prominent to the surface redox-active molecules compared to the dissolved analyte because no diffusion is involved. The molecules on the surface regenerated after the completion of one AC cycle could re-emit the ECL signal for detection in the next cycle. As a consequence, these molecules undergo repeatable redox cycling and generate successive ECL responses. Those responses could be accumulated for the detecting molecules in ultralow concentration and even monolayer. Note that the closed bipolar design is specifically important to the AC bipolar ECL experiment. Apart from the forward half cycle, which emits photons corresponding to the sensing reaction of the analyte, the reverse cycle with sufficient applied voltage would also generate ECL on the driving electrode in the reporting compartment. An open system with parallel bypass current could cause a much larger ECL emission from the driving electrode, overriding the useful ECL response from the forward half cycle.

3.3.3 Investigation of Potassium Ferricyanide as the Dissolved Species in Solution

In this section, potassium ferricyanide was used as a dissolved redox reversible analyte in solution to validify the behavior of the AC square wave bipolar ECL sensing platform. $Fe(CN)_6^{3-}$ was added into the sensing compartment at different concentrations in 0.1 M $NaClO_4$ (pH=7). AC symmetric square wave was applied to this bipolar ECL cell. In accordance with the basic reaction scheme described previously, during the forward half cycle when a positive potential is applied, reduction of $Fe(CN)_6^{3-}$ to $Fe(CN)_6^{4-}$ at one end of the BPE in the sensing compartment is accompanied by a complementary ECL emission at the other end of the BPE in the reporting compartment. During the second half cycle, a negative voltage is applied, the anode and the cathode poles are thus reversed with no ECL emission. Even though the electrochemical-generated $Fe(CN)_6^{4-}$ may possess an opportunity to diffuse away in the sensing compartment, the AC-driven voltage allows $Fe(CN)_6^{4-}$ to be oxidized backward to the original $Fe(CN)_6^{3-}$ on the same end of BPE during the reverse half cycle, leading to a cyclic renewal of the diffusion layer. In this section, the applied voltage waveform on the driving electrode was monitored by a two-channel handheld oscilloscope connected to the generator through the channel 2 (CH2). The PMT collected the ECL optical response which would be emitted from the half bipolar electrode in the reporting compartment. By connecting its signal out terminal to the channel 1 (CH1) of the same oscilloscope, the amplified analog voltage output corresponding to the ECL emission spectra was recorded simultaneously.

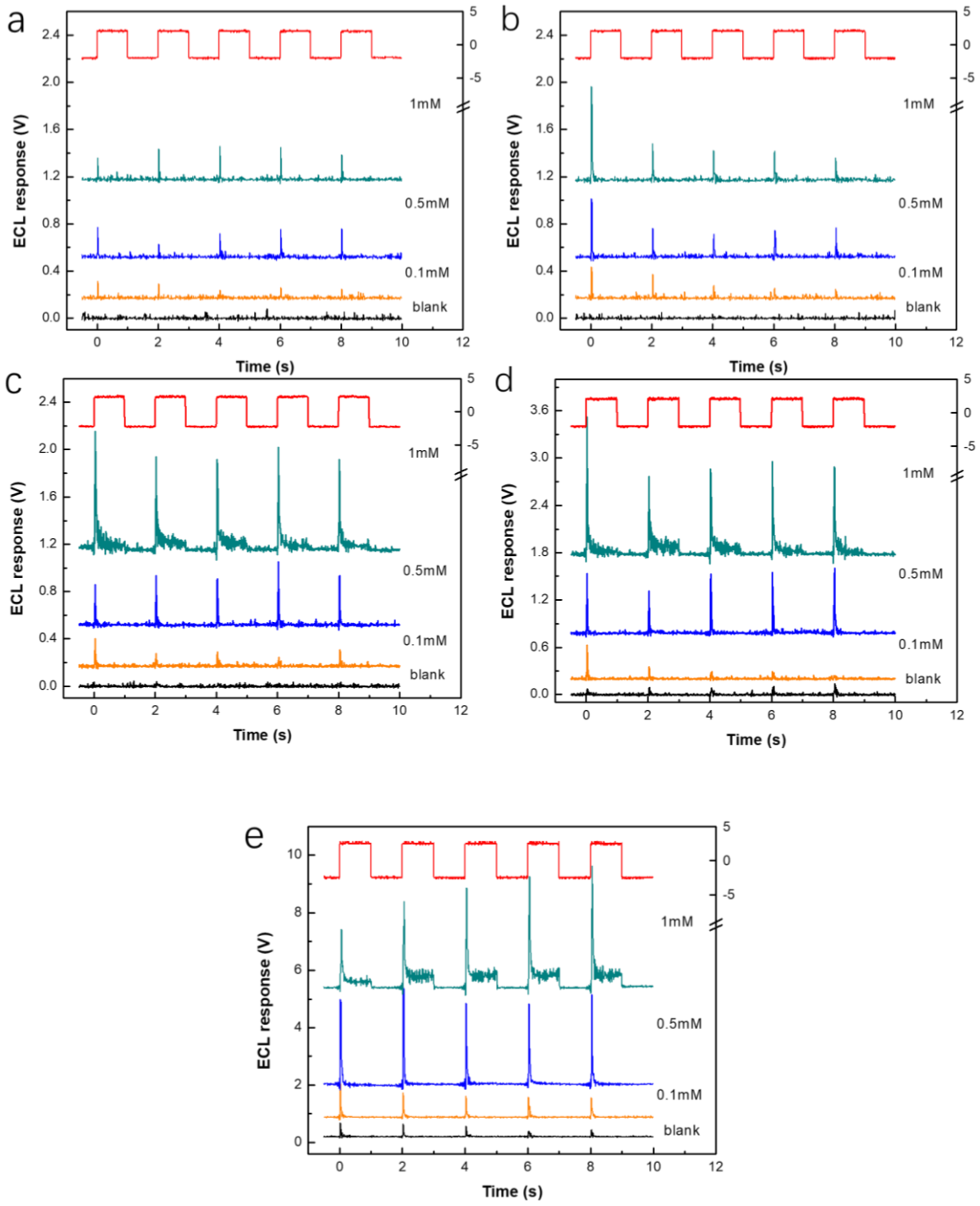

Figure 3.9.Real-time ECL response in AC square wave bipolar ECL cell of blank control (0.1 M $NaClO_4$), 0.1 mM, 0.5 mM, and 1 mM $K_3Fe(CN)_6$ at symmetric wave of (a) 4.5 V, (b) 4.7 V, (c) 5.0 V, (d) 5.2 V and (e) 5.5 V.

After a series of preliminary tests, a complete ECL behavior study on the diffusion-related electro-active species, ferricyanide in solution, was carefully investigated. Figure 3.9.(a) to (e) show the typical real-time ECL responses measured by the PMT and corresponding synchronized applied square voltage profile as a function of time with a demonstration of 5 cycles collected by the oscilloscope. A symmetrical square wave with a peak to peak magnitude of 4.5, 4.7, 5.0, 5.2, and 5.5 V was applied to

the same bipolar cell with $K_3Fe(CN)_6$ concentration ranging from 0 to 1 mM in 0.1 M $NaClO_4$ in the sensing compartment. The ECL responses of the blank control (0.1 M $NaClO_4$), 0.1 mM, 0.5 mM, and 1 mM $K_3Fe(CN)_6$ are demonstrated in black, orange, blue and dark green with an adapted offset for simultaneous comparison. The synchronized square waveform is plotted in red color at the top using a secondary vertical coordinate at the right. Taking (c) at 5.0 V as an example, the control experiment using only 0.1 M $NaClO_4$ exhibits background ECL emission on the reporting half BPE. Under these conditions, no redox reaction could occur in this closed BPE cell to trigger ECL in the absence of $Fe(CN)_6^{3-}$. On the contrary, when $Fe(CN)_6^{3-}$ is added into the sensing compartment, ECL emission coming from $Ru(bpy)_3^{2+}$ oxidation appears during the forward half cycle and recovers to the baseline level when the potential reverses to negative. A higher concentration of $Fe(CN)_6^{3-}$ analyte results in more intense ECL emission at the same voltage. When comparing (a) to (e), as the AC square wave voltage increases from 4.5 to 5.5 V, the ECL peak height for the same concentration of $Fe(CN)_6^{3-}$ shows a significant increase by a larger driving force. At 5.2 V, the background control of pure electrolyte of 0.1 M $NaClO_4$ also exhibits observable ECL peaks in the forward half cycle, indicating the participation of H_2 evolution as an interfering ECL signal. At 5.5 V, the phenomenon is more severe, telling that the potential must be controlled under careful attention.

The ECL signal corresponding to the reduction of $Fe(CN)_6^{3-}$ in each forward half cycle always shows a big spike at the beginning and then decreases exponentially during the time domain. According to our assumption, it should relate to the Cottrell behavior that describes the depletion of the diffusion-related electroactive species near the electrode surface. A simple electrochemical current simulation was operated to confirm this assumption. In our closed bipolar system, the potential along the whole half BPE could be essentially treated as the same without consideration of the potential gradient. According to the Cottrell equation for a planar electrode,

$$i = \frac{nFA{D_O}^{1/2}C_O^*}{\pi^{1/2}t^{1/2}}$$

where i is the current in unit A, n is the number of electrons transferred per molecule, F is Faraday constant, 96485 C/mol, A is the area of the planar electrode in cm^2. C_O^* is the initial concentration of electroactive species in mol/cm^3, D_O is the diffusion coefficient for the species in cm^2/s, and t is time in second. In our experiment, the surface area of half BPE is $0.35 \times 0.6 = 0.21$ cm^2 and the diffusion coefficient of $Fe(CN)_6^{3-}$ is 7.60×10^{-6} cm^2/s.

Note that the ECL response does not appear at precisely the same time as the application of the voltage waveform from the generator. Some instrumental and experimental limitations are present due to (1) the potentiostatic limitation: depending on its current and voltage output characteristics; (2) recording device limitation: during the initial part of the current transient, the recording device such as

oscilloscope as a transient recorder may be overdriven, and some time is required for the recovery of the accurate reading; (3) limitation imposed by R_u and C_d: the applied potential is always taken by the nonfaradaic charging which has an exponentially decay following the cell time constant R_uC_{dl} (where R_u is the uncompensated resistance in the cell, and C_{dl} is the double-layer capacitance on the driving electrodes) first before the faradaic process. Moreover, the reactions on BPE also require the charging of the double layer to establishes a change in overpotential. Other than this limitation, the necessary reaction mechanisms involving with co-reagent and the excited state annihilation will also retard the time a little bit for the ECL emission. For all these reasons, A time correction of the ECL delay after the excitation of the square wave was made by offsetting the initial time of ECL response about -0.02 s.

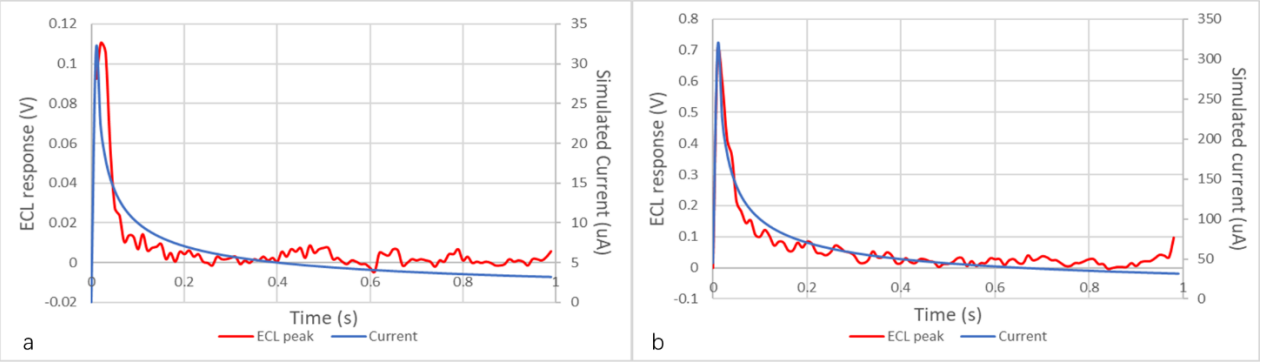

Figure 3.10.ECL peak and corresponding Cottrell current simulation in a single forward cycle for (a) 0.1 mM $K_3Fe(CN)_6$. (b) 1 mM $K_3Fe(CN)_6$ at 5.0 V. The ECL peak was smoothed by 5 points averaging.

After the time correction, the current was simulated by the Cottrell equation and fitted with ECL peak in an individual forward half cycle. The left vertical axis is the ECL response in V, and the right axis is the simulated current in μA. Figure 3.10 compares the current simulations of $K_3Fe(CN)_6$ in 0.1 mM and 1 mM with their ECL peaks. In each plot, the ECL response is shown to follow a similar diffusion-related Cottrell behavior as the simulated current.

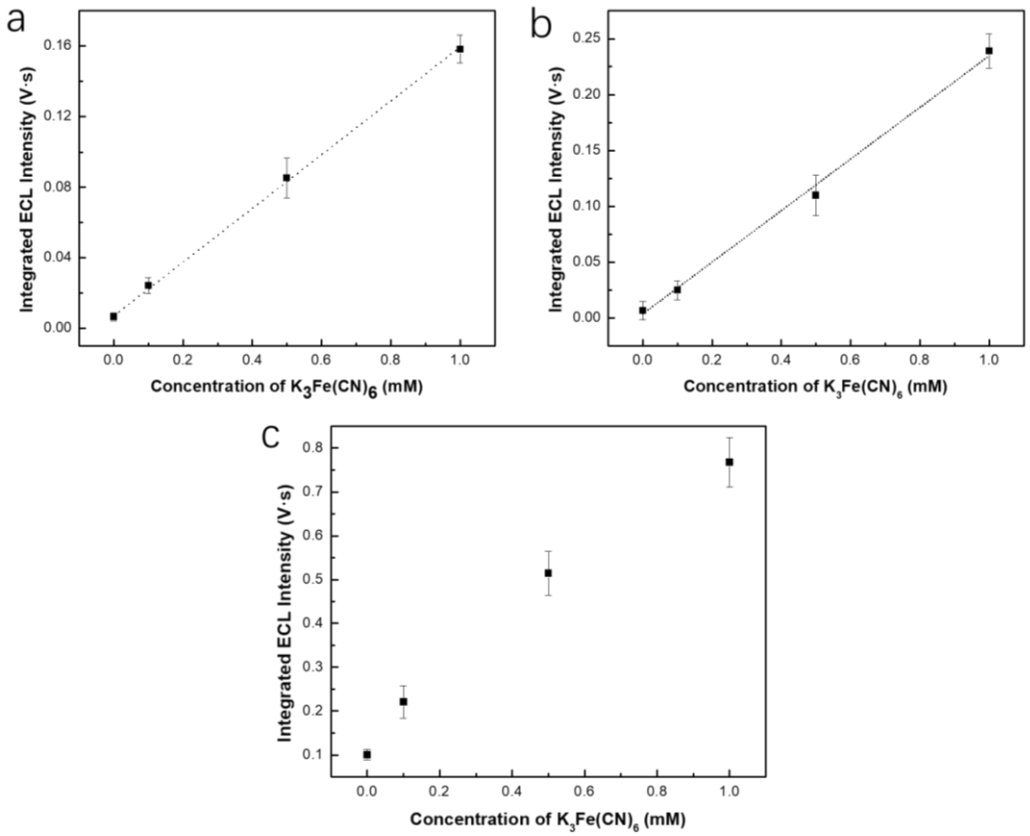

Figure 3.11.Calibration plot of integrated ECL intensity as a function of $K_3Fe(CN)_6$ concentration of 5 AC square wave cycles. (a) at 5.0 V (d) at 5.2 V (e) at 5.5 V. Error bar represents the standard deviation of three independent runs.

The calibration plot was made by integrating the ECL signal of 5 complete cycles as a function of the $Fe(CN)_6^{3-}$ concentration (Figure 3.11). In each cycle, the time interval for integration is the starting 0.2 s in the forward half cycle. At 4.5 V and 4.7 V, the integrated ECL intensity is proportional to the concentration while not in good linearity, because of such a low driving force which endows more kinetics limitation. In Figure 3.11(a) at 5.0 V, A linear relationship is obtained with excellent stability and reproducibility, convincing the feasibility of utilizing this AC closed bipolar ECL cell for the analyte detection. As the applied voltage increases to 5.2 V, the slope of the intensity-concentration curve also becomes steeper, indicating a larger driving force for the ECL reaction (Figure 3.11(b)). While increasing the voltage to 5.5 V, it is no longer linear because of the participation of a strong H_2 evolution (Figure 3.11(c)). As a result, 5.0 V was proved to be the best AC voltage for analyte detection, abiding by the rules mentioned in previous AC ECL literature. When an AC ECL experiment was carried out at a controlled potential, one must exercise caution under such a circumstance: it is easy to generate undesired species by applying too large a voltage to the cell. The reaction can be safely limited to the expected species by operating the cell at a voltage just higher than the threshold value required for luminescence.

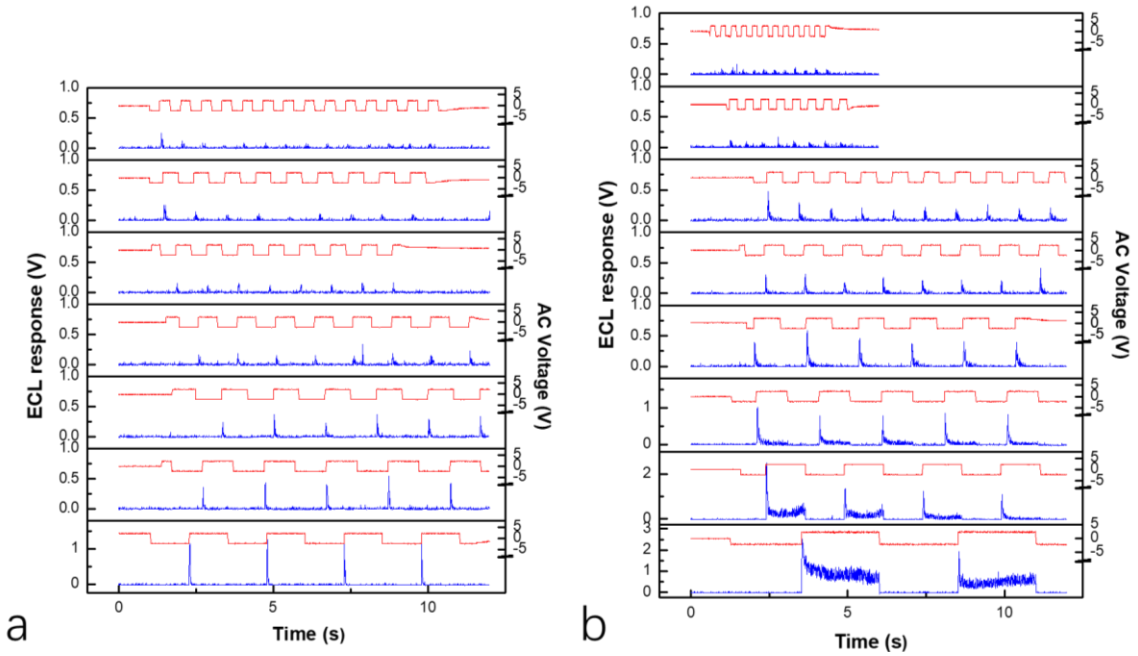

Figure 3.12.Real-time ECL response in AC square wave bipolar ECL cell at 5.0 V of (a) 0.5 mM $K_3Fe(CN)_6$ at frequency at 400 mHz, 500 mHz, 600 mHz, 800 mHz, 1 Hz, 2 Hz and 3 Hz; (b) 1 mM $K_3Fe(CN)_6$ at 200 mHz, 400 mHz, 500 mHz, 600 mHz, 800 mHz, 1 Hz, 2 Hz, 3 Hz and 5 Hz.

In addition to the concentration calibration, the frequency dependence of this bipolar ECL cell was also studied by using the AC square wave at different frequencies. 5.0 V was applied to the bipolar cell with $K_3Fe(CN)_6$ concentration of 0.5 mM and 1 mM at the frequency from 200 mHz to 5 Hz, and the corresponding ECL response was recorded. As shown in Figure 3.12(a) and (b), as the frequency increases, the ECL peak height decreases gradually, with feeble responses at 3 and 5 Hz. If the electric field the BPE experienced is the same, the ECL peak height should have the same magnitude. As a result, we here assume the electric field in the bipolar cell is changed by the frequency. This behavior in our bipolar ECL system is different from the AC ECL experiment under this frequency range of a traditional three-electrode system or a two-electrode system from previous literature. The little ECL increase during some of the forward half cycles such as at 200 mHz and 400 mHz is probably due to the electric field fluctuation.

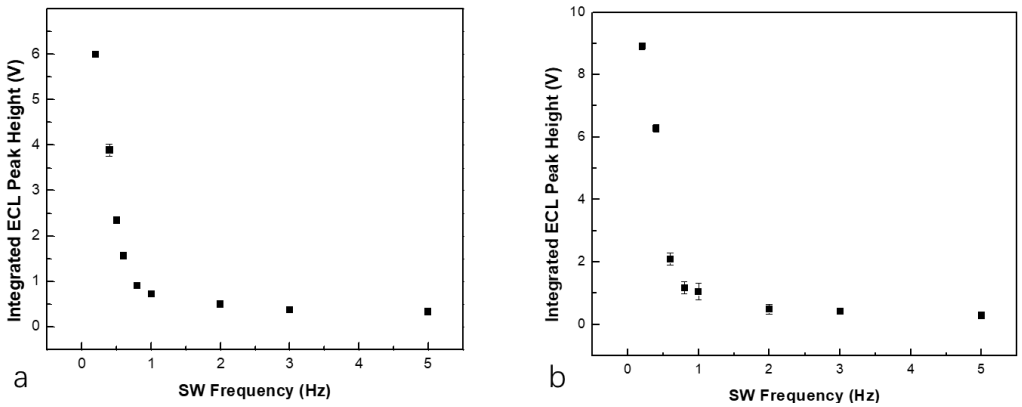

Figure 3.13.The dependence of integrated ECL peak height on AC square wave frequency of (a) 0.5 mM $Fe(CN)_6^{3-}$ and (b) 1 mM $Fe(CN)_6^{3-}$.

Then the peak height for 5 cycles was integrated to investigate its frequency dependence. For both 0.5 mM $Fe(CN)_6^{3-}$ and 1 mM $Fe(CN)_6^{3-}$, the integrated ECL peak height decreases monotonically as the frequency increases from 200 mHz to 5 Hz; the error bar represents the standard deviation of five independent runs (Figure 3.13(a) (b)). Since the concentrations of the analyte are always the same for ECL experiments at different frequencies, the significant ECL intensity difference should be relevant to the driving force of the BPE reactions. More accurately, it is the electric field that drives the reactions on the BPE by creating the interfacial potential difference.

On the purpose of proving our assumption that, the electric field would decrease as a function of the frequency, the potential difference profile measurement was carried out in a specific experimental design. Taking advantage of the method of measuring the solution potential difference by using two conductive probes immersed in the solution at a fixed distance discussed in Chapter 2, additional probes design was included on the gold substrate by the photolithography following the same procedure. Two narrow gold probes, with 4 mm in length and 1 mm in width, were pointing inside the cell, perpendicular to the length and towards the side of the BPE. Instead of the oscilloscope, a multifunction data acquisition system (DAQ) device interfaced with the computer was employed. Synchronized multichannel data acquisition was compiled by Labview (National Instruments^{TM}). The analog voltage input from the PMT and waveform from the generator were measured in the same deck via separate channels. A secondary deck was used solitarily to measure the solution potential difference between these two probes.

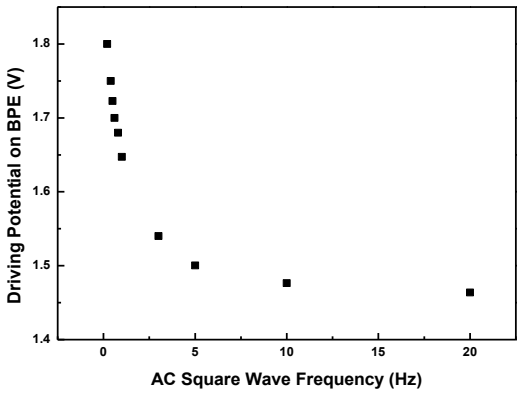

Figure 3.14.The potential difference across BPE as a function of AC square wave frequency when applying a voltage at 5.0 V.

Then the value of driving potential on BPE in the forward half cycle, which is the solution potential difference between two ends of the BPE, is plotted as a function of the AC square wave frequency. Due to the measured potential difference is fluctuating during each half AC cycle, we select the relatively stable value as the standard for calibration. As shown in Figure 3.14, the driving potential on the BPE decreases fast from 1.8 to 1.5 V when the AC frequency changes from 100 mHz to 5 Hz; then it decreases from 1.5 to 1.46 V slowly from 5 to 20 Hz. The exponential decay of electric field versus

time was shown, similar to the result in chapter 2, indicating that the inevitable nonfaradaic charging/discharging and depletion effect at both driving electrodes would influence on the electric field.

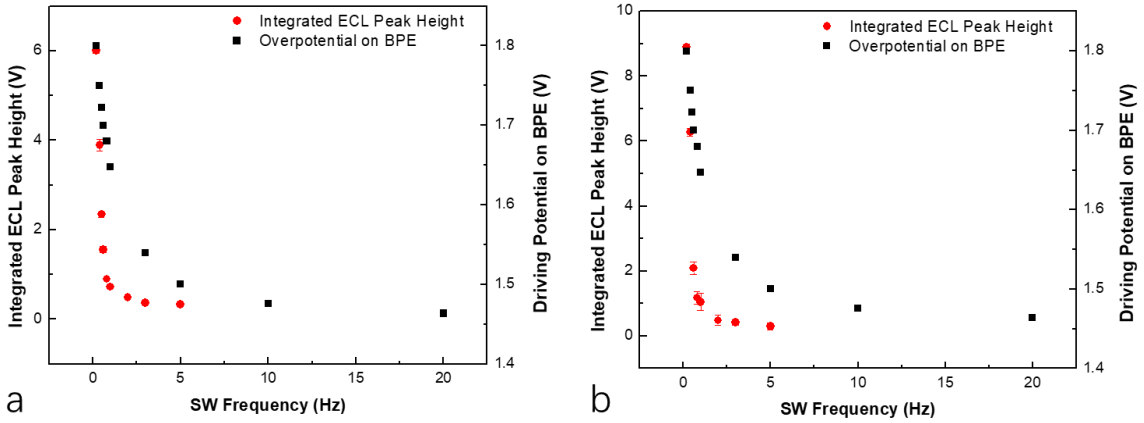

Figure 3.15.Comparing the dependence of ECL peak height and the potential difference across BPE on the AC square wave frequency of (a) 0.5 mM $Fe(CN)_6^{3-}$ and (b) 1 mM $Fe(CN)_6^{3-}$.

When the ECL change and potential difference are compared together in one plot with two vertical axes (Figure 3.15), obviously, both of them decrease versus the frequency in the AC bipolar cell. However, the ECL intensity decreases much faster than the potential difference. It could be understood that the ECL emission (the reaction rate on the BPE anode) is not linearly proportional to overpotential due to the heterogeneous kinetics. While in addition to that, the BPE itself also plays a role in determining the ECL intensity.

Theoretically, this ECL deterioration with increasing AC frequency is related to multiple influential factors that include the double layer charging effect, uncompensated resistance, and resulting electric field difference in the BPE system of those the effects depend on the frequency. The alternation of the frequency with a large electrode surface area (>1 cm^2) on the driving electrodes would imply a power dissipation due to the double layer charging[140]. Hence the potential waveform would encounter some extent of rounding via uncompensated resistance effect. More precisely, both the IR drop and the cell time constant R_uC_{dl} slow down the time of reaching the final potential by increasing the frequency. Also, the well-defined electrode boundary conditions and diffusive transport processes no longer apply, and the waveform shape becomes unpredictable (The alternation of frequency also could cause thermal heating of the solution resulting in convective transport, resulting in higher light output in the ECL system. However, it could be ignored in our closed BPE system with such a small current). As a result, the solution potential difference between two driving electrodes will be inversely proportional to the AC frequency since the double layer charging is proportional to $1/t^{1/2}$. This reduced electric field across the solution would provide a lower driving force for simultaneously bipolar reactions. In addition to the reduced electric field in solution, a similar effect from the double layer charging would also impose on the BPE itself and deteriorate the overpotential on the BPE surface for faradaic reactions. As a result,

the lowering of the electric field in solution and simultaneous more significant uncompensated IR drop at the BPE interface with a higher frequency, would both lead to a decrease in the ECL emission. Noteworthy, a much higher frequency will even end up in failure to generate the ECL signal since it does not have enough time to form electric double layers in the electrolyte.

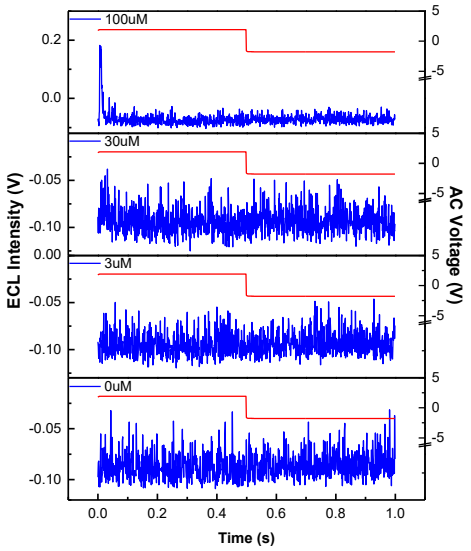

Figure 3.16.The added ECL response of the AC square wave bipolar ECL cell after one-one addition of 100 complete cycles as one cycle of $K_3Fe(CN)_6$ concentration of 0, 3, 30 and 100 µM when the square wave is between 1.9 and -1.8 V.

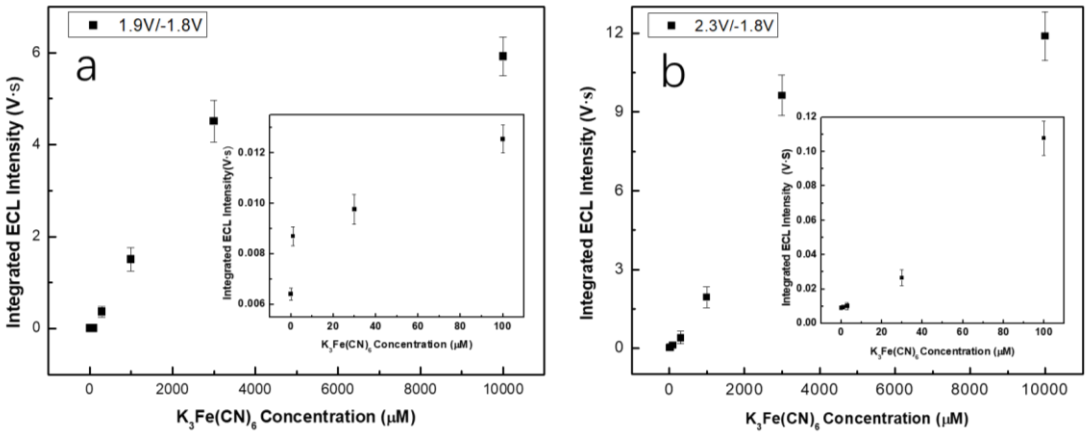

Figure 3.17.Calibration plots of integrated ECL intensity as a function of $K_3Fe(CN)_6$ concentration of 100 AC square wave cycles. (a) at 1.9 to -1.8 V. (b) at 2.3 to -1.8 V. Error bar represents the standard deviation of three independent runs.

An improved study on the ferricyanide as the diffusion-related redox reactive species was carried out by integrating many AC cycles using the DAQ device for multichannel synchronized data acquisition as well using an unsymmetric waveform. ECL solution with $Ru(bpy)_3^{2+}$ concentration changing to 5 mM was used to expand the upper limit of the detection. $K_3Fe(CN)_6$ concentration as high as 10 mM and as low as several µM were examined by the newly improved method with the voltage switched between 1.9 to -1.8 V or 2.3 to -1.8 V. Figure 3.16 represents the time-dependent ECL response by adding the real-time ECL response of one hundred AC cycles into one complete cycle. The ECL of the

concentration of 100 μM shows clearly a spike at the beginning of the forward half cycle and the ECL of 30 μM still shows an observable signal compared to the blank background (0 μM). The calibration curves of the integrated ECL intensity as a function of $K_3Fe(CN)_6$ concentration were then plotted. In either Figure 3.17(a) or (b), the integrated ECL intensities are proportional to $K_3Fe(CN)_6$, while at 10 mM, the linearity does not follow. Since our $Ru(bpy)_3^{2+}$ concentration is only one half of the analyte concentration, it can be easily explained by the skewing overpotential distribution along the BPE when the analyte is in excess and the restricted diffusion of the light emitted species. The inset pictures show that $K_3Fe(CN)_6$ concentration as low as several μM could almost be differentiated from the background using our AC square wave bipolar ECL system, that resembles the detection capability of the most sensitive electrochemical technique such as differential pulse voltammetry (DPV) and square wave voltammetry (SWV) without a further electrode modification and the application of a microelectrode.

3.3.4 Investigation of Polymerized Methylene Blue as the Surface-Confined Species

After successfully demonstrating the use of this system in the detection of ferricyanide as the model analyte, we studied the electrodeposited MB thin film as a model of the surface-confined analyte. To get closer to our final goal of monolayer detection, the electropolymerization of methylene blue (MB) was employed to synthesize surface redox-active molecules on the BPE. Electropolymerization is a simple but powerful method in targeting selective modification of different types of electrodes with desired matrices. Numerous conjugated polymers have been electrochemically synthesized in the fabrication of chemical and biochemical sensor devices. Among these conjugated polymers, azines such as phenazines, phenothiazines, and phenoxazines have been used extensively in bioelectrochemistry as redox indicators and mediators[156]. For example, electrically active and conducting layers of poly(methylene blue) (PMB) having stable contact with the electrode surface can be electropolymerized by methylene blue (MB) monomers on gold film electrodes to study its catalytic activity toward biomolecules.

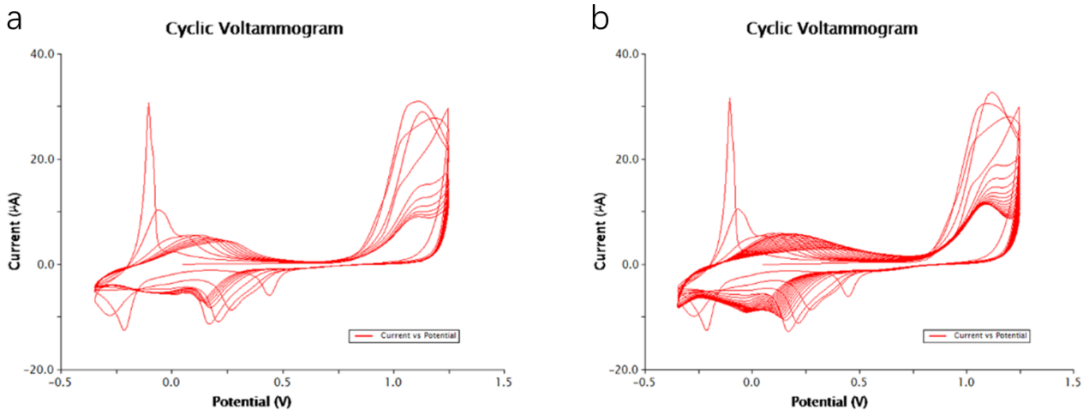

Figure 3.18.Electropolymerization of standard gold electrode in 2.5 mM MB solution in 0.1 M PBS buffer for (a) 10 cycles and (b) 20 cycles.

Electropolymerization was first conducted on a standard gold electrode to examine whether MB thin film could be successfully deposited. 2.5 mM MB was dissolved in 0.1 M PBS buffer at pH = 7, following the literature[157]. The potential started at –50 mV, and then it was swept between –350 mV to 1250 mV with a scan rate of 50 mV/s. Figure 3.18 shows the voltammogram with 10 and 20 cycles of electropolymerization. The growth of the polymer film is accompanied by an increase in the redox peak for polymeric MB and a decrease in the redox peak for MB monomer. Also, the reduction peak for the gold oxide reduction will gradually shift more negatively and become more indistinct as the number of cycles increases.

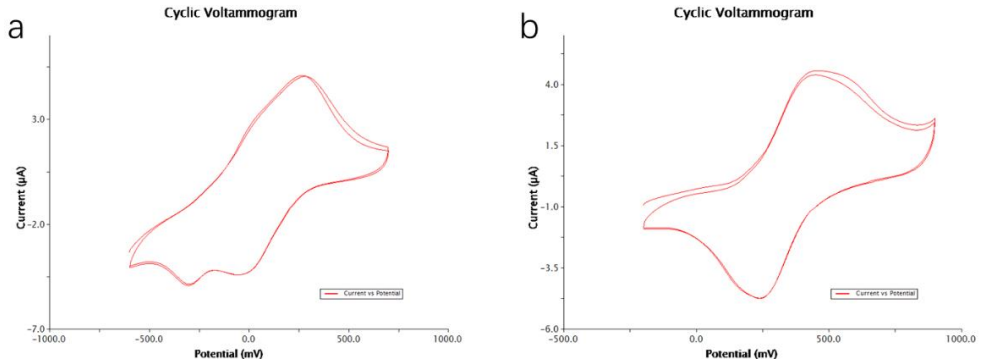

Figure 3.19.Following CV scan after electropolymerization in (a) 0.1 M PBS buffer (-600 to 700 mV) and (b) 0.1 M HCl (-200 to 900 mV), scan rate: 100 mV/s.

The presence of MB film was confirmed by sweeping the electropolymerized electrode in either 0.1 M PBS buffer (pH=7) or 0.1 M HCl solution (pH = 1). In PBS buffer, the oxidation peak appears at 270 mV in the forward scan, and two reduction peaks, at -34 mV and -300 mV, are shown in the reverse scan (Figure 3.19(a)). This peak feature reveals two separate one-electron-transfer mechanisms in the reduction of MB^+ in this neutral condition. While in 0.1 M HCl, the oxidation peak shifts to 450 mV, and only one reduction peak is obtained at a much more positive position of 240 mV (Figure 3.19(b)). The combined reduction peak explains a two-electron-transfer mechanism in MB reduction in the acidic condition. Both the positive shift of oxidation and reduction peaks indicate that MB oxidation and MB^+ reduction are involved with the participation of H^+.

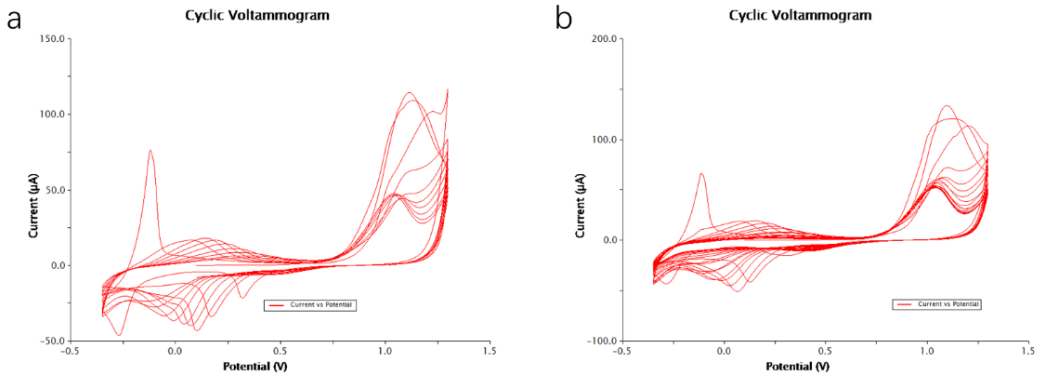

Figure 3.20.Electropolymerization of the half BPE in 2.5 mM MB solution in 0.1 M PBS buffer (a) 10 cycles and (b) 20 cycles.After its verification on the standard gold electrode, the

electropolymerization was then carried out on the half BPE in the sensing compartment. The resulting MB polymerized film on the gold surface could then serve as the surface-confined analyte that triggered the ECL emission in the reporting compartment. Different cycles of electropolymerization were carried out in 2.5 mM MB monomer solution in pH = 7 PBS buffer as in the standard gold electrode. The current level in the polymerization process is about 3~4 times larger than that from the standard gold electrode due to an enlarged gold surface area (Figure 3.20(a) and (b)).

After the electropolymerization, the sensing compartment was rinsed with distilled water several times to wash out the free MB monomer. Then AC square wave bipolar ECL experiment was operated with the sensing compartment filled with pure 0.1 M PBS buffer and reporting compartment filled with 0.5 mM $Ru(bpy)_3^{2+}$ ECL solution. A symmetric waveform with no offset was applied to the driving electrodes with positive and negative potential in each half cycle sharing identical absolute value.

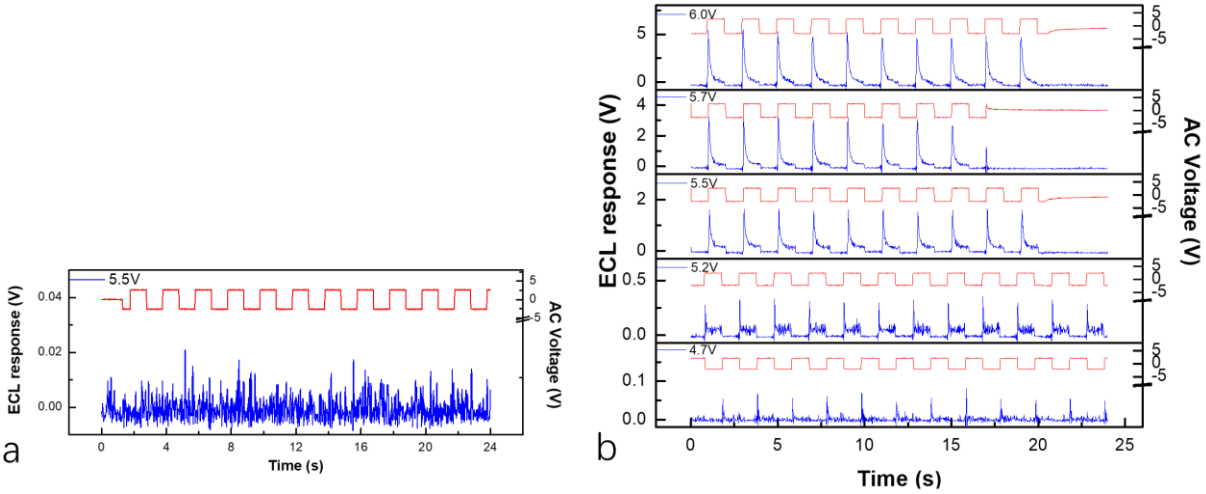

Figure 3.21.Real-time ECL response of the AC square wave BPE cell with the symmetric waveform of (a) blank PBS buffer and (b) 10 cycles of electropolymerization.

When comparing the ECL response of the electropolymerized one with the control experiment in pure PBS buffer, it seems to be reasonable that ECL signals at a voltage below 5.5 V (such as 4.7V, 5.2V, and 5.5 V) are from the reduction of MB thin film reduction (Figure 3.21). A calibration plot was once tried to correlate the integrated ECL intensity versus electropolymerization cycles yet failed. First, the amount of MB polymerized on the surface is in practice not proportional to the number of cycles and an approach is required to quantify the MB. Second, at this stage, due to the use of a symmetric square waveform and the lack of a more convincing control experiment, we can not distinguish the correspondence of the signal.

After a series of related experiments, we realized that not only the positive potential in the forward half cycle but also the negative potential in the reverse half cycle plays an essential role in determining the ECL response, sometimes in an unexpected direction. As we know, for an electro-active species which is reversible, the negative potential would regenerate the analyte. Less enough negative potential is not

capable of re-oxidizing the reduced species back. However, if the negative voltage exceeds the threshold, the generation of gold oxide would raise a severe problem that could lead to a misinterpretation of the correspondence of the ECL response. For example, when taking the CV on the standard gold electrode in the PBS buffer, the gold surface would start to be oxidized at around 800 mV. The same phenomenon happens when the potential is negative enough in the reverse half cycle.

Taking polymerized MB thin film on the half BPE as an example, with enough positive voltage in the forward half cycle, there would possibly be at the same time three reactions possible of triggering the ECL emission. The first one should be the reduction of polymerized MB on the sensing half BPE, and its corresponding ECL emission is no doubt the designated signal for the analyte detection. However, H_2 evolution in the aqueous environment would also drive an ECL mission under enough cathodic potential. In the solution environment of PBS buffer with pH=7, the reduction potential of H^+ is around -400 mV which is close to the reduction potential of polymerized MB on the gold surface. The differentiation of signal from the analyte reduction and H_2 evolution would endow a problem. In addition, an unexpected third reduction, which is the reduction of gold oxide, could also become a source of ECL emission. Even though gold oxide is not initially present on the BPE surface, if a considerable negative potential is applied in the reverse half cycle, the gold electrode surface could be oxidized to generate AuO. As a result, in the following forward half cycle, it is much easier for the reduction of AuO which has a reduction potential at around 600 mV other than the MB oxidation at about -250 mV. Due to the surface-confined property of gold oxide, its reduction would exhibit a similar ECL behavior as polymerized MB molecules.

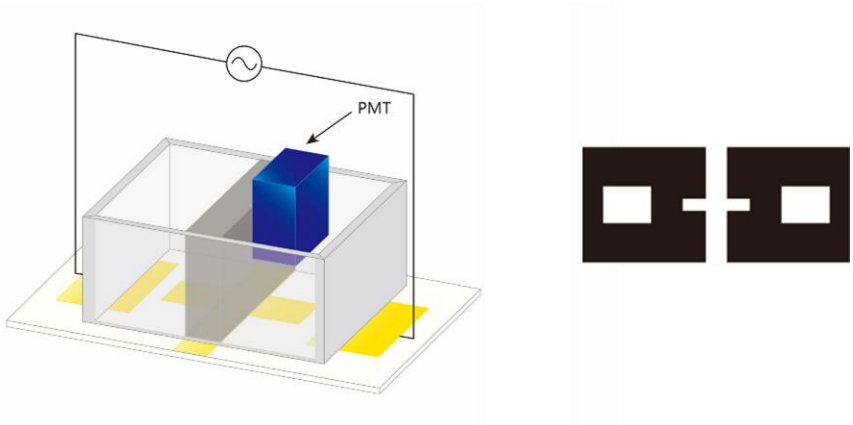

Scheme 3.3.Left: Illustration of modified AC square wave bipolar ECL cell. Right: the mask design for photolithography. Inset: Electrode design on transparent paper.

Due to the necessity of quantifying the MB loading on the half BPE surface after electropolymerization, the previous electrode design was modified with a central bipolar part for the electrical connection. The gold substrate is switched from the CD to a more uniform and stable gold-coated glass slide. Also, instead of using a thermal transfer paper, a more controllable photolithography method was utilized with the photosensitive dry film. Other than the expensive and time-consuming spin coating of a

photoresist, the photosensitive dry film was much cheaper and easier to operate. The detailed procedure was described in the experimental section. Scheme 3.3 (right) demonstrated the electrode design printed on the transparency film paper. In addition to the old driving and bipolar electrodes pattern, there was a central strip vertical to the old BPE in the middle. As a result, the resulting BPE part would be cross-shaped with one strip laterally as the bipolar electrode and the other strip vertically as the electric contact region. The final cell configuration is illustrated in Scheme 3.3(left), the vertical strip extruded out of the framework of the cell and could be wrapped with copper tape as the connection to perform the electrochemistry instead of making a connection to the half BPE in the reporting compartment.

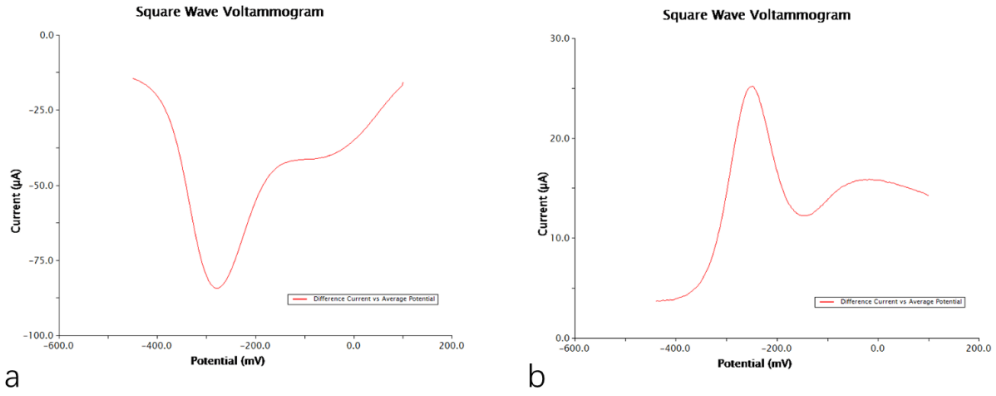

Figure 3.22.SWV characterization of half BPE electropolymerized in 2.5 mM MB solution at 5 cycles. (a)100 to -450 mV (b) -450 to 100 mV. Amplitude: 50 mV, period: 16 ms. increment: 1 mV. sampling width: 1 ms.

In order to accurately characterize the amount of polymerized MB on the BPE surface, square wave voltammogram (SWV) was selected as a highly sensitive method for quantification. For example, after 5 cycles of electropolymerization in 2.5 mM MB monomer solution, SWV was then operated on the half BPE through the newly created connection region. The potential range was from 100 mV to -450 mV with positive to negative sweep in a falling trend, and negative to positive sweep in a rising trend. The other parameters were set in the following values: amplitude: 50 mV, period: 16 ms, increment: 1 mV, sampling width: 1 ms. Figure 3.22 demonstrated the typical characterization of the MB loading on the half BPE after the electropolymerization: significant reduction and oxidation peaks are shown in (a) and (b) respectively. The maximum of the reduction peak at -80 µA is larger than the absolute value of the oxidation peak. We attribute it to the presence of the ambient oxygen which could provide a catalytic effect.

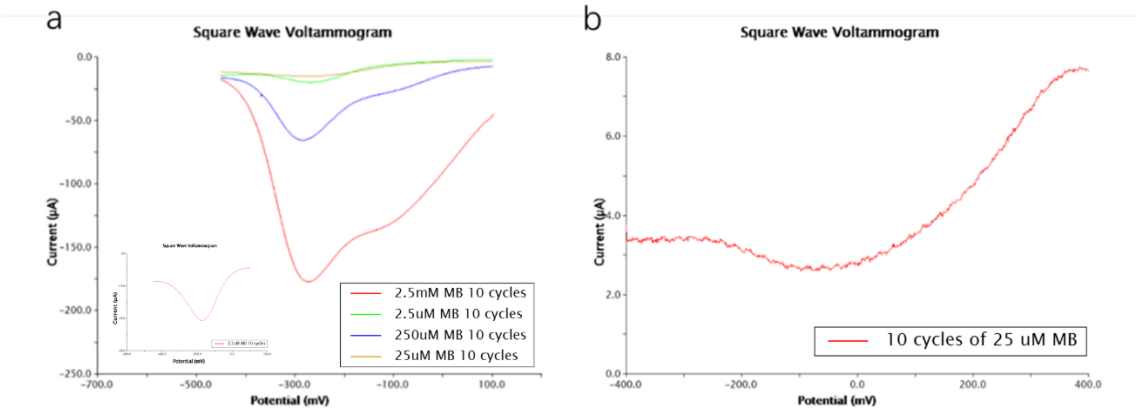

Figure 3.23.(a) SWV characterization after 10 cycles electropolymerization of 2.5 mM, 250 μM, 25 μM, 2.5 μM MB in positive to negative sweep (±). (b) of 25 μM in negative to positive sweep (∓).

MB electropolymerization was then sequentially carried out on MB monomer solution in different concentrations from 2.5 mM to 2.5 μM to find out the appropriate concentration range. After 10 cycles of electropolymerization, SWV was used to characterize MB molecules polymerized on the BPE surface. As shown in Figure 3.23(a), the highest concentration at 2.5 mM results in a considerable reduction peak with its height at about -180 μA. As lowering down the monomer concentration, the reduction peak also minimizes. At 2.5 μM, even though still observing a reduction peak at around -200 mV(inset), in the negative to positive sweep (∓) there is no oxidation peak present as in Figure 3.23(b). The reduction peak in the positive to negative sweep (±) can not be attributed to the MB reduction but the kinetics change of O_2 reduction on the gold electrode surface after the electropolymerization. Moreover, even the oxidation potential of gold surface in PBS buffer seems to be lowered down by the electropolymerization (This is testified in following experiments). The potential sweep on BPE from -200 to 1350 mV in PBS buffer will alter the electrochemical behavior on the gold surface such as what the electrochemical cleaning does in a similar potential range. According to the experiment, a low concentration of MB monomer (<25 μM) is not applicable to the electropolymerization since there is no clear oxidation peak for the MB molecule in the SWV.

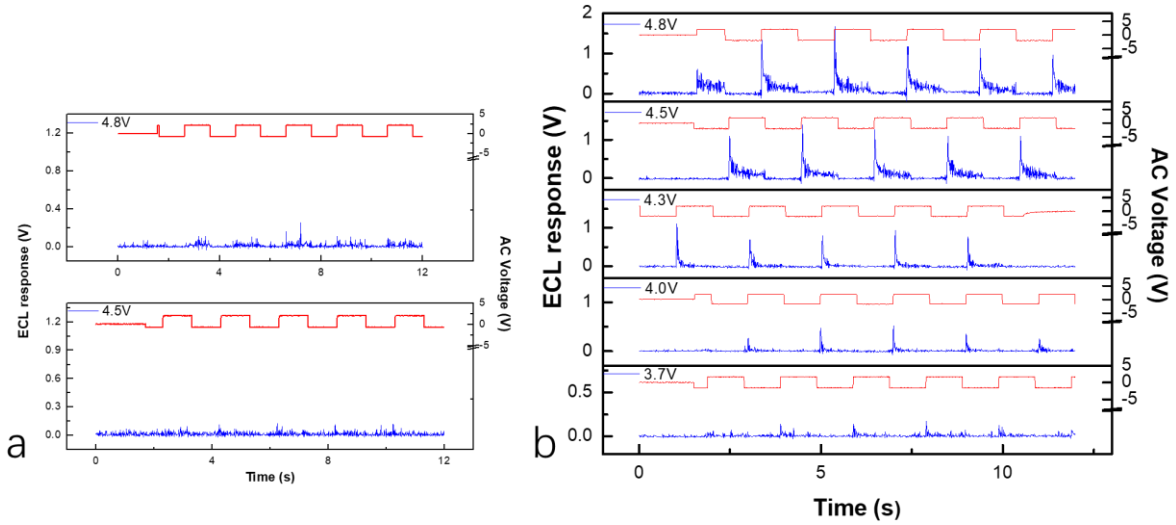

Figure 3.24.Real-time ECL response in AC square wave bipolar ECL cell (a) In 0.1 M PBS buffer at 4.5 V, 4.8 V. (b) after 10 cycles of electropolymerization in 2.5 mM MB at 3.5 V, 3.7 V, 4.0 V, 4.3 V, and 4.5 V.

The presence of polymerized MB on the half BPE surface was re-confirmed by comparing the control experiment and the ECL experiment after the electropolymerization. The control experiment was operated when the sensing compartment was only filled with 0.1 M PBS buffer. The ECL response was monitored when gradually increasing the symmetric voltage until the appearance of a clear signal. This voltage was then assigned as the threshold of side reaction which corresponds to ECL emission in the bipolar cell. In the typical control experiment in Figure 3.24(a), the ECL signal does not show up until 5.5 V is applied. Figure 3.24(b) shows gradual increasing ECL signals from 3.7 to 4.5V after 10 cycles of electropolymerization on the half BPE in 2.5 mM MB. The much smaller onset voltage and prodigious ECL emission at the same voltage should reflect the presence of MB film on the BPE surface after electropolymerization.

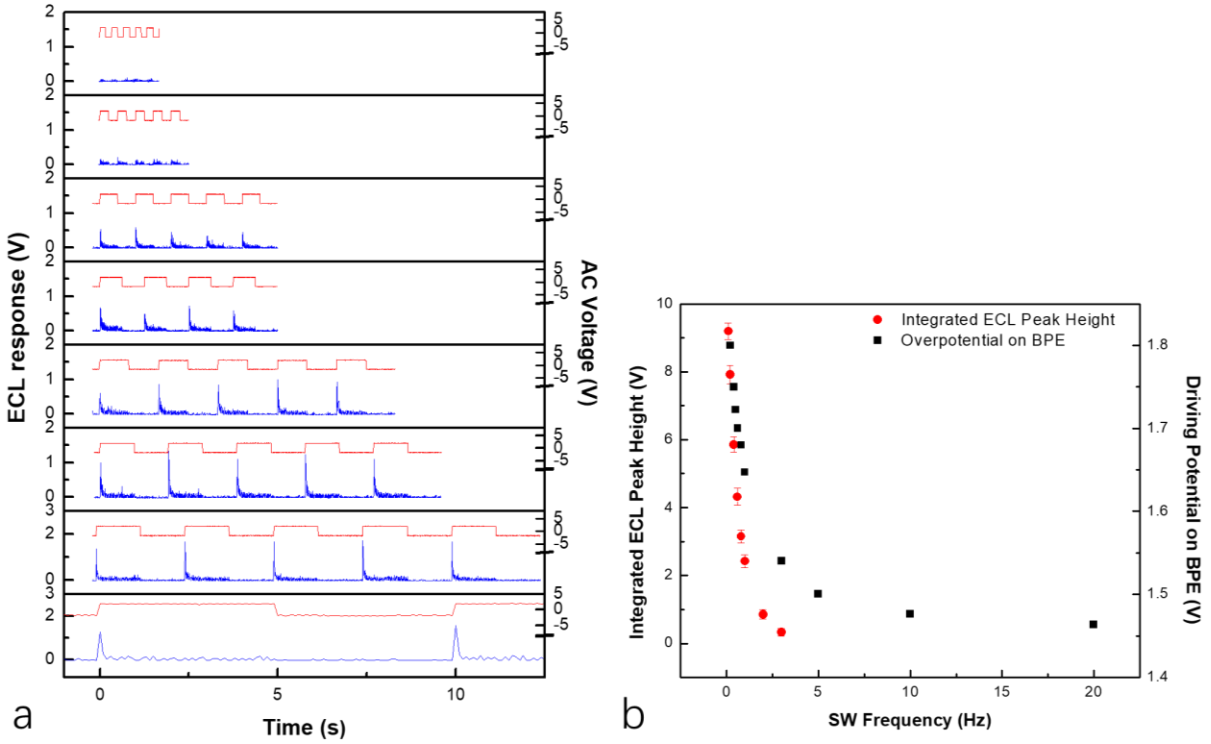

Figure 3.25.(a) Real-time ECL response of the AC square wave bipolar ECL cell at 4.5 V of 10 cycles of electropolymerization of 2.5 mM MB at a frequency at 100 mHz, 400 mHz, 500 mHz, 600 mHz, 800 mHz, 1 Hz, 2 Hz, 3 Hz. (b) The dependence of integrated ECL peak height on AC square wave frequency of electropolymerized MB for 10 cycles (monomer concentration:2.5 mM). Error bar represents the standard deviation of five independent runs.

The frequency dependence was also examined using this polymerized MB as a surface-confined analyte on the half BPE with a symmetric wave of 4.5 V. As shown in Figure 3.25(a), the real-time ECL responses were collected with frequencies changing from 100 mHz to 3 Hz. The largest ECL peak appears at a frequency of 100 mHz, and the smallest peak appears at a frequency of 3 Hz. Then the peak height for 5 cycles was also integrated to calibrate its frequency dependence (Figure 3.25(b)). The plot is in agreement with the previous result from ferricyanide that the ECL peak height and intensity decrease gradually as the frequency increases. Still, the ECL intensity decreases much faster than the potential difference across the BPE.

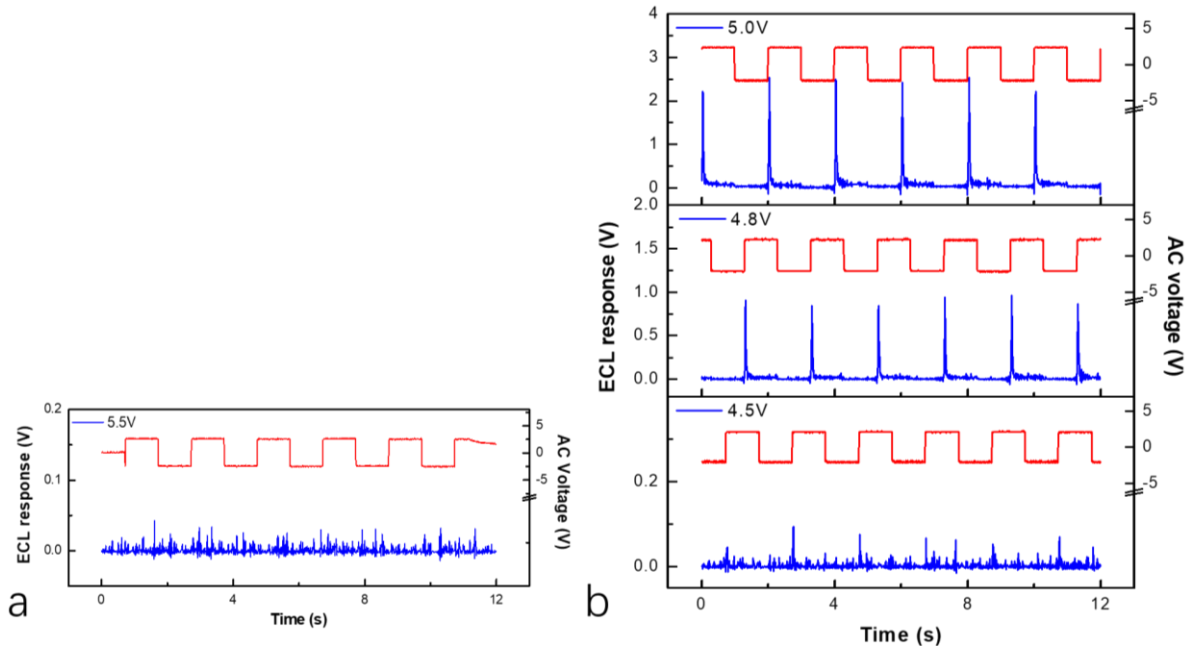

Figure 3.26.(a) Real-time ECL response of the bipolar cell before the electropolymerization in 0.1 M PBS buffer at AC square wave of 5.5 V (b) Real-time ECL response of the bipolar cell after electropolymerization 2.5 μM MB for 10 cycles at 4.5 V, 4.8 V and 5.0 V.

However, by the direct comparison of the ECL response to the control experiment in the same symmetric voltage, we can still not wholly exclude the interference from side reaction such as gold oxidation. It is owing to gold surface change after sweeping to the extreme potential in PBS buffer. The electropolymerized surface and the bare gold electrode surface would have different behavior with changing kinetics, not merely the amount of MB loading. This kinetic change on the gold BPE surface was then tested by another cell which was electropolymerized in 2.5 μM MB solution for 10 cycles. This monomer concentration is not capable of producing MB thin film on the BPE surface. Before electropolymerization, a symmetric AC square wave of 5.5 V does not trigger any ECL emission (Figure 3.26(a)). However, after electropolymerization, even with no oxidation peak of MB shown in the SWV characterization, the onset voltage of the ECL is minimized a lot to 4.5 V (Figure 3.26(b)). As a result, in addition to the kinetics of O_2 reduction, the oxidation of gold in PBS buffer also alters after the electropolymerization. The ECL spikes can only be ascribed to the reduction of gold oxide which forms more easily after the electropolymerization. The potential sweep during it shifts downward the oxidation potential of gold surface in PBS buffer. For example, for a square wave at 4.5 V, a negative potential around -2.2 V is capable of oxidizing the gold surface, while before polymerization at 5.5 V, a negative potential around -2.7 V can not do the same job. As far as we know, phosphate anions can absorb on the gold surface. Au cation can form a solvated metal complex with phosphate ligand that may lower down the thermodynamics for its electrochemical oxidation.

From then on, in addition to the symmetric AC applied voltage, an offset voltage, was used to alter the positive voltage in the forward half cycle and negative voltage in the reverse half cycle. To represent the potential waveform, the positive voltage and negative voltages are specified in each experiment.

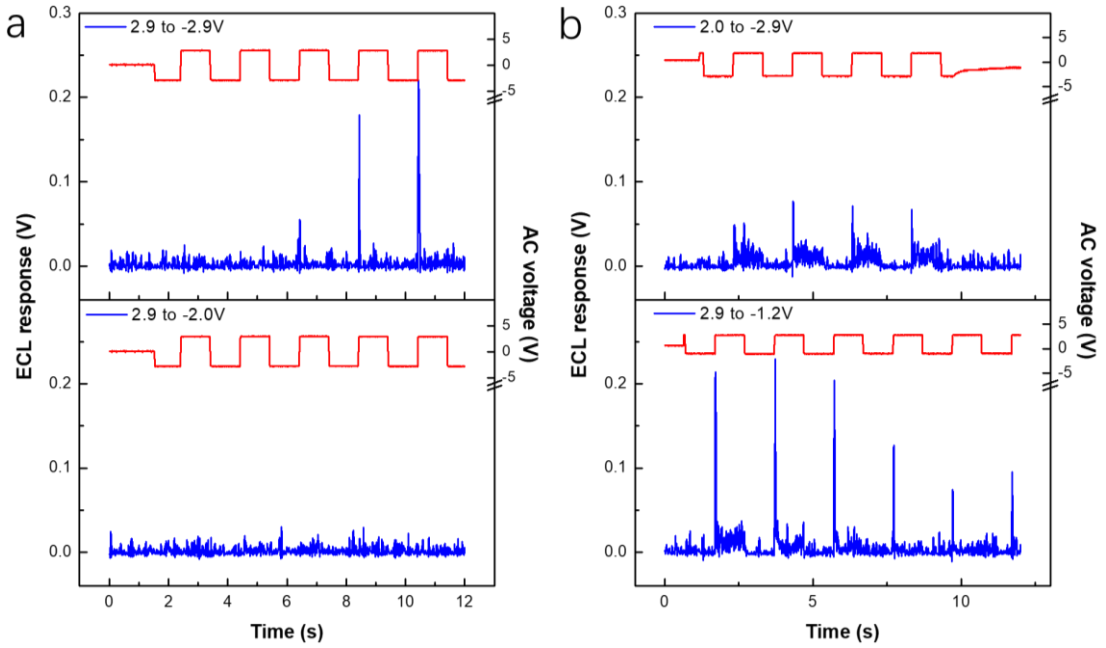

Figure 3.27.Real-time ECL response of the bare bipolar ECL cell in 0.1 M PBS buffer with AC square wave of (a) 2.9 to -2.0 V, (b) 2.9 to -2.9 V, (c) 2.9 to -1.2 V immediate after 2.9 to -2.9 V, (d) 2.0 to -2.9 V.

As discussed before, the negative voltage in the reverse cycle would have a significant influence in determining the following ECL response in the next forward half cycle. In addition to the sufficient negative voltage required to regenerate the analyte, an excess negative value would easily oxidize the gold BPE surface in PBS buffer in the reverse half cycle and produce the gold oxide. Its more positive reduction potential allows the AuO to be reduced back and trigger the same type of ECL emission as well as the MB reduction. A testing experiment was first done on the bare BPE cell before its electropolymerization in 0.1 M PBS buffer, to confirm the generation of gold oxide under a sufficient negative voltage. As shown in Figure 3.27(a), an AC square wave between 2.9 to -2.0 V does not produce any ECL emission, showing no H_2 evolution in the forward half cycle as well as no gold oxidation in the revere half cycle. However, when switching the negative potential to -2.9 V with the same positive potential, a noticeable ECL spike was shown at the beginning of each forward half cycle (Figure 3.27(b)). It must be related to the reduction of gold oxide generated from the previous reverse half cycle. An experiment with a square wave between 2.9 to -1.2 V was carried out immediately after that, as shown in Figure 3.27(c). Even -1.2 V is not capable of oxidizing the gold, ECL spike still exists due to the remaining gold oxide from the previous run. Also, when the positive potential was lowered down from 2.9 to 2.0 V with same negative potential at -2.9 V which could generate gold oxide, ECL spikes are still observed during the experiment (Figure 3.27(d)). Since 2.0 V is far less enough to trigger

H_2 evolution, the ECL signal comes from the gold oxide with a much positive reduction potential. When comparing (b) and (d), a small positive potential at 2.0 V could only reduce a small amount of produced gold.

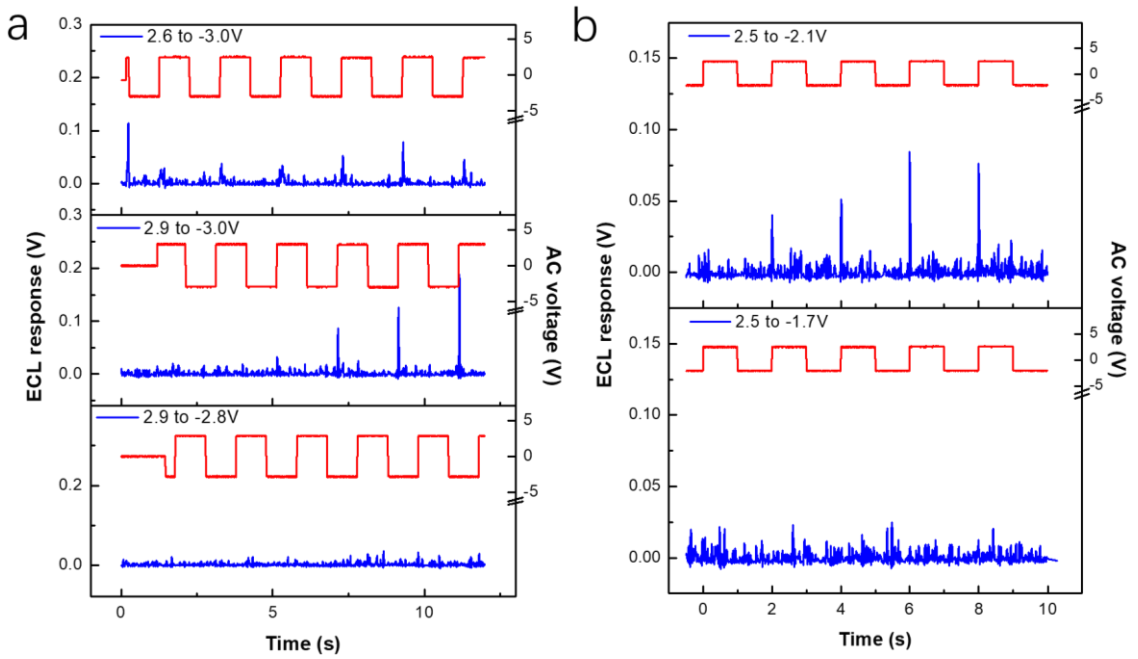

Figure 3.28.Real-time ECL response of the bipolar ECL cell in 0.1 M PBS buffer of (a) bare BPE before electropolymerization (b) after electropolymerization in 2.5 μM MB for 10 cycles.

According to the test, the negative potential around -2.9 V is the threshold of electrooxidation of the half gold BPE surface. However, it is only applicable to the bare bipolar cell before electropolymerization with the potential sweep. After the electropolymerization, in addition to the kinetics change on the gold surface, the oxidation potential of gold BPE in PBS buffer is shifted negatively as illustrated in Figure 3.18. As discussed before, electropolymerization in 2.5 μM MB monomer solution could not polymerize MB on the BPE surface since no oxidation peak is observed around -260 mV in the SWV characterization. The bare BPE was first tested as shown in Figure 3.28(a). At potential between 2.9 and -2.8 V, there is no ECL response. While at 2.9 to -3.0 V, ECL spike is gradually shown indicating the gold oxidation in the reverse half cycle. Even when the positive potential is decreased to 2.6 V, the ECL spikes are still present due to the smaller potential requirement for the gold oxide reduction. Then it was changed to a bipolar cell electropolymerized in 2.5 μM MB for 10 cycles. As shown in Figure 3.28(b), under a positive potential at 2.5 V, the experiment does not show any ECL emission of negative potential at -1.7 V. When changing it to -2.1 V, now ECL spikes appear, validating the oxidation of gold in the reverse half cycle. As a result, the electrochemical behavior change on the gold BPE after the electropolymerization should be taken into consideration. The negative potential of -2.1 V, instead of -2.9 V, becomes the new indication of the negative potential threshold to avoid interfering signal from gold oxide.

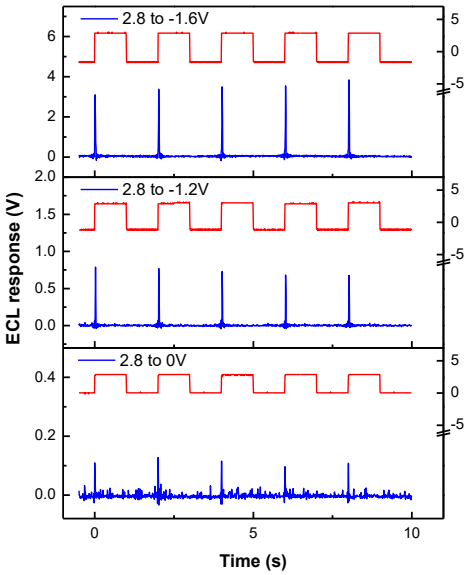

Figure 3.29.Real-time ECL response of the bipolar ECL cell in 0.1 M PBS buffer after electropolymerization in 2.5 mM MB for 5 cycles of positive potential at 2.8 V with a negative potential of 0, -1.2 V, and -1.6 V.

To a certain amount of MB on the BPE surface, its ECL emission intensity is not only be determined by the positive potential, which drives polymerized MB reduction in the forward half cycle, but also by the value of negative potential, which guarantees the regeneration of the oxidized form of MB in the reverse half cycle. The result in Figure 3.29 of the half BPE polymerized with MB (2.5 mM) for 5 cycles shows the importance of negative potential. For the positive potential maintain at 2.8 V, when the negative voltage is zero, only a small ECL spike in each cycle is involved, representing the gradually diminished MB thin film remaining on the BPE surface. As it shifts to more negative, a much enhanced ECL response is observed, confirming the effective re-oxidization of MB in the reverse cycle.

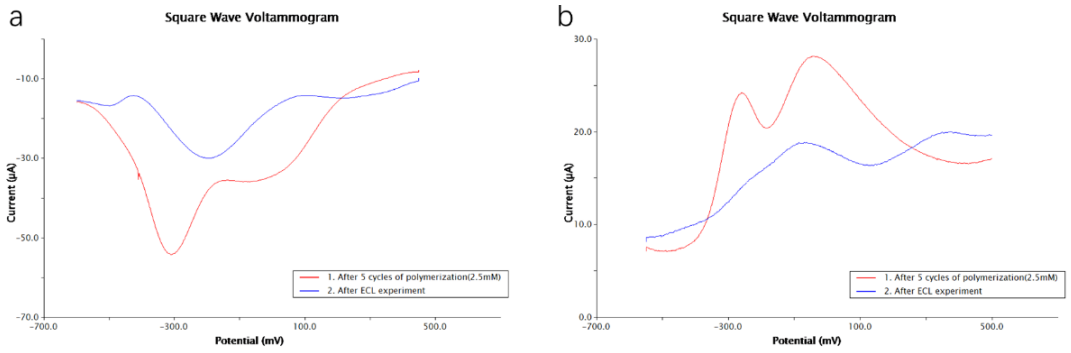

Figure 3.30.SWV characterization of the bipolar ECL cell in 0.1 M PBS buffer after electropolymerization in 2.5 mM MB for 5 cycles (red) and after (a) 500 to -600 mV(±), (b) -600 to -500 mV (∓).

What is also noteworthy is the gradual loss of MB while doing the ECL experiment. Since the polymerized MB thin film forms on the electrode surface through only an electrostatic force, the fast voltage alternation between cycles would weaken the binding between MB molecules by changing the charge distribution. Figure 3.30 shows that after the AC bipolar ECL experiment, the re-SWV

characterization exhibits a reduced reduction or oxidation peak than before it. Regardless of the bipolar electrochemistry, even the CV or the SWV characterization with pulse alternation in the three-electrode system could also “kick off” the MB. Besides, the polymerized MB can dissolve into the pure buffer as time goes on after electropolymerization.

In summary, from previous experiments, we realized that both the positive potential in the forward half cycle and negative potential in the reverse half cycles would influence the ECL emission in this system. During the forward half cycle, if the applied potential is not enough to trigger an electrochemical reaction, no ECL will be emitted. When the anodic and cathodic overpotentials exceed the thermodynamic thresholds, the analyte will be reduced at the cathodic end of the BPE, accompanied by the oxidation of $Ru(bpy)_3^{2+}$ at the anodic end. However, other faradaic processes, such as proton reduction, may contribute to the intensity of ECL emission, depending on the formal potential of the analyte and the potential window of the electrolyte solution. Care also must be taken not to damage the components related to the sensing process during the reverse half cycle. With an excessive negative potential applied, gold oxide would form on the bipolar gold surface in the sensing compartment and therefore damaging the surface immobilized molecules if present. Besides, in the following forward half cycle, its reduction would correspond to a similar ECL emission which can be superimposed to the desired response.

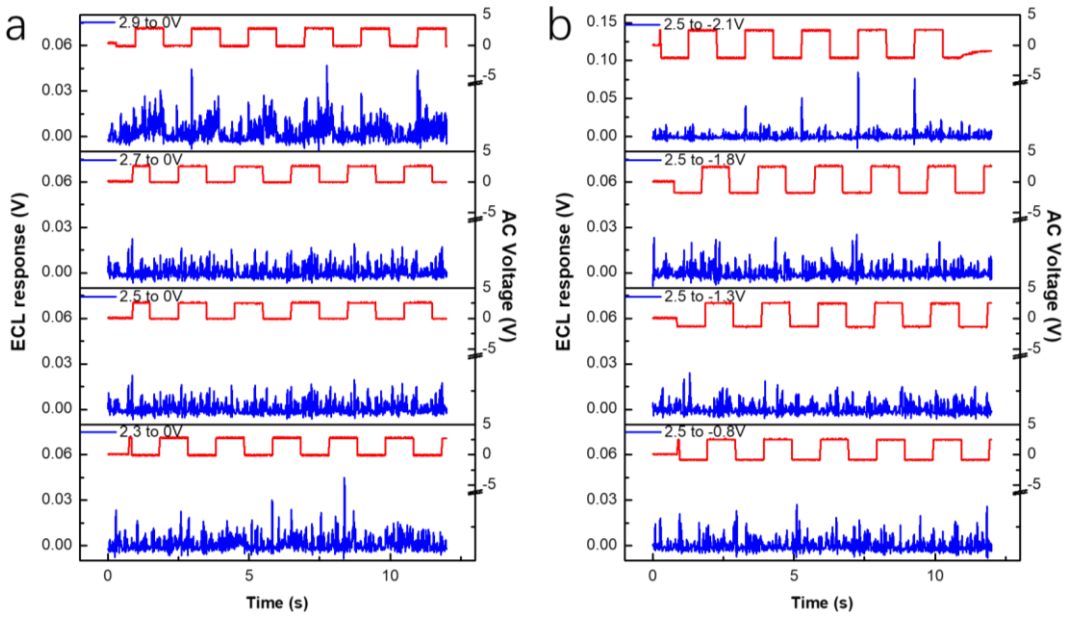

Figure 3.31.The positive and negative potential thresholds investigation using treated BPE cell in 0.1 M PBS buffer. (a) the negative potential is kept at zero when increasing the positive potential. (b) the positive potential is kept at 2.5 V when decreasing the negative potential.

Due to the reasons mentioned above, it is rational to find both the positive potential threshold and the negative potential threshold before the analyte is involved in order to get a maximized driving force without the misleading interference. A control experiment was operated carefully using the blank cells or treated cell to determine the appropriate working voltage range. First, the potential in the reverse half

cycle was set to be zero, the positive potential at the forward half cycle was gradually increased until the appearance of H_2 evolution. Then, the voltage during the reverse half cycle was shifted more negative while keeping the positive voltage below the value of H_2 evolution to determine the threshold for gold oxidation. Fortunately, the threshold of negative potential in 0.1 M $NaClO_4$ is about -3.0 V. Since the largest symmetric waveform used in $Fe(CN)_6^{3-}$ was 5.5 V which had a negative potential around -2.8 V, no issue was involved from the gold surface oxidation. Figure 3.31 shows a typical illustration of the potential threshold for the cell pretreated with 2.5 μM MB in PBS buffer. In Figure 3.31(a), the negative potential is kept as zero while the positive potential increases from 2.3 to 2.9 V. Clearly, at 2.9 V, ECL signals are present in the forward half cycle from H_2 evolution. Then the positive potential is kept at 2.5 V while gradually decreasing the negative potential (Figure 3.31(b)). At -2.1 V, the BPE surface gets oxidized with corresponding ECL spikes from the surface gold oxide reduction. By this way, for all the following experiments for analyte detection, the potential range is rigidly controlled with adjustable offset setting to make sure it is always below the potential of H_2 evolution and gold oxide formation.

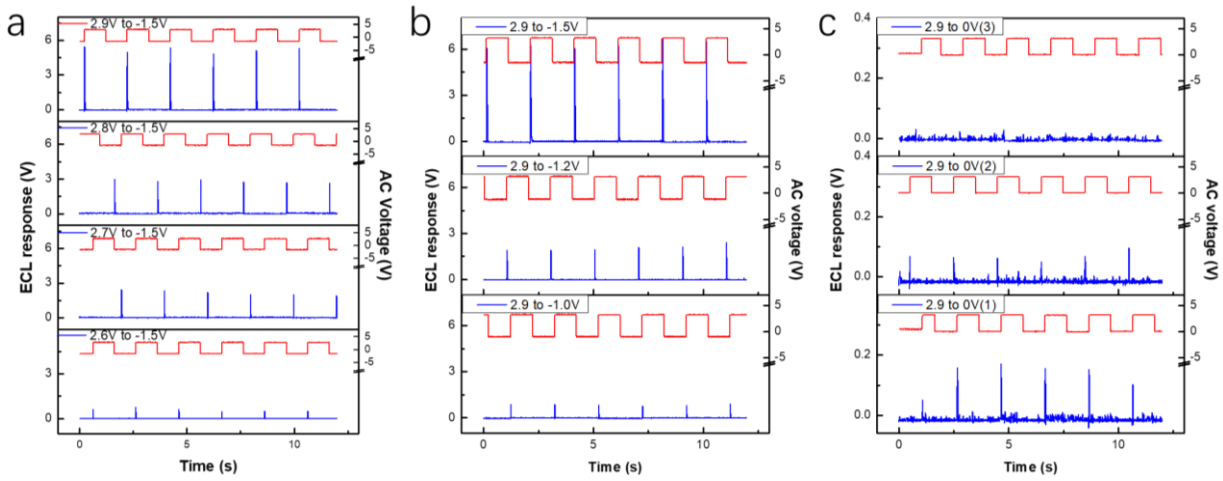

Figure 3.32.Real-time ECL response of the bipolar ECL cell in 0.1 M PBS buffer after the electropolymerization in 2.5 mM MB for 5 cycles of (a) negative potential is kept at -1.5 V when increasing the positive potential. (b) the positive potential is kept at 2.9 V when decreasing the negative potential (c) positive potential is kept at 2.9 V, and the negative potential is kept at 0 V right after -1.5 V.

After figuring out the positive and negative threshold of the system, then the appropriate potential range could be selected to detect the amount of MB polymerized on the BPE. Figure 3.32 shows the corresponding ECL response of BPE electropolymerized in 2.5 mM MB solution for 5 cycles. In Figure 3.32(a), when the keeping the negative potential at -1.5 V, an increase in the positive potential from 2.6 to 2.9 V results in a larger ECL response. When keeping the positive potential at 2.9 V, the ECL response becomes more intense as the negative potential switches from -1.0 to -1.5 V (Figure 3.32(b)). Three following ECL experiments were taken with the negative potential set at zero (Figure 3.32(c)). (2) has smaller ECL spikes than (1); and (3) has no ECL spikes, indicating the consumption of MB^+ without regeneration.

At last, the correlation between ECL response of this AC bipolar cell after the electropolymerization as a function of the amount of polymerized MB surface was done by combined two separate sets of experiments using a low concentration of MB monomer solution at 25 µM and a high concentration of MB monomer solution at 2.5 mM. Square wave voltammetry (SWV) was used to quantify the amount of MB on the BPE surface. After the electropolymerization, the sensing compartment was rinsed throughout by PBS buffer and then ready for the SWV characterization together with following AC ECL experiments in the absence of MB monomers in the solution.

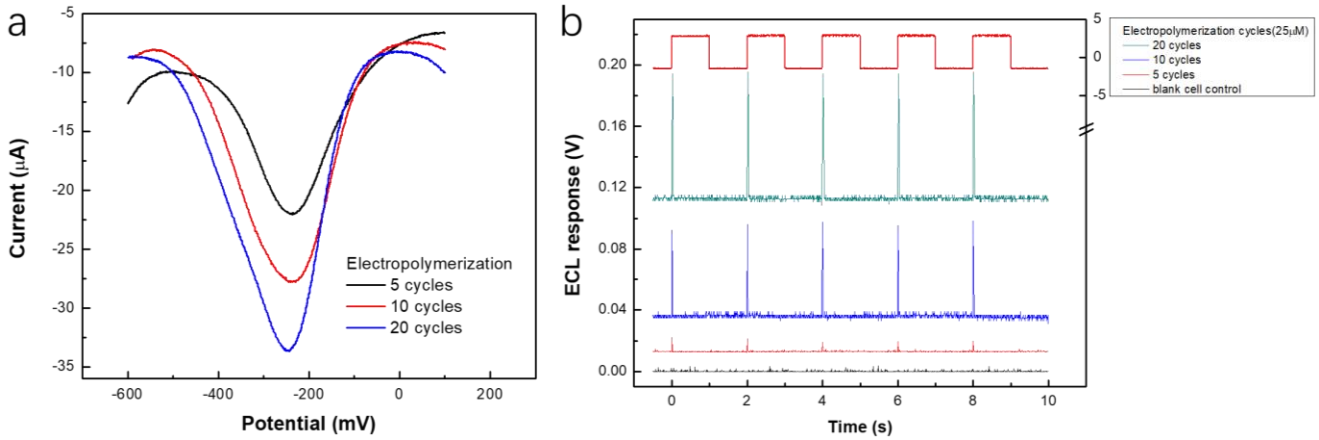

Figure 3.33.(a) SWV characterization of the half BPE after the electropolymerization in 25 µM MB monomer solution for 5, 10, and 15 cycles. (b) Real-time ECL response of the AC bipolar cell of voltage switching between 2.8 and -1.7 V.

The low amount of MB surface loading was achieved by electrochemically sweeping the half BPE in 25µM MB solution the sensing compartment for 5, 10, and 15 cycles. As the number of cycles increases, there will be a larger reduction peak representing more MB polymerized on the BPE as shown in Figure 3.33(a), from their SWV characterization. Figure 3.33(b) shows the typical time-dependent ECL response of different amount of MB loading together with a blank control in pure PBS buffer. The synchronized SW waveform on top has a peak to peak voltage of 5.0 V with an offset at +0.6 V to prevent the undesirable surface oxidation. The real potential generated is alternately shifted between 2.8 and -1.7 V. In the blank control, no ECL signal other than the background is present. After the half BPE was electropolymerized in the MB monomer solution for 5 cycles, there were weak spikes at the beginning of each forward half cycle. With more MB loading on the half BPE as the number of electropolymerization cycles increases to 10 and 15 cycles, the heights of ECL spikes grow up, manifesting a thicker MB film on the BPE gold surface that is also demonstrated by the SWV characterization. The narrow ECL spike probably reflects its fast surface-confined feature of MB film.

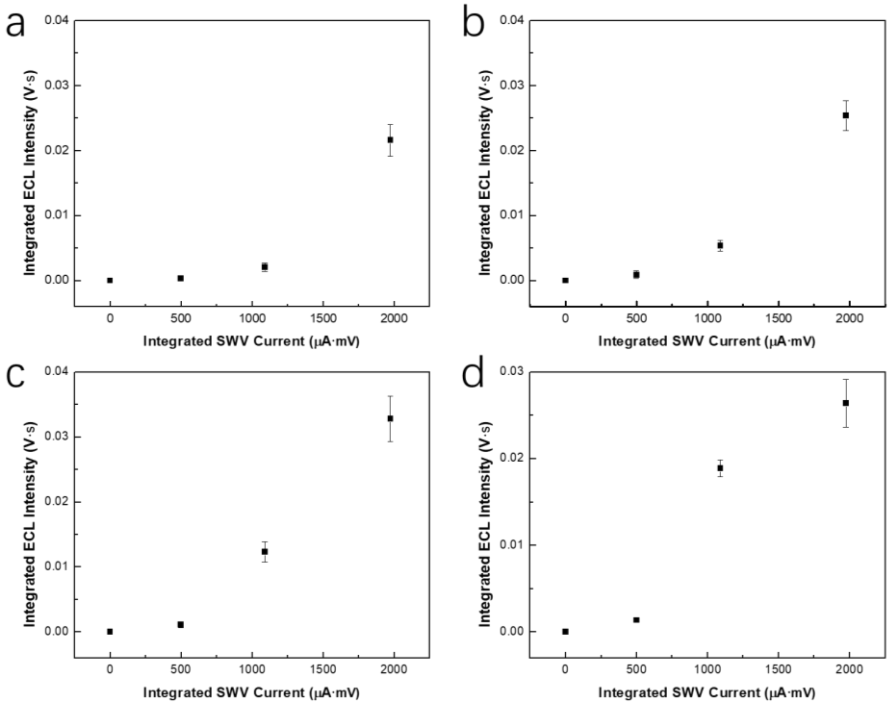

Figure 3.34.Integrated ECL intensity of five square wave cycles for AC BPE cell after the electropolymerization in 25 μM MB monomer as a function of integrated SWV current at (a) 2.6 to -1.7 V (b) 2.7 to -1.7 V (c) 2.8 to -1.7 V (d) 2.9 to -1.7 V.

Figure 3.34 indicates the integrated ECL intensity of five AC cycles as a function of the integrated SWV current signal, which represents the amount of MB deposited on the BPE. The positive potential of the square wave voltage is 2.6, 2.7, 2.8 and 2.9 V from (a) to (d), and the negative voltage is maintained at -1.7 V that is negative enough to oxidize back sufficient MB. As the driving voltage increases, the slope of the intensity-concentration curve rises (from 0.0016 to 0.009 V/μA·mV), reflecting more polymerized MB involved in the reduction by a larger electric field in the BPE system. The ECL signal from 5 cycles of polymerization is not too much higher than the blank control. As a result, a meager amount of MB loading is barely capable of producing enough ECL signal above the cut-off of the PMT.

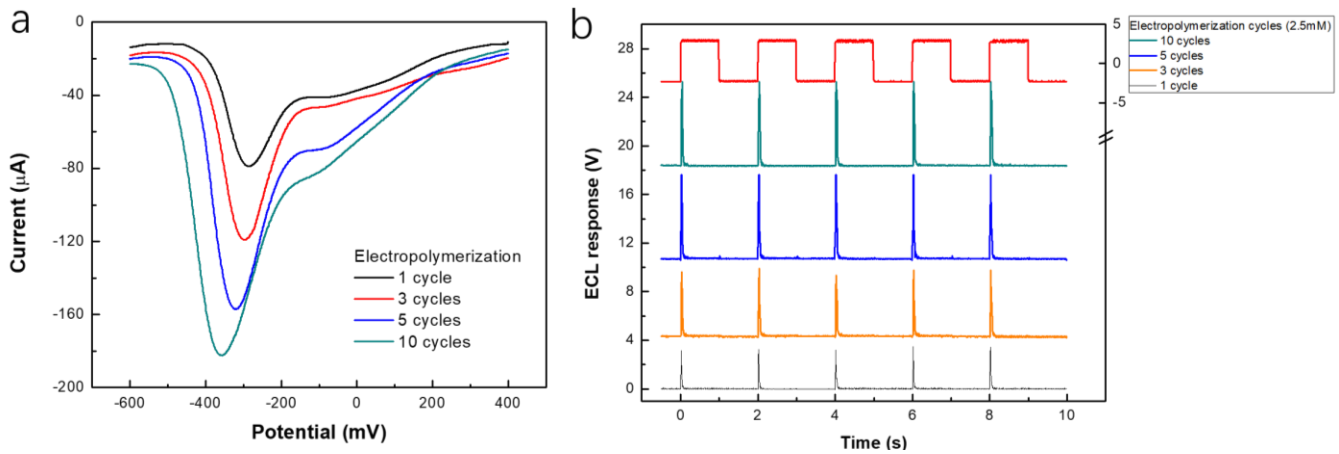

Figure 3.35.(a) SWV characterization of the half BPE after electropolymerization in 2.5 mM MB solution for 1, 5, 10, and 15 cycles. (b) Real-time ECL response of the bipolar cell of voltage switching between 2.8 and -1.7 V.

The high amount of MB surface loading was achieved by electropolymerizing the half BPE in the sensing compartment using a more concentrated MB monomer solution of 2.5 mM at 1, 3, 5, and 10 cycles. A visible color change to blue could be observed by naked eyes afterward. The SWV characterization in Figure 3.35(a) shows enormous reduction peak currents which are proportional to the number of cycles. The small negative shift with more cycles is in agreement with the negative shift of the redox peak of polymeric MB with more cycles during the electropolymerization process. It should be related to the increased charge transfer barrier from a thicker polymer film on the gold electrode surface. Their corresponding ECL responses, as in Figure 3.35(b), are much larger than those electropolymerized using 25μM MB solution. As expected, the height of ECL spikes increases as the number of cycles increases (from the black curve to blue curve). The broadening of these ECL spikes is due to that a long time is required for reducing a large quantity of MB during one AC cycle.

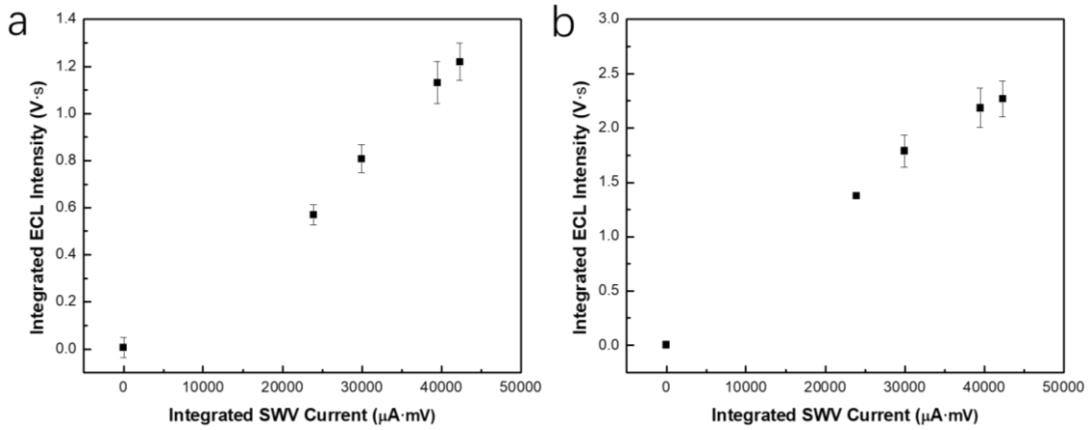

Figure 3.36.Integrated ECL intensity of five square wave cycles for AC BPE cell after electropolymerization in 2.5 mM MB monomer as a function of integrated SWV current at (a) 2.7 to -1.7 V (b) 2.9 to -1.7 V.

In Figure 3.36(a), the resulting integrated ECL intensity of five AC cycles for voltage between 2.7 to -1.7 V, is directly proportional to the MB polymerized on the BPE surface, suggesting an excellent linear correlation in this high loading situation. The slope of the intensity-concentration curve rises with a higher driving voltage, while bends a little at the high loading of polymerized MB (Figure 3.36(b)). In such a high surface loading, the ECL emission starts to be rate-limited by the local concentration and diffusion of $Ru(bpy)_3^{2+}$ at the other half BPE in the reporting compartment.

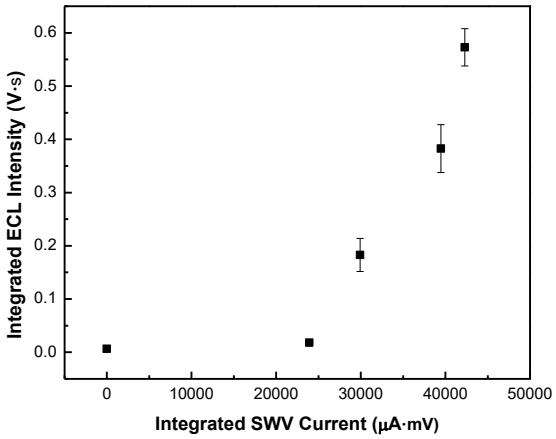

Figure 3.37.Integrated ECL intensity of five square wave cycles for AC BPE cell after electropolymerization in 2.5 mM MB monomer as a function of integrated SWV current at (a) 2.5 to -1.7 V.

Even though the electropolymerization in 2.5 mM MB solution will produce much more polymerized MB on the half BPE surface rather than 25μM, this bipolar cell still requires enough driving voltage to generate measurable ECL emission. As shown in Figure 3.37, when decreasing the positive potential from 2.7 to 2.5 V, even though with a substantial integrated current value about 24000 uA·mV, the collected ECL intensity is very close the background signal. In a word, the ECL intensity may not surpass the detection limit of PMT, by both the reason of small loading of MB polymer and insufficient driving voltage.

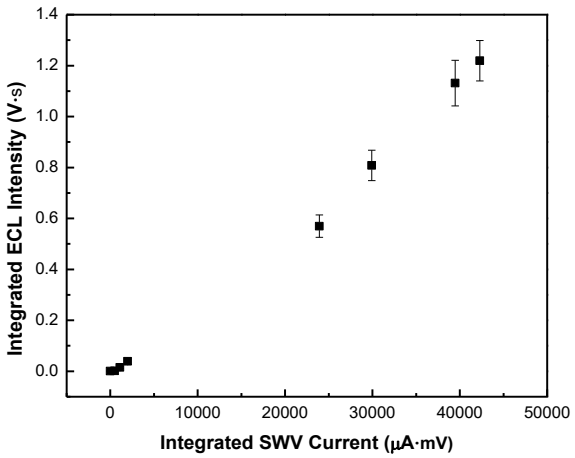

Figure 3.38.Normalized integrated ECL intensity of five square wave cycles for AC BPE cell after combining electropolymerization in both 25 μM and 2.5 mM MB monomer as a function of integrated SWV current 2.7 to -1.7 V.

After combining two sets of ECL experiments of the half BPE electropolymerized in both low and high concentration of MB solution, the calibration curve of ECL emission intensity versus the amount of MB polymerized on the BPE surface can be drawn (Figure 3.38). It displays a perfect linear relationship with well-defined dynamic range of integrated SWV current from 500 to 50000 uA·mV that corresponds to the MB coverage from 3 to 300 pM/cm^{-2}. 10 cycles of electropolymerization in 2.5 mM MB is set as the upper limit for the polymerized MB in this system since more MB loading is difficult

to achieve by the electropolymerization method. When taking the previous section of determining $Fe(CN)_6^{3-}$ from µM to mM concentration into consideration, this system possesses the capability of detecting the analyte in the broader concentration range.

3.3.5 Investigation of MB-DNA for Monolayer Detection

In the previous sections, we demonstrated that either the electroactive species in solution or the polymerized molecule on the BPE surface could be detected by using this AC square wave bipolar ECL system. The protocol is expected to be further extended to the detection of an ultralow amount of redox molecule, such as a self-assembled monolayer. With the help of analyte regeneration through repeatable redox cycling, its sensitivity could be significantly improved by the accumulation of ECL response from each AC cycle. In addition to a good candidate for the electroactive polymer on the electrode surface, methylene blue (MB) is also a very useful biomarker as the signaling redox moiety. For example, via the electrostatic interaction between the cationic charge of MB and negatively charged phosphate backbone, it can bind to the double-stranded DNA via intercalation[158]. Other than intercalation, MB-tagged DNA could exhibit detectable electrochemical signal after self-assembled onto a gold electrode by means of the facile gold-thiol chemistry. A large conformational change would be induced in the confine-surface, altering the electron-transfer tunneling distance between the electrode and the redox label[159]. This type of electrochemical biosensor has been renewed interest of late since the DNA analyte can be encoded into an electrochemical signal for readout. In our experiments, the gold BPE in the sensing compartment was treated by the self-assembly of single-strand thiolated-DNA (T-DNA) via the alkanethiol moiety at the 5′ terminus. Upon the following incubation, 3′-modified MB-DNA was hybridized to the T-DNA, bringing its conjugated MB molecule to the gold surface close enough for the electrochemical current enhancement to achieve monolayer detection, such as the electrochemical proximity assay (ECPA) co-developed in our laboratories[160,161]. Self-assembled monolayers (SAMs) of MB-labeled DNA are thus an excellent model to validate our use of the square wave ECL bipolar electrochemistry. The ECL emission from the BPE end in the reporting compartment would correspond to the reduction of MB molecules in the DNA monolayer on the other BPE end in the sensing compartment. In our experiments, the sensing compartment was filled with HEPEs buffer (10 mM HEPEs, 0.5 M $NaClO_4$, pH=7) instead of PBS buffer, abiding by the solution environment used for incubation. Note that in our previous test, HEPEs buffer could easily form precipitation with $Ru(bpy)_3^{2+}$ ECL solution and destroy the DNA hybridization. It is in another way emphasizes the importance of phase separation using closed BPE system.

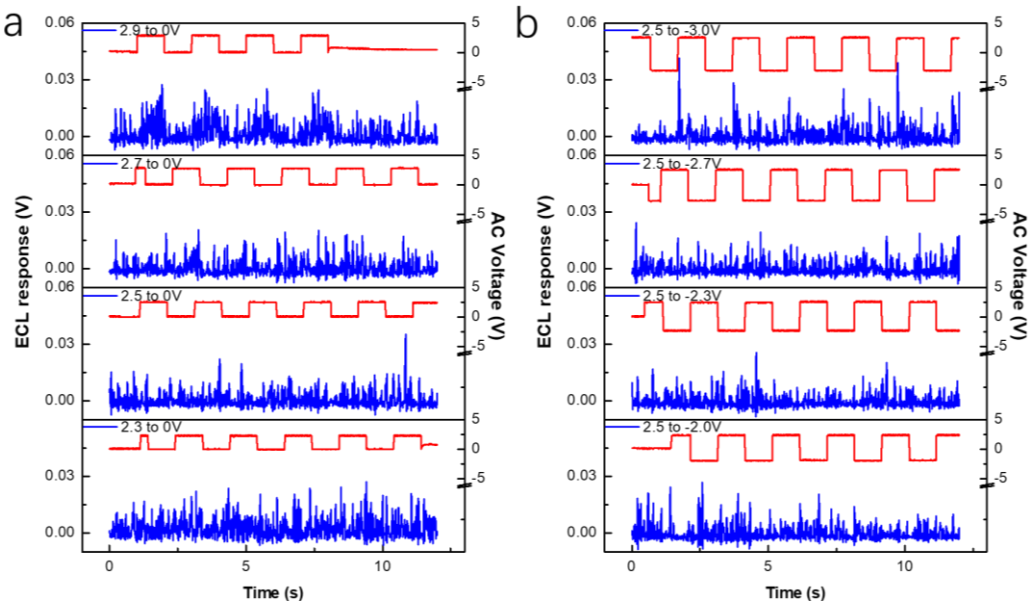

Figure 3.39.The positive and negative potential thresholds investigation using treated BPE cell in 0.1 M HEPEs buffer. (a) the negative potential is kept at zero when increasing the positive potential. (b) the positive potential is kept at 2.5 V when decreasing the negative potential.

The positive and negative potential threshold of the BPE system in the MB-DNA experimental model in HEPEs buffer were investigated to eliminate the possible interference from extreme applied potential by employing control experiments carefully. As shown in Figure 3.39(a), when the voltage in the reverse half cycle is set to be zero, the ECL signal related to H_2 evolution is not observed until a positive potential of 2.9 V. Then the positive potential is kept at 2.5 V while gradually decreasing the negative potential. The ECL signal corresponding to surface gold oxide reduction appears at -3.0 V, that is a much larger negative potential threshold than that in PBS buffer (Figure 3.39(b)).

However, compared to the ferricyanide model and electropolymerized MB model, the DNA assembled monolayer, which is immobilized on the BPE gold surface through a relatively weak thiol-Au bond and following hybridization with the secondary MB-DNA, may not be only affected by the extreme potentials those can lead to H_2 evolution and Au surface oxidation. From the reference literature, the thiol group of the DNA could be oxidized and destroyed much easier before the oxidation of the electrode surface itself[162]. The extreme potential could as well influence the hybridization and the binding affinity between the T-DNA and secondary MB-DNA. A violent side reaction such as H_2 evolution with the bubble formation would necessarily break up the self-assembled DNA monolayer.

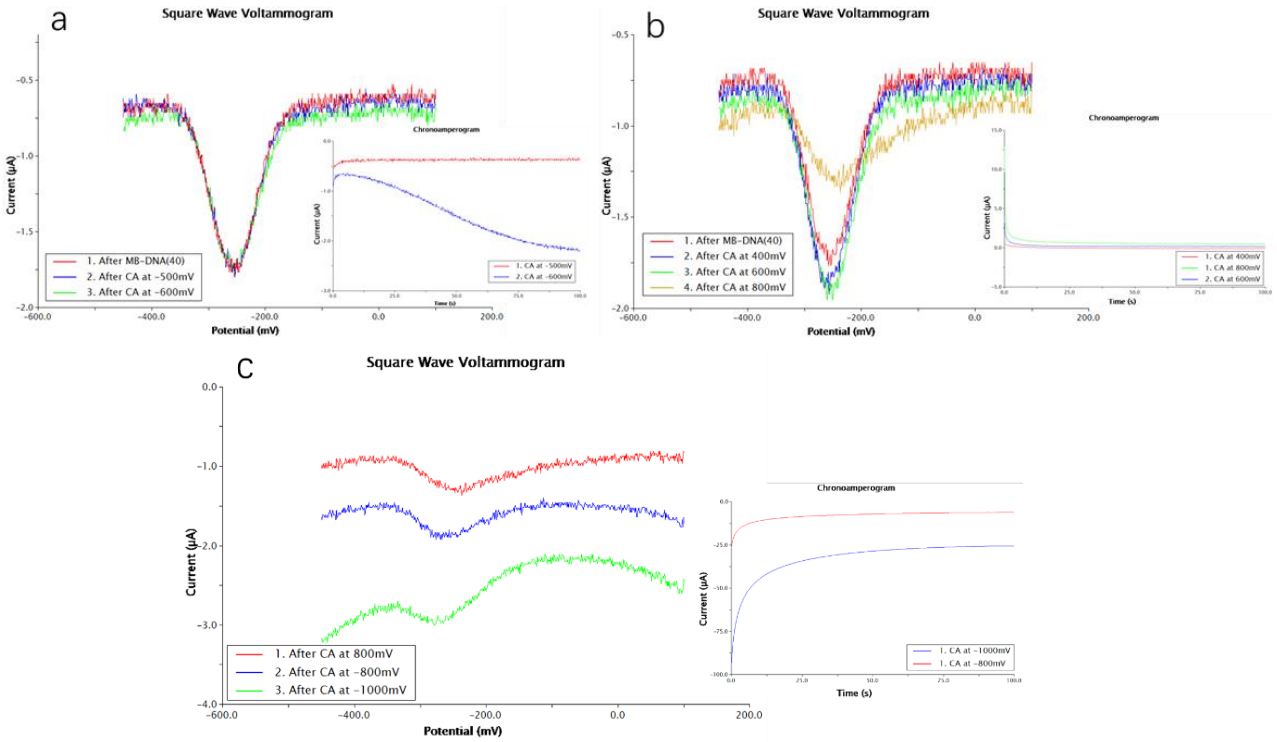

Figure 3.40.SWV characterization of the half BPE immobilization with T-DNA (40) and MB-DNA (40) after (a) CA at -500 mV and -600 mV. (b) CA at 400 mV, 600 mV, and 800 mV. (c) CA at -800 mV and -1000 mV. Inset: the CA curve.

The stability of the self-assembled DNA monolayer was first examined using the half BPE as a working electrode in the conventional three-electrode system. After the T-DNA (40) immobilization, the half BPE was then incubated with MB-DNA (40) followed by the SWV characterization. After that, chronoamperometry (CA) at -500 mV and -600 mV were applied to the half BPE for 100 s, and the SWV was operated again to monitor the change of MB signal as the indicator on the integrity of the assembled DNA layer. Even though -500 mV and -600 mV have already passed the potential of H_2 evolution on the gold surface in pH=7 solution (around -400 mV) and a CA difference was observed in the inset, there is no difference between SWVs afterward. (Figure 3.40(a)). Chronoamperometry at positive potential from 400 mV to 800 mV and following characterizations were carried out similarly. After 600 mV, the MB signal does not change (only a slight shift on the baseline). However, after the CA at 800 mV, a significant decrease in signal is observed, verifying the damage of the DNA assembly (Figure 3.40(b), yellow). Further negative potentials of -800 mV and -1000 mV were applied right away, showing no change in the absolute signal but a downward shift in the baseline of the SWV current (Figure 3.40(c)). We attribute this shift to the H_2 evolution which has more accessibility after the break-up of the monolayer. It can also be proved in the inset in which the result of CA shows a much larger current response than before.

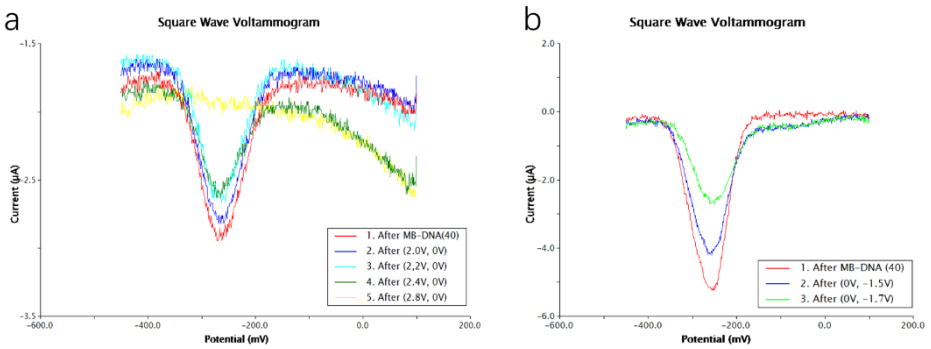

Figure 3.41.SWV characterization of the half BPE immobilization with T-DNA (40) and MB-DNA (40) after (a) positive potential test. (b) negative potential test for 150 AC cycles.

After that, the bipolar ECL experiments were carried out under AC square wave for 150 AC cycles with designated positive and negative potentials using new cells immobilized with MB-DNA (40). At first, the negative potential in the reverse half cycle is kept as zero while gradually increasing the positive potential in the forward half cycle (Figure 3.41(a)). The MB signal decreases a little bit from 1.8 to 2.4 V, while at 2.8 V, almost all the signal disappears. In the reverse case when the positive potential is zero, only at -1.5 V, the signal starts to decrease. At -1.7 V, about 50% of signal disappears (Figure 3.41(b)).

As a result, the DNA monolayer is much easier to be damaged by an oxidation potential (negative) rather than the reduction potential (positive). On the one hand, the thiol bond can be oxidized under a moderate anodic potential, and the T-DNA is then de-attached from the gold surface. On the other hand, even though reaching the cathodic potential for H_2 evolution on the bare gold surface, the densely packed monolayer could block the access of H^+ to the electrode surface and shift its reduction negatively. Also, the mild generation of hydrogen bubbles would not damage the monolayer within a wide potential range.

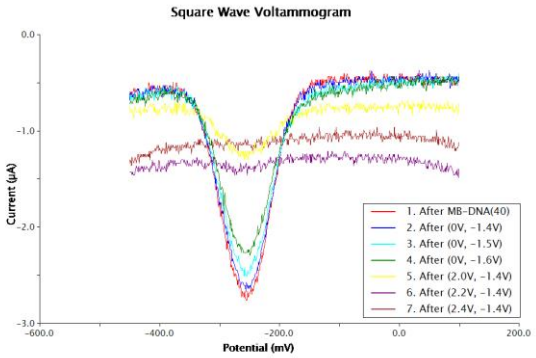

Figure 3.42.SWV characterization of the half BPE immobilization with T-DNA (40) and MB-DNA (40) when both positive potential and negative potential are applied for 150 AC cycles.

When combing the positive potential with the negative potential, the stability of the DNA assembly turns out to be different from the positive potential or negative potential only. As shown in Figure 3.42,

after being applied with a square wave of 0 to -1.6 V, a small decrease in the MB signal is observed. However, when adding the positive potential (2.0 to -1.4 V for example), the signal from MB reduction drops a lot (yellow). Other than the absolute value of the positive potential/negative potential, the total amplitude of the square wave would affect the DNA layer assembled on the BPE surface. A possible explanation of this behavior may be related to the real electric field the BPE experiences in two different conditions. In consideration of the charging effect and double layer formation, every time switching the potential between positive and negative, the pre-built double layer which has a counterions distribution with respect to the previous polarity of the electrode, will then be added into the current electric field provided by the reversed polarity, causing an increase in the electric field in solution compared to only one potential is applied. Also, the fast voltage alternation between cycles may impair the hybridization between T-DNA and secondary MB-DNA.

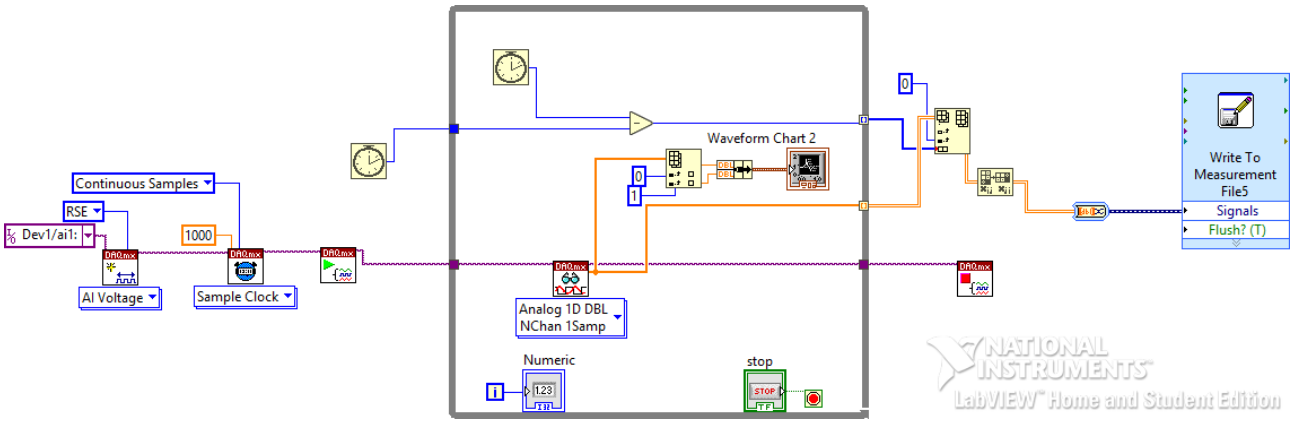

Scheme 3.4.The block diagram in Labview (National Instruments™) for measuring the AC square waveform and PMT signal using the DAQ devices.

With the help of SWV characterization, the ECL experiments were carried out to detect the presence of MB-DNA using the appropriate potential range. In the previous sections regarding the detection of ferricyanide and polymerized MB, the real-time PMT reading and simultaneous AC square wave profile in most cases were recorded by a two-channel oscilloscope for a few numbers of cycles. However, when this square wave bipolar ECL protocol was moved towards monolayer detection, on account for the small amount redox-active analyte confined on the bipolar electrode, information from a large number of AC cycles should be collected for the signal amplification. A multifunction data acquisition system (DAQ) device interfaced with a digital computer was employed instead of the oscilloscope. Synchronized multichannel data acquisition was compiled by the Labview (National Instruments™) visual programming language, as separate channels measuring the analog voltages input from PMT and waveform from generator simultaneously (Scheme 3.4. The continuous measurement was achieved by recording the analog input by one-point sampling in a round-robin mode and convert the index into a 2D array. The sampling rate was set at 1000/s to have enough temporal resolution. At last, the 2D arrays were written out as the .EXL document. For data generated from vast numbers of AC cycles, the integration of individual cycle is no longer applicable. Instead, one-one point addition strategy was

utilized to avoid tedious data processing: Each data point of ECL intensity with the same time-mapping among all the forward half cycles was algebraically added together, the same treatment to all the points from reverse cycles. Finally, collected data from many cycles could be simplified and converged to only one integral cycle. To prepare the calibration curves and calculate standard deviations, ECL intensities were analyzed by Origin 8 with baseline correction, in a specific time domain integration.

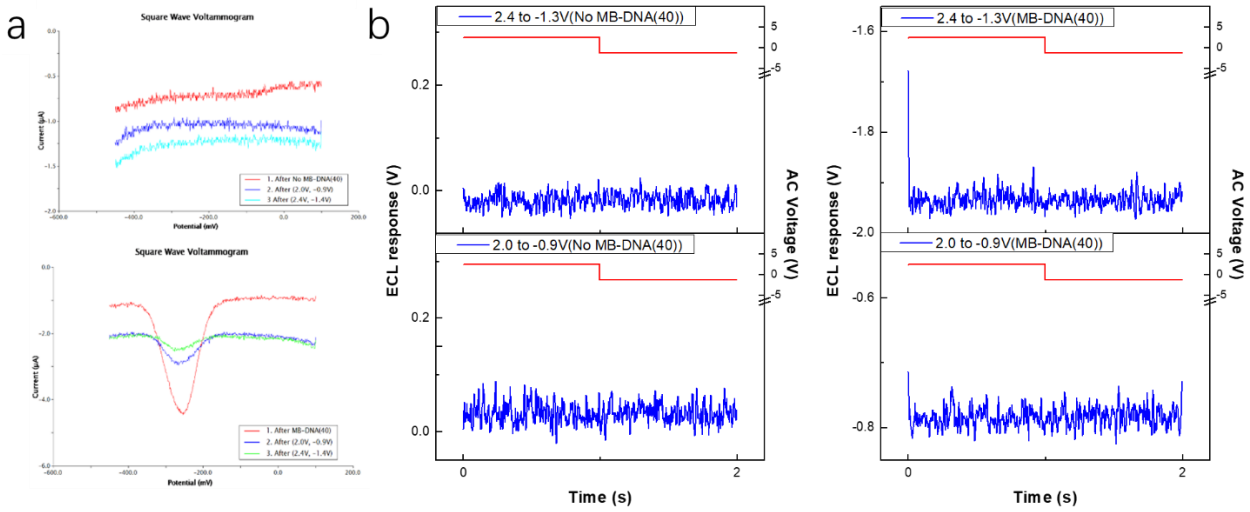

Figure 3.43.(a) SWV characterization of the BPE incubated with No MB-DNA (40) (upper) and MB-DNA (40) (bottom) and after their ECL experiment. (b) Time-dependent ECL response of the BPE incubated with No MB-DNA (40) for 90 cycles. (c) Time-dependent ECL response of the BPE incubated with MB-DNA (40) for 90 cycles.

Instead of using a blank cell or BPE immobilized with T-DNA only, the BPE hybridized with No MB-DNA (40), which has the same sequence yet with no MB molecule attached, is more worthwhile as the control experiment. By this way, the control experiment would have the same double-stranded DNA structure on the BPE surface and the same charge transfer resistance in exception of the MB tag. For example, after the incubation with No MB-DNA, the BPE cell was performed under AC square waves of 2.0 to -0.9 V and 2.4 to -1.3 V (Figure 3.43(b)). Neither of them shows the ECL response other than noise, and their SWV characterizations also have the same feature without any redox peak (Figure 3.43(a), upper) (Only the baseline of the voltammogram shifts downwards owing to increase of the capacitance by the change of DNA assembly). If MB-DNA (40) is incubated, at 2.0 to -0.9 V, there is a small ECL spike at the beginning of the forward half cycle (Figure 3.43(c)). The following SWV characterization shows that after the ECL experiment, 80% MB signal is lost (Figure 3.43(a), bottom, blue). Another ECL experiment carried out at 2.4 to -1.3 V displays a higher ECL spike. Even though a considerable amount of signal has been missing already, the increase of driving force would lead to a higher electrochemical response. Besides, there is a further decrease in the MB signal in a later SWV characterization. The similar effect in Figure 3.42 indicates the damage to the DNA layer by the voltage alternation.

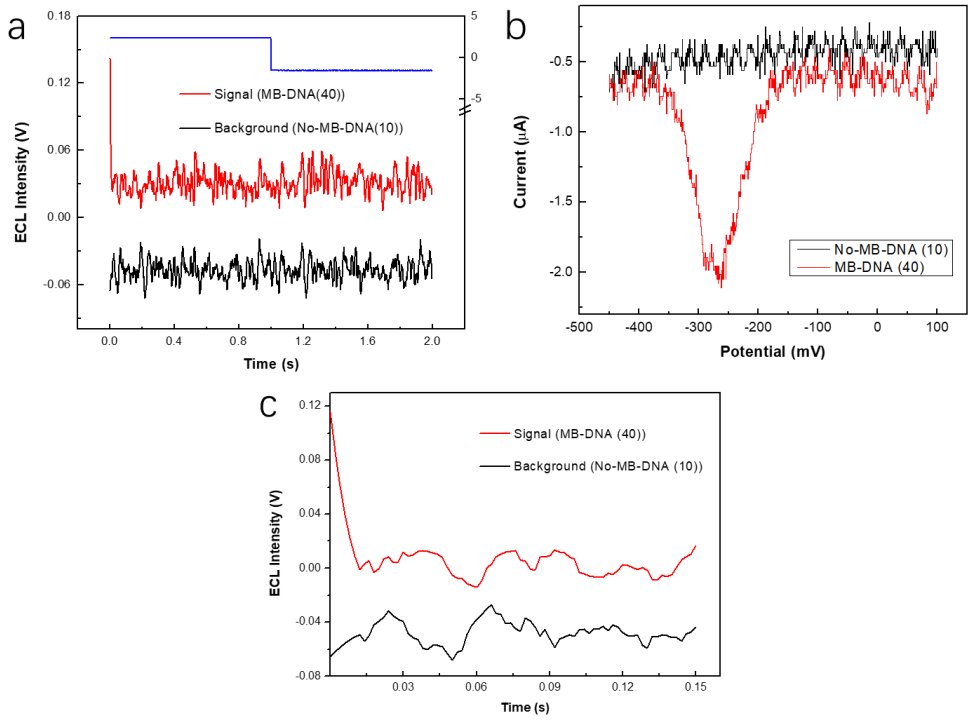

Figure 3.44.(a) Time-dependent ECL response of a complete AC measure-regenerate cycle after one-one addition of 100 cycles for BPE hybridized with No MB-DNA (10) and replaced with MB-DNA (40). (b) Corresponding SWV characterization. (c) 13-point Savitzky-Golay smooth on the raw data (a) in a smaller time domain of 0.15 s.

As a result, it is better to go directly to the threshold voltage instead of gradually increasing the voltage. The more voltage alternation it experiences, the more DNA assembly could be damaged. If slightly increasing the voltage at each run, only a small amount of MB-DNA on the BPE surface can undergo redox reaction, and possibly degrade after some number of cycles. Also, instead of comparing the ECL responses of two separate cells, a more direct control experiment could be done by using the same cell for both DNA assembly. According to this criteria, after the assembly of T-DNA, the first step of a signal-on test was first operated by incubating the BPE in the sensing compartment with a secondary DNA which is 10 base pair match to the T-DNA but without MB attachment, named as No MB-DNA (10). Hence there would be no reduction of MB molecule occurring on the electrode surface to trigger a corresponding ECL emission under a specific voltage. After this ECL experiment, the same BPE was directly added with 1 μM MB-DNA (40) and incubated for another two hours. Relying on the difference in binding affinity of the secondary DNA with respect to the T-DNA, MB-DNA (40) will compete with and finally replace the former No MB-DNA (10). Another ECL experiment was operated just after this replacement with the same applied voltage. Figure 3.44(a) demonstrates the total ECL response versus time after adding 120 cycles together. When the T-DNA assembled on the BPE surface is hybridized with No MB-DNA (10), PMT only collects the background noise under a voltage alternation between 2.4 and -1.5 V(black). While after the replacement, its ECL response shows a narrow spike at the beginning of the forward half cycle (red), indicating the reduction of MB molecule on the secondary DNA. The SWV characterization was performed before each ECL experiment to examine the

background from No MB-DNA (10) and the success of MB-DNA replacement (Figure 3.44(b)). When hybridized with MB-DNA (40), its SWV has a significant reduction peak positioned at about -280 mV, rather than a flat baseline when hybridized with No MB-DNA (10). Figure 3.44(c) represents a 13-point Savitsky-Golay smooth applied to the raw data with a narrowed time domain for a more clear demonstration.

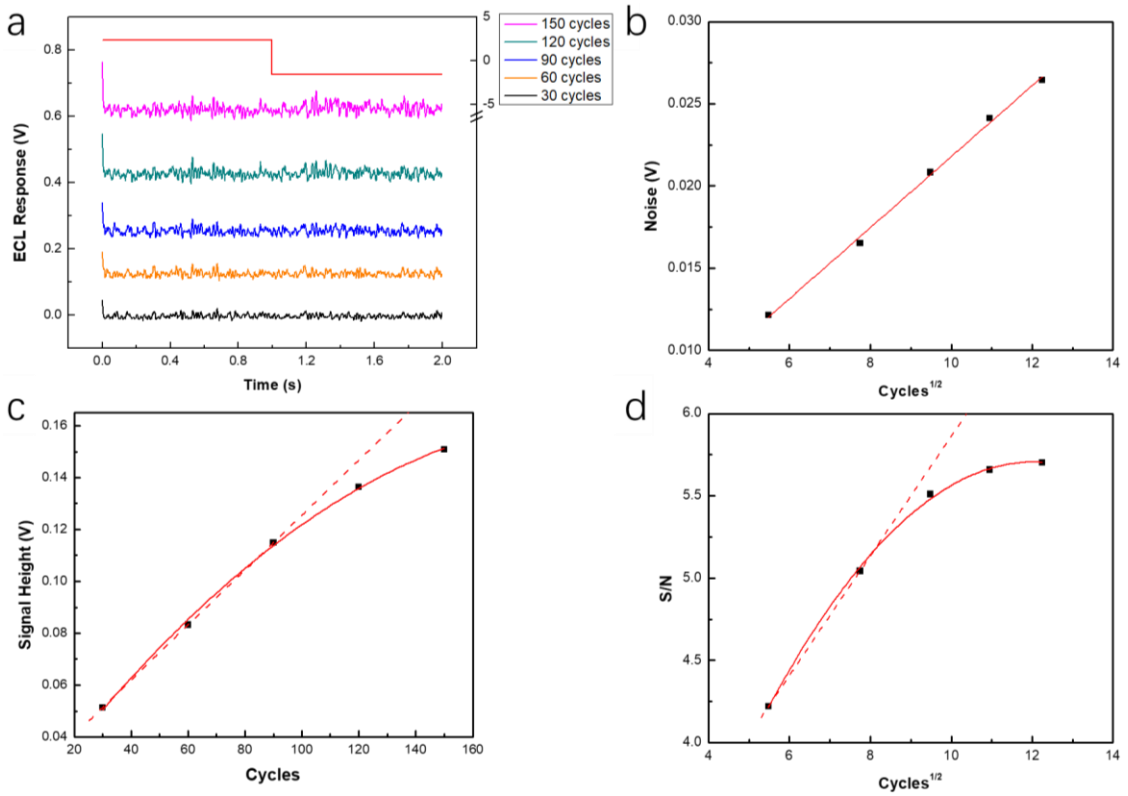

Figure 3.45.Time-dependent ECL response of a complete AC cycle after one-one addition of 30, 60, 90, 120, and 150 cycles after hybridized with MB-DNA (40). (b) The noise (standard deviation) versus cycle$^{1/2}$. (c) ECL signal height versus cycle number. (d) S/N versus cycle$^{1/2}$.

The expectation of signal amplification is validated by comparing the ECL response of a different number of cycles together after the hybridization with MB-DNA (40) (Figure 3.45). As more cycles accumulated, the ECL spike at the beginning of the integral cycle grows up (from black to purple in Figure 3.45(a)). The standard deviations of the background signal from different cycles of accumulation show an exact linear relationship as a function of cycle$^{1/2}$, as expected (Figure 3.45(b)). At the same time, the signal height is showing an increasing trend as a function of the number of AC cycles, indicating the amplified ECL signal with more cycles (Figure 3.45(c)). Figure 3.45(d) illustrates the S/N ratio change versus cycle$^{1/2}$ that has a fast increase at the beginning and then towards a level-off. This deviation from the expected behavior should be from the SAM degradation of the DNA assembly during the application of the AC square wave. According to our previous observation, plausible explanations include the use of multiple voltage alternation, the persistence of side reaction on the BPE surface and the dissociation of MB-DNA.

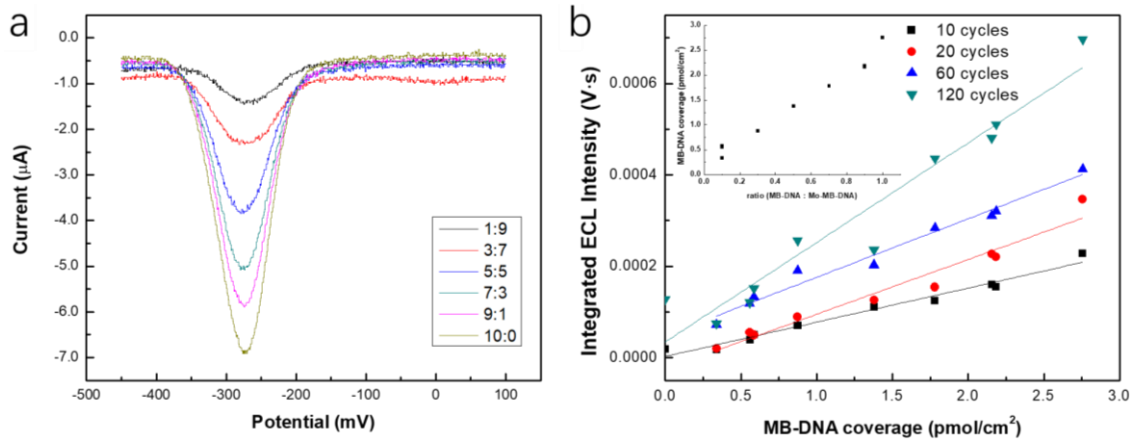

Figure 3.46.(a) The SWV characterization of the BPE immobilized with MB-DNA (40) and No MB-DNA (40) in varying ratio of 1:9, 3:7, 5:5, 7:3, 9:1, 10:0 (after 5-points smooth). (b) Signal-averaged ECL response as a function of MB-DNA surface coverage on the BPE from 10 cycles to 120 cycles. Inset: the relationship between MB-DNA (40) surface coverage and MB-DNA (40): No MB-DNA (40) ratios.

Owing to the benefit of signal amplification, DNA monolayer detection and quantification were finally accomplished by using this AC square wave bipolar ECL system. After the self-assembly of T-DNA on the half gold BPE surface, different quantity of MB-DNA (40) and No MB-DNA (40) were mixed together in ratios (1:9, 3:7, 5:5, 7:3, 9:1, 10:0) to a same final concentration of 1μM/L. These DNA solutions were then used to incubate the BPE surface in a random sequence. Both the MB-DNA (40) and No MB-DNA (40) are 40 base pair match to the T-DNA with a same binding affinity, so their relative ratio can easily adjust the MB-DNA present in the monolayer. SWV was employed to quantify the amount of MB-DNA hybridized on the BPE surface with the current peak height ranging from 0.5μA to 6μA, corresponding to an MB-DNA (40): No MB-DNA (40) ratio from 1:9 to 10:0 (Figure 3.46(a)). In order to obtain the actual surface coverage of MB-DNA, parallel cyclic voltammetry was also carried out along with SWV to acquire the relationship between the MB-DNA quantify and integrated SWV signal (MB-DNA quantity = Q_{CV} / 2F). As the ratio of MB-DNA (40) grows, it exhibits a higher current corresponding to a better surface coverage of MB-DNA (40) (Figure 3.46(b), inset). Figure 3.46(b) demonstrated the typical co-added time-dependent ECL response in different cycle numbers. The integrated ECL intensity is obtained by only integrating the ECL signal from 0 s to 0.05 s in the forward AC cycle. Remarkably, a strong dependence of ECL intensity on surface coverage of MB-DNA in the calibration curve is depicted, with an excellent linear correlation. As more cycles accumulated, there would be an enhanced ECL response together with a larger slope in its calibration curve. Based on the ECL readout, this sensing system possesses a limit of detection (LOD) as low as 300 fmol/cm^{-2}. Even though it is a closed system, there is still a slight potential gradient present in the BPE cell. It could be possible that not the whole surface area immobilized with MB-DNA that participates in the reduction/oxidation. The actual detection limit may be even lower.

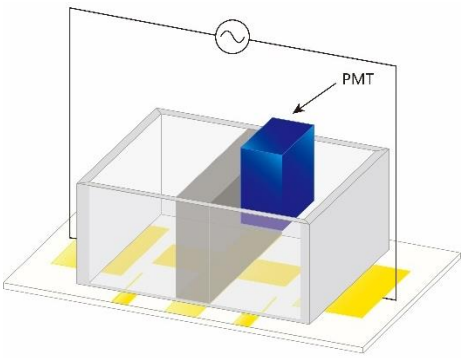

Scheme 3.5.Illustration of modified AC square wave bipolar ECL cell with probes measuring the solution potential difference.

As we mentioned in the previous section in the AC bipolar ECL sensing in ferricyanide and polymerized MB, the electric field study was represented by measuring the solution potential difference between two created probes in the sensing and reporting compartments (Scheme 3.5). Specifically, a second DAQ deck solitarily used for the potential difference measurement is suggested instead of having two analog input channels for in the same decks. There are three modes in the measurement configuration in the data acquisition device, differential (DIFF), nonreferenced single-ended (NRSE), or referenced single-ended (RSE). The Diff mode is usually used to measure the "differential" voltage between two separated points across the individual element in an electrical circuit. The latter two both belong to the ground reference method in which the voltage is measured with respect to a common ground point. Often, these "grounds" are stable and most commonly around 0 V. Historically, the term ground originated from the usual application of ensuring the voltage potential is at 0 V by connecting the signal directly to the earth. The ground reference is provided by either the device taking the measurement or by the external signal being measured. When provided by the device, this setup is called the ground referenced single-ended mode (RSE), and when provided by the signal, the setup is called the non-referenced single-ended mode (NRSE). The type of signal sources determines the selection of measuring mode to use. For a floating signal source which has an isolated ground reference point, Diff mode is preferred. The ground reference of a floating signal must be connected to the ground of the device to establish a local or onboard reference for the signal. Low-level signal (less than 1 V) in a noise environment is particularly well-suited for Diff mode. For a ground referenced signal source, which has been already connected to the building system ground, the common ground point of it, should be adapted to the RSE model. Non-isolated outputs of instruments and devices that plug into the building power system fall into this category. The difference in ground potential between two instruments connected to the same building power system is typically between 1 and 100 mV. By appropriate connections to the ground signal source, the ground potential difference can be eliminated from the measured signal.

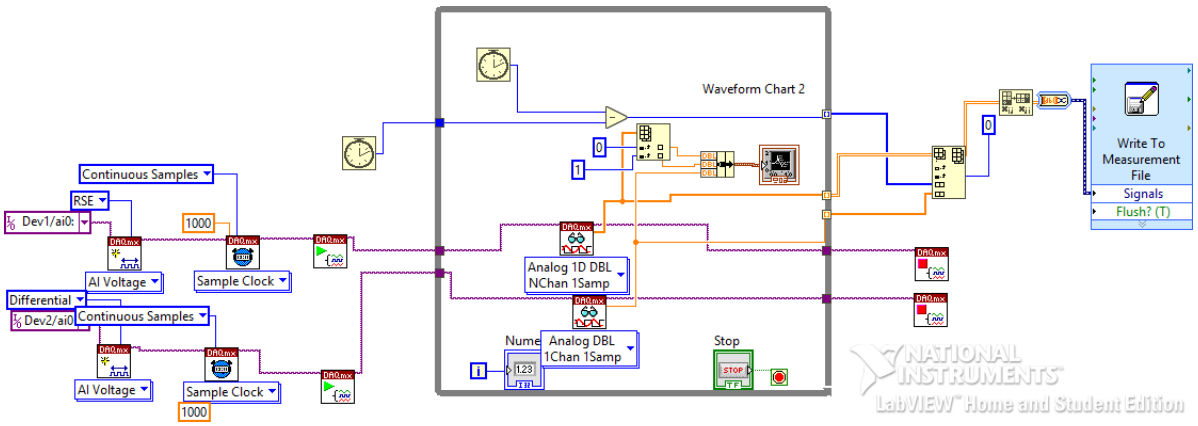

Scheme 3.6.The block diagram in Labview (National Instruments^{TM}) for measuring the AC square waveform and PMT signal together with solution potential measurement in a secondary DAQ device.

In our system, the analog voltage input from PMT was measured in the mode of RSE, since its power source is grounded through the building power system. The AC square wave input was also measured in a separate channel using the RSE mode in which the negative terminal of the generator is grounded. However, when measuring the solution potential difference through the probe, the RSE mode is not suitable anymore. The potential difference between the tips of two probes in solution, resembling the differential voltage between two separated points in an electrical circuit, works as a floating signal source. As a result, a Diff mode is necessary. If the potential difference measurement is operated in a third channel still using RSE mode, one of the probes would be biased to the same ground as one of the driving electrodes. It will lead to a double-driving electrode configuration in which the probe behaves as another closer driving electrode to the BPE that affects the electric field distribution in solution. In another aspect, in the Labview (National Instruments^{TM}) program, only consistent input terminal configurations can be executed by one DAQ device. Otherwise, an error message would export. Consequently, a secondary DAQ device was thus solitarily used for the potential difference measurement. These simultaneous measurements, even with two DAQ decks, could be synchronized in the same time domain and available for comparison. Scheme 3.6 shows the flowchart of the program.

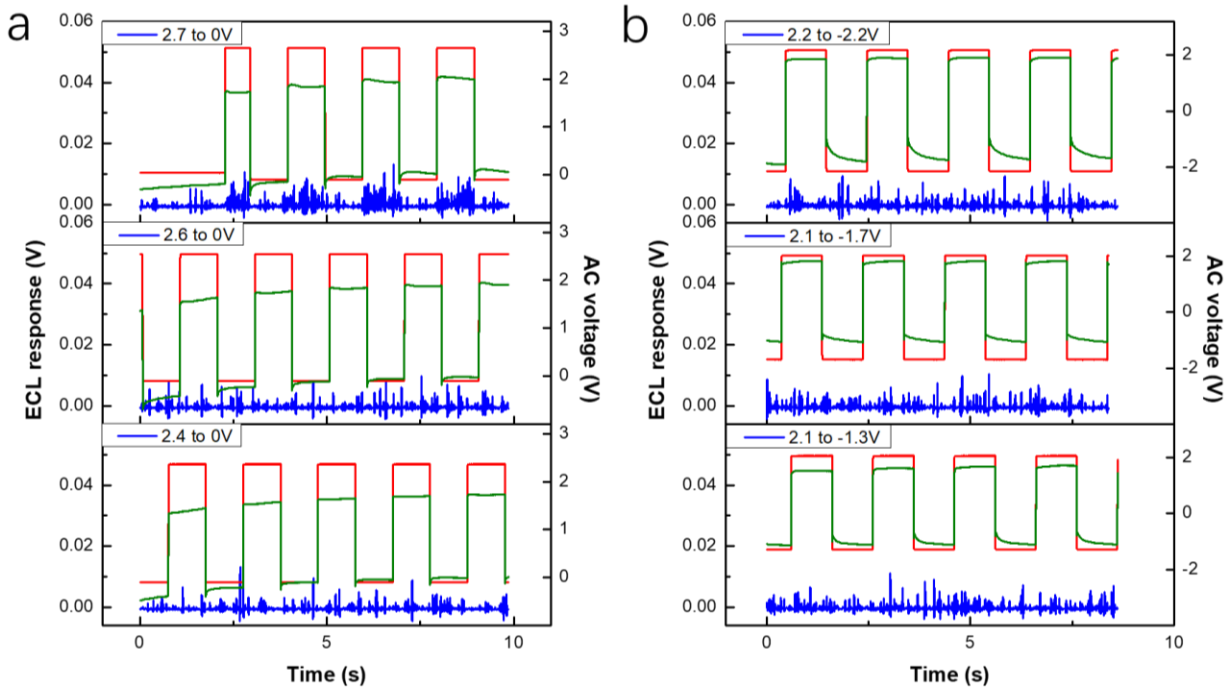

Figure 3.47.The real-time ECL response, applied AC voltage, and measured solution potential (a) with only increasing positive potential. (b) decreasing the negative potential while maintaining the positive potential.

In order to understand the influence of applied voltage and frequency on the real electric field in the AC bipolar system, a systematic study was carried out by the solution potential measurement. A blank cell without the DNA assembly on the surface was used as the simple model under a frequency of 500 mHz. First, the solution potential was measured under the AC voltage which had only positive potential in the forward half cycle (2.4 to 2.7 V) but zero potential in the reverse half cycle(Figure 3.47(a)). What we can observe is that in each forward half cycle, the measured potential difference (green) is about 0.5 to 1 V less than the applied positive potential. That should be the interfacial potential on the driving electrodes and small solution IR drop. While in the reversed half cycle, the measured potential is quite close to zero as we expected. Note that when the number of cycle increases, the measured potential difference in the forward half cycle increases. In another way, the electric field in the solution shifts positively as the number of cycles increases. It could also be manifested by the increase in ECL signal over cycles at 2.7 to 0 V due to an enhanced driving force. In this case, the electric field needs time to increase and then be settled down at a stable value. The possible explanation should be the requirement of time to fully positive charge driving electrode and build up the double layer at the interface. However, the behavior changes when introducing the negative potential in reverse half cycle. Figure 3.47(b) shows a negative potential difference in the reverse half cycle instead of a zero value (Figure 3.47(b)). Even though there is still a difference between the measured potential difference and applied voltage, it becomes much smaller (less than 0.3 V) than positive potential only. In the meantime, the measured potential difference can be settled down initially without running multiple AC cycles. It seems like the application of the negative potential plus the positive potential would contribute to a steady electric

field. Since the interfacial potential at the driving electrodes and solution IR drop keep the same in both cases, the increase in measured potential difference is assumed to be the local enhancement of electric field at the driving electrode. For example, upon the sudden alternation to a driving anode, in addition to the positively charged driving electrode, the positively charged double layer from last half cycle, will also contribute to the electric field before its break-up, leading to a local electric field enhancement.As discussed in the previous section, the onset voltage and ECL response of this system also rely on frequency. Low frequency would result in a lager ECL signal than the high frequency with the same applied voltage due to its higher electric field in the solution. However, high frequency also has its advantages such as much faster measurement speed and more cycles accumulation. More importantly, because of the minimized time interval of each half cycle, the tendency of DNA monolayer to be damaged by hydrogen evolution and gold oxidation is suppressed. In such a small time interval, the small amount of surface-confined analyte could be resolved without the participation of other side reactions. For example, it is plausible to use a positive voltage which is higher than the threshold value of hydrogen evolution. The fast AC cycle alternation will essentially only involve the surface reaction in a short period before the bulk H+ can diffuse to the BPE surface. Based on this assumption, 100 Hz was used instead of 500 mHz to testify it detectability on the DNA monolayer. The sampling rate of the DAQ deck was changed from 1000 per second to 10000 per second to ensure enough data points collection in such a high AC frequency.

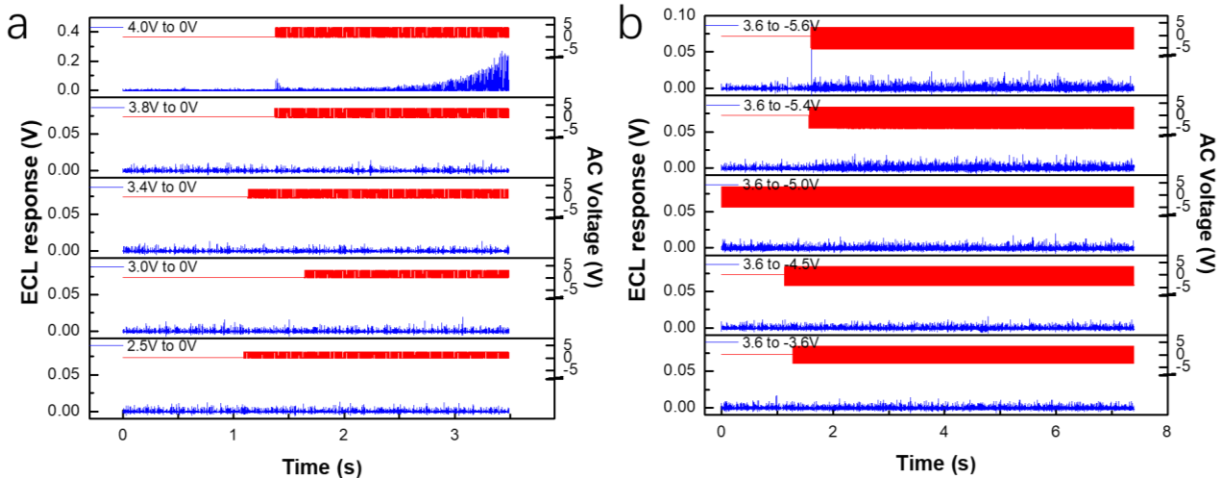

Figure 3.48.The positive and negative potential thresholds investigation using treated BPE cell in 0.1 M HEPEs buffer at 100 Hz. (a) the negative potential is kept at zero when increasing the positive potential. (b) the positive potential is kept at 3.6 V when decreasing the negative potential.

In the beginning, the control experiment of potential threshold investigation was performed in this frequency range. As shown in Figure 3.48.(a), when the negative potential in the reverse half cycle is zero, there is no observable ECL signal from H_2 evolution until the positive potential increases to 4.0 V. This value is much larger than in the frequency domain at 500 mHz of which is around 2.6 to 2.8 V. After that, the positive potential is maintained at 3.6 V while gradually decreasing the negative potential (Figure 3.48.(b)). The potential threshold is found at around -5.4 to -5.6 V which is incredibly much

more negative compared to the one at 500 mHz. As a result, at high frequency, both the onset voltage for H_2 evolution and AuO oxidation are enlarged. It may also suggest a less extent of damage to the DNA assembly a smaller time interval.

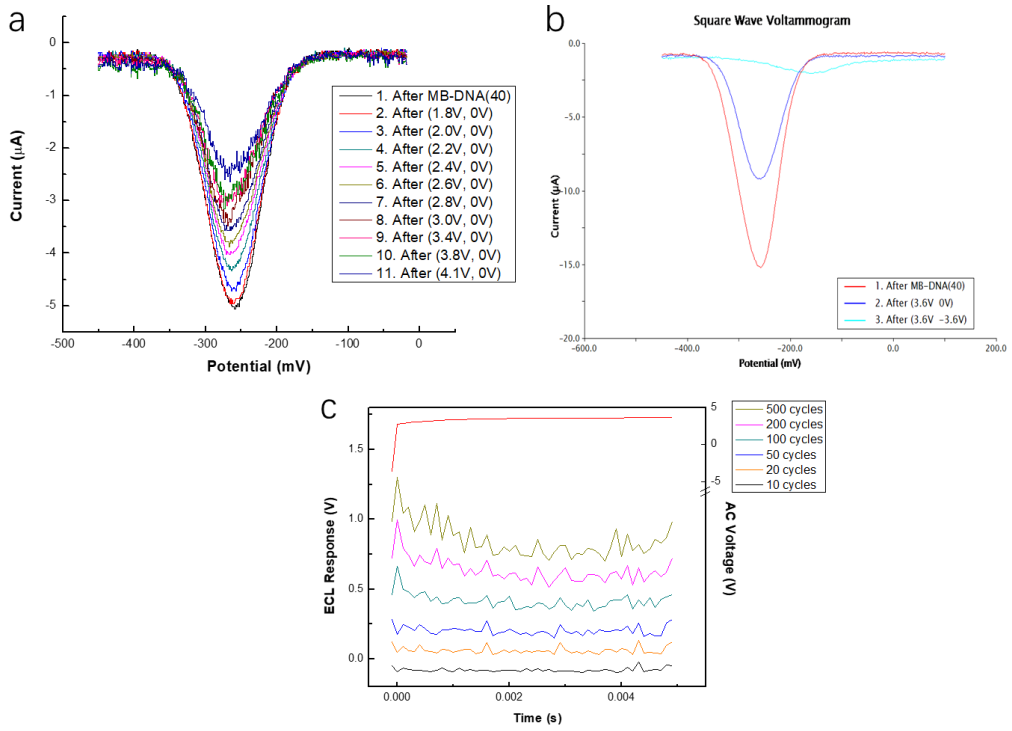

Figure 3.49.(a) SWV characterization of the half BPE immobilization with MB-DNA (40) at 100 Hz under (a) positive potential test. (b) when the negative potential of -3.6 V is applied. (c) Time-dependent ECL response of it at a square wave of 3.6 to -3.6 V at 100 Hz.

Similar to what we did before, the stability of self-assembled DNA monolayer was tested out under AC square wave with designated positive and negative potentials. In Figure 3.49(a), when setting the negative potential at zero, as the positive potential changes from 1.8 to 4.1 V, there is a gradual signal decrease from the reduction of MB. Even after 4.1 V, about 40% of the signal remains. This large positive potential. In Figure 3.49(b), after directly applying a square wave between 3.6 to 0 V, the signal for MB keeps about 60%. However, when the square waveform is shifted from 3.6 to -3.6 V, more than 90% of the signal is lost. The voltage waveform and corresponding ECL emission were collected by the DAQ devices using a much higher sampling rate of 10000/s. The time-dependent ECL response is described in Figure 3.49(c) with varying cycles of integration from 10 to 500. There is no ECL signal peak observed with the integration of cycle number below 50. When collecting more than 100 cycles, it shows an apparent peak at the beginning with an uplifting of the baseline. We treated the baseline shift first as the overspread of the ECL response in such a rapid measurement. Nonetheless, it turned out to be a problem related to the collecting instrument.

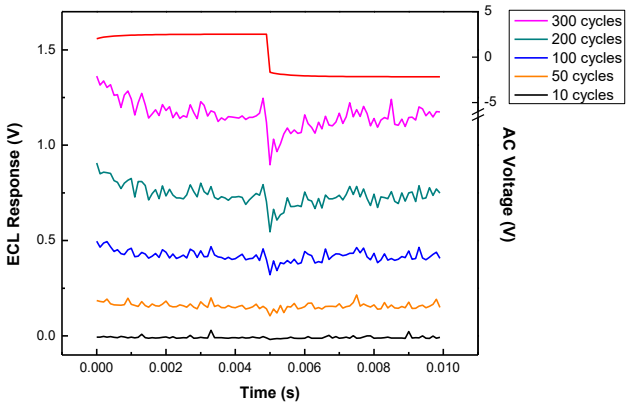

Figure 3.50.Collected time-dependent ECL response of an empty cell without the solution at a square wave of 2.5 to -2.2 V at 100 Hz.

A verification experiment was performed using an empty BPE cell without any solution filling inside. Both the ECL response and potential profile were recorded as a “control experiment” while still applying the AC square wave at 100 Hz. As shown in Figure 3.50, when hundreds of cycles are counted, an uplift of the baseline in the front end of the forward half cycle appears. Also, at the time of potential inverse, a sudden jump down in the background occurs.

As we see, as the number of cycles increases, the positive cycle will accumulate the positive response and the negative cycle will accumulate the negative response from the instrument itself. We owe it to the possible noise coupling from an improper measurement configuration or the inter-analog channel crosstalk (ghosting) of the DAQ devices. Regarding the noise coupling, for example, the conductive coupling can be eliminated or minimized by breaking ground loops (if any) and providing separated ground returns for both low-level and high-level, high-power signals. In our system, if selecting RSE modes as the input configuration of both the PMT and AC generator, the PMT output would share the same ground with the generator as well as the DAQ deck. At each time the applied voltage is reversed, the remaining charges in the channel monitoring the AC generator may interfere with the PMT signal channel.

The ghosting happens when the signal source has a high impedance. High source impedance on a scanned channel causes its settling time to increase. The small internal capacitance on the analog-to-digital converter (ADC) combines with the high source impedance to create a low pass filter. As the source impedance increases, so do the time constant of this filter and thus its settling time. As the multiplexer switches from one channel to the next, the capacitor starts to charge from the voltage of the previous channel to the voltage of the connected channel. If the impedance is too large, such as the PMT source which is measured, the capacitor will not be charged (or discharged) to the correct voltage and will show remnants from the previously scanned channel. Reducing the sampling rate and increasing the interchannel delay to allow enough settling tie for the amplifier could solve it, but it is not accepted

in our high-frequency ECL experiment. Alternatively, using another DAQ device for simultaneous sampling is optimal to solve the ghosting by avoid multiplexing.

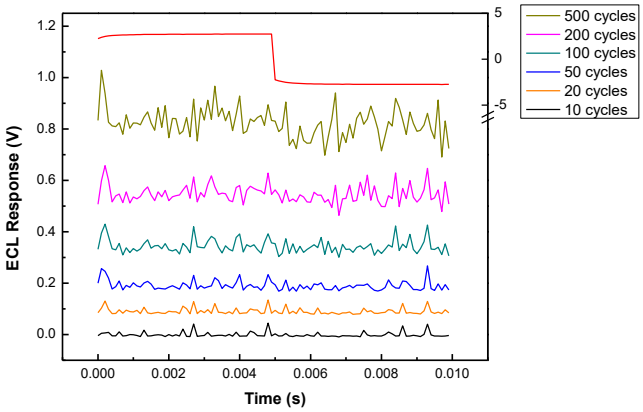

Figure 3.51.Time-dependent ECL response of a complete AC cycle at 2.7 to -2.5 V after one-one addition of 10, 20, 50, 100, 200, and 500 cycles after hybridized with MB-DNA(40).

By using two DAQ devices with one only for the potential difference measurement, the issue from the signal crosstalking was finally solved. Figure 3.51 shows the typical result with ECL peaks at the beginning of the forward half cycle, and more important, in the absence of the baseline upshift and sudden jump at the moment the potential is reversed. Signal amplification from cycles accumulation is achieved with less time used, compared to the experiment at 500 mHz. As the number of cycles increase, the ECL emission peak at the starting point of the cycle grows up, indicating an improved S/N ratio. The AC voltage here is altered from 2.7 to -2.5 V, revealing an expanded potential window. In the high-frequency scenario, the MB-DNA could be relatively stable on the BPE surface even with more AC cycles and high applied voltage by both the reason: (1) the minimized time interval prevents the monolayer to be damaged by other reaction and voltage alternation. (2) the less total operation time of the lowering down the opportunity of MB-DNA to dissociate from T-DNA in buffer solution.

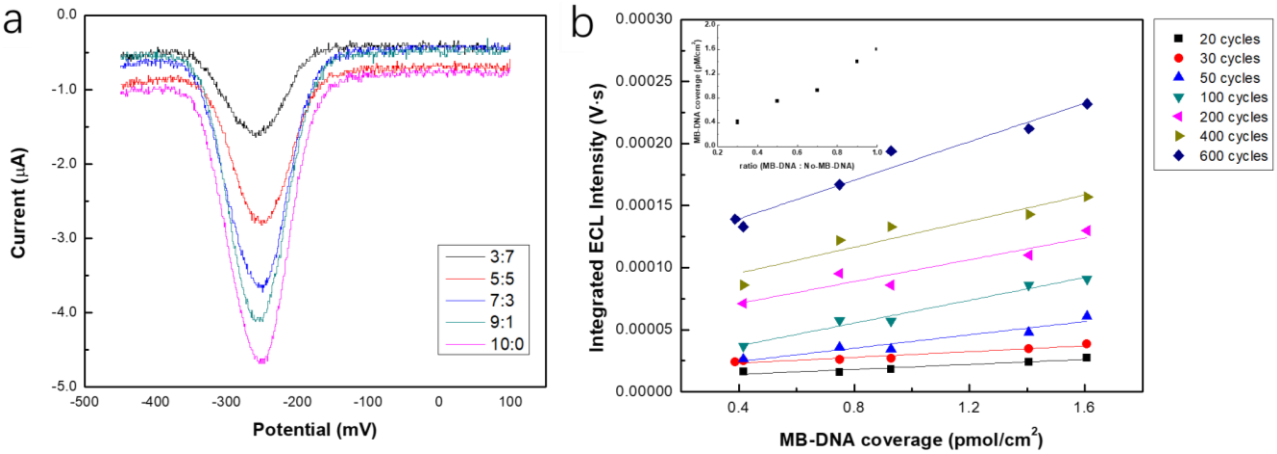

Figure 3.52.(a) The SWV characterization of the BPE immobilized with MB-DNA (40) and No MB-DNA (40) in ratios of 3:7, 5:5, 7:3, 9:1, 10:0 (after 5-points smooth). (b) Signal-averaged ECL response as a function of MB-DNA coverage on the BPE from 20 cycles to 600 cycles. Inset: MB-DNA (40) coverage versus MB-DNA (40): No MB-DNA (40) ratios.

DNA monolayer quantification is achieved by the same way of incubating the T-DNA modified half BPE with MB-DNA (40) / No MB-DNA (40) mixture in ratios of 3:7, 5:5, 7:3 and 10:0 in a random sequence. Figure 3.52(a) indicates the enhanced SWV peak current as the ratio of MB-DNA (40) increases. After the ECL experiment, the integrated ECL emission intensity was calculated by integrating the ECL response within the first 2ms in each AC cycle. In the calibration curve in Figure 3.52(b), the ECL intensity is directly proportional to the amount of MB-DNA in the monolayer. For a few numbers of AC cycles, it shows a very weak ECL signal and also a flat slope versus the MB-DNA loading. While for a large number of cycles, the ECL response is significantly enhanced and the slope of the calibration curve increases as expected.

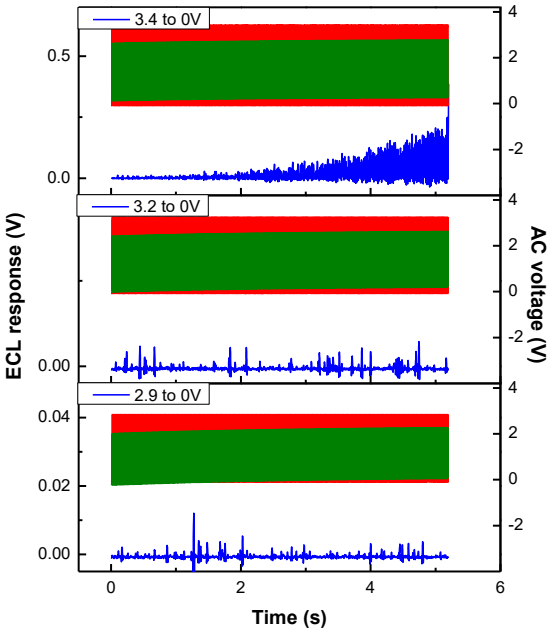

Figure 3.53.Real-time ECL response, AC square waveform and the measured potential difference with only positive at 100 Hz.

A similar electric field study was also carried out at a high frequency of 100 Hz. Due to the fast alternation of the voltage, a sampling rate of 10000/s must be used to ensure enough sampling points. When only the positive potential was applied, clearly, the measured potential difference in the forward half cycle gradually increases with more AC cycles, and then reaches a relatively stable value as the upside of the green segment approaching the upside of the red segment (Figure 3.53, the reason of the colored segment is because of hundreds of AC cycles packed together). It confirms the progress of positive charging of driving electrodes accompanying with also the upward shift of negative potential in the reverse half cycle. When increasing the voltage from 3.2 to 3.4 V, the ECL response corresponding to H_2 evolution appears and shows a growing trend versus time. This higher requirement of the positive potential is in agreement with our conclusion that the electric field in the AC bipolar system deteriorates as a function of frequency.

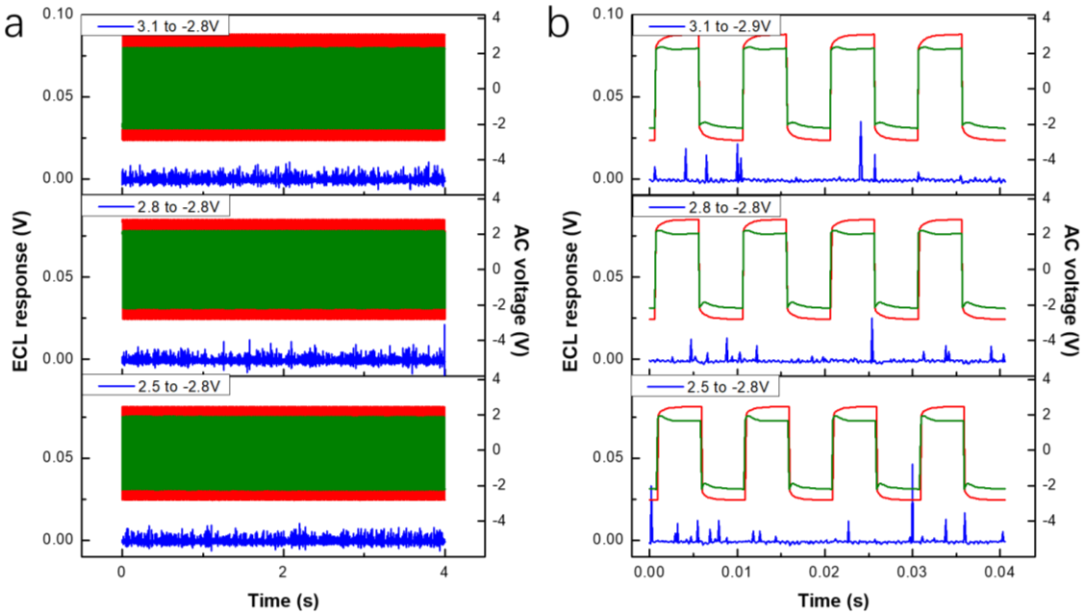

Figure 3.54.(a) Real-time ECL response, AC square waveform and the measured potential difference with both positive and negative potential at 100 Hz. (b) the expanded time window of 0.04 s.

In the case that both positive potential and negative potential are both present, the potential difference between the red and green waveform is minimized a lot. The behavior of the measured solution potential difference is quite stable from the beginning to the end in hundreds of cycles, that is similar to the behavior at low frequency as well (Figure 3.54(b)). A zoom-in in Figure 3.54(b) shows a more clear result in a millisecond, with a closer value between the measured potential difference and the applied voltage in the forward half cycle as in the 500 mHz test.

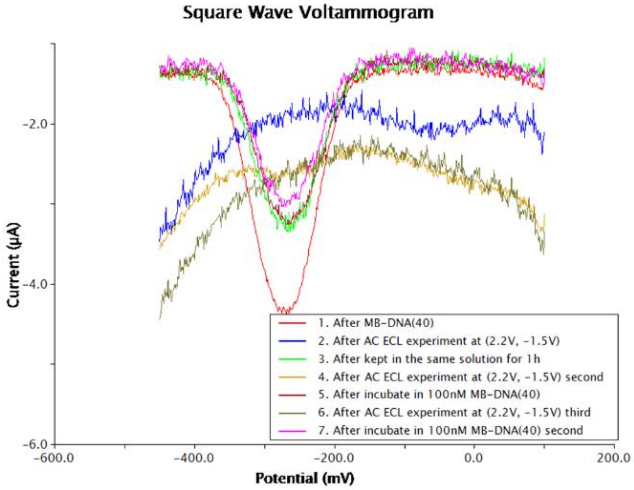

Figure 3.55.The stability exploration of DNA monolayer assembly by SWV characterization right after AC ECL experiment and re-incubation. (a) AC frequency at 500 mHz.

The stability of DNA monolayer was investigated under the influence of AC square wave. Since the DNA assembled monolayer on the gold BPE consists of two DNA molecules: T-DNA and MB-DNA, of which the damage that the AC square wave in the ECL experiment created is not evident. The confirmatory experiment was carried out by comparing the reduction peaks of SWV right after the AC

ECL experiment at 500 mHz and waiting for a re-incubation in solution (Figure 3.55(a)). In the beginning, after the T-DNA immobilization and MB-DNA (40) hybridization, it shows the largest reduction peak (in red). Then a secondary SWV characterization was operated right after an ECL experiment with AC square wave between 2.2 to -1.5 V. It shows a background baseline with no signal from MB reduction temporarily. However, when keeping the BPE in the same HEPEs solution for 1 h, the reduction peak of SWV recoveries a lot (green). It suggests the MB-DNA comes back to the gold surface when the BPE stays in the same HEPEs buffer. While during the ECL experiment, the applied AC voltage "peel off" the DNA assembly and make it diffuse into the bulk solution. The partial recovery seems to suggest not all MB-DNAs can re-assemble on the surface. It may be either the reason of the loss of T-DNA which can not be immobilized again without the presence of a concentrated T-DNA pool, or the de-hybridization of MB-DNA which can not form the complex in quite low concentration. To confirm that, a subsequent ECL experiment was then done using the same voltage. Again, it shows a baseline value with no MB reduction peak (yellow). After that, the half BPE was re-incubated in 100 nM MB-DNA (40) for 4 h. As a result, the SWV reduction exhibits exact the same value before the subsequent ECL experiment (wine). The same recovery under a sufficient MB-DNA pool supports the idea that the AC voltage leads to a permanent loss of T-DNA. Since all the MB signal is temporarily missing after the ECL experiment, the AC voltage in cycles de-hybridizes all the MB-DNA and detaches some of the T-DNA. Since the first ECL and secondary ECL share the same AC square wave, there is no more loss of T-DNA in this circumstance. It could explain why the recoveries of MB reduction signal in the original HEPEs buffer and MB-DNA solution are the same. A third ECL experiment and another re-incubation of MB-DNA shows a similar result as the second one, further confirming our conclusion.

3.3.6 Investigation of DNA Loop for the ECPA Model

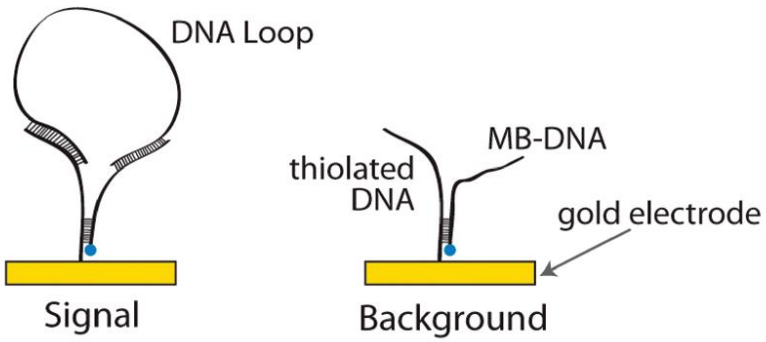

Figure 3.56.DNA loop-base model for ECPA. The background is modeled by simply adding MB-DNA without the loop[160]. Reprinted with permission from [160]. Copyright © (2012) American Chemical Society.

From previous experiments and corresponding calibration, the sensitivity and reproducibility of our AC square wave bipolar ECL system have been validated by the successful quantification of the MB-DNA monolayer assembled on the BPE surface. In the process towards the final goal of direct ECL readout

of the separation-free, point-of-care diagnostics of a specific analyte such as protein, DNA, RNA. A simplified experimental model used in the electrochemical proximity assay (ECPA) technique invented by our and the collaboration group[160] was then addressed in the following research (Figure 3.56). In the ECPA technique, to sensitively quantify the protein, T-DNA, MB-DNA, and two antibody/aptamer arms are utilized. Instead of MB-DNA (40), MB-DNA (10) which was ten base pair match to the T-DNA served as the secondary DNA with electrochemically active MB label. The binding affinity of MB-DNA (10) to T-DNA is significantly reduced with a much lower percentage of MB-DNA hybridization if only these two strands are present. In the presence of the target protein, a five-part complex is formed. The electrochemically active label, methylene blue (MB) is moved close to the electrode surface by the proximity effect that dramatically strengthens the hybridization between T-DNA and MB-DNA, inducing a considerable electrochemical signal enhancement. The simultaneous recognition of the target molecule by a pair of affinity probes would increase the effective concentration of active label. In the simplified model, the DNA loop (80 nucleotides) which is 10 base pair match to the T-DNA and 20 base pair match to the MB-DNA(40) forms a three-part complex with the T-DNA and MB-DNA. This DNA loop mimics the formation of ECPA complex, under an assumption that probe affinity for the target protein is infinite.

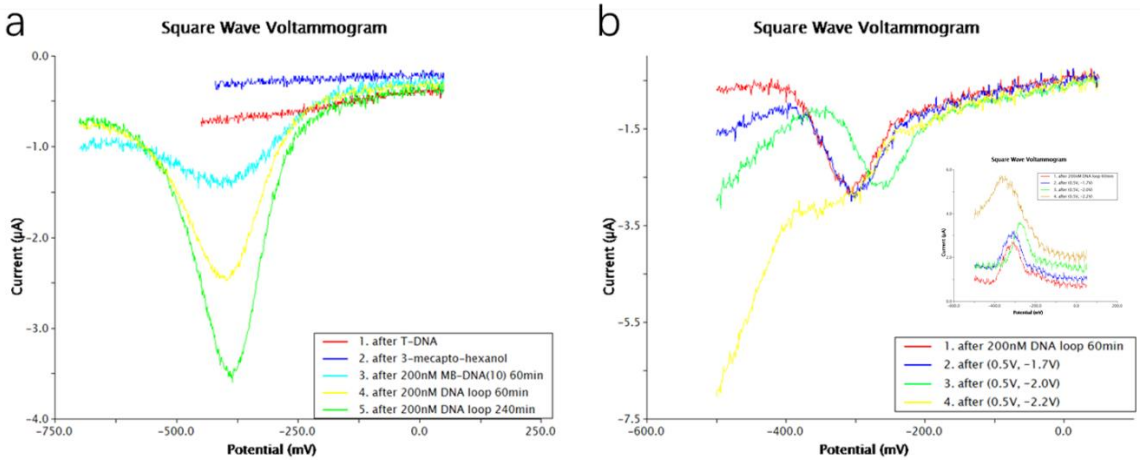

Figure 3.57.(a) SWV characterization of the BPE after each process of incubation: T-DNA, 3-mecatohexanaol, MB-DNA (10) and DNA loop. (b) SWV characterization before and after the negative potential test. Inset: ∓ scan.

Since the gold BPE used in our AC square wave ECL cell is different from the standard gold electrode employed in the literature of ECPA, we developed a modified protocol. Different concentrations of MB-DNA (10) in an aliquot of 100 μL was used as the first incubation solution for 60 min, following by the SWV characterization. After that, a second aliquot of the incubation solution with DNA loop and MB-DNA (10) together in an equal concentration as before, was added on top of half BPE to form the probe-target complex. After the hybridization, the MB molecule immobilized by the proximity effect was re-quantified by SWV. Figure 3.57(a) shows that after the incubation with 200 nM MB-DNA (10), the reduction peak changes from the baseline to about -1.3 μA as the background. With the addition of

the DNA loop, there is a significant peak current increase to -3.0 μA. A longer time incubation of 240 min would further contribute to the electrochemical response. The stability of the DNA complex was also tested by applying the AC square wave to the BPE incubated with 200 nM loop (Figure 3.57(b)). We maintain the positive potential at 0.5 V while decreasing negative potential. Different from the behavior in the previous section that the double-stranded DNA complex starts to dissociate at -1.6 V, now the signal from MB keeps surviving at -2.0 V. Even at -2.2 V, the reduction peak of MB is still present but overlapped with the other reduction reaction, which should be H_2 evolution. The remaining of MB is validated in the negative to positive scan where the oxidation peak heights are always the same, even though with an upshift of the baseline after -2.2 V (Figure 3.57(b), inset). The expanded negative potential threshold for the probe-target complex may be due to a larger mass of this new assembly, and the more densely packed DNA layer would retard the oxidation of the thiol bond.

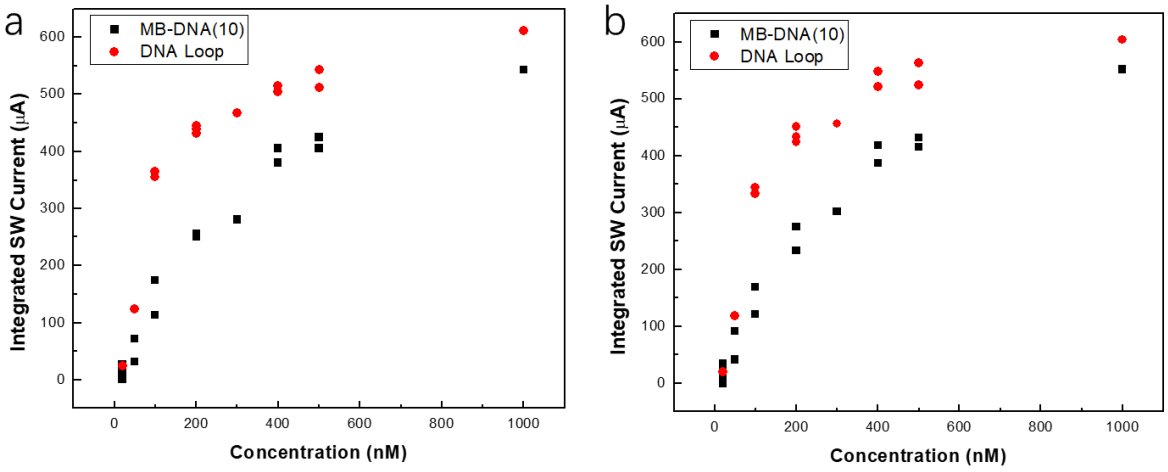

Figure 3.58.The integrated SWV current of the BPE incubated with MB-DNA (10) only for 60 min (black) and DNA loop for 120 min (red). (a) reduction peak (b) oxidation peak.

The resulting SWV currents after MB-DNA (10) only and after the addition of DNA loop were integrated and plotted as a function of MB-DNA (10) and loop concentration. The significant difference appears in the concentration range between 50 to 300 nM (Figure 3.58). After that, the relative enhancement becomes smaller since the use of too much MB-DNA (10). MB-DNA (10) concentration below than 20 nM can not show the current peak even in the presence of the loop. In the ECPA using a standard gold electrode, the concentration of MB-DNA was controlled at 15 nM in an aliquot with a volume of 200 μL. The calculated total MB-DNA amount was about 1.8×10^{13} molecules in the incubation solution. According to the literature, the theoretical surface coverage of hybridized DNA with 100% efficiency was roughly 4×10^{12} molecules/cm^{2}[163]. In this standard gold electrode with 1 mm in diameter, the total amount of MB-DNA is about 15 times more than the requirement of full coverage. Since our half BPE is about 6 times larger than the surface area of the standard gold electrode, the MB concentration below 20 nM would not provide enough MB-DNA for hybridization even under the proximity effect.

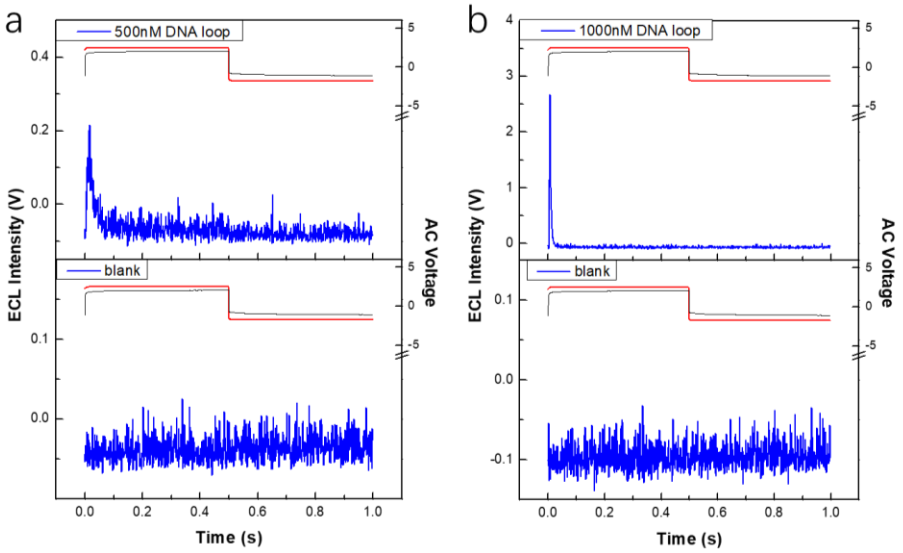

Figure 3.59.Time-dependent ECL response of the BPE cell in blank condition and after DNA loop incubation at 2.6 to -1.3 V for 100 cycles of MB-DNA (10) and loop concentration of (a) 500 nM (b) 1000 nM.

Corresponding ECL experiments were carried out after the DNA loop incubation for 120 min under the AC square wave switched between 2.6 to -1.3 V. From the previous section, we realized that the ECL emission tended to be quite weak and indiscernible from the background fluctuation, especially in the case of low MB-DNA coverage. In an attempt to amplify the signal, we keep the ambient oxygen dissolved in the HEPEs buffer without degassing. After the reduction of MB, O_2 with a more positive reduction potential should be able to oxidize the MB^- back to its oxidized form chemically and catalyze the electrochemical reaction. On the other hand, thanks to the better stability of the three-strand complex, ECL signal of repeatable MB reduction could be accumulated with more measure-regenerated AC cycles to improve the performance of this system. As shown in Figure 3.59, an obvious ECL peak is present at the beginning of the forward half cycle with loop concentration of 500 nM or 1000 nM. The magnitude of the ECL emission is significantly enhanced compared to the result from the previous work.

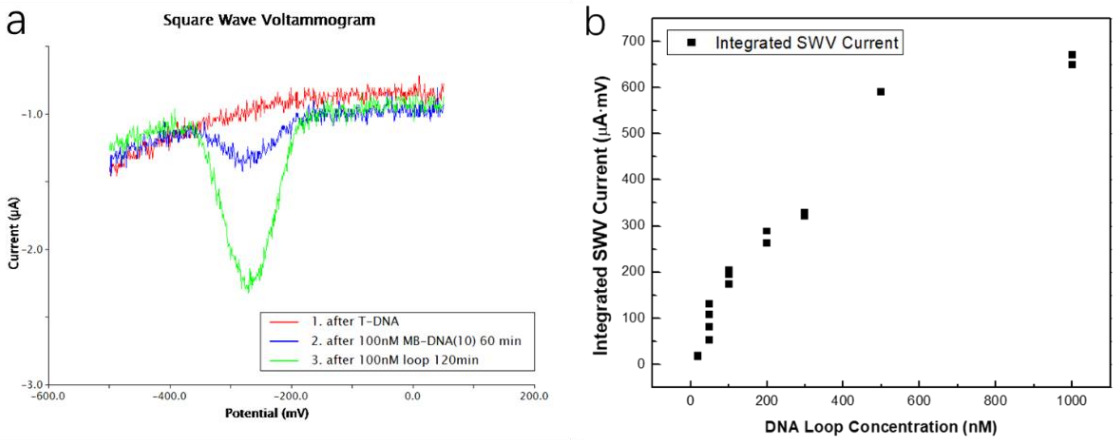

Figure 3.60.SWV characterization of the BPE after each process of incubation: 1 μM T-DNA, 100 nM MB-DNA (10), and 100 nM DNA loop. (b) The calibration plot of the integrated SWV current as a function of DNA loop concentration for 120 min using different cells.

Higher concentration of MB-DNA (10) always gives a higher signal. However, the proximity effect only lies in the differentiation between the background in MB-DNA only and the presence of the target DNA loop. Based on Figure 3.59, MB-DNA (10) concentration of 100 nM was selected for incubation to ensure a considerable difference between the background and after the loop incubation. After incubated with it for 60 min, then the same BPE surface was added with different concentrations of DNA loop with MB-DNA (10) concentration still at 100 nM for 120 min. Figure 3.60(a) shows an example of the SWV data for a loop concentration at 100 nM. After its addition of 100 nM loop, the signal (green) increases a lot to about -2.8 µA compared to the small background response (blue). The calibration plot is drawn in Figure 3.60(b), with the same concentration of MB-DNA (10), as the DNA loop concentration increases, the integrated SWV current increases in a gradual bend curve.

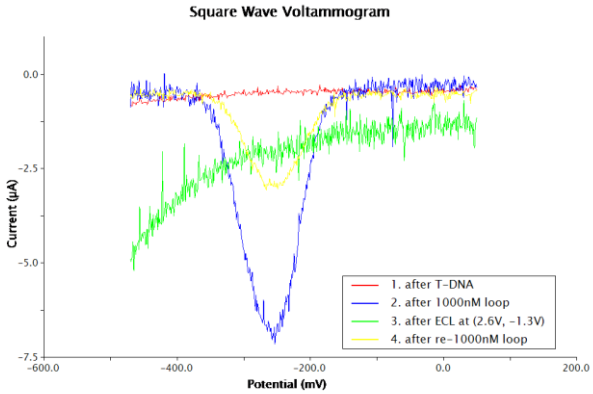

Figure 3.61.SWV characterization of the BPE after incubation with 1000 nM DNA loop, after ECL experiment with square wave application and after re-incubation.

The ECL experiment was carried out immediately after the incubation of the DNA loop at 1000 nM at the AC square wave potential switched between 2.6 and -1.3 V. As shown in Figure 3.61, no MB signal could be observed right after the application of square wave, while it recovers to about 40% after the re-incubation. It again confirms that the MB signal loss is not only from the de-attachment of T-DNA but also from the dissociation of MB-DNA and DNA loop after many voltage alternations.

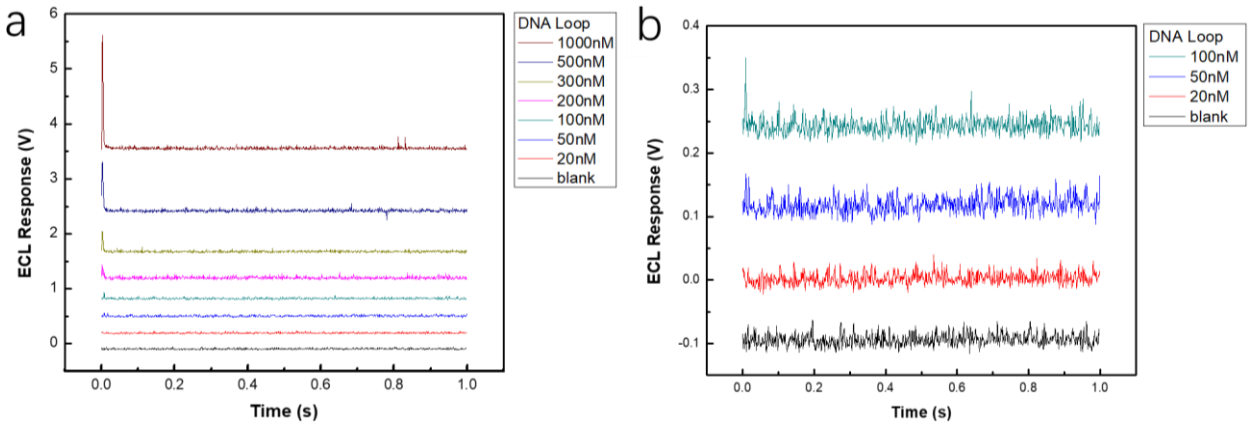

Figure 3.62.(a) The overlapped time-dependent ECL response for varying DNA loop concentrations at AC square wave potential of 2.6 to -1.3 V after one-one addition for 100 cycles. (b) concentration range from 0 to 100 nM.

The corresponding time-dependent ECL responses for varying DNA loop concentrations were overlapped together in one plot in Figure 3.62(a). With a higher loop concentration, the ECL spike at the beginning becomes higher also, indicating more MB molecules are involved in the reduction. In the expanded picture for low-concentration range in Figure 3.62(b), below 50 nM it is hard to distinguish between the real signal and the background fluctuation.

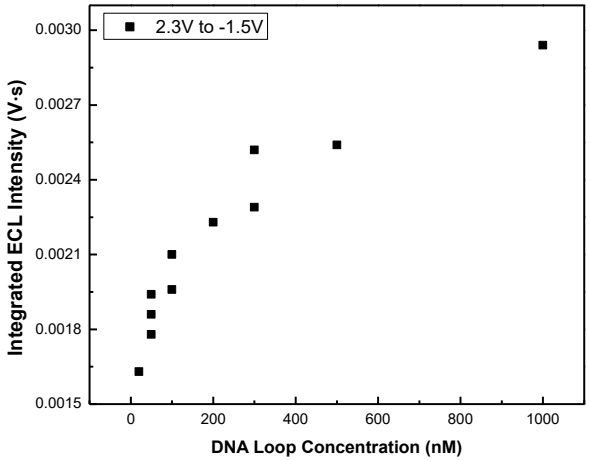

Figure 3.63.The calibration plot of the integrated ECL intensity as a function of DNA loop concentration for 120 min using different cells.

At last, we calibrate the ECL responses integrated from 100 cycles versus the loop concentration (Figure 3.63). An increase in DNA loop concentration would lead to a larger ECL signal in the plot and mimic the same trend as in the SWV response shown in Figure 3.60(b). By using this direct ECL readout, it is capable of detecting the DNA loop level at least of 50 nM with a dynamic range up to 1000 nM.

3.4 Conclusions

An electrochemiluminescence (ECL) sensing system based on a closed bipolar electrode (BPE) configuration has been developed using the AC square wave excitation with high sensitivity. The BPE cell consists of a bipolar electrode fabricated by photolithography and two separate compartments constructed using the 3D printing technique. The closed configuration allows a wide variety of redox-active analytes to be detected in the sensing compartment without chemical interference from the reporting compartment and background ECL emission on the driving electrode, greatly expanding the applicability of the ECL reporting system. A redox-initiated change in the analyte at the one end of the closed BPE is directly read out by a photomultiplier tube (PMT) above the other end where ECL is occurring. In contrast to conventional bipolar sensing systems that are controlled using the DC voltage, the AC square wave technique described herein allows an electroactive analyte to be regenerated by applying a reverse potential during a second half cycle. Significant signal amplification can be achieved by accumulating ECL signals over multiple measure-regenerate cycles. Using $Fe(CN)_6^{3-}$ as a representative analyte, we demonstrated the basic working principle for diffusion-based systems with a

detection limit of several μM. To model surface-confined analytes, electropolymerized methylene (MB) thin films were characterized. In the following step, we presented the ability to detect < 300 fmol MB-conjugated DNA assembled on the BPE at both low and high frequency, proving its capability as a sensitive biosensor of detecting monolayer level analyte through the ECL. At last, the DNA loop as a model target for the ECPA system was studied using the AC square wave bipolar ECL system. A loop concentration above 50 nM could be well-resolved by the ECL spike after cycles integration. The stability of the DNA assembly and the influence by AC voltage was studied. In addition, the frequency-dependent electric field distribution in the AC bipolar cell was revealed. It turned out to be affected by the double layer charging and uncompensated resistance on both driving electrodes and the BPE. This detection system is extremely flexible, capable of detecting a wide variety of analytes over a broad concentration range, and even amenable for monolayer detection as well as protein quantification via the ECL readout, showing great promise in numerous analytical applications.

Chapter 4 Preliminary Studies on Improving the Performance of the AC Square Wave Bipolar ECL System

The experimental section follows the same protocol in Section 3.2; additional information is described in each of the following sections respectively.

4.1 Carbon Electrode

Molecular diagnostics has expanded rapidly in the past decades with the development of more sensitive, faster, and simpler methods. Among all the methods, radioactive labels are extremely sensitive but have apparent disadvantages of short shelf life, risks associated with the exposure of personnel to radiation, cost, storage, and disposal issues. On the other hand, non-radioactive enzymatic or luminescence labels, are less sensitive and flexible. However, an electrochemical biosensor which relies on the conversion of recognition event into a useful electrical signal is highly sensitive, inexpensive, easy-to-use, portable and compatible with microfabrication technologies. Electrochemical transduction of the recognition event can be divided into two broad classes. The first one involves the approach where a redox active species is utilized as a label with the redox activity at a low potential[164]. The second label-free method addresses the change of electrical properties of an electrode interface upon recognition[165]. In the labeled method, antibodies or aptamers (artificial nucleic acids ligands) are often used as the capture probes immobilized on the modified electrode with high affinity and specificity to a wide variety of target molecules including proteins, enzymes, antigens, antibiotics, toxins, and pharmaceutical drugs.

In the previous chapter, the gold BPE surface self-assembled with T-DNA was discussed throughout. However, the gold-thiol bond can only withstand reasonably mild potentials since alkanethiols are prone to thermal desorption and oxidative damage[166]. Beyond that, the precursors of SAMs might not be stable and are easily oxidized in air[167,168], resulting in a gradual reduction in DNA immobilization. As learned in our experiments, the considerable negative potential and repetitive voltage alternation would impair our monolayer, leading to the electrochemical signal deterioration. Moreover, the potential window of the gold electrode is limited by hydrogen evolution. In our system, the reduction of MB molecule (around -300 mV) is quite close to the H_2 evolution at -400 mV in neutral solution. Often the signal correspondence can not be differentiated, and that could lead to a misunderstanding of the signal. Fierce bubble formation would even break up the DNA assembly on the surface by thermal and hydrodynamic force. If the potential is kept at a low value to avoid H_2 evolution, it may not be enough to trigger a sufficient MB reduction across the BPE under a small driving force.

In contrast, carbon electrodes are free of this problem by their broader potential window range. The appearance of H^+ reduction is shifted more negatively because of its slow kinetics. Also, the oxidation potential of carbon is more positive than Au. More importantly, the linkage between DNA and the carbon surface is often a stronger covalent bond compared to the weak thiol-Au bond. Since the historical application of graphite electrodes for the electrochemical production of alkali metals, electrodes made of carbon material have been widely used in analytical electrochemistry with their low cost, broader potential window, relatively inert electrochemistry, and electrocatalytic activity for a variety of redox reactions. Many carbon sources have been elaborately studied, including graphite, glassy carbon, pencil lead, carbon paste, carbon tape, screen-printed carbon and even boron-doped diamond. The structure and chemistry of a carbon electrode surface are vitally important to electrochemical applications. Several methods have been developed in carbon surface modification including the adsorption of polyaromatic hydrocarbons[169], the amide bond formation between amine groups and surface carboxylate groups[170,171], reactions of acid chloride reagents with surface hydroxyl groups, and the radical-carbon surface covalent bonding by the reduction of a phenyl diazonium reagent or a primary amine[172,173]. Among them, the high efficiency is more likely achieved by covalent modification due to their alterable surface functionalities[174,175], in addition to their availability in various physical structures. The covalent bond, which is much stronger than the thiol-Au bond, has a promising aspect in improving the stability of the DNA monolayer on the BPE surface in our ECL system.

One way of modifying the carbon surface is to directly oxidize the carbon electrode surface through the electrochemical pretreatment such as pre-anodization. In the early time, the pretreatment was done to improve its electrochemical behavior towards redox active species. Blaedel et al. found that glassy carbon electrodes (GCEs) required a pretreatment of applying 1.35 and -1.35 V for 2 min to decrease the half-wave potential for the oxidation of NADH[176]. Pyrolytic carbon film and glassy carbon electrodes showed improved catalytic abilities toward the ferricyanide-ferrocyanide system following an application of 8 V at a frequency of 70 Hz performed immediately before an experiment[177]. The researchers suggest that the pretreatment involves the oxidation-reduction of functional groups on the carbon surfaces such as quinone, phenol, lactone, chromene, carboxyl, and carbonyl groups[178,179]. The negative surface charge resulting from some surface oxides on carbon, notably carboxylates, can have significant electrochemical effects on adsorption and electron-transfer rates. Royce reported that a pre-anodization at a voltage higher than 1.5 V in potassium nitrate with the following pre-cathodization were required to activate the GCEs[180]. The oxidation of the surface could produce functionalities capable of catalyzing the electrochemical reaction or remove impurities from the surface oxidatively. The pre-cathodization then reduced the oxide layer and made the surface active towards electroactive species. The effect of pretreatment on carbon electrode depends on many variables such as the oxidation/reduction potential, the composition, and pH of the electrolyte solution, as well as the length of time under pretreatment. Anjo et al. found out an optimum pretreatment condition in the analysis of

dopamine, was in a solution at pH=1 for a duration of 5 min[181]. The type of oxide on the carbon surface was verified to be pH dependent since the surface oxide species could include H atom[182].

In using the carbon electrode as a biosensor, the probe immobilization step plays a major role in determining the overall performance. The first method is called adsorption accumulation. Adsorption forces are used to immobilize DNA on carbon and by the electrostatic binding of DNA to positively charged carbon electrodes[183]. An oxidative pretreatment of carbon surfaces is necessary to enhance the adsorptive accumulation of DNA. On the other hand, the potential applied during immobilization enhances the stability of the probe through the electrostatic attraction between the positively charged surface and negatively charged sugar-phosphate backbone of DNA[184]. This binding is sufficiently strong, leaving the bases accessible to interact with target DNA. However, stringent washing steps cannot be performed because of the desorption of the non-covalently bound hybrid. Moreover, on account of multiple sites of binding, most of the immobilized DNA probes are not accessible for hybridization, resulting in poor efficiency. Wang illustrated the use of double-stranded (ds) DNA-coated screen-printed electrode (SPE) to monitor the conformational change in DNA and photoconversion of the guanine-DNA moiety to a non-electroactive monomeric base product by measuring the well-defined chronopotentiometric anodic peak associated with the oxidation of guanine-DNA residue[185]. The SPE was pretreated by applying a potential of +1.8 V for 1 min, followed by an adsorptive accumulation for 2 min at +0.2 V in the stirred DNA solution. Potentiometric stripping analysis (PSA) was employed for monitoring the adsorbed DNA species at carbon electrodes by passing a constant anodic current.

Mascini's group reported the immobilization of synthetic oligonucleotides onto disposable carbon strips using an avidin-biotin based procedure[186]. This procedure involves the controlled formation of avidin layers (by adsorption) onto the electrode surface and the subsequent binding of the DNA probe biotinylated at the 5-end. However, the avidin layer inhibits the electrochemical oxidation indicator used for detection.

In 1993, Mikkelsen's group reported a working prototype of a sequence-selective DNA biosensor based on hybridization indicators[187]. The immobilized DNA probe provides recognition of the analyte sequence through hybridization, and the indicator converts the recognition event into a measurable electronic signal. It was covalently attached to the carboxylic acid groups oxidized on glassy carbon electrode surfaces using 1-[3-(dimethylamino)-propyl]-3-ethylcarbodiimide for their activation[188]. The hybridization indicator ($Co(bpy)_3^{3+}$ and $Co(phen)_3^{3+}$) was preconcentrated at the electrode surfaces through its association with double-stranded DNA and was detected voltammetrically.

In another study related to the carbon paste electrode, the graphite/mineral oil of carbon paste was modified with additives, such as octadecylamine or stearic acid to provide functional groups for the

covalent attachment of DNA. Additives from 0.4% to 10% (w/w) were combined with the carbon powder/mineral oil mixture and tightly packed into an electrode holder. In the presence of a carbodiimide reagent, the primary amine group of octadecylamine would form a phosphoramidate bond with the 5'-terminal phosphate group on the DNA.

In addition to the glassy carbon and carbon paste, graphene oxide has also attracted increasing attention as a novel class of 2D carbon-based nanomaterials[189]. Of particular interest is the GO nanosheets that are soluble in water and many other common polar solvents and can form large-scale uniform films on various substrates. Li et al. demonstrated the electrostatic stabilization of GO colloids via carboxylic acid groups in the GO sheet[190]. Liu presented a direct, simple way to utilize the carboxyl groups of GO as the target for the immobilization of enzyme to fabricate a biocompatible glucose sensor with broad linearity, good sensitivity, excellent reproducibility, and storage stability[191]. The GO aqueous dispersion was prepared by oxidizing graphite in a mixture of H_2SO_4, NNO_3 and $KMnO_4$, followed by the reaction with 30% H_2O_2 for 120 min, known as Hummer's method[192]. The amine groups of glucose oxidase were covalently attached to the carboxyl acid groups of GO in the presence of 1-ethyl-3-(3-dimethylaminoprophy)carbodiimide hydrochloride (EDC) and N-hydroxyl succinimide (NHS)[193].

Different oxidative treatments were widely applied to multiwall carbon nanotubes (MWNTs) for many purposes, such as purification, chemical modification, and dispersion in solvents[194]. Other than the air or oxygen plasma treatment, liquid-phase oxidation in the HNO_3/H_2SO_4 mixed solution could form carboxylic acid groups on the surface of MWNTs and was examined by infrared spectra and its work function[195,196].

Masoud described an electrochemical method for the differentiation of various types of single-base mismatch targets according to the long-range charge transport through DNA films using a groove binder molecule with four negative charges, $CuPcS_4$[197]. The strategy of using long-range charge transfer to construct DNA hybridization biosensors have been exploited byBarton and co-workers since 1997[157,198-200]. GCE surface was oxidized by applying a potential of +1.20 V to the electrode in 0.1 M acetate buffer at pH 5 for 200 s followed by EDC and NHS treatment. The use of $CuPcS_4$ with four negative charges could avoid the direct electron transfer with the electrode surface and position the redox reporter before the mismatch position.

In order to design a new AC square bipolar ECL cell, we tested GCEs as the substrate in making biosensor towards DNA monolayer and ECPA study. Several modification methods have been tried by directly oxidizing the surface to carboxylic groups on GCEs, followed by EDC and NHS treatment. Instead of T-DNA with a thiol group at 5′ terminal, the amino group modified single-strand DNA (amino-DNA), which has the same sequence as the T-DNA (10) in chapter 3, was employed here to

covalently attached to the GCEs by the formation of an amide bond. Then the GCE was incubated in MB-DNA (40) solution and characterized by square wave voltammetry (SWV).

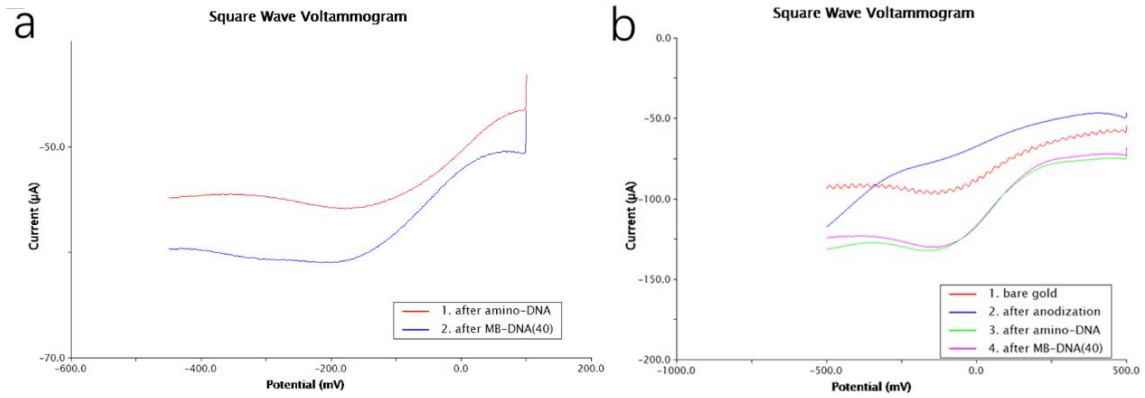

Figure 4.1.SWV characterization of modified GCE (anodization) immobilized with amino-DNA and MB-DNA (40), (a) in 0.1 M KNO_3, (b) in 0.5 M H_2SO_4.

(1) Anodization was performed on the glassy carbon electrode at a potential of 1.8 V for 5 min in 0.1 M potassium nitrate (Figure 4.1(a)) or 0.5 M H_2SO_4 (Figure 4.1(b)). The generated carboxylic acid groups on the surface of GCE were activated by immersing in PBS buffer solution containing 5 mM EDC and 8 mM NHS for 2 h with following incubation of amino-DNA for 4 h. Then the GCE was incubated in 1 µM MB-DNA (40) solution for the hybridization. However, as shown in Figure 4.1, in the SWV, there is no difference before/after the hybridization of MB-DNA(40). Even though there is a substantial reduction peak, it should be related to the reduction of oxygen in the ambient environment. Similar results were also obtained from the anodization in PBS buffer[201] and acetate buffer as well[197].

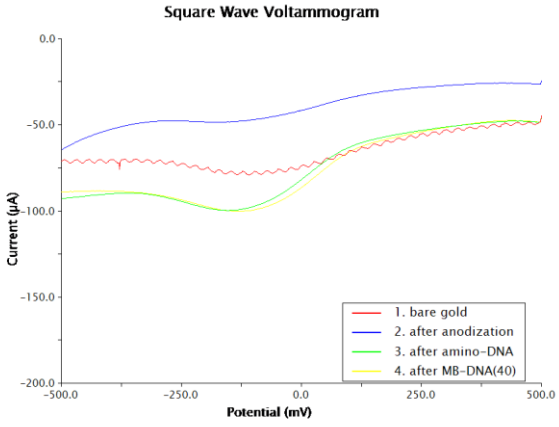

Figure 4.2.SWV characterization of modified GCE (oxidation in $K_2Cr_2O_7$ and 10% HNO_3) immobilized with amino-DNA and MB-DNA (40).

(2) The GCE was oxidized at +1.5 V for 15 s in an aqueous solution containing 2.5% $K_2Cr_2O_7$ and 10% HNO_3[187]. After being rinsed, the electrode was treated with 100 µL MES buffer solution (pH=5.0) containing 5 mM EDC and 8 mM NHS for 2 h and then amino-DNA (1 uM) to attach it to the surface

covalently. However, after incubation with 1 µM MB-DNA(40), there is still no difference compared with the probe amino-DNA only (Figure 4.2).

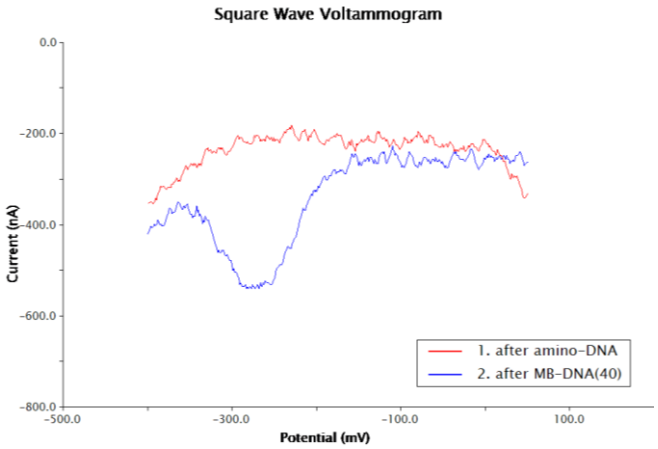

Figure 4.3. SWV characterization of standard gold electrode immobilized with 3-mercaptopropionic acid after amino-DNA coupling and MB-DNA (40) hybridization (after 3-point Savitzky-Golay smooth).

The failure in the fabrication of the sensor may lie in two reasons. First, the surface oxidation to carboxylic groups was not well-achieved. Second, the activation of carboxylic groups by EDC and NHS process was not successful. The EDC and NHS coupling was tested by immobilizing various of SAMs on the standard gold electrode surface such as L-cysteine[85,89], 3-mercaptopropionic acid or thioctic acid[136,202-207]. Taking 3-mercaptopropionic acid as an example, the GCE was immediately immersed in 100 µL 3-mercaptopropionic acid (100 mM) in 0.1 M PBS buffer or ethanol at room temperature for 12 h. Figure 4.3 shows a clear reduction appears after the hybridization of MB-DNA compared to amino-DNA only, indicating the successful coupling of carboxylic groups SAMs to the amino groups on the probe DNA.

As a result, the absence of expected electrochemical response is referred to the lack of carboxylic groups after oxidization treatment. The carboxylic groups produced by direct oxidation generally has a low surface coverage (<10%) and is unstable toward acidic or basic media. Besides, this type of modification often results in strong surface/adsorbate bonds. Other than this low coverage, the capacitive current from the carbon electrode in Figure 4.1 is more than 50 µA, which is much larger than that from the gold electrode in Figure 4.3 about only a few hundred nA. This large capacitance would necessarily conceal the faradaic current from the redox tag for detection. After this, a series of experiments using different carbon sources such as carbon paste and screen-printed carbon electrode were tested using different modification methods including adsorptive accumulation, bulk modification of carbon paste, yet with unsatisfied results with unobserved signal and large capacitance.

As a result, a better approach of generating more functional groups for probe immobilization and reducing the capacitance of carbon electrode is of urgent necessity.

4.2 Photon Counting PMT

Even though the use of the voltage-mode PMT has already endowed us with the capability of sensitively detecting DNA monolayer in a very low limit of detection. However, when the sensing platform is moved forward to the ECPA study towards protein quantification, a more sensitive PMT is expected in next the blueprint, especially when the concentration of analyte comes down to sub-nanomolar scale. Unlike prementioned MB-DNA and DNA loop, which have infinite binding affinities, the insufficient binding from the aptamers (or antibodies) to the target protein would further reduce the amount of redox label loaded on the surface. Also, the kinetic process in ECPA before reaching the thermodynamic equilibrium could cause even a smaller electrochemical signal. The minimized corresponding ECL emission calls up a more sensitive PMT of photon counting mode.

Photon counting is a useful technique in Raman spectroscopy, fluorescence analysis, and chemical or biological luminescence analysis where the absolute magnitude of the light is extremely low. The method of processing the output signal of a photomultiplier tube can be broadly divided into analog and digital modes, depending on the incident light intensity and the bandwidth of the output processing circuit. In the analog mode measurement, the output signal is the mean value of the signals including the AC components. In contrast, the photon counting method uses a pulse height discriminator that separates the signal pulse from the noise pulses, enabling high-precision measurement with a better signal-to-noise ratio compared to the analog mode. It makes the photo counting exceptionally efficient in detecting low-level light. When the light incident on a photomultiplier tube becomes very low and reaches a state in which no more than two photoelectrons are emitted within the time resolution of the PMT, this light level is called the single photoelectron region. In this region, the number of emitted electrons per photon is one or zero, and the quantum efficiency can be viewed as the ratio of the number of photoelectrons emitted from the photocathode to the number of incident photons per unit time. The probability that the photoelectrons emitted from the photocathode will impinge on the first dynode and contribute to gain is referred to as collection efficiency. Additionally, in the photon counting mode, the ratio of the number of counted pulses to the number of incident photons is called detection efficiency.

In the typical circuit configuration of photon counting, the current output pulse from the PMT is converted to a voltage by a wide-band preamplifier and amplified. These voltage pulses are fed to a discriminator and then to a pulse shaper. Finally, the number of pulses is counted by a counter. The discriminator compares the input voltage pulses with the preset reference voltage and eliminates those pulsed with amplitudes lower than this value. In general, the lower level discrimination (LLD) and upper-level discrimination (ULD) are set to eliminate noise pulses with lower and higher amplitudes. It has many advantages in comparison with the analog mode such as higher operating stability against supply voltage variation/gain fluctuation and better signal-to-noise ratio.

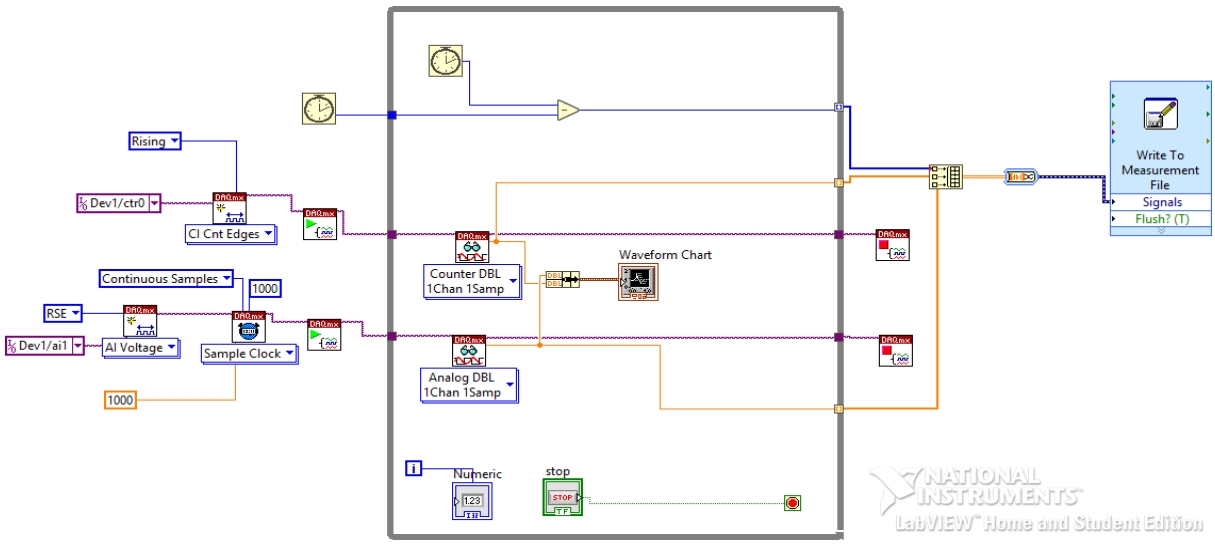

Scheme 4.1.The block diagram in Labview (National Instruments^{TM}) for photon counting PMT response collection together with the AC square waveform.

In our instrumentation of measurement, the inter-channel crosstalking between analog inputs on the DAQ device would lead to an interfering signal at the beginning of each voltage alternation. While in photon counting mode, its output is no long the analog voltage, but real-time count number instead. The separation of output mode from the PMT and applied voltage, would eliminate the accumulated interfering charges and enable the applicability of this AC bipolar ECL sensing system at high frequency. Scheme 4.1 shows the terminal configuration in Labview (National Instruments^{TM}). The response from the photon counting PMT is recorded by creating a channel to count the number of rising edges. A preset of sampling rate in the digital counter is not allowed in the program. The synchronized voltage and PMT responses are not observed until decreasing the sampling rate of the analog input to 1000/s. During the experiment, a compact head-on photon counting PMT (HAMAMATSU, H7828) was used by just connecting to a +5 V power supply.

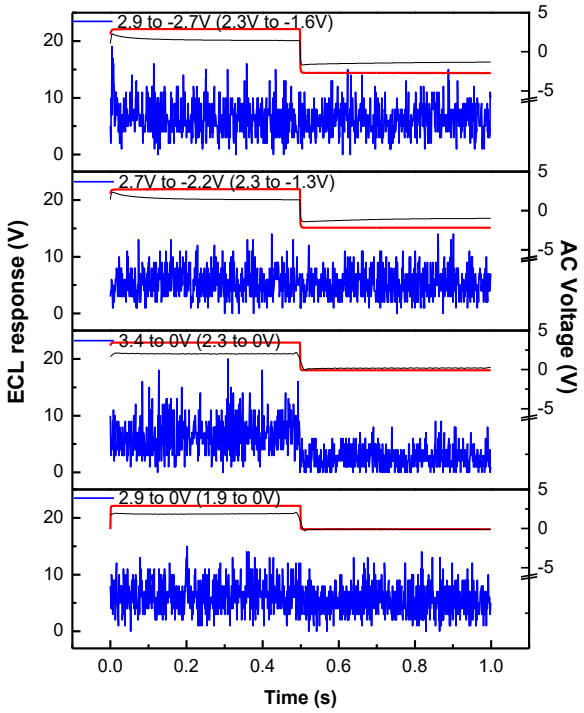

Figure 4.4.The integrated time-dependent ECL response of blank BPE cell in 0.1 M HEPEs buffer monitored by photon counting PMT for 100 cycles.

Since the sampling rate was restricted to below 1000/s, it is not appropriate to apply it in ECL experiments at high frequency like 100 Hz with such few sampling points (10 points per AC cycle). In the current stage, the frequency of 1 Hz was used to test the monolayer detection of MB-DNA. The control experiment in the BPE cell was done first to compare it with the previous result using an analog PMT. The interfacial potential difference between two ends of the BPE was also measured using a secondary DAQ device. As shown in Figure 4.4, at zero negative potential, when the positive potential is more than 2.9 V (3.4 V, for example), the ECL signal corresponding to H_2 evolution appears and spreads in the whole forward half cycle. At this time, the potential difference is about 2.3 V, fulfilling the potential requirement of H_2 evolution coupled with $Ru(bpy)_3^{2+}$ oxidation. When introducing the negative potential in the reverse half cycle, for example, at -2.7 V, it shows the ECL response from gold oxide reduction. The measured potential difference at -1.6 V in the reverse half cycle, is larger than the potential requirement of gold oxidation in HEPEs buffer coupled with H_2 evolution in the ECL solution.

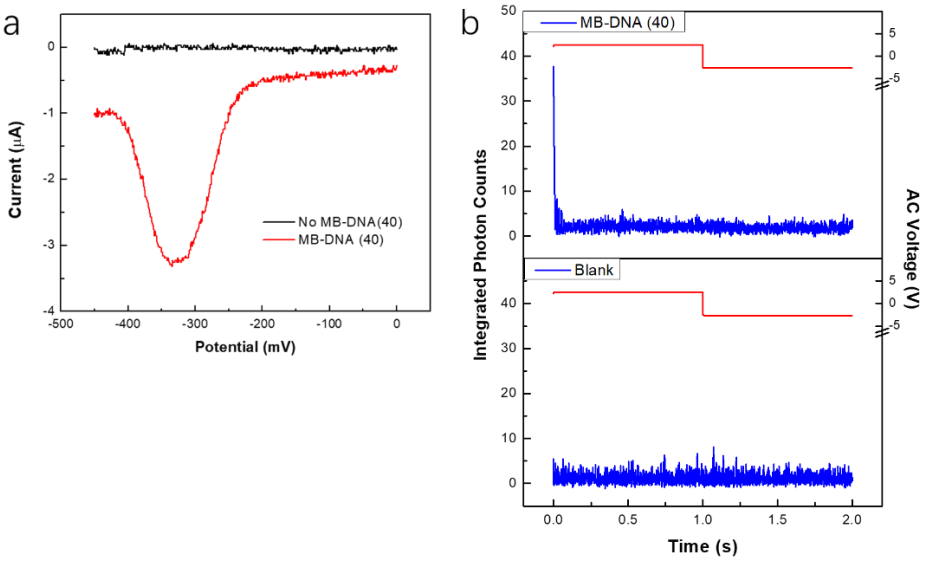

Figure 4.5.(a) SWV of BPE incubated with No MB-DNA (40) and MB-DNA (40). (b) Integrated time-dependent photon counts of the ECL experiment after incubation at AC square voltage between 2.5 to -1.3 V at 1 Hz.

After that, the T-DNA was immobilized on the half BPE surface followed by the hybridization with MB-DNA (40). A control experiment hybridized with No MB-DNA (40) was also carried out in parallel. In the SWV characterization, the one with MB-DNA (40) shows a significant reduction peak while the one with No MB-DNA (40) only exhibits a background baseline (Figure 4.5(a)). In the corresponding ECL experiment with an AC square wave of 2.5 to -1.3 V, the BPE incubated with MB-DNA (40) shows a clear ECL spike about 40 counts. Besides, the much smoother background compared to the analog one, allows us to improve the detection limit of our ECL sensing system by reducing the noise level.

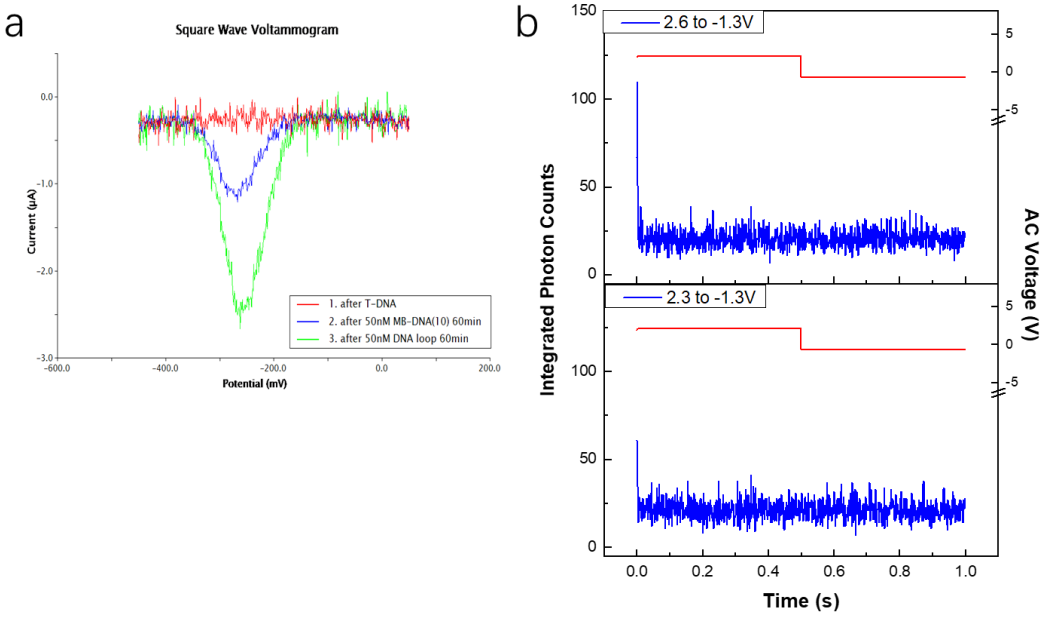

Figure 4.6.(a) SWV of BPE after T-DNA immobilization, incubation with 50 nM MB-DNA (10) and 50 nM DNA loop. (b) Integrated time-dependent photon counts of the ECL experiment after incubation at AC square voltage between 2.6 to -1.3 V at 1 Hz for 100 cycles.

Other than the double-stranded DNA, it was also studied on the DNA loop model under the proximity effect. In Figure 4.6(a), after the incubation of 50 nM DNA loop for 60 min, the current response from MB reduction is increased from -1.0 μA in the case of 50 nM MB-DNA(10) only to -2.5 μA. Figure 4.6(b) shows the integrated time-dependent ECL for 100 AC cycles. Under a square wave of 2.3 to -1.3 V, the ECL spike accumulates at the beginning of the forward half cycle. A larger driving force of 2.6 V enhances the height of spike to 110 counts.

In a nutshell, this preliminary test of using the photon counting PMT opens up the door of improving the performance of this AC square wave bipolar ECL system by increasing its sensitivity and reducing the fluctuation from background noise.

4.3 MB Intercalation

In addition to the attempts of changing the electrode substrate and switching to photon counting PMT, an alternative way of improving the performance of our AC square wave bipolar ECL system is to amplify the electrochemical response after DNA hybridization directly.

Two main methods are investigated to convert the hybridization event into the electrochemical signal by the redox label. The first one is the direct covalent labeling of the DNA sequence used for recognition, as same as the principle we have discussed in Chapter 3. Barton's group cross-linked daunomycin to the two amino groups of guanine (G) as the redox-active label[208]. A remarkable fast electron transfer was observed over long distances to the gold electrode when forming the helix of a 15-mer duplex. The charge migration through the DNA helix was found to be entirely suppressed by the presence of a single-base mismatch. Kertesz reported the DNA hybridization by tethering the anthraquinone molecule to the 2′- O position of a 20-mer uridine nucleotide[209]. Palecek described the use of paramagnetic beads covalently bound to the DNA probe to detect target DNA previously modified with osmium tetroxide, 2,2-bipyridine (Os(bipy)) by linear sweep voltammetry[210].

From our previous result in Chapter 3, H_2 evolution which has a close reduction potential to the MB reduction would lead to an ECL interference and limit the application of large positive potential in the forward half cycle. The replacement of MB to another label molecule with a more positive reduction potential could somehow relieve this issue by shifting the signal positively. The use of ferrocene-labeled oligonucleotides for sequence-specific detection, mismatch discrimination and gene expression monitoring in sandwich-type assays, has been reported by Umek et al[211]. After the immobilization of thiol-modified capture DNA probe, the target DNA, containing adenine residues modified with a ferrocene group, was hybridized with the capture probe. Ihara and co-workers then invented a sandwich-type hybridization assay base on the ferrocene-conjugated DNA probe and characterized it by DPV

technique[212]. Since then, ferrocene-conjugated DNA has been widely used in the sequence-specific detection of DNA[213-215].

Even though the label of ferrocene produces slightly improved single signal gain and target affinity, it comes with the disadvantage at a potentially significant price: the ferrocene-conjugated DNAs are far less stable than their methylene blue counterparts, particularly with regards to long-term storage, repeated electrochemical interrogations, and employment in complex sample matrices such as blood serum[159]. The attenuation of signaling current after each consecutive cycle would be much more severe in our system with repetitive AC square wave application. While the attached MB label, which is not highly distance-dependent as ferrocene, could intercalate into the DNA stem double helix after hybridization. The intercalative stacking rather than covalent σ-bonding is essential for efficient reduction of MB. This intercalation limits the diffusion of the label and thereby improves the electrochemical performance and stability[216].

However, the insufficient MB label is critical in restricting the sensitivity of our AC square wave bipolar ECL system. Only one molecule could be brought close to the electrode surface after the formation of DNA complex at one recognition event. More seriously, due to the radical annihilation mechanism, the ECL emission is also suppressed by its very small quantum efficiency (~2%). Therefore, an amplification method for the electrochemical signal is in urgent need.

Methylene blue (MB) is an organic dye that belongs to the phenothiazine family. We have already used it as the monomer of electropolymerization for growing thin film on the BPE and as the redox label on the secondary DNA for electrochemical current enhancement after hybridization. Nevertheless, MB also serves as an intercalation indicator toward double-stranded DNA. In particular, the cationic charge of MB would improve the DNA binding affinity by the electrostatic interaction with the phosphate backbone. Yang proved that there was a specific interaction of MB with guanine bases on the DNA when using carbon paste electrode[217]. Rohs et al. reported a modeling study for MB binding to DNA with alternating guanine-cytosine base sequence. The conformation of MB–guanine complex according to molecular dynamics was then simulated, showing three modes on its position and orientation: T-shaped, non-stacked and face-to-face[218]. Kelley first studied the intercalation of MB into a thiol-terminated self-assembled monolayer of oligonucleotides on gold employing chronocoulometry, cyclic voltammetry and ellipsometry[198]. Tani et al. stated that there was a shift in the peak potentials of the square wave voltammetric signals of MB from this condition[219].

MB intercalation was then developed as an efficient approach of detecting DNA hybridization[220]. Spectroscopic studies confirm the decrease in electrochemical signal upon hybridization is due to that MB has a higher affinity for ss-DNA rather than ds-DNA[221]. Ozsoz's group did a series of researches about the use of MB as a hybridization indicator which strongly associated with the free guanine (G)

bases of single-stranded DNA. After hybridization, the decrease of the peak current would reflect the extent of duplex formation. It also shows a transition of the interaction of MB from electrostatic to intercalative with increasing ionic strength. The hybridization limits the interaction between guanine and MB by preventing the well-known intercalative properties of this tricyclic heteroaromatic compound from coming into effect[157,158]. Single-base mutations on the DNA sequence in short synthetic oligonucleotides were also demonstrated with the use of DPV and SWV, respectively[222,223]. Yang utilized it to quantify the amount of calf thymus DNA immobilized onto the carbon paste electrode (CPE) surface by comparing the signal from ss-DNA and ds-DNA. A cathodic shift of the MB reduction peak at ss-DNA relative to ds-DNA and bare CPE suggests the stabilization of MB due to interactions with the ss-DNA.

Enlighted by the method of intercalation, we applied it to our DNA assembly on the gold BPE surface in order to amplify the electrochemical response. The existing DNA sequence was studied at this time considering the cost performance and time efficiency. From a brief calculation, there are 11 guanine bases (Gs) on the T-DNA (10) and 1 G on the MB-DNA (10); while for the ECPA model, 16 Gs are present on the DNA loop. That means after the formation of the sandwich complex, it would provide an extra 16 Gs for MB intercalation.

The presence of some nonspecific adsorption of MB to the gold BPE was observed using square wave voltammetry (SWV) on the bare electrode. While after the immobilization of T-DNA, the background current from nonspecific adsorbed MB was significantly reduced by a SAM formation, encouraging the use of MB intercalation on the gold BPE.

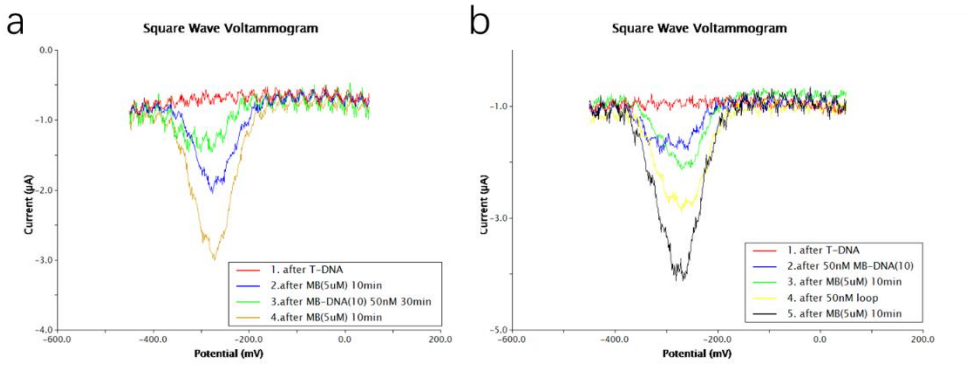

Figure 4.7.(a) SWV of BPE after T-DNA immobilization and 50 nM MB-DNA (10) with the following intercalation in 5 μM MB solution for 10 min. (b) SWV of BPE after T-DNA immobilization, 50 nM MB-DNA (10), and 50 nM DNA loop with following with the following intercalation in 5 μM MB solution for 10 min and loop incubation.

The DNA immobilization and hybridization in the experiments followed the same procedure described in Chapter 3. After the DNA assembling, we performed the intercalation by incubating the BPE in MB solution in 20 mM Tris–HCl buffer solution (pH 7.0) containing 20 mM NaCl. The BPE was then rinsed with HEPEs buffer for at least five times and ready for SWV characterization. It was found 10 to 20

min was the best time range for MB accumulation. Figure 4.7(a) compares the intercalation just after the T-DNA immobilization and after the MB-DNA (10) hybridization. With 5 µM MB intercalated for 10 min, the reduction peak appears other than the current baseline. MB-DNA (10) hybridization carried out immediately demonstrates a decreased peak. The MB molecules intercalated on the Gs in ss-DNA are driven away by duplex formation due to a weak interaction between the MB and ds-DNA. After a second MB intercalation, a current signal higher than that of the first intercalation shows up. Though there is only one G in the MB-DNA (10), the covalent attached MB label which is close to the electrode surface with fast electron transfer contributes to the signal increase a lot. The noisy fluctuation shown here should be the result of oscillatory noise. In Figure 4.7(b), MB-DNA (10) hybridization is followed right after the immobilization of T-DNA. The result of subsequent intercalation shows that a slight increase in the reduction peak, confirming a small contribution from the single G on MB-DNA (10). Followed by that, the BPE was incubated with 50 nM DNA loop for 60 min and has a decent current increase. The formation of the three-strand complex brought more covalently attached MB labels to the surface. At last, the third intercalation produces a higher signal since the DNA loop offers 16 more Gs.

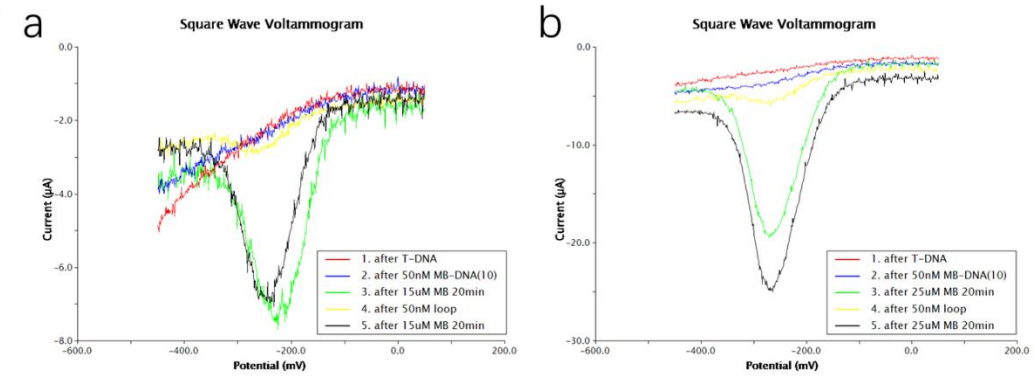

Figure 4.8.(a) SWV of BPE after T-DNA immobilization and 50 nM MB-DNA (10) with the following intercalation in 15 µM MB solution for 10 min and loop incubation. (b) SWV of BPE after T-DNA immobilization, 50 nM MB-DNA (10), and 50 nM DNA loop with following with the following intercalation in 25 µM MB solution for 10 min and loop incubation.

Since the signal from the attached MB label only is comparable with the signal after the intercalation of 5 µM MB, a higher concentration of MB was then used to reach a better amplification effect. Different from the previous signal at -4 µA, Figure 4.8 manifests the amplified current peak at about -8 µA or -25 µA in 15 µM MB or 25 µM MB solution respectively. In both cases, the signals after intercalation are significantly enhanced in a more concentrated MB environment. In Figure 4.8(b), the signal from the intercalation in 25 µM MB solution after loop incubation is slightly larger than that after MB-DNA (10) hybridization. While in Figure 4.8(a) with 15 µM MB solution, the intercalated signal after loop incubation is otherwise a little smaller than that after MB-DNA (10) hybridization. We ascribe the close current level in the presence and absence of the DNA loop to the steric inhibition of the reducible groups of MB to pack between the bulky double helix of the hybrid. Even though introducing16 Gs, the majority of them would be base pair matched with the T-DNA and MB-DNA

(10). Moreover, four free guanine bases on the T-DNA are hybridized with the DNA loop. The increment of MB-G interaction by the addition of the DNA loop can not transcend the decrement by the hybrids. On the other hand, the signal increase from the strand of MB-DNA (10) can almost be ignored because the addition of only one G. The signal provided by the attached MB label is no longer remarkable in the case of intercalation in high MB concentration.

Chapter 5 Conclusions and Future Directions

5.1 The Bipolar Electrode Thin-layer (BETL) System

So far, we have investigated a novel bipolar electrode thin-layer (BETL) system for low-concentration analyte ECL sensing using a commercially-available CCD camera. One of the key advantages of this system is the sensing and ECL reporting events decouple physically and chemically due to the phase separation created by the isolated double-cell design, while still in an open bipolar electrode configuration. Even though the driving electrodes and bipolar electrodes are both present in the same channel, the analyte would not be consumed on the driving electrode, but completely sealed in the thin layer itself, avoiding the interference or contamination from the ECL reporting solution. In this open bipolar electrochemistry, the electric field applied across the solution is substantially uniform and consecutive, as a result, the driving force for the thin-layer cell is proportional to its length, no matter the composition of active species and supporting electrolyte both in the peripheral cell and thin layer[19,133]. That is in contrast to closed electrochemistry in which the potential profile across the solution would change by accommodating the condition along the closed section from the resistance on the BPE/solution interface and depolarizer in the thin layer.

The concentration profile of analyte and further detailed information were provided by addressing electrochemical reactions within the thin layer instantaneously by way of ECL readout in the absence of a heavy-duty potentiostat setup. The easy fabrication from a household 3D printer and the commercially-available CCD camera make it a simple, inexpensive and portable device for analyte detection. Benefiting from these merits, the simplified instrumentation with lower energy loss and reduced cost can be easily assembled with other analytical tools, such as chromatography, mass spectrometry, and microfluidics chips, offering a convenient approach for the real-time analysis. By introducing bipolar arrays, multiple responses from separated bipolar electrodes can be obtained simultaneously.

This is, so far as we know, the first time of reporting the electrochemical thin-layer electrochemistry using ECL instead of the current readout that requires a direct electrical connection. By the signal amplification from repeating redox cycling of electrochemically active species within the thin layer, the ECL signal from a small volume of analyte could be directly readout using an easy-of-use, inexpensive, and portable personal camera for sensitive analysis, with the avoiding of a heavy-loaded potentiostat for the current recording. The isolation of analyte, volume confinement, and signal enhancement could

be simultaneously achieved in the BETL system, which is not feasible in a normal DC-driven BPE system[13].

The BETL system presented here can be further extended beyond model analytes and applied to the determination of various electroactive molecules. By further studies on the BETL system, not only the concentration profile of active species but its diffusional parameters, electron-transfer kinetics, and even homogeneous chemical process and surface chemistry (adsorption, desorption) on the electrode could be addressed by ECL, instead of the conventional voltammetric method that employs an electrochemical potentiostat. For example, in a first- or higher-order chemical reaction following (or preceding) electron transfer, the homogeneous solution kinetics could be investigated by the ECL emission deterioration. More importantly, because only the faradaic reaction can generate ECL on the bipolar electrode, the transient current by potential switching and capacity current from double-layer formation showed in the current recording measurement of traditional thin-layer electrochemistry can now be removed. The BETL system could even easily be miniaturized using a small battery providing the necessary DC power, which is capable of generating the steady-state response under constant potential. The replacement of the present CCD camera with a more advanced one or a photomultiplier tube can improve the limit of detection effectively. By the concept of repeated redox cycling, its signal would be even greatly amplified by narrowing down the thickness of the thin layer, towards promising analyte detection of ultra-low concentration and even single molecule scale in nanogap, especially after excluding the interference from nonfaradaic charging effect and effectively lowering the stochastic noise from the current fluctuation. The reporting method can somehow vary, by either the instant change on the bipolar electrode outside like ECL or accumulated effects like metal deposition or dissolution[69,70], which has its own advantage than optical reporting. Altogether, these benefits endow the BETL system a promising platform for a variety of electrochemical sensing applications with excellent signal amplification, complete phase separation, low cost, simple operation, and field-deployable device as key attributes. It can also be easily assembled with other analytical tools, such as chromatography, mass spectrometry, and microfluidics chips, providing a convenient way for real-time joint analysis.

Further works are required to investigate this BETL system. First, a more detailed study of the hydroquinone/benzoquinone system of which the reactivity can be easily influenced by the protonation and deprotonation forms. Second, a variety of potential analyte could be studied including ascorbic acid, dopamine, H_2O_2, glucose (incubation with glucose oxidase), and even unprocessed human serum sample for real point-of-care diagnostics. Due to its authenticity in ECL reporting of electrochemical behavior in the thin layer, the kinetics of coupled homogenous chemical reactions could be solved by the ECL method. Examples include the following hydrolysis to benzoquinone by the oxidation of p-aminophenol (PAP), the reduction of aromatic hydrocarbon 9,10-diphenylanthracene (DPA) and the dimerization of activated olefin.

There are two main directions of further improving the BETL system. The first direction is towards an easy-to-use, simplified, miniaturized, portable, and point-of-care device with cost-control. One example is to replace the DC power supply with a simple battery. As for the thin-layer structure, the flow cell configuration still shows much potential for improvement, such as the use of conducting material (gold, ITO, etc.)-coated glass slides. A well-defined thin layer could be created between two separate conducting slides with appropriate electrodes design. The ends of the two fabricated bipolar electrodes are spaced by either a gasket or a "dual-plate microtrench" made by epoxy etching[137,224,225]. The other exposed end can act as either the half BPE anode in the reporting compartment for ECL emission or the half BPE cathode in the cathodic compartment. Two driving electrodes, that are etched out at the other side of the slides, could be integrated with the BPEs. The anodic compartment and cathodic compartment could be individually enclosed in the polydimethylsiloxane (PDMS) chip with a molded reservoir. In the gasket method, the sample would be introduced by an inlet-outlet design as we described before. In the microtrench configuration, the sample solution could be just infilled into the trench by capillary action under immersion.

The other direction would focus on the aspect of a high-throughput nanogap device towards single molecule detection as well as its kinetics and dynamics. Single molecule electrochemistry can be achieved by narrowing the thin layer to the nanoscale. Other than the intrinsic benefits of the electrochemical method, the BETL system is of great importance in eliminating the nonfaradaic charging current by using ECL readout. One example of the cell design requires electron-beam evaporation and optical lithography based on a lift-off process. Designated electrode spacing would be created by the sacrificial layer and wet etching. The difference from the literature would be to pattern the feed line of the bottom electrode to connect to an outer electrode deposited beyond the passivation layer. As a result, the bottom and top electrode would serve together as two BPEs with one end within the nanogap and the other end exposed. The systematic fabrication approach, combined with a relatively large electrode surface area, allows a detailed characterization of the device geometry and its surface properties. The completed devices would be mechanically robust, can be stored for extended periods, and easily combined with microelectronics or a microfluidics chip to create large parallel assays at a relatively low cost. With reservoirs created by photolithography, these nanoscale devices could be assembled into the peripherical cell for ECL reporting. Driving electrodes could be inserted into the reservoir to provide an external electric field in our BETL system. This nanofluidic bipolar ECL sensor or sensor array, which has excellent spatial and temporal resolution with single molecule detection capability, can not only be employed in the theoretical investigation of electrochemistry but also promising in quantitively real-time biological diagnostics and integrated lab-on-chip applications.

5.2 The AC Square Wave Bipolar ECL System

We have developed a full-featured highly sensitive electrochemiluminescence (ECL) sensing platform based on the closed bipolar configuration using the AC voltage-driven method. The BPE cell consisting of two separate compartments can be easily fabricated by simplified photolithography and 3D printing technique. Owing to the phase separation, various analytes can be detected in the sensing compartment without potential interference from the reporting compartment, which greatly expands its application range. A redox-initiated change at one end of the closed BPE would be directly read out by a photomultiplier tube (PMT) at the other end. Different from the BPE system driven by a DC voltage, the AC technique allows the electro-active analyte to be regenerated by applying a negative potential in the reverse half cycle, and thus significant signal amplification can be achieved by accumulating ECL response through repeatable redox-cycling. $Fe(CN)_6^{3-}$, electropolymerized methylene (MB), MB-conjugated DNA monolayer, and DNA loop as a simplified model for ECPA were studied with low detection limit. Also, the effect of the applied AC frequency is also investigated regarding the electric field and ECL response. This system is extremely flexible, capable of detecting a wide variety of analyte in a broad concentration range, and amenable for monolayer as well as protein quantification, showing great promise in various analytical applications. Taking advantage of the closed configuration, it can be extended from the current model analyte to any redox-active species which could assemble on the BPE by either electrochemical deposition or surface modification. Biomolecules, such as protein and DNA linked with a biocompatible marker could be well-addressed using this system. The physical separation between the sensing and reporting compartment allows distinct reactions on both sides without mutual interference. This amplification method based on repeatable redox cycling is also suitable for molecules in trace volume if constructing a thin layer between the driving electrode and the BPE in the sensing compartment. Altogether, the demonstrated advantages of the AC bipolar ECL system make it a promising platform for electrochemical detections where analyte regeneration and repeatable signal accumulation are key attributes.

To further improve this system, some efforts can be implemented in its fabrication and modification. A biosensor is a device that incorporates a biologically active layer as the recognition element and converts the physical parameters of the biological interaction into a measurable analytical signal. Even though many methods have been proposed based on PCR, fluorescence, radioactivity, etc., the large-scale, routine clinic screening based on gene diagnostics is limited by the currently available technologies. Compared to other techniques, electrochemical biosensors relying on the conversion of a recognition event into a useful electrical signal are highly sensitive, inexpensive, easy-to-use, portable, and compatible with microfabrication technologies. Thus, they seem to be excellent candidates for the rapid and inexpensive diagnosis[226].

We have already tried some attempts at using the carbon electrode in the fabrication of the biosensor for the MB-conjugated DNA monolayer study. However, it does not provide expected results due to the low amount of surface loading of the capture probe DNA and the large capacitance on the carbon electrode. These two problems require the same solution of maximizing the surface coverage of modified functional groups such as carboxylates. The improved functionalities would result in high efficiency in target recognition with the help of the enhanced electrochemical response. Moreover, a more densely packed DNA layer would necessarily reduce the background capacitance by the inhibition of other species to the electrode surface.

A covalently modified carbon electrode surface made by the electrochemical reduction of phenyl diazonium ions was reported by Delamar et al. in 1992[227][227]. The reaction of a wide range of phenyl amines with $NaNO_2$ leads to phenyl diazonium reagents, usually isolated as a tetrafluoroborate salt. This reagent can be reduced electrochemically by the carbon electrode by one electron to form a phenyl radical and N_2; then the phenyl radical reacts with the carbon surface by coupling to an unsatisfied valence bond or adding to a double bond. Diazonium ion reduction has made it attractive for surface modification since the uncovered regions of the electrode surface are more likely to reduce diazonium ions than modified regions since the electron does not have to traverse an organic layer by tunneling or hopping. As a consequence, this film formation is "self-patching" with the result being relatively even surface coverage[228]. The fraction of electrogenerated phenyl radicals that bond to the surface is generally a little less than 100%, with values of 56% reported for a HOPG surface and 84% for GC[229]. Molecular layers formed on graphitic and diamond surfaces by diazonium reduction have also been characterized with quantitatively estimated coverage in the region of 4×10^{-10} mol/cm^2 [230-233]. The high coverage and strong surface bond resulting from diazonium modification have proven useful for a variety of applications. High coverage of the modification layer can completely inhibit the electron transfer for reactions requiring adsorption to the carbon surface. The utility of diazonium ion bonding to carbon surfaces can be broadened to a wider range of reagents by a two-step modification in which a "primer" is first attached to the surface by diazonium reduction and then a second reagent is then attached to the primer, such as a biodiagnostic probe. For example, the biological molecule such as horseradish peroxidase has been immobilized on the carbon electrode after previously reacting with a phenyl diazonium reagent containing a *para* carboxylic acid group[234].

Electrochemical oxidation of the primary aliphatic amine yields an amine radical, which can then bond to an unsatisfied valence or double bond on the carbon electrode surface. An example is the oxidation of three aliphatic amines on the glassy carbon in acetonitrile electrolyte. Its coverage is assessed by the voltammetry of following oxidation of surface-bound nitrophenyl groups on GC and turns out to be in the range of $(3\text{-}6) \times 10^{-10}$ mol/cm[235], close to the expected monolayer coverage.

Teh designed an electrochemical DNA biosensor based on the recognition of target DNA by hybridization with a well-defined recognition interface. A synthesized 21-mer amino-modified single-stranded DNA (ssDNA) capture probe was covalently attached through free amines on the DNA bases using EDC and NHS cross-linking reaction on a carboxylate-terminated 4-aminobenzoic acid (4-ABA) monolayer modified GCE[236]. Square wave voltammetry (SWV) was used to monitor the hybridization on the electrode by a decrease in the peak current of the electroactive intercalator MB with increasing concentration of target DNA. Briefly, the electrochemical modification of the clean GCE was carried out by 4-ABA via C-N covalent bond in the ethanol solution containing 3 mM 4-ABA and 0.1 M $LiClO_4$ by cyclic scanning between 0 and +1.40 V versus SCE for 20 cycles at a scan rate of 10 $mV \cdot s^{-1}$.

Another possible carbon electrode surface modification is base on the "click" cycloaddition chemistry to a surface-bound azide group[237]. Cu(I)-catalyzed cycloaddition of alkynes to azides yields a stable triazole ring, which is used in a variety of applications. For graphitic carbon electrodes, the azide may be covalently attached to the surface by addition of iodine azide, IN_3, across a double bond on a graphitic edge plane[238]. The use of "click" chemistry for carbon surface modification can be employed by bonding a primer to the surface using a single reagent, followed by the coupling to a wide range of alkynes to yield functionalized surfaces.

All the three mentioned carbon modification methods including diazonium ion reduction, amine electrochemical oxidation and "click" chemistry, could be examined in the future to maximize the surface coverage of functional groups on the carbon electrode surface. In this way, the carbon electrode is supposed to be utilized in the AC bipolar ECL system as an alternative to the gold electrode. This modified carbon electrode not solely is limited to the ECL system yet suggests a promising direction of optimizing the original ECPA technique.

The replacement of the electrode material is one of the several aspects of improving the performance of our system. In addition, an enhanced sensitivity could be achieved by either using a more advanced detecting device or amplifying the electrochemical signal from the DNA assembly. If putting a PMT with single photon sensitivity into use, an ultra-low detection limit may be realized prior to the ECPA with SWV readout (a cooling system and external circuit design may be incorporated to minimize the noise level). The main flaw in the SWV characterization is the presence of the nonfaradaic charging current imposed to the faradaic current from the target analyte. Even though the component from the charging current can be depressed by selecting an appropriate sampling time point which is usually larger than five times the cell time constant, it would also sample the analyte signal in an attenuated value, especially for limited electro-active species in the monolayer-level. Whereas, the ECL sensing, even though with a low quantum efficiency, is capable of excluding all the charging effect by only producing the ECL emission corresponding to the faradaic reaction. Our AC bipolar ECL system would still benefit from the renewal of redox-active species (in the diffusion layer or surface-confined) as in

the SWV while with no interference from the charging current. It is more likely to accomplish an extremely sensitive detection when the analyte concentration comes down to an ultra-low level.

Another aspect addresses amplifying the electrochemical response concerning the case of probe-target recognition. In all the recognition events, the DNA hybridization is commonly developed via an increase in the current signal of an electroactive indicator (either be attached to the target DNA or binds to the single/double-stranded DNA, or from other hybridization-induced changes in electrochemical parameters.

A variety of small molecules interact reversibly with the double-stranded DNA, through either intercalation or electrostatic binding in well-defined binding sites. Heterocyclic dyes, such as ethidium, anthracyclines, phenothiazines, and acridine derivatives, bind through intercalation, with the planar, aromatic group stacked between base pairs[239-241]. Some square planar and octahedral transition metal complexes, notably Pt, Ru, Co, and Fe with bi- or tridentate, planar, aromatic ligands also associate reversibly with the double-stranded DNA through ligand intercalation[242-246]. For tris(l,10-phenanthrolino)ruthenium(II), this interaction occurs in the major groove of the double helix and shows enantiomeric selectivity. By using electroactive intercalators such as MB and daunomycin, a pronounced signal could be observed even with a very low concentration of intercalator molecule by long-range electron transfer via ionic crystal structure of ds-DNA. The presence of just a single intervening mismatch was sufficient to shut off the reaction completely. Some complexes do not exhibit intercalative binding but associate selectively with the double-stranded DNA through electrostatic binding to the negatively charged phosphate backbone; tris(2,2'-bipyridyl)ruthenium(II), for example, binds electrostatically in the minor groove of the double helical DNA.

Another common approach in the development of electrochemical DNA-hybridization biosensors uses redox indicators which have different affinities for single strands (ss-) relative to double strands (ds-) DNA on the electrode. We have used MB as the polymerized film and redox label attached to the secondary DNA in the previous chapter. Other than that, MB has been widely employed as an electrochemical intercalator to monitor the DNA hybridization reaction[157,219-223,247]. In addition to the DNA-mediated charge transport from its intercalation into the well-stacked base pairs of the double helix, MB has also been reported to bind specifically to the free guanine bases. A lower current signal is thus observed upon the hybridization since less MB can bind to dsDNA[217].

In the ECPA study, it forms a five-part circular complex on the electrode surface under the proximity effect. The intercalation method which relies on the nanometer-length scale, long-range electron transport through the DNA can be adopted[214]. As mentioned before, methylene blue (MB) is an aromatic heterocycle that binds to DNA via intercalation. In particular, the cationic charge of MB would improve the DNA binding affinity by the electrostatic interaction with the phosphate backbone. As an

intercalator, the redox reaction of MB is not highly distance-dependent. Its electron communication with electrodes is coupled with the highly efficient electron transfer within π-stacked base pairs[215].

According to the literature, in a short completely paired double-stranded DNA, the MB prefers to bind reversibly to DNA sites that are close to the bulk solution (15-mer, for example)[157]. However, in our ECPA structure, the formed complex is not as densely packed as the short duplex, leaving much more space for the MB molecule to diffuse into different binding sites on the DNA. In addition, the DNA strands used here are not fully matched, leaving abundant free bases. These bases could be utilized for MB-guanine interaction to enhance its electrochemical response greatly.

In order to reduce the background and maximally amplify the signal in the presence of the analyte, the sequence of T-DNA as the capture probe (on the gold electrode) and the signaling probe (MB-DNA for example) need to be carefully designed in addition to minimizing the chance of cross-hybridization. The capture probe immobilized on the surface should have as few G numbers as possible, while the signaling probe, which could be hybridized sufficiently in the presence target under the proximity effect, should have as many Gs as possible for MB intercalation. It would be the primary principle of the DNA sequence design. In addition, due to either two antibody arms or two aptamers hybridizing with the capture and signaling probe, the sequences of them also need to be considered. First, the antibody arm or aptamer (Apt 1 or Ab 1) that hybridizes with the capture DNA should have few Gs in order to suppress the background, while Apt 2 or Ab 2 which binds with the signaling probe is expected to have more Gs. Besides, MB has a weak intercalation affinity to the G on ds-DNA compared to ss-DNA. If G must be present to avoid cross-hybridization, it is preferred to code inside the base regions that hybridize between the probes and antibody arms (or aptamers).

As a matter of fact, in the case of intercalation with enough MB indicator, the signal from the covalently attached single MB molecule may not be necessary anymore. Common ss-DNA without 3′-terminal modification could be utilized to decrease the cost of DNA preparation. And also, the ECPA assay design could be refined with fewer DNA strands by integrating the signaling probe and aptamer/antibody arm into a single strand.

The achievement of high sensitivity and selectivity requires the maximization of hybridization efficiency and the minimization of non-specific adsorption, respectively. Control of the surface chemistry and coverage is essential for assuring the high reactivity, orientation, accessibility, and stability of the surface-confined probe as well as minimizing non-specific adsorption events. One of the issues related to the intercalation on the carbon electrode is the much stronger nonspecific adsorption of MB due to the non-uniform morphology of the carbon surface. By using the common oxidation method for modification, the small yield of the carboxylic group coverage (<10%) will leave the most surface area uncovered and ready for nonspecific adsorption. Yang showed that the amount of

nonspecifically adsorbed MB was insufficient to be observed by adsorption accumulation[217]. The CPE surface was pretreated by applying -1.70 V for 1 min, creating a surface on which the DNA would adsorb through electrostatic interaction with carboxyl moieties. ss- or ds-DNA was then adsorbed on the surface of the pretreated CPE by applying a potential at 0.5 V for 5 min in the DNA solution. After that, the MB was accumulated at the DNA-modified CPE by intercalation. We could employ the same technique to grow a thin probe DNA film on the carbon electrode in the next generation of this biosensor. As a result, the inevitable nonspecific adsorption of MB and the large capacitance can be simultaneously minimized by a densely packed DNA layer.

Instead of MB that binds with guanine, the minor groove binding substance whose voltammetric response is influenced by DNA hybridization could serve as another alternative way of amplifying the signal in the ECPA. In 1992, Mikkelsen reported a new electrochemical method for detecting DNA bound to carbon electrode surfaces. The double-stranded DNA was detected voltammetrically, in the presence of tris(2,2'-bipyridyl)cobalt(III), a complex which had been shown to associate reversibly through electrostatic interactions with the minor groove of the double-helical DNA[248]. The electrode-bound DNA showed no electroactivity over the +1.0 to -0.9 V (vs. SCE) potential range while the cobalt complex was reversibly electroactive with a formal potential of + 0.11 V. Thus, voltammetry at the modified carbon electrode using a dilute solution of the cobalt complex, showed a preconcentration of the complex at the electrode surface, resulting in larger peak currents than expected for a diffusional redox couple. Masoud described an electrochemical method for the detection of different types of single-base mismatch on the long-range charge transport through DNA films using a groove binder molecule with four negative charges, $CuPcS_4$[197].

If utilizing minor groove binding substances in our system, the increase in the number of base pair matches in the presence of target would produce a larger electrochemical response by the electrostatic binding of the transition metal complex to the DNA assembly. In this scenario, the number of complementary bases of aptamers/antibody arms to the probe DNA should be reduced yet with a maximized number towards the signaling probe.

The exploitation of the catalytic effect is another effective way of enhancing the electrochemical response. Thorp and co-workers reported the catalytic guanine oxidation with an exogenous inorganic ruthenium complex, $[Ru(bpy)_3]^{2+}$, as an oxidation catalyst. A two-step electrochemical oxidation of $[Ru(bpy)_3]^{2+}$ to Ru(III) species, followed by the chemical oxidation of guanine in a redox reaction to regenerate the $[Ru(bpy)_3]^{2+}$ is suggested[249-252].

Barton et al. reported a new strategy to improve the sensitivity for the electrochemical detection of DNA hybridization by employing an exogenous electrocatalytic species for signal amplification[198]. Before the introduction of catalytic species, under the duplex formation, the original signal from the charge

transport was through self-assembled monolayers of oligonucleotides between the intercalated indicator MB and the gold electrode surface. After the introduction of the solution-based mediator, potassium ferricyanide, the resulting voltammetric signal was significantly improved by the catalytic effect through the back-oxidation of MB. With a single base pair mismatch on the hybrids, the signal was dramatically lowered. by the prevention of electron transfer through the hybrid

As a result, MB or other intercalated species such as the grove binder could be utilized to amplify the signal with its specific DNA design. On the other hand, the catalytic effect from a solution mediator with a suitable formal potential, such as ferricyanide in the case of MB label, is capable of further enhancing the electrochemical response under our DNA hybridization event. The combination of the two methods is suggested to be applied to our AC square wave bipolar ECL system on either gold electrodes or potential carbon electrodes to have an ultimate amplification. It is noteworthy that the original ECPA could take advantage of them as well.

In the ECPA, attention should also be given to direct, label-free electrochemical detection, which is not accepted by the ECL system due to most of the time no faradaic reaction is involved. Instead of the electrochemical signal from reduction or oxidation, other electrical parameter changes induced by the DNA conformation change could be monitored without the use of an indicator which is often toxic or carcinogenic compounds. The first indicator-free method was introduced by Wang et al. by the decrease of the guanine peak from the immobilized probe upon the addition of complementary target[253]. Then it was improved by using the inosine-modified (guanine-free) probe which forms a specific base-pair with the cytosine residue[254]. The duplex formation was thus detected through the appearance of the guanine oxidation peak of the target sequence. A different label-free approach, based on doping nucleic-acid probes within conducting polymer films, was also proposed by Wang. Distinct transient hybridization current peaks, with opposite directions in the presence of complementary and non-complementary DNA sequences, were obtained as a result of the changed conductivity of the host PPy network. However, the label-free technique based on guanine oxidation will suffer from the high background if there is nonspecific adsorption of guanine containing sequences to the sensor surface[255]. More severely, the reusability of the DNA sensor may be unexpected under the oxidation of guanine. An electrochemical genomagnetic hybridization assay was then developed by him to take advantage of a new and efficient magnetic separation/mixing process on a thick-film carbon electrode in the pulse voltammetric mode[254]. Magnetic bead capture could be used to eliminate non-specific adsorption effects based on stripping potentiometric measurements of the target guanine at graphite electrodes[256]. Zhou constructed a graphite electrode sensor coated with DNA films [257]. The DNA damage by toxic metabolites such as styrene oxide was evaluated by the oxidation peaks from known covalent adducts with guanine and adenine in DNA with genetic consequences[258]. To amplify the small SWV peak current, the catalytic electrochemical oxidation of the transition metal complex $Ru(bpy)_3^{2+}$ to guanine bases was utilized.

They prepared the sensor by an alternate layer-by-layer adsorption of PDDA cations and ds-DNA on oxidized pyrolytic graphite electrodes[259]. The double-helix structure of ds-DNA shielded guanine from efficient contact with $Ru(bpy)_3^{2+}$. When the double helix was destroyed, guanine became more available and reacts more rapidly with the catalyst, thus providing a way to distinguish between ds- and ss-DNA.

Masoud et al. employed the glassy carbon electrode (GCE) as a label-free biosensor to determine the concentration of sodium diclofenac (DCF) by covalently immobilizing the amino-functionalized diclofenac binding aptamer (DBA) on the surface[201]. The introduction of DCF induces an alteration in the conformation of the surface immobilized DBA and causes a decrease in the charge transfer resistance of the aptasensor. However, by the incubation in a secondary DBA, the charge transfer resistance is increased and could be monitored using voltammetric and electrochemical impedance spectroscopic (EIS) techniques.

Even though the technique from guanine oxidation of DNA is not applicable in our ECPA system, the induced impedance change by DNA conformation after the formation of DNA complex may pave up another path in the label-free detection of the biomolecular target.

In summary, Great signal amplification from the marriage of bipolar electrochemistry and AC square wave give greatly signal amplification can be achieved by ECL signal accumulation with the help of a unique and successive analyte regeneration chemistry. Carbon electrodes, advanced detecting devices and the introduction of signal amplification methods such as intercalation and catalytic effect are going to be incorporated in the next generation of the AC square wave bipolar ECL system as well as the original ECPA. The significant advantages such as extra-high sensitivity, simplicity, rapid response, reusability, and low cost, make it an up-and-coming sensing platform of various redox-active species and biomolecules such as DNA and proteins.

References

(1) Ishiguro, Y.; Inagi, S.; Fuchigami, T. *J. Am. Chem. Soc.* **2012**, *134*, 4034.

(2) Laws, D. R.; Hlushkou, D.; Perdue, R. K.; Tallarek, U.; Crooks, R. M. *Anal. Chem.* **2009**, *81*, 8923.

(3) Perdue, R. K.; Laws, D. R.; Hlushkou, D.; Tallarek, U.; Crooks, R. M. *Anal. Chem.* **2009**, *81*, 10149.

(4) Anand, R. K.; Sheridan, E.; Hlushkou, D.; Tallarek, U.; Crooks, R. M. *Lab on a Chip* **2011**, *11*, 518.

(5) Anand, R. K.; Sheridan, E.; Knust, K. N.; Crooks, R. M. *Anal. Chem.* **2011**, *83*, 2351.

(6) Sheridan, E.; Knust, K. N.; Crooks, R. M. *Analyst* **2011**, *136*, 4134.

(7) Knust, K. N.; Sheridan, E.; Anand, R. K.; Crooks, R. M. *Lab on a Chip* **2012**, *12*, 4107.

(8) Sheridan, E.; Hlushkou, D.; Knust, K. N.; Tallarek, U.; Crooks, R. M. *Anal. Chem.* **2012**, *84*, 7393.

(9) Scida, K.; Sheridan, E.; Crooks, R. M. *Lab on a Chip* **2013**, *13*, 2292.

(10) Chow, K.-F.; Mavré, F.; Crooks, R. M. *J. Am. Chem. Soc.* **2008**, *130*, 7544.

(11) Wang, T.; Fan, S.; Erdmann, R.; Shannon, C. *Langmuir* **2013**, *29*, 16040.

(12) Zhang, X.; Chen, C.; Yin, J.; Han, Y.; Li, J.; Wang, E. *Anal. Chem.* **2015**, *87*, 4612.

(13) Yu, S.; Mehrgardi, M.; Shannon, C. *Electrochem. Commun.* **2018**, *88*, 24.

(14) Loget, G.; Kuhn, A. *Nat. Commun.* **2011**, *2*, 535.

(15) Guerrette, J. P.; Percival, S. J.; Zhang, B. *J. Am. Chem. Soc.* **2013**, *135*, 855.

(16) Sentic, M.; Loget, G.; Manojlovic, D.; Kuhn, A.; Sojic, N. *Angew. Chem. Int. Ed.* **2012**, *51*, 11284.

(17) Loget, G.; Zigah, D.; Bouffier, L.; Sojic, N.; Kuhn, A. *Acc. Chem. Res.* **2013**, *46*, 2513.

(18) Mavré, F. o.; Chow, K.-F.; Sheridan, E.; Chang, B.-Y.; Crooks, J. A.; Crooks, R. M. *Anal. Chem.* **2009**, *81*, 6218.

(19) Mavré, F. o.; Anand, R. K.; Laws, D. R.; Chow, K.-F.; Chang, B.-Y.; Crooks, J. A.; Crooks, R. M. *Anal. Chem.* **2010**, *82*, 8766.

(20) Loget, G.; Kuhn, A. *Anal. Bioanal. Chem.* **2011**, *400*, 1691.

(21) Loget, G.; Kuhn, A. *Specialist periodical reports electrochemistry; J. Wadhawan, R. Compton, Eds* **2012**, 71À103.

(22) KUSAKABE, K.; MOROOKA, S.; KATO, Y. *J. Chem. Eng. Jpn.* **1982**, *15*, 45.

(23) King, C.; Wright, A. *Electrochim. Acta* **1977**, *22*, 1135.

(24) Duval, J. m.; Kleijn, J. M.; van Leeuwen, H. P. *J. Electroanal. Chem.* **2001**, *505*, 1.

(25) Duval, J.; Minor, M.; Cecilia, J.; Van Leeuwen, H. *J. Phys. Chem. B.* **2003**, *107*, 4143.

(26) Duval, J. F.; Buffle, J.; van Leeuwen, H. P. *J. Phys. Chem. B.* **2006**, *110*, 6081.

(27) Ulrich, C.; Andersson, O.; Nyholm, L.; Björefors, F. *Angew. Chem. Int. Ed.* **2008**, *47*, 3034.

(28) Marsh, R. A.; Russell, P. G.; Reddy, T. B. *J. Power Sources* **1997**, *65*, 133.

(29) Gangwal, S.; Cayre, O. J.; Bazant, M. Z.; Velev, O. D. *Phys. Rev. Lett.* **2008**, *100*, 058302.

(30) Himmelhaus, M.; Takei, H. *Sens. Actuators, B-Chem.* **2000**, *63*, 24.

(31) Loget, G.; Kuhn, A. *J. Mater. Chem.* **2012**, *22*, 15457.

(32) Perro, A.; Reculusa, S.; Ravaine, S.; Bourgeat-Lami, E.; Duguet, E. *J. Mater. Chem.* **2005**, *15*, 3745.

(33) Jiang, S.; Chen, Q.; Tripathy, M.; Luijten, E.; Schweizer, K. S.; Granick, S. *Adv. Mater.* **2010**, *22*, 1060.

(34) Loget, G.; Roche, J.; Kuhn, A. *Adv. Mater.* **2012**, *24*, 5111.

(35) Nie, Z.; Li, W.; Seo, M.; Xu, S.; Kumacheva, E. *J. Am. Chem. Soc.* **2006**, *128*, 9408.

(36) Perro, A.; Reculusa, S.; Pereira, F.; Delville, M.-H.; Mingotaud, C.; Duguet, E.; Bourgeat-Lami, E.; Ravaine, S. *Chem. Commun.* **2005**, 5542.

(37) Snyder, C. E.; Yake, A. M.; Feick, J. D.; Velegol, D. *Langmuir* **2005**, *21*, 4813.

(38) Petit, L.; Manaud, J.-P.; Mingotaud, C.; Ravaine, S.; Duguet, E. *Mater. Lett.* **2001**, *51*, 478.

(39) Cayre, O.; Paunov, V. N.; Velev, O. D. *Chem. Commun.* **2003**, 2296.

(40) Kline, T. R.; Paxton, W. F.; Mallouk, T. E.; Sen, A. *Angew. Chem. Int. Ed.* **2005**, *44*, 744.

(41) Bradley, J.-C.; Babu, S.; Mittal, A.; Ndungu, P.; Carroll, B.; Samuel, B. *J. Electrochem. Soc.* **2001**, *148*, C647.

(42) Ndungu, P. G. *The use of bipolar electrochemistry in nanoscience: Contact free methods for the site selective modification of nanostructured carbon materials*, 2004.

(43) Babu, S.; Ndungu, P.; Bradley, J.-C.; Rossi, M. P.; Gogotsi, Y. *Microfluidics and Nanofluidics* **2005**, *1*, 284.

(44) Bradley, J. C.; Ma, Z. *Angew. Chem. Int. Ed.* **1999**, *38*, 1663.

(45) Loget, G.; Lapeyre, V.; Garrigue, P.; Warakulwit, C.; Limtrakul, J.; Delville, M.-H. l. n.; Kuhn, A. *Chem. Mater.* **2011**, *23*, 2595.

(46) Fattah, Z.; Garrigue, P.; Lapeyre, V. r.; Kuhn, A.; Bouffier, L. *J. Phys. Chem. C* **2012**, *116*, 22021.

(47) Loget, G.; Larcade, G.; Lapeyre, V.; Garrigue, P.; Warakulwit, C.; Limtrakul, J.; Delville, M.-H.; Ravaine, V.; Kuhn, A. *Electrochim. Acta* **2010**, *55*, 8116.

(48) Coleman, B. D.; Finnegan, N.; Bohn, P. W. *Thin Solid Films* **2004**, *467*, 121.

(49) Ramakrishnan, S.; Shannon, C. *Langmuir* **2010**, *26*, 4602.

(50) Ramaswamy, R.; Shannon, C. *Langmuir* **2010**, *27*, 878.

(51) Shida, N.; Ishiguro, Y.; Atobe, M.; Fuchigami, T.; Inagi, S. *ACS Macro Letters* **2012**, *1*, 656.

(52) Inagi, S.; Ishiguro, Y.; Atobe, M.; Fuchigami, T. *Angew. Chem. Int. Ed.* **2010**, *49*, 10136.

(53) Ishiguro, Y.; Inagi, S.; Fuchigami, T. *Langmuir* **2011**, *27*, 7158.

(54) Loget, G.; Roche, J. r.; Gianessi, E.; Bouffier, L.; Kuhn, A. *J. Am. Chem. Soc.* **2012**, *134*, 20033.

(55) Kong, S.; Fontaine, O.; Roche, J. r. m.; Bouffier, L.; Kuhn, A.; Zigah, D. *Langmuir* **2014**, *30*, 2973.

(56) Bard, A. J. *J. Am. Chem. Soc.* **2010**, *132*, 7559.

(57) Fernández, J. L.; Walsh, D. A.; Bard, A. J. *J. Am. Chem. Soc.* **2005**, *127*, 357.

(58) Fernández, J. L.; White, J. M.; Sun, Y.; Tang, W.; Henkelman, G.; Bard, A. J. *Langmuir* **2006**, *22*, 10426.

(59) Smotkin, E. S.; Diaz-Morales, R. R. *Annual Review of Materials Research* **2003**, *33*, 557.

(60) Jeon, M. K.; Lee, C. H.; Park, G. I.; Kang, K. H. *J. Power Sources* **2012**, *216*, 400.

(61) Sullivan, M. G.; Utomo, H.; Fagan, P. J.; Ward, M. D. *Anal. Chem.* **1999**, *71*, 4369.

(62) Guerin, S.; Hayden, B. E.; Lee, C. E.; Mormiche, C.; Owen, J. R.; Russell, A. E.; Theobald, B.; Thompsett, D. *J. Comb. Chem.* **2004**, *6*, 149.

(63) Strasser, P.; Fan, Q.; Devenney, M.; Weinberg, W. H.; Liu, P.; Nørskov, J. K. *J. Phys. Chem. B.* **2003**, *107*, 11013.

(64) Tesfu, E.; Maurer, K.; Ragsdale, S. R.; Moeller, K. D. *J. Am. Chem. Soc.* **2004**, *126*, 6212.

(65) Woodhouse, M.; Parkinson, B. *Chem. Mater.* **2008**, *20*, 2495.

(66) Ye, H.; Lee, J.; Jang, J. S.; Bard, A. J. *J. Phys. Chem. C* **2010**, *114*, 13322.

(67) Shan, X.; Díez-Pérez, I.; Wang, L.; Wiktor, P.; Gu, Y.; Zhang, L.; Wang, W.; Lu, J.; Wang, S.; Gong, Q. *Nat Nanotechnol.* **2012**, *7*, 668.

(68) Chow, K.-F.; Chang, B.-Y.; Zaccheo, B. A.; Mavré, F.; Crooks, R. M. *J. Am. Chem. Soc.* **2010**, *132*, 9228.

(69) Fosdick, S. E.; Crooks, R. M. *J. Am. Chem. Soc.* **2011**, *134*, 863.

(70) Fosdick, S. E.; Berglund, S. P.; Mullins, C. B.; Crooks, R. M. *Anal. Chem.* **2013**, *85*, 2493.

(71) Zhan, W.; Alvarez, J.; Crooks, R. M. *J. Am. Chem. Soc.* **2002**, *124*, 13265.

(72) Miao, W. *Chem. Rev.* **2008**, *108*, 2506.

(73) Arora, A.; Eijkel, J. C.; Morf, W. E.; Manz, A. *Anal. Chem.* **2001**, *73*, 3282.

(74) Noffsinger, J. B.; Danielson, N. D. *Anal. Chem.* **1987**, *59*, 865.

(75) Leland, J. K.; Powell, M. J. *J. Electrochem. Soc.* **1990**, *137*, 3127.

(76) Chow, K.-F.; Mavré, F.; Crooks, J. A.; Chang, B.-Y.; Crooks, R. M. *J. Am. Chem. Soc.* **2009**, *131*, 8364.

(77) Wei, H.; Wang, E. *Luminescence* **2011**, *26*, 77.

(78) Chang, B.-Y.; Chow, K.-F.; Crooks, J. A.; Mavré, F.; Crooks, R. M. *Analyst* **2012**, *137*, 2827.

(79) Zhang, X.; Chen, C.; Li, J.; Zhang, L.; Wang, E. *Anal. Chem.* **2013**, *85*, 5335.

(80) Wu, M.-S.; Qian, G.-s.; Xu, J.-J.; Chen, H.-Y. *Anal. Chem.* **2012**, *84*, 5407.

(81) Klett, O.; Nyholm, L. *Anal. Chem.* **2003**, *75*, 1245.

(82) Chang, B.-Y.; Mavré, F. o.; Chow, K.-F.; Crooks, J. A.; Crooks, R. M. *Anal. Chem.* **2010**, *82*, 5317.

(83) Cao, W.; Ferrance, J. P.; Demas, J.; Landers, J. P. *J. Am. Chem. Soc.* **2006**, *128*, 7572.

(84) Bouffier, L.; Doneux, T.; Goudeau, B.; Kuhn, A. *Anal. Chem.* **2014**, *86*, 3708.

(85) Wu, M.-S.; Yuan, D.-J.; Xu, J.-J.; Chen, H.-Y. *Chemical Science* **2013**, *4*, 1182.

(86) Guerrette, J. P.; Oja, S. M.; Zhang, B. *Anal. Chem.* **2012**, *84*, 1609.

(87) Cox, J. T.; Guerrette, J. P.; Zhang, B. *Anal. Chem.* **2012**, *84*, 8797.

(88) Zhang, X.; Li, J.; Jia, X.; Li, D.; Wang, E. *Anal. Chem.* **2014**, *86*, 5595.

(89) Wu, M.-S.; Liu, Z.; Shi, H.-W.; Chen, H.-Y.; Xu, J.-J. *Anal. Chem.* **2014**, *87*, 530.

(90) Tyurin, R.; Lyalikov, Y. S.; Zhdanov, S. I. *Russ. Chem. Rev.* **1972**, *41*, 1086.

(91) Christensen, C. R.; Anson, F. C. *Anal. Chem.* **1964**, *36*, 495.

(92) Osteryoung, R.; Anson, F. *Anal. Chem.* **1964**, *36*, 975.

(93) Hubbard, A.; Osteryoung, R.; Anson, F. *Anal. Chem.* **1966**, *38*, 692.

(94) Christensen, C. R.; Anson, F. C. *Anal. Chem.* **1963**, *35*, 205.

(95) Hubbard, A. T.; Anson, F. C. *Anal. Chem.* **1966**, *38*, 58.

(96) Hubbard, A.; Anson, F. *Anal. Chem.* **1964**, *36*, 723.

(97) Bamberger, R.; Strohl, J. *Anal. Chem.* **1969**, *41*, 1450.

(98) Konopka, S.; McDuffie, B. *Anal. Chem.* **1970**, *42*, 1741.

(99) Bard, A. J.; Faulkner, L. R. *Electrochemical Methods* **2001**, *2*, 482.

(100) Anderson, L. B.; Reilley, C. N. *J. Electroanal. Chem.* **1965**, *10*, 538.

(101) Anderson, L. B.; Reilley, C. N. *J. Electroanal. Chem.* **1965**, *10*, 295.

(102) McDuffie, B.; Anderson, L.; Reilley, C. *Anal. Chem.* **1966**, *38*, 883.

(103) Oglesby, D. M.; Omang, S. H.; Reilley, C. N. *Anal. Chem.* **1965**, *37*, 1312.

(104) Yildiz, A.; Kissinger, P. T.; Reilley, C. N. *Anal. Chem.* **1968**, *40*, 1018.

(105) Fan, F. R. F.; Bard, A. J. *J. Am. Chem. Soc.* **1987**, *109*, 6262.

(106) Lemay, S. G.; Kang, S.; Mathwig, K.; Singh, P. S. *Acc. Chem. Res.* **2012**, *46*, 369.

(107) Zhang, J.; Kuznetsov, A. M.; Medvedev, I. G.; Chi, Q.; Albrecht, T.; Jensen, P. S.; Ulstrup, J. *Chem. Rev.* **2008**, *108*, 2737.

(108) Fan, F.-R. F.; Bard, A. J. *Science* **1995**, *267*, 871.

(109) Singh, P. S.; Kätelhön, E.; Mathwig, K.; Wolfrum, B.; Lemay, S. G. *ACS nano* **2012**, *6*, 9662.

(110) Byers, J. C.; Paulose Nadappuram, B.; Perry, D.; McKelvey, K.; Colburn, A. W.; Unwin, P. R. *Anal. Chem.* **2015**, *87*, 10450.

(111) Nadappuram, B. P.; McKelvey, K.; Al Botros, R.; Colburn, A. W.; Unwin, P. R. *Anal. Chem.* **2013**, *85*, 8070.

(112) Ebejer, N.; Schnippering, M.; Colburn, A. W.; Edwards, M. A.; Unwin, P. R. *Anal. Chem.* **2010**, *82*, 9141.

(113) Ebejer, N.; Güell, A. G.; Lai, S. C.; McKelvey, K.; Snowden, M. E.; Unwin, P. R. *Annu. Rev. Anal. Chem.* **2013**, *6*, 329.

(114) Kang, S.; Nieuwenhuis, A. F.; Mathwig, K.; Mampallil, D.; Lemay, S. G. *ACS nano* **2013**, *7*, 10931.

(115) Walsh, D. A.; Lovelock, K. R.; Licence, P. *Chem. Soc. Rev.* **2010**, *39*, 4185.

(116) Lovelock, K. R.; Cowling, F. N.; Taylor, A. W.; Licence, P.; Walsh, D. A. *J. Phys. Chem. B.* **2010**, *114*, 4442.

(117) Gebbie, M. A.; Dobbs, H. A.; Valtiner, M.; Israelachvili, J. N. *Proc. Natl. Acad. Sci.* **2015**, *112*, 7432.

(118) Ma, C.; Contento, N. M.; Bohn, P. W. *J. Am. Chem. Soc.* **2014**, *136*, 7225.

(119) Kang, S.; Mathwig, K.; Lemay, S. G. *Lab on a Chip* **2012**, *12*, 1262.

(120) Kätelhön, E.; Hofmann, B.; Lemay, S. G.; Zevenbergen, M. A.; Offenhäusser, A.; Wolfrum, B. *Anal. Chem.* **2010**, *82*, 8502.

(121) Rassaei, L.; Singh, P. S.; Lemay, S. G. *Anal. Chem.* **2011**, *83*, 3974.

(122) Kätelhön, E.; Wolfrum, B. *Rev. Anal. Chem* **2012**, *31*, 7.

(123) Rothberg, J. M.; Hinz, W.; Rearick, T. M.; Schultz, J.; Mileski, W.; Davey, M.; Leamon, J. H.; Johnson, K.; Milgrew, M. J.; Edwards, M. *Nature* **2011**, *475*, 348.

(124) Vandaveer, W. R.; Woodward, D. J.; Fritsch, I. *Electrochim. Acta* **2003**, *48*, 3341.

(125) Thomas, J. H.; Kim, S. K.; Hesketh, P. J.; Halsall, H. B.; Heineman, W. R. *Anal. Chem.* **2004**, *76*, 2700.

(126) Yoon, H.; Hankins, P. T.; Varadan, V. K.; Harbaugh, R. E. *Electroanalysis* **2008**, *20*, 1147.

(127) Zevenbergen, M. A.; Krapf, D.; Zuiddam, M. R.; Lemay, S. G. *Nano Lett.* **2007**, *7*, 384.

(128) Wolfrum, B.; Zevenbergen, M.; Lemay, S. *Anal. Chem.* **2008**, *80*, 972.

(129) Brooks, J. C.; Ford, K. I.; Holder, D. H.; Holtan, M. D.; Easley, C. J. *Analyst* **2016**, *141*, 5714.

(130) Rubinstein, I.; Bard, A. J. *J. Am. Chem. Soc.* **1981**, *103*, 512.

(131) Ege, D.; Becker, W. G.; Bard, A. J. *Anal. Chem.* **1984**, *56*, 2413.

(132) Ordeig, O.; Godino, N.; del Campo, J.; Muñoz, F. X.; Nikolajeff, F.; Nyholm, L. *Anal. Chem.* **2008**, *80*, 3622.

(133) Fosdick, S. E.; Knust, K. N.; Scida, K.; Crooks, R. M. *Angew. Chem. Int. Ed.* **2013**, *52*, 10438.

(134) Jones, D. *Principles and Prevention of Corrosion*; NJ: Prentice-Hall, 1996.

(135) Oesch, U.; Janata, J. *Electrochim. Acta* **1983**, *28*, 1237.

(136) Hoogvliet, J.; Dijksma, M.; Kamp, B.; Van Bennekom, W. *Anal. Chem.* **2000**, *72*, 2016.

(137) Dale, S. E.; Vuorema, A.; Sillanpää, M.; Weber, J.; Wain, A. J.; Barnes, E. O.; Compton, R. G.; Marken, F. *Electrochim. Acta* **2014**, *125*, 94.

(138) Koizumi, Y.; Shida, N.; Tomita, I.; Inagi, S. *Chem. Lett.* **2014**, *43*, 1245.

(139) Koizumi, Y.; Shida, N.; Ohira, M.; Nishiyama, H.; Tomita, I.; Inagi, S. *Nat. Commun.* **2016**, *7*.

(140) Bard, A. J. *Electrogenerated chemiluminescence*; CRC Press, 2004.

(141) Feldberg, S. W. *J. Am. Chem. Soc.* **1966**, *88*, 390.

(142) Cruser, S. A.; Bard, A. J. *J. Am. Chem. Soc.* **1969**, *91*, 267.

(143) Collinson, M. M.; Wightman, R. M. *Anal. Chem.* **1993**, *65*, 2576.

(144) Van Duyne, R. P.; Fischer, S. F. *Chem. Phys.* **1974**, *5*, 183.

(145) Keszthelyi, C. P.; Tachikawa, H.; Bard, A. J. *J. Am. Chem. Soc.* **1972**, *94*, 1522.

(146) Pastore, P.; Magno, F.; Collinson, M.; Wightman, R. *J. Electroanal. Chem.* **1995**, *397*, 19.

(147) Miaw, L.-H. L.; Perone, S. *Anal. Chem.* **1979**, *51*, 1645.

(148) Collinson, M. M.; Wightman, R. M. *Science* **1995**, *268*, 1883.

(149) Collinson, M. M.; Pastore, P.; Maness, K. M.; Wightman, R. M. *J. Am. Chem. Soc.* **1994**, *116*, 4095.

(150) Wightman, R. M.; Curtis, C. L.; Flowers, P. A.; Maus, R. G.; McDonald, E. M. *J. Phys. Chem. B.* **1998**, *102*, 9991.

(151) Angnes, L.; Richter, E. M.; Augelli, M. A.; Kume, G. H. *Anal. Chem.* **2000**, *72*, 5503.

(152) Mehrgardi, M. A.; Ahangar, L. E. *Biosens. Bioelectron.* **2011**, *26*, 4308.

(153) Mehdi khoshfetrat, S.; Mehrgardi, M. A. *ChemElectroChem* **2014**, *1*, 779.

(154) Khoshfetrat, S. M.; Mehrgardi, M. A. *Analyst* **2014**, *139*, 5192.

(155) Kashefi-Kheyrabadi, L.; Mehrgardi, M. A.; Wiechec, E.; Turner, A. P.; Tiwari, A. *Anal. Chem.* **2014**, *86*, 4956.

(156) Karyakin, A. A.; Karyakina, E. E.; Schmidt, H. L. *Electroanalysis* **1999**, *11*, 149.

(157) Kelley, S. O.; Barton, J. K.; Jackson, N. M.; Hill, M. G. *Bioconjugate Chem.* **1997**, *8*, 31.

(158) Tuite, E.; Norden, B. *J. Am. Chem. Soc.* **1994**, *116*, 7548.

(159) Kang, D.; Zuo, X.; Yang, R.; Xia, F.; Plaxco, K. W.; White, R. J. *Anal. Chem.* **2009**, *81*, 9109.

(160) Hu, J.; Wang, T.; Kim, J.; Shannon, C.; Easley, C. J. *J. Am. Chem. Soc.* **2012**, *134*, 7066.

(161) Hu, J.; Yu, Y.; Brooks, J. C.; Godwin, L. A.; Somasundaram, S.; Torabinejad, F.; Kim, J.; Shannon, C.; Easley, C. J. *J. Am. Chem. Soc.* **2014**, *136*, 8467.

(162) Willey, T. M.; Vance, A. L.; Van Buuren, T.; Bostedt, C.; Terminello, L.; Fadley, C. *Surf. Sci.* **2005**, *576*, 188.

(163) Steel, A. B.; Herne, T. M.; Tarlov, M. J. *Anal. Chem.* **1998**, *70*, 4670.

(164) Wong, E. L.; Mearns, F. J.; Gooding, J. J. *Sens. Actuators, B-Chem.* **2005**, *111*, 515.

(165) Gooding, J. J. *Electroanalysis* **2002**, *14*, 1149.

(166) Gooding, J. J.; Mearns, F.; Yang, W.; Liu, J. *Electroanalysis* **2003**, *15*, 81.

(167) Chaki, N. K.; Vijayamohanan, K. *Biosens. Bioelectron.* **2002**, *17*, 1.

(168) Liu, J.; Cheng, L.; Liu, B.; Dong, S. *Langmuir* **2000**, *16*, 7471.

(169) Jaegfeldt, H.; Kuwana, T.; Johansson, G. *J. Am. Chem. Soc.* **1983**, *105*, 1805.

(170) Brooks, S. A.; Ambrose, W. P.; Kuhr, W. G. *Anal. Chem.* **1999**, *71*, 2558.

(171) Pantano, P.; Kuhr, W. G. *Anal. Chem.* **1993**, *65*, 623.

(172) Barbier, B.; Pinson, J.; Desarmot, G.; Sanchez, M. *J. Electrochem. Soc.* **1990**, *137*, 1757.

(173) Deinhammer, R. S.; Ho, M.; Anderegg, J. W.; Porter, M. D. *Langmuir* **1994**, *10*, 1306.

(174) Zen, J. M.; Senthil Kumar, A.; Tsai, D. M. *Electroanalysis* **2003**, *15*, 1073.

(175) Downard, A. J. *Electroanalysis* **2000**, *12*, 1085.

(176) Blaedel, W.; Jenkins, R. A. *Anal. Chem.* **1974**, *46*, 1952.

(177) Gonon, F.; Fombarlet, C.; Buda, M.; Pujol, J. F. *Anal. Chem.* **1981**, *53*, 1386.

(178) Garten, V.; Weiss, D.; Willis, J. *Aust. J. Chem.* **1957**, *10*, 295.

(179) Evans, J. F.; Kuwana, T. *Anal. Chem.* **1977**, *49*, 1632.

(180) Engstrom, R. C. *Anal. Chem.* **1982**, *54*, 2310.

(181) Anjo, D. M.; Kahr, M.; Khodabakhsh, M.; Nowinski, S.; Wanger, M. *Anal. Chem.* **1989**, *61*, 2603.

(182) Beilby, A. L.; Sasaki, T. A.; Stern, H. M. *Anal. Chem.* **1995**, *67*, 976.

(183) Palek, E.; Fojta, M. *Anal. Chem.* **1997**, *69*, 1457.

(184) Wang, J.; Rivas, G.; Fernandes, J. R.; Paz, J. L. L.; Jiang, M.; Waymire, R. *Anal. Chim. Acta* **1998**, *375*, 197.

(185) Wang, J.; Rivas, G.; Ozsoz, M.; Grant, D. H.; Cai, X.; Parrado, C. *Anal. Chem.* **1997**, *69*, 1457.

(186) Marrazza, G.; Chianella, I.; Mascini, M. *Biosens. Bioelectron.* **1999**, *14*, 43.

(187) Millan, K. M.; Mikkelsen, S. R. *Anal. Chem.* **1993**, *65*, 2317.

(188) Rasmussen, S. R.; Larsen, M. R.; Rasmussen, S. E. *Anal. Biochem.* **1991**, *198*, 138.

(189) Schedin, F.; Geim, A.; Morozov, S.; Hill, E.; Blake, P.; Katsnelson, M.; Novoselov, K. *Nat. Mater.* **2007**, *6*, 652.

(190) Li, D.; Müller, M. B.; Gilje, S.; Kaner, R. B.; Wallace, G. G. *Nat Nanotechnol.* **2008**, *3*, 101.

(191) Liu, Y.; Yu, D.; Zeng, C.; Miao, Z.; Dai, L. *Langmuir* **2010**, *26*, 6158.

(192) Hummers Jr, W. S.; Offeman, R. E. *J. Am. Chem. Soc.* **1958**, *80*, 1339.

(193) Lin, Y.; Lu, F.; Tu, Y.; Ren, Z. *Nano Lett.* **2004**, *4*, 191.

(194) Wong, S. S.; Joselevich, E.; Woolley, A. T.; Cheung, C. L.; Lieber, C. M. *Nature* **1998**, *394*, 52.

(195) Chen, J.; Hamon, M. A.; Hu, H.; Chen, Y.; Rao, A. M.; Eklund, P. C.; Haddon, R. C. *Science* **1998**, *282*, 95.

(196) Ago, H.; Kugler, T.; Cacialli, F.; Salaneck, W. R.; Shaffer, M. S.; Windle, A. H.; Friend, R. H. *J. Phys. Chem. B.* **1999**, *103*, 8116.

(197) Mehrgardi, M. A.; Daneshtalab, R. *J. Electroanal. Chem.* **2011**, *650*, 214.

(198) Kelley, S. O.; Boon, E. M.; Barton, J. K.; Jackson, N. M.; Hill, M. G. *Nucleic Acids Res.* **1999**, *27*, 4830.

(199) Boon, E. M.; Ceres, D. M.; Drummond, T. G.; Hill, M. G.; Barton, J. K. *Nat. Biotechnol.* **2000**, *18*, 1096.

(200) Boon, E. M.; Barton, J. K.; Bhagat, V.; Nersissian, M.; Wang, W.; Hill, M. G. *Langmuir* **2003**, *19*, 9255.

(201) Kashefi-Kheyrabadi, L.; Mehrgardi, M. A. *Biosens. Bioelectron.* **2012**, *33*, 184.

(202) Cheng, Q.; Brajter-Toth, A. *Anal. Chem.* **1992**, *64*, 1998.

(203) Dijksma, M.; Kamp, B.; Hoogvliet, J.; Van Bennekom, W. *Langmuir* **2000**, *16*, 3852.

(204) Akram, M.; Stuart, M. C.; Wong, D. K. *Anal. Chim. Acta* **2004**, *504*, 243.

(205) Dijksma, M.; Boukamp, B. A.; Kamp, B.; Van Bennekom, W. *Langmuir* **2002**, *18*, 3105.

(206) Abad, J. M.; Mertens, S. F.; Pita, M.; Fernández, V. M.; Schiffrin, D. J. *J. Am. Chem. Soc.* **2005**, *127*, 5689.

(207) Limbut, W.; Kanatharana, P.; Mattiasson, B.; Asawatreratanakul, P.; Thavarungkul, P. *Biosens. Bioelectron.* **2006**, *22*, 233.

(208) Kelley, S. O.; Jackson, N. M.; Hill, M. G.; Barton, J. K. *Angew. Chem. Int. Ed.* **1999**, *38*, 941.

(209) Kertesz, V.; Whittemore, N. A.; Chambers, J. Q.; McKinney, M. S.; Baker, D. C. *J. Electroanal. Chem.* **2000**, *493*, 28.

(210) Paleček, E.; Fojta, M.; Jelen, F. *Bioelectrochemistry* **2002**, *56*, 85.

(211) Umek, R. M.; Lin, S. W.; Vielmetter, J.; Terbrueggen, R. H.; Irvine, B.; Yu, C.; Kayyem, J. F.; Yowanto, H.; Blackburn, G. F.; Farkas, D. H. *J. Mol. Diagn.* **2001**, *3*, 74.

(212) Nakayama, M.; Ihara, T.; Nakano, K.; Maeda, M. *Talanta* **2002**, *56*, 857.

(213) Fan, C.; Plaxco, K. W.; Heeger, A. J. *Proc. Natl. Acad. Sci.* **2003**, *100*, 9134.

(214) Anne, A.; Bouchardon, A.; Moiroux, J. *J. Am. Chem. Soc.* **2003**, *125*, 1112.

(215) Zuo, X.; Song, S.; Zhang, J.; Pan, D.; Wang, L.; Fan, C. *J. Am. Chem. Soc.* **2007**, *129*, 1042.

(216) Boon, E. M.; Jackson, N. M.; Wightman, M. D.; Kelley, S. O.; Hill, M. G.; Barton, J. K. *J. Phys. Chem. B.* **2003**, *107*, 11805.

(217) Yang, W.; Ozsoz, M.; Hibbert, D. B.; Gooding, J. J. *Electroanalysis* **2002**, *14*, 1299.

(218) Rohs, R.; Sklenar, H.; Lavery, R.; Röder, B. *J. Am. Chem. Soc.* **2000**, *122*, 2860.

(219) Tani, A.; Thomson, A. J.; Butt, J. N. *Analyst* **2001**, *126*, 1756.

(220) Kerman, K.; Ozkan, D.; Kara, P.; Meric, B.; Gooding, J. J.; Ozsoz, M. *Anal. Chim. Acta* **2002**, *462*, 39.

(221) Erdem, A.; Kerman, K.; Meric, B.; Ozsoz, M. *Electroanalysis* **2001**, *13*, 219.

(222) Erdem, A.; Kerman, K.; Meric, B.; Akarca, U. S.; Ozsoz, M. *Anal. Chim. Acta* **2000**, *422*, 139.

(223) Meric, B.; Kerman, K.; Ozkan, D.; Kara, P.; Erensoy, S.; Akarca, U. S.; Mascini, M.; Ozsoz, M. *Talanta* **2002**, *56*, 837.

(224) Hammond, J. L.; Gross, A. J.; Estrela, P.; Iniesta, J.; Green, S. J.; Winlove, C. P.; Winyard, P. G.; Benjamin, N.; Marken, F. *Anal. Chem.* **2014**, *86*, 6748.

(225) Hasnat, M. A.; Gross, A. J.; Dale, S. E.; Barnes, E. O.; Compton, R. G.; Marken, F. *Analyst* **2014**, *139*, 569.

(226) Lucarelli, F.; Marrazza, G.; Turner, A. P.; Mascini, M. *Biosens. Bioelectron.* **2004**, *19*, 515.

(227) Delamar, M.; Hitmi, R.; Pinson, J.; Saveant, J. M. *J. Am. Chem. Soc.* **1992**, *114*, 5883.

(228) Anariba, F.; DuVall, S. H.; McCreery, R. L. *Anal. Chem.* **2003**, *75*, 3837.

(229) McCreery, R. L. *Chem. Rev.* **2008**, *108*, 2646.

(230) Downard, A. J. *Langmuir* **2000**, *16*, 9680.

(231) Brooksby, P. A.; Downard, A. J.; Yu, S. S. *Langmuir* **2005**, *21*, 11304.

(232) Brooksby, P. A.; Downard, A. J. *J. Phys. Chem. B.* **2005**, *109*, 8791.

(233) Cruickshank, A. C.; Tan, E. S.; Brooksby, P. A.; Downard, A. J. *Electrochem. Commun.* **2007**, *9*, 1456.

(234) Polsky, R.; Harper, J. C.; Dirk, S. M.; Arango, D. C.; Wheeler, D. R.; Brozik, S. M. *Langmuir* **2007**, *23*, 364.

(235) Adenier, A.; Chehimi, M. M.; Gallardo, I.; Pinson, J.; Vila, N. *Langmuir* **2004**, *20*, 8243.

(236) Teh, H. F.; Gong, H.; Dong, X.-D.; Zeng, X.; Tan, A. L. K.; Yang, X.; Tan, S. N. *Anal. Chim. Acta* **2005**, *551*, 23.

(237) Tornøe, C. W.; Christensen, C.; Meldal, M. *J. Org. Chem.* **2002**, *67*, 3057.

(238) Devadoss, A.; Chidsey, C. E. *J. Am. Chem. Soc.* **2007**, *129*, 5370.

(239) Waring, M. *J. Mol. Biol.* **1965**, *13*, 269.

(240) Chaires, J. B.; Dattagupta, N.; Crothers, D. M. *Biochemistry* **1982**, *21*, 3933.

(241) Wakelin, L. P.; Atwell, G. J.; Rewcastle, G. W.; Denny, W. A. *J. Med. Chem.* **1987**, *30*, 855.

(242) Odani, A.; Shimata, R.; Masuda, H.; Yamauchi, O. *Inorg. Chem.* **1991**, *30*, 2133.

(243) Barton, J. K.; Goldberg, J. M.; Kumar, C. V.; Turro, N. J. *J. Am. Chem. Soc.* **1986**, *108*, 2081.

(244) Pyle, A.; Rehmann, J.; Meshoyrer, R.; Kumar, C.; Turro, N.; Barton, J. K. *J. Am. Chem. Soc.* **1989**, *111*, 3051.

(245) Dougherty, G. *J. Inorg. Biochem.* **1988**, *34*, 95.

(246) Carter, M. T.; Rodriguez, M.; Bard, A. J. *J. Am. Chem. Soc.* **1989**, *111*, 8901.

(247) Kara, P.; Kerman, K.; Ozkan, D.; Meric, B.; Erdem, A.; Ozkan, Z.; Ozsoz, M. *Electrochem. Commun.* **2002**, *4*, 705.

(248) Millan, K. M.; Spurmanis, A. J.; Mikkelsen, S. R. *Electroanalysis* **1992**, *4*, 929.

(249) Johnston, D. H.; Cheng, C.-C.; Campbell, K. J.; Thorp, H. H. *Inorg. Chem.* **1994**, *33*, 6388.

(250) Johnston, D. H.; Glasgow, K. C.; Thorp, H. H. *J. Am. Chem. Soc.* **1995**, *117*, 8933.

(251) Armistead, P. M.; Thorp, H. H. *Anal. Chem.* **2000**, *72*, 3764.

(252) Holmberg, R. C.; Thorp, H. H. *Anal. Chem.* **2003**, *75*, 1851.

(253) Wang, J.; Cai, X.; Tian, B.; Shiraishi, H. *Analyst* **1996**, *121*, 965.

(254) Wang, J.; Kawde, A.-N.; Erdem, A.; Salazar, M. *Analyst* **2001**, *126*, 2020.

(255) Ariksoysal, D. O.; Karadeniz, H.; Erdem, A.; Sengonul, A.; Sayiner, A. A.; Ozsoz, M. *Anal. Chem.* **2005**, *77*, 4908.

(256) Wang, J.; Xu, D.; Erdem, A.; Polsky, R.; Salazar, M. A. *Talanta* **2002**, *56*, 931.

(257) Mbindyo, J.; Zhou, L.; Zhang, Z.; Stuart, J. D.; Rusling, J. F. *Anal. Chem.* **2000**, *72*, 2059.

(258) Latham, G. J.; Lloyd, R. S. *J. Biol. Chem.* **1994**, *269*, 28527.

(259) Zhou, L.; Rusling, J. F. *Anal. Chem.* **2001**, *73*, 4780.